

**PROCESSING AND PROPERTIES OF HIGH CARBON
MICROALLOYED STEELS**

By

Abdelbaset Elwazri

**A Thesis Submitted to the Faculty of Graduate Studies and Research in Partial
Fulfillment of the Requirements for the Degree of Doctor Philosophy**

Department of Mining, Metals and Materials Engineering

**McGill University
Montréal, Canada**

February 2004

© A. M. Elwazri



Library and
Archives Canada

Bibliothèque et
Archives Canada

Published Heritage
Branch

Direction du
Patrimoine de l'édition

395 Wellington Street
Ottawa ON K1A 0N4
Canada

395, rue Wellington
Ottawa ON K1A 0N4
Canada

Your file *Votre référence*
ISBN: 0-612-98246-7
Our file *Notre référence*
ISBN: 0-612-98246-7

NOTICE:

The author has granted a non-exclusive license allowing Library and Archives Canada to reproduce, publish, archive, preserve, conserve, communicate to the public by telecommunication or on the Internet, loan, distribute and sell theses worldwide, for commercial or non-commercial purposes, in microform, paper, electronic and/or any other formats.

The author retains copyright ownership and moral rights in this thesis. Neither the thesis nor substantial extracts from it may be printed or otherwise reproduced without the author's permission.

AVIS:

L'auteur a accordé une licence non exclusive permettant à la Bibliothèque et Archives Canada de reproduire, publier, archiver, sauvegarder, conserver, transmettre au public par télécommunication ou par l'Internet, prêter, distribuer et vendre des thèses partout dans le monde, à des fins commerciales ou autres, sur support microforme, papier, électronique et/ou autres formats.

L'auteur conserve la propriété du droit d'auteur et des droits moraux qui protègent cette thèse. Ni la thèse ni des extraits substantiels de celle-ci ne doivent être imprimés ou autrement reproduits sans son autorisation.

In compliance with the Canadian Privacy Act some supporting forms may have been removed from this thesis.

Conformément à la loi canadienne sur la protection de la vie privée, quelques formulaires secondaires ont été enlevés de cette thèse.

While these forms may be included in the document page count, their removal does not represent any loss of content from the thesis.

Bien que ces formulaires aient inclus dans la pagination, il n'y aura aucun contenu manquant.


Canada

ABSTRACT

Five steels were used in the present work to investigate the dynamic, static and metadynamic recrystallization behavior of hypereutectoid steels of 1 % carbon, alloyed with high silicon and microalloying levels of vanadium. Compression tests were performed using single and double hit schedules at temperatures between 875-1100 °C, strain rates of 0.01s^{-1} - 1s^{-1} , and inter-pass times of 0.1-500 seconds and 0.1-30 seconds for static recrystallization and metadynamic recrystallization, respectively. For dynamic recrystallization, it was found that an increase in carbon and vanadium content led to smaller grain sizes. Equations were generated that can be used to predict the critical strain for dynamic recrystallization. Of interest is the finding that there is an activation energy for deformation specifically associated with dynamic recrystallization (i.e. peak strain). This activation energy associated with the peak strain is lower than that associated with the steady state stress. This is contrary to Sellar's original observation that the peak strain is a function of the activation energy for deformation according to the Zener-Hollomon relationship. The static recrystallization kinetics were measured, and the appearance of 'plateau' regions where softening is arrested for a period of time was used to quantify the kinetics of strain-induced precipitation and generate the precipitation temperature time diagrams for the three steels. Despite the wide range of V levels, the steels exhibited very similar precipitation kinetics at all temperatures tested, being particularly close below 950 °C. A kinetic equation for static recrystallization is proposed which takes the V and Si concentrations into account. The metadynamic recrystallization results show that there is a transition strain region in which both static and metadynamic recrystallization take place during the inter-pass time. The results also revealed that V and Si have a strong solute drag effect, on the kinetics of metadynamic recrystallization. A kinetic equation for metadynamic recrystallization is proposed which takes the V and Si concentrations into account. The influence of chemistry on the microstructural characteristics and the mechanical properties in these steels was also investigated. The results show that a grain boundary cementite network exists in hypereutectoid steel without vanadium, with the thickness of this network increasing with increasing reheat temperature. Vanadium additions result in the formation of discrete

grain boundary cementite particles rather than a continuous network along the grain boundaries. The mechanical properties of the resulting microstructures were evaluated by shear punch tests at room temperature. The results show that alloying and hot working increase the strength and ductility of these steels.

RESUME

Dans cette thèse, nous avons étudié la recristallisation dynamique, statique et méta-dynamique de cinq nuances d'acier hypereutectoïde contenant 1% de carbone ainsi qu'une teneur élevée en silicium et différents niveaux de micro-addition de vanadium. Des tests de compressions (comprenant une déformation unique ou deux déformations successives) ont été réalisés à des températures comprises entre 875 et 1100 °C. Nous avons étudié des vitesses de déformation comprises entre 0.01s^{-1} et 1s^{-1} , des temps inter-passes entre 0.1 et 500 secondes, dans le cas de la recristallisation statique, et entre 0.1 et 30 secondes dans le cas de la recristallisation méta-dynamique. Dans le cas de la recristallisation dynamique, il a été mis en évidence qu'une augmentation de la teneur en carbone et vanadium provoquait un affinement de la taille de grain. Nous avons dérivé des équations qui permettent de prédire la déformation à laquelle la recristallisation dynamique débute (déformation critique). Il est particulièrement intéressant qu'une énergie d'activation pour la déformation soit reliée à la recristallisation dynamique (c'est-à-dire à la déformation correspondant à la contrainte maximale). Cette énergie d'activation est plus basse que celle correspondant à la contrainte dans le domaine stationnaire. Ceci est différent des observations de Sellars pour qui la déformation à contrainte maximale est reliée à l'énergie d'activation pour la déformation par la relation de Zener-Hollomon. Les cinétiques de recristallisation statique ont été mesurées. La présence de plateaux durant lesquels l'adoucissement est interrompu a permis de quantifier les cinétiques de précipitation induite par la déformation et de générer les diagrammes précipitation - température - temps des trois nuances. Malgré la large gamme de niveaux de V, les différentes nuances présentent des cinétiques de précipitation très similaires, surtout à des températures plus basses que 950 °C. Une équation pour représenter la cinétique de recristallisation statique est proposée. Cette équation prend en compte les teneurs en V et Si. Les résultats concernant la recristallisation méta-dynamique démontrent l'existence d'une gamme de niveaux de déformation dans laquelle la recristallisation est à la fois statique et méta-dynamique. Les résultats démontrent également que le silicium et le vanadium ralentissent les cinétiques de recristallisation méta-dynamique (*solute drag*). Une équation pour représenter la cinétique de

recristallisation statique est proposée. Cette équation prend en compte les teneurs en V et Si. L'influence de la composition sur les caractéristiques microstructurales a aussi été étudiée. Dans l'alliage sans vanadium, un réseau de cémentite est présent le long des joints de grain. L'épaisseur de ce réseau augmente lorsque la température de réchauffage augmente. Le réseau de cémentite disparaît avec l'addition de vanadium et est remplacé par des particules individuelles de cémentite. Les propriétés mécaniques ont été obtenues lors d'essais de poinçonnage. L'ajout d'éléments d'alliage ainsi que la déformation à chaud augmentent la résistance et la ductilité de ces aciers.

ACKNOWLEDGMENTS

I would like to express my sincere gratitude to my thesis supervisor, Professor S. Yue for his guidance, support and encouragement throughout the whole course of this research work. His knowledge in the field of physical metallurgy and material science was of great importance in this research work, and his patience and personal attitude have been inspiring during my graduate studies.

I am very grateful to Dr. P. Wanjara for her suggestion and encouragement in my graduate studies. I would like to express my appreciation to Edwin Fernandez and Lorraine Mello for their aid and friendship. Also, I would like to thank all the friends I have made during my time at McGill for making it a pleasant and enjoyable experience.

Last but not least, I wish to express my heartfelt gratitude to my family for their guidance, support and encouragement. Without their love none of this would have been possible.

TABLE OF CONTENTS

ABSTRACT	i
RESUME	iii
ACKNOWLEDGMENTS	v
TABLES OF CONTENTS	vi
LIST OF FIGURES	xi
LIST OF TABLE	xviii

CHAPTER 1

1. INTRODUCTION	1
1.1. Preface	1
1.2. Ferrite/Pearlite Structures of Plain Carbon Steels	3
1.2.1. Eutectoid Steels	3
1.2.2. Hypoeutectoid Steels	3
1.2.3. Hypereutectoid Steels	4
1.3. Research Objectives	6
1.4. Scope of the Thesis	7

CHAPTER 2

2. Literature Review	8
2.1. Metallurgical Aspects of Hot Deformation	8
2.1.1. Microstructural Changes During Hot Deformation	8
2.1.1.1. Restoration	8
2.1.1.2. Dynamic Recovery	9
2.1.1.3. Dynamic Recrystallization	10
2.1.1.4. Dynamically Recrystallized Grain Size	13
2.1.1.5. Static Recovery	15
2.1.1.6. Static Recrystallization	15
2.1.1.7. Statically Recrystallized Grain Size	18
2.1.1.8. Metadynamic Recrystallization	18
2.1.1.9. Metadynamically Recrystallized Grain Size	19
2.2 The Effect of Alloying Elements on Microstructural Evolution During Hot Deformation	20
2.2.1. Carbon	20
2.2.2. Effect of Other Alloying Elements in Solid Solution on Recrystallization	22
2.2.3. Effect of Alloying Elements As Precipitates	23

2.3. Pearlite Formation.....	23
2.4. Mechanical Properties of Pearlitic Steels	26
2.4.1. Effect of Alloying on Mechanical Properties of Medium to High Carbon Steels	28
2.4.1.1. Vanadium.....	29
2.4.1.2. Nitrogen.....	29
2.4.1.3. Silicon.....	31
2.4.1.4. Manganese	33

CHAPTER 3

3. Experimental Techniques.....	34
3.1. Experimental Materials.....	34
3.1.1. Steels Composition	34
3.1.2. Specimen Preparation.....	35
3.2. Experimental Equipment	36
3.2.1. Compression testing apparatus	36
3.2.2. Furnaces	37
3.2.4. Constant Strain Rate Testing	39
3.3. Thermal Cycles and Deformation Schedule.....	40
3.3.1. Solution Treatment	40
3.3.2. Single Hit Compression Testing Schedule.....	41
3.3.3. Double Hit Compression Tests	42
3.3.4. Measuring the Softening.....	43
3.3.5. Continuous Cooling Compression Testing Procedure.....	44
3.3.6 Mechanical Property.....	45
3.3.6. Heat-treated Specimens	45
3.3.7. Deformed Specimens.....	46
3.4. Mechanical Property Measurements	46
3.4.1. Shear Punch Test	46
3.4.2. Data Manipulation	47
3.5. Metallography.....	51
3.5.1. Optical microscopy.....	51
3.5.2. Field Emission Scanning Electron Microscopy (FE-SEM).....	52
3.5.3. Quantifying Pearlite.....	53

CHAPTER 4

4.1. Reheated Austenite Grain Size	56
4.2. Flow Curves	59
4.2.1. Single Hit Flow Curves	59
4.2.2. Double Hit Flow Curves.....	63
4.3. Continuous Cooling Compression (CCC)	67
4.4. Microstructural Results	69
4.4.1. Dynamically Recrystallized Grain Size	69

4.4.1.1. Vanadium and Silicon Steels	69
4.4.1.2. Hypereutectoid Steel	72
4.4.2. Metadynamically Recrystallized Grain Size	73
4.4.2.1. Vanadium and Silicon Steels	73
4.4.2.2. Hypereutectoid Steel	76
4.4.3. Statically Recrystallized Grain Size	77
4.4.3.1. Vanadium and silicon steels	77
4.4.3.2. Hypereutectoid Steel	80
4.5. Metadynamic Recrystallization Characteristics	81
4.5.1. Effect of Deformation Parameters on the Metadynamic	
Softening	81
4.5.1.1. Strain	81
4.5.1.2. Strain Rate	82
4.5.1.3. Deformation Temperature	85
4.5.1.4. Initial Grain Size	87
4.6. Static Recrystallization Characteristic	88
4.6.1. Effect of Deformation Parameters on the Softening.....	88
4.6.1.1. Strain	88
4.6.1.2. Strain Rate.....	91
4.6.1.3. Deformation Temperature	92
4.6.1.3.1. Hypereutectoid Steel.....	92
4.6.1.3.2. Vanadium and Silicon Steels	93
4.6.1.4. Initial Grain Size	96
4.6.2. Precipitation Time Temperature Diagrams	97
4.7. Effect of Thermomechanical Variables on Pearlite	
Characteristics	99
4.7.1. Effect of Heat Treatment	99
4.7.1.1. Hypereutectoid steel.....	99
4.7.1.2 Vanadium and Silicon Steels	101
4.7.2. Effect of Deformation on Microstructure.....	108
4.8. Precipitation Characteristics	112
4.9. Mechanical Properties	116
4.9.1. Heat Treated Specimens	116
4.9.1.1. Strength.....	116
4.9.1.2. Ductility	121
4.9.1.3. Formability	121
4.9.2. Hot Deformed Specimens.....	125
4.9.2.1. Strength.....	125
4.9.2.2. Ductility	127
4.9.2.3. Formability	129

CHAPTER 5

5.1. Dynamic Recrystallization	131
5.1.1. Effect of the Deformation Temperature on the Peak Strain ...	131
5.1.2. Activation Energy of Deformation	132

5.1.3. Comparison of High Carbon Steel with Low Carbon Steel.....	137
5.2. Static Recrystallization (Microalloyed Steels).....	140
5.2.1. Modeling the Kinetics of static recrystallization.....	140
5.2.1.1. Determination of “n”.....	141
5.2.2. Determination of the Dependence of $t_{0.5}$ on the Deformation Parameters	144
5.2.2.1. Effect of Strain.....	144
5.2.2.2. Effect of Strain Rate.....	145
5.2.2.3. Activation Energy of Deformation.....	145
5.2.3. Recrystallization Precipitation Temperature Time Diagram..	149
5.2.4. Modeling of Precipitation Kinetics.....	151
5.3. Metadynamic Recrystallization	156
5.3.1. Determination of n	157
5.3.2. Determination of the Dependence of $t_{0.5}$ on the Deformation Parameters	159
5.3.2.1. Effect of Strain Rate.....	159
5.3.2.2. Activation Energy of Metadynamic Recrystallization	160
5.3.2.3. Effect of Strain on Softening Behavior	163
5.3.3. Modeling Static Softening.....	165
5.3.3.1. Region I: $\varepsilon < \varepsilon_c$	166
5.3.3.2. Region III: $\varepsilon > \varepsilon_T$	167
5.3.3.3. Region II: $\varepsilon_c < \varepsilon < \varepsilon_T$	167
5.3.3.4. Comparison of the Empirical Restoration Kinetics with Experimental Data for Steel A.....	170
5.4. Hypereutectoid Steel.....	173
5.4.1. Modelling the Effect of Deformation Conditions on the Kinetics of Metadynamic and Static Recrystallization	173
5.4.1.1. Determination of n	173
5.4.1.2. Effect of Strain Rate.....	175
5.4.1.3. Effect of Strain.....	176
5.4.1.4. Activation Energy of Deformation.....	177
5.4.2. Effect of Carbon Content on Static Restoration	180
5.5. Microstructures	183
5.5.1. Heat treatment Effect on Nodule Size	184
5.5.2. Heat treatment Effect on Pearlite Colony Size.....	187
5.6. Mechanical Properties	190
5.6.1. Heat treated Specimens.....	190
5.6.1.1. Strength.....	190
5.6.1.1.1. Hypereutectoid Steel	190
5.6.1.1. Vanadium and Silicon Steels	193
5.6.1.2. Ductility	196
5.6.2. Hot deformed specimens.....	199
5.6.2.1. Strength.....	199
5.6.2.1.1. Hypereutectoid Steel	199
5.6.2.1.2. Vanadium and Silicon Steels	200

5.6.2.2. Ductility201

CHAPTER6

Conclusions204

Statement of Originality and Contribution to Knowledge207

References208

LIST OF FIGURES

CHAPTER 1

Figure (1-1) The Iron-Iron Carbide phase diagram. Schematic representation of changes in microstructure during the slow cooling of a) Hypoeutectoid steels b) Eutectoid steels c) Hypereutectoid steels	5
--	---

CHAPTER 2

Figure (2-1) Schematic illustration of a true stress-strain curve for dynamic recovery ..	10
Figure (2-2) Schematic stress-strain curve for austenite at elevated temperature	11
Figure (2-3) Steady state grain size D_s dependence on Z and the relationship the initial grain size [11]	14
Figure (2-4) Variation in the peak strain with Z for high and low carbon steels [51].....	21
Figure (2-5) Schematic representation of pearlite formation by nucleation and growth; (a) through (d) indicate successive steps in time sequence	25
Figure (2-6) Schematic diagram illustration of pearlite morphology	27
Figure (2-7) Yield and tensile strength plotted against Si content [93].....	32
Figure (2-8) Interlamellar spacing plotted against Si content [93]	32

CHAPTER 3

Figure (3-1) Schematic cross-section through the compression testing equipment	37
Figure (3-2) Quenching system, (A) lever arm, (B) quench chute, (C) salt bath and (D) furnace digital controller.	38
Figure (3-3) Schematic illustration of the TMP schedule for characterizing dynamic recrystallization.	42
Figure (3-4) Schematic illustration of the TMP schedule for characterizing static and metadynamic recrystallization.	43
Figure (3-5) Measurement of the softening by the 0.2% offset.	44
Figure (3-6) Continuous Cooling Compression (CCC) test schedule.	45
Figure (3-7) Schematic illustration showing the shear punch unit.....	47
Figure (3-8) A typical load-displacement curve for steels.....	49
Figure (3-9) Comparison of the shear yield data with yield strength from uniaxial tensile data. The solid line is the regression line for the yield data.	50

Figure (3-10) Comparison of the ultimate tensile strength determined by the shear punch and uniaxial tensile data. The solid line is the regression line for the maximum load data.	50
Figure (3-11) Comparison of D_f/t with percent elongation measured in uniaxial tension. The solid line is the regression line for the ductility data.	51

CHAPTER 4

Figure (4-1) Reheated austenite microstructures of the A steel: (a) 1200°C, (b) 1100°C (c) 1000°C and (d) 900°C.	57
Figure (4-2) Reheated austenite microstructures for four steels at 1000°C: (a) A, (b) B (c) C and (d) E.	58
Figure (4-3) Effect of austenitizing temperature on prior austenite grain size.	59
Figure (4-4) Stress-Strain curves for steels (a) A, (b) B, (c) C, (d) D and (e) E.	62
Figure (4-5) Stress-strain curves determined for steel A showing the softening taking place at 1050°C for different unloading times (a) 0.01 s^{-1} and (b) 0.1 s^{-1}	64
Figure (4-6) Stress-strain curves determined for steel B showing the softening taking place at 925°C for different unloading times at a strain rate 0.01 s^{-1}	65
Figure (4-7) Stress-strain curves determined for steel C showing the softening taking place at 1050°C for different unloading times at strain rate 0.01 s^{-1}	65
Figure (4-8) Stress-strain curves for steel E showing the softening taking place at (a) 1050°C and (b) 950°C for different unloading times at strain rate 0.01 s^{-1}	66
Figure (4-9) Theoretical flow stress behavior during CCC testing.	67
Figure (4-10) True stress-strain curves of steels A, B, C and E obtained by continuous cooling compression testing. Arrows labeled 1 and 2 represent the first and second deviations.	69
Figure (4-11) Dynamically recrystallized microstructure of steel A deformed (a) 950°C at strain rate = 1 s^{-1} and (b) 1000°C at strain rate = 1 s^{-1}	70
Figure (4-12) Dynamically recrystallized grain size for vanadium and silicon steels. ...	71
Figure (4-13) Effect of silicon and vanadium on the constant B_{rex}	72

Figure (4-14) Metadynamically recrystallized microstructures in the B steel after deformation strain rate = $0.1s^{-1}$ (a) $1050^{\circ}C$ and (b) $1000^{\circ}C$	73
Figure (4-15) Metadynamically recrystallized microstructures in the B steel after deformation at $1050^{\circ}C$ (a) $0.1s^{-1}$ and (b) $1s^{-1}$	74
Figure (4-16) Grain size (MDRX) for V and Si steels.	75
Figure (4-17) Effect of V and Si on the constant B_{mdrx}	75
Figure (4-18) $\ln(d_{mdrx})$ plotted as function of the $\ln(Z)$	77
Figure (4-19) Statically recrystallized microstructures after deformation at $1050^{\circ}C$ at strain rate $0.1s^{-1}$ (a) steel A and (b) steel C.....	78
Figure (4-20) $\ln(d_{srx})$ plotted as function of the $\ln(\text{strain})$	79
Figure (4-21) Effect of V and Si on the constant B_{srx}	79
Figure (4-22) $\ln(d_{srx})$ plotted as function of the $\ln(\text{strain})$	80
Figure (4-23) Effect of strain on softening in steels (a) A, (b) E	82
Figure (4-24) Effect of strain rate on softening in steels (a) A, (b) B and (c) C, and (d) E	84
Figure (4-25) Effect of temperature deformation on softening in steels (a) A, (b) B and (c) C, and (d) E.....	87
Figure (4-26) Effect of strain on softening in steels (a) A, (b) B (c) C and (d) E.....	90
Figure (4-27) Effect of strain rate on softening in steel A.....	91
Figure (4-28) Effect of strain rate on softening in steel E.	92
Figure (4-29) Effect of temperature deformation on softening in steel E.	93
Figure (4-30) Effect of temperature on static softening kinetics for steel A at a strain rate of $0.01s^{-1}$	94
Figure (4-31) Effect of temperature on static softening kinetics for steel B at a strain rate of $0.01s^{-1}$	95
Figure (4-32) Effect of temperature on static softening kinetics for steel C at a strain rate of $0.01s^{-1}$	95
Figure (4-33) Effect of initial grain size on softening.	97
Figure (4-34) Precipitation start temperature time curves, P_s , for the steel A, B and C acquired by the present double compression technique at strain rate $0.01s^{-1}$	98

Figure (4-35) Precipitation finish temperature time curves, P_f , for the steel A, B and C acquired by the present double compression technique at strain rate $0.01s^{-1}$	99
Figure (4-36) Optical micrographs showing the microstructure of the steel E.....	101
Figure (4-37) Optical micrographs showing the microstructure of the A.	102
Figure (4-38) FE-SEM images showing the microstructure of steels A and C austenitized at $1200^{\circ}C$ and transformed at $620^{\circ}C$	103
Figure (4-39) Low voltage imaging using a FE-SEM at higher magnifications to show the grain boundary cementite particles in steel A austenitized at $1200^{\circ}C$ and transformed at $620^{\circ}C$	103
Figure (4-40) Optical micrographs showing the microstructure of the steel E.....	109
Figure (4-41) FE-SEM micrograph of steel E, isothermally transformed at $620^{\circ}C$ for 10 minutes showing ferritic lamellae separated by cementite plates.	114
Figure (4-42) FE-SEM micrographs of steel A, isothermally transformed at $620^{\circ}C$ for 10 minutes, showing cementite plates (white arrow) and fine precipitates in ferritic lamellae (black arrow).....	114
Figure (4-43) FEG-SEM micrographs of steel A showing fine precipitates (arrows) in the ferrite phase and no precipitation in the cementite structure.	115
Figure (4-44) EDAX of the precipitate phase in ferrite lamella showing the presence of V and C in the precipitate (solid line) and no vanadium in the ferrite next to the precipitate (dashed line).	115
Figure (4-45) Ultimate stress after heat treatment at (a) $1200^{\circ}C$, (b) $1100^{\circ}C$, (c) $1000^{\circ}C$ and (d) $900^{\circ}C$	118
Figure (4-46) Yield stress after heat treatment at (a) $1200^{\circ}C$, (b) $1100^{\circ}C$, (c) $1000^{\circ}C$ and (d) $900^{\circ}C$	120
Figure (4-47) Elongation after heat treatment at (a) $1200^{\circ}C$, (b) $1100^{\circ}C$ (c) $1000^{\circ}C$ and (b) $900^{\circ}C$	123
Figure (4-48) Formability after heat treatment at (a) $900^{\circ}C$, and (b) $1200^{\circ}C$	124
Figure (4-49) Ultimate stress after deformation at (a) $1200^{\circ}C$ and (b) $900^{\circ}C$	126
Figure (4-50) Yield stress after deformation at (a) $1200^{\circ}C$ and (b) $900^{\circ}C$	127
Figure (4-51) Elongation after deformation at (a) $900^{\circ}C$, and (b) $1200^{\circ}C$	128

Figure (4-52) Formability after deformation at (a) 1200°C, and (b) 900°C	130
---	-----

CHAPTER 5

Figure (5-1) Peak strain as a function of the inverse absolute temperature at strain rate 0.01s ⁻¹ . Solvus temperature for VC are circled.	132
Figure (5-2) Effect of temperature on the peak strain at strain rate 0.01s ⁻¹	133
Figure (5-3) Effect of temperature on the steady state stress at strain rate 0.01s ⁻¹	134
Figure (5-4) Effect of V on activation energy.....	135
Figure (5-5) Effect of V on the constant A _{ep}	136
Figure (5-6) Comparison between predicted and measured ε _p values using equation 5-3	137
Figure (5-7) Comparison between the present work (Compression), CANMET McGill model and Sellars (Torsion) equation for plain carbon steels.....	139
Figure (5-8) Comparison between the present work (convert the compression values to the torsion values), CANMET McGill model and Sellars equation for plain carbon steels (Torsion values).....	140
Figure (5-9) Dependence of ln(ln(1/1-X)) on ln(time) for steels A, B and C.....	143
Figure (5-10) Effect of strain on the static t _{0.5}	144
Figure (5-11) Plot of t _{0.5} against the reciprocal of the temperature for V and Si steels.	146
Figure (5-12) Effect of V and Si on the constant A _{srx}	147
Figure (5-13) Comparison between measured t _{0.5} and those predicted with effect of [Si + V] included. (The line indicates a perfect correlation.).....	148
Figure (5-14) Comparison between measured t _{0.5} and those predicted without effect of [Si + V] showing poor agreement. (The line indicates a perfect correlation.).....	148
Figure (5-15) Recrystallization-precipitation-temperature-time diagram.	150
Figure (5-16) Comparison between experimental PTT data and the VC precipitation equation 5-21 for steels A, B and C.....	154
Figure (5-17) Comparison between the Dutta-Sellars model modified for VN precipitation in a low C steel, and the data of Medina [186].....	156
Figure (5-18) Dependence of ln(ln(1/1-X)) on ln(time) for steels A, B and C.....	158

Figure (5-19) Effect of strain rate on the metadynamic $t_{0.5}$	159
Figure (5-20) $\ln(t_{0.5}/Z^{-0.6})$ plotted as function of the inverse absolute temperature.....	160
Figure (5-21) Effect of silicon and vanadium on the constant A_{MDRX}	161
Figure (5-22) Comparison between measured $t_{0.5}$ and those predicted with effect of [Si + V] included. (The line indicates a perfect correlation)	162
Figure (5-23) Comparison between measured $t_{0.5}$ and those predicted without effect of [Si + V] showing poor agreement. (The line indicates a perfect correlation).....	163
Figure (5-24) Effect of strain on softening for steel A	165
Figure (5-25) Effect of strain on static softening processes	166
Figure (5-26) Modeling of post-dynamic softening in the three ranges of deformation.....	171
Figure (5-27) Comparison between model and experimental results.....	172
Figure (5-28) Dependence of $\ln(\ln(1/1-X))$ on $\ln(\text{time})$ metadynamic recrystallization.	174
Figure (5-29) Dependence of $\ln(\ln(1/1-X))$ on $\ln(\text{time})$ static recrystallization.	174
Figure (5-30) Effect of strain rate on the static and metadynamic recrystallization $t_{0.5}$	176
Figure (5-31) Effect of strain on the static recrystallization $t_{0.5}$	177
Figure (5-32) $\ln(t_{0.5}/Z^{-0.61})$ plotted as function of the inverse absolute temperature. ...	178
Figure (5-33) $\ln(t_{0.5})$ plotted as function of the inverse absolute temperature.....	179
Figure (5-34) Comparison between the model for static recrystallization and the data of Xu for high carbon steel [207].....	181
Figure (5-35) Effect of reheat temperature on the nodule size for the hypereutectoid steels A, B, C and E processed at a transformation temperature of 620°C.	185
Figure (5-36) Effect of prior-austenite grain size on the nodule size for the hypereutectoid steels A, B, C and E processed at a transformation temperature of 620°C.	185
Figure (5-37) Effect of the transformation temperature on nodule size for different prior-austenite grain sizes (reheat temperature) for steel E.	186

Figure (5-38) Effect of the transformation temperature on nodule size for different prior-austenite grain sizes (reheat temperature) for steel A	187
Figure (5-39) The effect of the average pearlite transformation temperature on pearlite colony size in steels A, B, C and E.	189
Figure (5-40) The effect of the prior austenite grain size on pearlite colony size in steels A, B, C and E.....	189
Figure (5-41) Predicted and measured yield stress for hypereutectoid steel. The line indicates a perfect correlation between prediction and measured values.	191
Figure (5-42) Predicted and measured yield stress for hypereutectoid steel. The line indicates a perfect correlation between prediction and measured values.	192
Figure (5-43) Predicted and measured yield stress for steels A B and C	195
Figure (5-44) Predicted and measured yield stress for steels A B C and E.....	196
Figure (5-45) Elongation versus interlamellar spacing of pearlite for steels A B C and E.....	197
Figure (5-46) Predicted and measured elongation for steels A, B, C and E.....	198
Figure (5-47) Predicted and measured yield stress for hypereutectoid steel	200
Figure (5-48) Predicted and measured yield stress for steels A B C and E.....	201
Figure (5-49) Elongation versus interlamellar spacing of pearlite for steels A B C and E	202
Figure (5-50) Predicted and measured elongation for steels A, B, C and E.....	203
Figure (5-51) Predicted and measured elongation for steels A, B, C and E with out the prior austenite grain size parameter.....	203

LIST OF TABLES

CHAPTER 3

Table 3-1. Chemical composition of experimental steels (wt%)	35
Table 3-2 Calculated solution temperatures of the steels	41

CHAPTER 4

Table 4-1 Nose temperature for steels A B and C	98
Table 4-2 Thicknesses of the cementite network	100
Table 4-3 The effect of heat treatment on the microstructure of steel A	105
Table 4-4 The effect of heat treatment on the microstructure of steel B	106
Table 4-5 The effect of heat treatment on the microstructure of steel C	107
Table 4-6 The effect of heat treatment on the microstructure of steel E	108
Table 4-7 Thicknesses of the cementite network	109
Table 4-8 The effect of deformation on the microstructure of steel A	110
Table 4-9 The effect of deformation on the microstructure of steel B	110
Table 4-10 The effect of deformation on the microstructure of steel C	111
Table 4-11 The effect of deformation on the microstructure of steel E.....	111
Table 4-12 Percentage decrease in pearlite microstructural characteristics after at 1200°C	112
Table 4-13 Mechanical properties of steels austenitized at 900°C with transformation temperatures.....	121

CHAPTER 5

Table 5-1 Values of activation energy for deformation and associated constants for the four steels.....	135
Table 5-2 Activation energies hot deformation.....	146
Table 5-3 Precipitation start time for the three tested steels as detected by the fractional softening method.....	151
Table 5-4 Precipitate start times for steels A, B and C; predicted and measured	154
Table 5-5 Listing of exponent 'n' values for SRX and MDRX	157
Table 5-6 Values of parameters.....	164

Table 5-7. List of equations used to model the fraction recrystallized in the microalloyed hypereutectoid steels	169
Table 5-8. List of equations used to model the fraction recrystallized in the hypereutectoid steel.....	180
Table 5-9 Prediction equations for static recrystallization of C-Mn steels	182
Table 5-10 Some reported value of Hall-Petch parameters	190
Table 5-11 Yield Stress analyses for hypereutectoid steel.....	193
Table 5-12 Ductility analyses for hypereutectoid steel.....	199

CHAPTER 1

1. Introduction

1.1. Preface

Steels are quantitatively and historically one of the most important materials in structural applications. Steels are inexpensive and have the unparalleled advantage over most materials of possessing a wide range of mechanical properties. The final advantage of steels lies in the fact that they can be processed very economically to adopt the desired component shape.

Microalloyed steels usually have low carbon content. However, high carbon microalloyed steels are of interest for wire rod and rails. Fine pearlite has relatively high strength, but it is also characterized by good drawability, which is important for wire rod applications, and by high wear resistance, which is of much importance for rails. The present work is to study the influence of V and Si content on the mechanical properties of high carbon microalloyed steels. The addition of V in steel is considered to have two primary effects: i) as an inhibitor of austenite grain coarsening during reheating, and ii) precipitation hardening due to V(C, N) in the low temperature transformation product.

The effect of Si on the thermodynamics of precipitation was taken into account as early as the 1950s, and continues to be of interest. It has been suggested that Si addition decreases the solubility of V(C, N) because it increases the activities of C and N. It

therefore, *increases* the precipitation rate of V(C, N), in microalloyed steels and can prevent softening during hot rolling [1].

The characteristic phase mixture of ferrite and cementite in steels, known as pearlite, was discovered about 160 years ago and the fundamental theories of its formation and mechanical properties were considered to be firmly established between the 1940s and the 1960s.

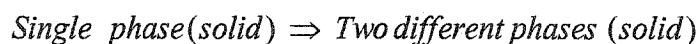
Since the 1970s, a great deal of progress has been made on the microalloying of low carbon steels, especially in the area of thermomechanical processing, by examining the microstructural evolution during hot rolling using mathematical models. Microalloying and controlled processing is a direct and cost competitive route to improved strength levels for ferrite/pearlite structures, and can be compared favorably with more conventional approaches of normalizing or quenching and tempering. In the case of microalloyed steel, the main mechanisms responsible for strengthening low carbon steels with a predominantly ferrite microstructure are the refinement of ferrite grains, and precipitation strengthening [2, 3]. The effect of microalloying additions on eutectoid steels, which are more or less 100% pearlitic, is not as well documented, and is the topic of this thesis.

One of the most influential microalloying elements is V. It is added to develop high strength in low-alloyed steels up to eutectoid composition range. Vanadium forms a nitride, which leads to a fine ferrite grain size, and precipitates as a carbide or carbonitride in ferrite, which imparts precipitation strengthening. In high carbon steels, it has been found to provide useful increases in tensile strength for as-hot rolled pearlitic rod; this benefit is retained during wire drawing.

1.2. Ferrite/Pearlite Structures of Plain Carbon Steels

1.2.1. Eutectoid Steels

The carbon content of a eutectoid steel is 0.8 wt%. If it is heated into the austenite region and allowed to cool slowly, pearlite forms, as presented in Figure (1-1). The phase change from austenite to ferrite and cementite takes place at the constant temperature of 723°C, and below this temperature the structure consists of a lamellar arrangement of ferrite and cementite. This structure is also termed *eutectoid*. The *eutectoid reaction* may be expressed as:



The eutectoid steel is hard and brittle. The α (ferrite) is a soft phase containing just a little carbon in solid solution. The Fe_3C (cementite) is a hard, brittle phase, which impedes dislocation motion in the ferrite and therefore *increases* strength but *decreases* ductility.

1.2.2. Hypoeutectoid Steels

The prefix “hypo” literally means “below”. Thus, hypoeutectoid steel is of composition below that of the eutectoid. Consider the slow cooling of such a steel from the austenite phase as shown in Figure (1-1). The grains of austenite begin to transform to grains of ferrite, which begin to nucleate at the austenite grain boundaries. The microstructure at room temperature consists of primary ferrite and pearlite.

1.2.3. Hypereutectoid Steels

Hypereutectoid steels are of a composition above the eutectoid. When cooled from the single phase austenite region, the austenite decomposes by initially forming cementite at the grain boundaries and, also, within the austenite grains. The composition of the remaining austenite decreases, with respect to carbon, as the temperature decreases, until the austenite achieves the eutectoid composition. This remaining austenite then transforms to pearlite at the eutectoid temperature.

Hypereutectoid steels have been generally rejected by industry as a structural material due to brittleness at room temperature, and industrial needs for higher strength steels has been directed to various developments of alloyed steels. The primary reason for the low ductility in hypereutectoid steels is the presence of the proeutectoid carbide network.

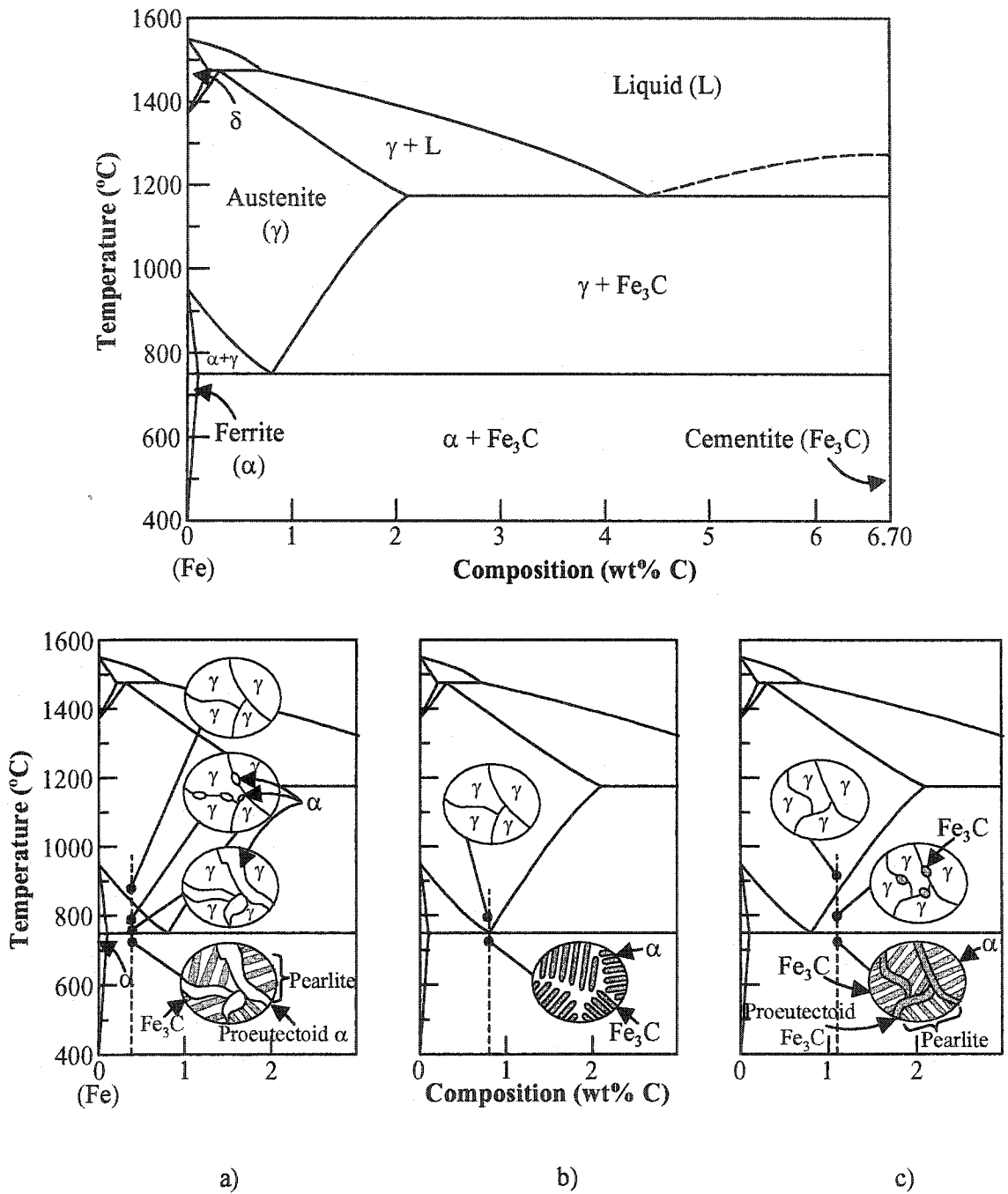


Figure (1-1) The Iron-Iron Carbide phase diagram. Schematic representation of changes in microstructure during the slow cooling of a) Hypoeutectoid steels b) Eutectoid steels c) Hypereutectoid steels.

1.2. Research Objectives

The objectives of this research are:

- To study the influence of V and Si on the dynamic recrystallization characteristics. These steels are targeted for rod production, which inevitably involves dynamic recrystallization. Dynamic recrystallization was measured by the single hit deformation technique using compression testing. These results were then used to determine the dependence of the peak strain on vanadium and silicon content.
- To characterize both static and metadynamic recrystallization and to develop a mathematical expression that can be incorporated into models for prediction of microstructural evolution in hypereutectoid steel during hot deformation.
- To study the influence of the V and Si levels on static recrystallization kinetics. The recrystallized fraction was measured by a double deformation technique. These results were used to calculate the time for 50 % recrystallization and to measure its dependence on the V and Si content, both in dissolved and precipitate form, as well as to find the temperature at which recrystallization starts to be inhibited.
- To examine the effect of heat treatments, deformation and transformation temperature on microstructure and mechanical properties in hypereutectoid steels of 1% C with different levels of V and Si.

1.4. Scope of the Thesis

The metallurgical aspects of hot deformation are reviewed in chapter 2. Specifically, the effect of carbon on microstructure during hot deformation is presented and the formation pearlite is described. The mechanical properties of pearlitic steels are also considered. In chapter 3, the experimental material and equipment employed in this work are described, and three methods referred to here as the continuous cooling compression test, isothermal compression test and heat treatment are reviewed. The microstructures were characterized using optical microscopy, image analysis and Field Emission Scanning Electron Microscopy (FE-SEM). Finally, the room temperature mechanical properties were determined using a shear punch test method. The experimental results pertaining to dynamic, metadynamic and static recrystallization are gathered and heat treatment and deformation on pearlite structure are given in chapter 4. In chapter 5, the experimental results are discussed. Finally, the conclusions of this study are presented in chapter 6.

CHAPTER 2

2. Literature Review

In this chapter, the metallurgical concepts relevant to hot deformation are reviewed. The mechanisms during deformation are first considered and the restoration mechanisms are described. The effect of alloying elements in solid solution on recrystallization is presented. The connection between microstructure and mechanical properties is then considered.

2.1. Metallurgical Aspects of Hot Deformation

There presently exists a good understanding of much of the metallurgy of hot working, but empiricism has been used extensively to develop thermomechanical-processing models for microstructural control.

2.1.1. Microstructural Changes During Hot Deformation

2.1.1.1. Restoration

During the process of controlled rolling, softening can occur by the mechanisms of recovery and recrystallization, either during deformation, or between successive deformations. The predominant softening mechanisms depend on the processing

parameters: temperature, strain and strain rate and the microstructural parameters, such as grain size, stacking fault energy and precipitate characteristics [4, 5].

When crystalline materials are deformed at elevated temperatures, two processes of restoration continuously reduce the accumulated dislocation density. Recovery leads to the annihilation of dislocations, as well as to the formation of sub-grains and sub-boundaries. In high stacking fault energy materials, such recovery processes completely balance the effects of straining and of work hardening, leading to the establishment of steady state flow. By contrast, in materials of moderate to low stacking fault energy, the dislocation density increases to appreciably higher levels; eventually the local differences in dislocation density are high enough to permit the nucleation of recrystallization during deformation, leading to the elimination of large numbers of dislocations by the migration of high angle grain boundaries. There are three different types of recrystallization: dynamic, static and metadynamic.

2.1.1.2. Dynamic Recovery

Restoration occurring during the deformation process is referred to as dynamic. For ferrite in carbon steels, dynamic recovery is the only restoration process during hot deformation, even at large strains [6, 7]. For austenite, recovery is more difficult, and increasing strains eventually lead to dynamic recrystallization. When dynamic recovery alone occurs, the flow curve is as shown in Figure (2-1). Beyond yielding, work hardening is being offset by dynamic recovery, but the work hardening predominates. Eventually the steady-state strain, ϵ_{ss} , is reached where the dislocation density remains constant because the rate of recovery is equal to the rate of dislocations production. The level of the steady-state flow stress (σ_{ss}) depends on the prevailing conditions of temperature, strain and strain rate.

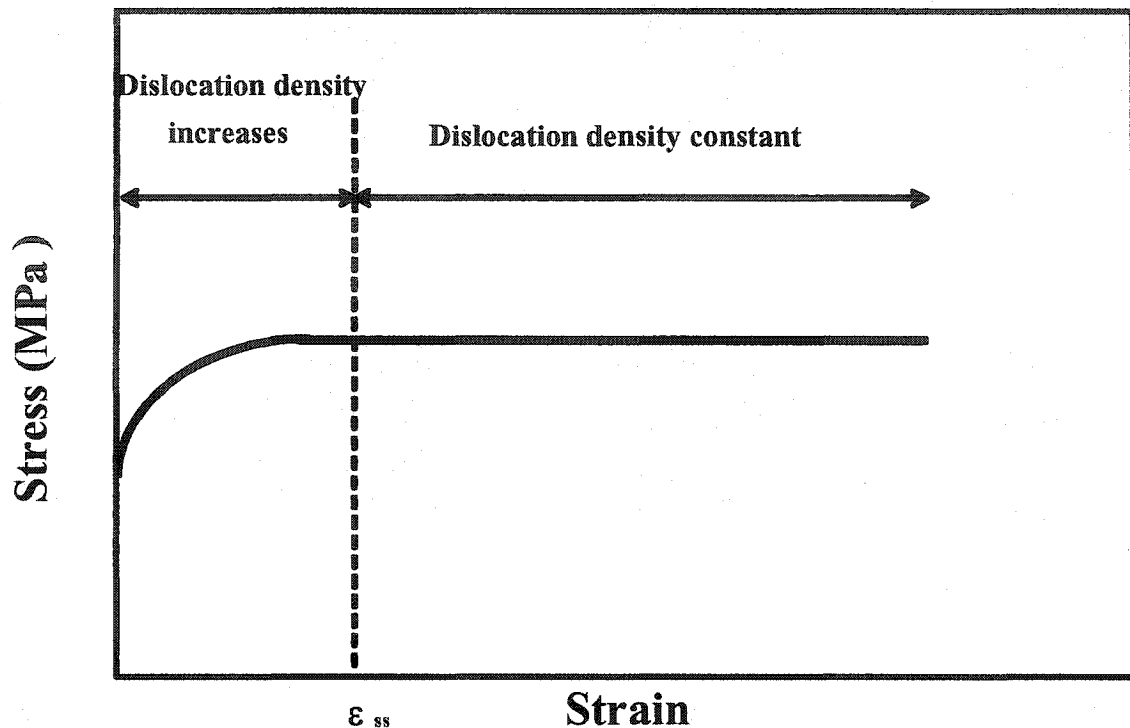


Figure (2-1) Schematic illustration of a true stress-strain curve for dynamic recovery.

2.1.1.3. Dynamic Recrystallization

For isothermal deformation of austenite, the characteristic form of the stress-strain curve for a constant strain rate is as shown in Figure (2-2). At the critical strain, ϵ_c , dynamic recrystallization is nucleated in austenite. The critical strain is basically an indication of the critical dislocation density driving force required for successful development of dynamic recrystallization. It has been suggested that nucleation occurs predominantly at grain boundaries by a bulging mechanism [8]. Up to the critical strain, the stress is established by a balance between work hardening and dynamic recovery. The critical strain ranges in most cases, between 0.65 to 0.8 ϵ_p (strain to the peak stress), and can be established from direct microstructural observation [9]. An increase in strain past ϵ_p results in an increase in the volume fraction of dynamically recrystallized material, and a decrease in the stress occurs until steady state is reached (σ_{ss}). At this point, there

is a balance between the generation of new strain-free grains and the work hardening of dynamically recrystallized grains [10].

There is a transition from cyclic to single peak recrystallization, as the strain rate is increased, or the temperature is decreased [11,12], single peak behavior is associated with grain refinement while multiple peak flow is due to grain coarser [13].

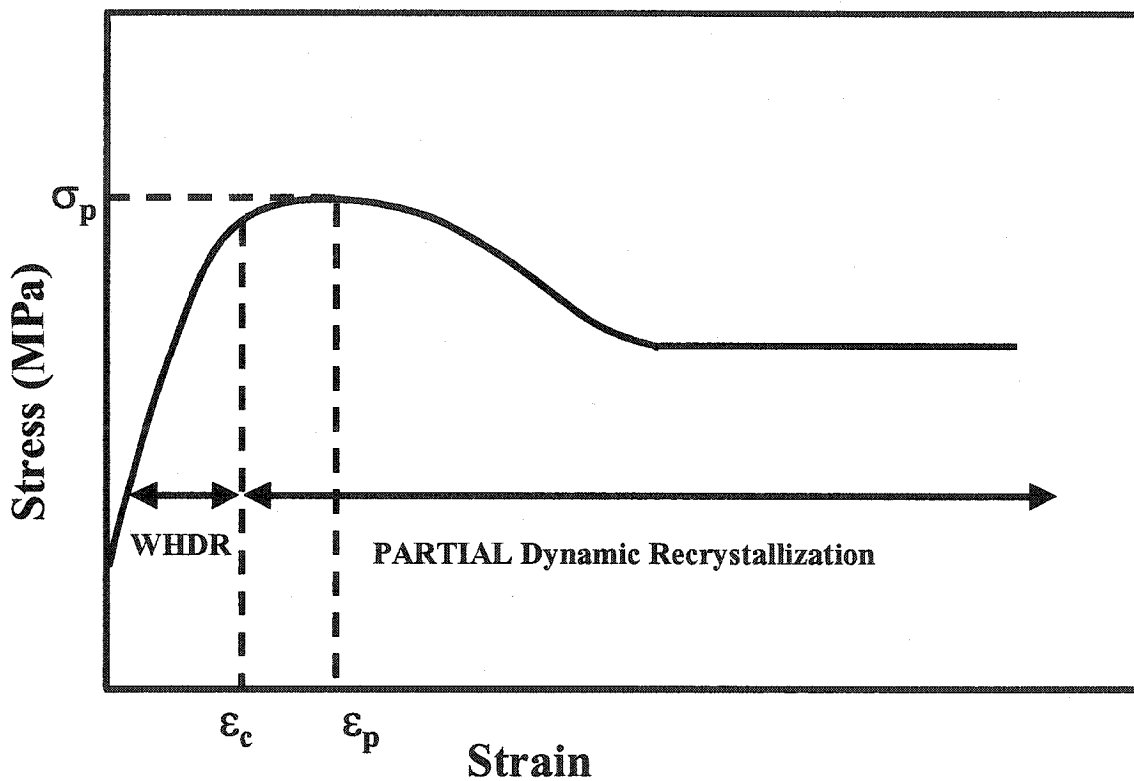


Figure (2-2) Schematic stress-stain curve for austenite at elevated temperature.

The critical strain for the nucleation of dynamic recrystallization can be determined from the following equation [9]:

$$\epsilon_c = A Z^p \dots\dots\dots 2-1$$

where A is a function of the initial grain size and composition, Z is the Zener-Hollomon parameter, $Z = \dot{\epsilon} \exp\left(\frac{Q_{def}}{RT}\right)$, $\dot{\epsilon}$ is the strain rate (sec^{-1}), Q_{def} is an apparent activation energy for deformation (Jmol^{-1}), R is the gas constant ($\text{J K}^{-1}\text{mol}^{-1}$), T is an absolute temperature (K) and p is a constant

The kinetics of dynamic recrystallization can be described, for constant strain rate tests, by the following Avrami-type equation:

$$X = 1 - \exp\left(-K(\epsilon - \epsilon_c)^n\right) \dots\dots\dots 2-2$$

where K and n are constants. This can be regarded as 'kinetics' because the applied strain, ϵ , depends on time.

In a given material, the characteristics of dynamic recrystallization depend on three parameters: initial grain size, temperature, and strain rate. The finer the initial grain size, the more rapid the kinetics [14,15], which leads to lower critical and peak strains; this is because dislocations accumulate more rapidly and the higher specific grain boundary area increases the number of dynamic recrystallization nucleation sites. The peak stress is also found to be slightly dependent on the initial grain size [16]. The steady state stress (σ_{ss}) has been found to depend only on the strain rate, temperature and composition with no influence of initial grain size and strain [14-16] according to the relations given below:

$$\sigma_{ss} = A_{ss} Z^{-q} \dots\dots\dots 2-3$$

where A_{ss} , and q are constants.

Pervious investigators have considered the role of steel composition on the dynamic recrystallization behavior. For instance, Jaipal et al. [17] studied the effect of C content on the dynamic recrystallization behavior of two plain carbon steels (0.15-0.62 wt%) with temperature 800°C to 1100°C and at strain rates between 0.007 s⁻¹ and 70 s⁻¹. It was observed that the dynamic recrystallization pattern for high carbon and low carbon steels is quite similar. Cho et al [18] studied the effect of Mn on recrystallization kinetics of Nb microalloyed steel. They found that the dynamic recrystallization is increased with increasing Mn. Serajzadeh and Karimi [19] studied the effect of Si on dynamic recrystallization behavior of C-Mn steels with Si contents from 0.07 to 1.1 wt% at temperatures 900-1200°C and strain rates of 0.01-2s⁻¹. It was found that increasing the Si content cause a decrease of both the rates of dynamic recovery and recrystallization due to the effect of solid solution hardening.

2.1.1.4. Dynamically Recrystallized Grain Size

Full dynamic recrystallization and a constant mean grain size characterize the steady-state region. The fully dynamically recrystallized grain size has been found to be dependent only on the Zener-Hollomon parameter, Z and is given by

$$d_{rex} = B Z^q \dots\dots\dots 2-4$$

Comparing the recrystallized grain size d_{rex} with the initial grain size D_o , Sakai and coworkers noticed that the single peak flow curves were associated with a large decrease in grain size, whereas multiple peak behavior displayed grain size coarsening. The transition occurs when the initial grain size is twice the steady state grain size as given by:

$$D_o = 2 D_s \dots\dots\dots 2-5$$

Thus, $D_o > 2D_s$ leads to grain refinement whereas $D_o < 2D_s$ leads to grain coarsening (Figure (2-3)).

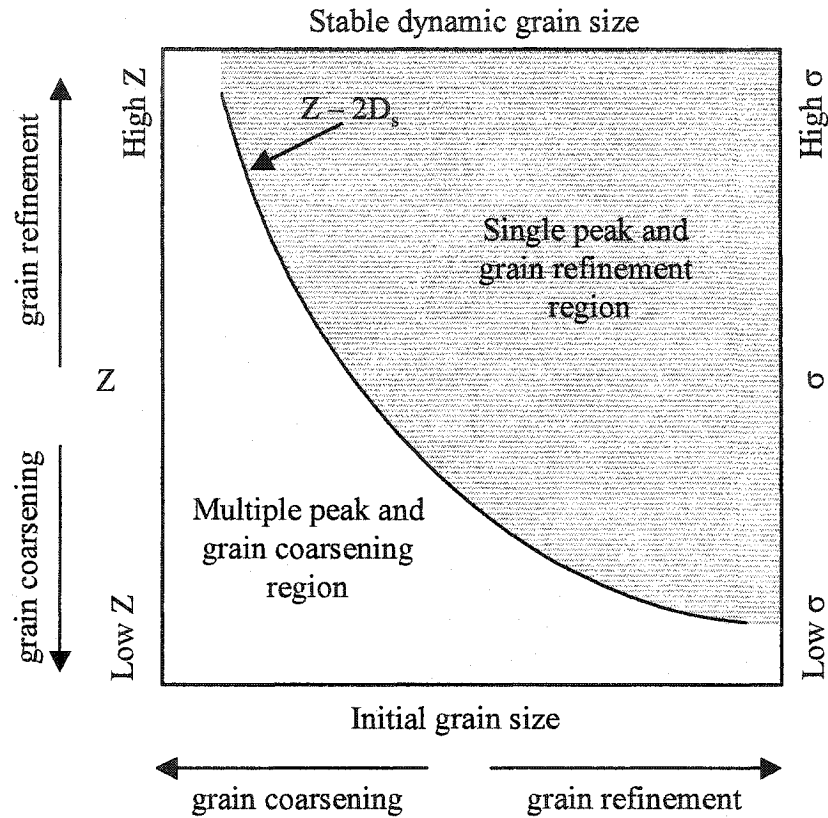


Figure (2-3) Steady state grain size D_s dependence on Z and the relationship the initial grain size [11].

For most industrial hot working conditions, single peak behavior is expected because the relatively high strain rates lead to a relatively fine dynamically recrystallized grain size.

2.1.1.5. Static Recovery

After plastic deformation, the strain energy that is stored within the deformed material will be released by inhabitation or rearrangement of dislocations. During the process, no motion of grain boundaries occurs. The sub-boundaries become sharper and the dislocation density within the sub grains is reduced, with little change in their shape or size. The rate of recovery increases as the temperature is increased because of enhanced thermal activation. Increasing strain and strain rate also increases the rate of recovery due to dislocation density increases.

2.1.1.6. Static Recrystallization

Static recrystallization takes place after unloading. Despite the annihilation of dislocations by dynamic recovery, dislocations are accumulated during deformation. If the accumulated strain exceeds a certain critical value, static recrystallization can then occur by nucleation and growth of dislocation-free austenite grains. The nucleation process is thermally activated and requires an incubation time for nuclei to form [20-22].

The modified Avrami equation [9,23], which incorporates an empirical time constant for recrystallization, t_x , serves as the basis for most static recrystallization kinetic predictions:

$$X = 1 - \exp \left(-A \left(\frac{t}{t_x} \right)^n \right) \dots\dots\dots 2-6$$

where X is the fractional softening, n is an Avrami exponent, t is the holding time after deformation, (s), t_x is the time for a given volume fraction, x, to recrystallize, (sec) and A is $-\ln(1-x)$.

For a given set of deformation conditions, plots of $\log \left(\ln \left(\frac{1}{1-X} \right) \right)$ versus $\log(t)$ are used to obtain the Avrami exponent, n . The time for a given fraction to recrystallize, t_x , is calculated using the following equation [7]:

$$t_x = B \varepsilon^{-p} D_0^q Z^r \exp \left(\frac{Q_{\text{rex}}}{RT} \right) \dots\dots\dots 2-7$$

where B , p , q and r are constants, Q_{rex} is the apparent activation energy for recrystallization (Jmol^{-1}) and D_0 is the initial grain size, (μm)

An increase in the strain has the effect of increasing the recrystallization rate (decreasing t_x) by increasing the driving force. As well the number of nucleation sites increases, with the creation of deformation bands at large strains, and sub-grains at large initial grain sizes. Both of these features have been observed to act as sites for the nucleation of static recrystallization [24].

The grain size prior to deformation plays a strong role in determining the number of nucleation sites per unit volume available for nucleation because of the tendency for recrystallization to be nucleated on grain boundaries. Because of its influence on the mobility and migration rate of the interface between recrystallized and unrecrystallized regions, temperature also controls the recrystallization rate.

For C-Mn steels, various authors have found a wide range of constants for equations 2-6 and 2-7. However, no noticeable difference in recrystallization kinetics has been found in studies where a wide range of compositions was examined [25]. It may be that the constants in equation 2-7 have been developed for specific ranges of deformation conditions (temperature, strain, and grain size), and may be of limited general use.

The literature on the effect of C on static recrystallization is mixed; with one paper reporting no effects [26] and one that noting that C increases the static recrystallization rate [27,28]. Collinson et al. [29] studied the effect of C on the static recrystallization kinetics for two steels with C contents of 0.15 and 0.62% at 825 and 1100°C and a strain rate of 3 s^{-1} . It was observed that the C additions could cause an order of magnitude drop in the time required for 50% static recrystallization at 850°C and 3 s^{-1} . Hence, the effect of C on recrystallization may be dependent on the processing conditions. Whittaker et al. [30] suggested that the static recrystallization kinetic increases with increasing C and Mn content, but no systematic effects were observed by Irvine et al. [31].

The role of the substitutional elements, Mn and Si, are not clear in the literature. Grangen et al. [32] and Tanaka et al. [33] show that Mn content has little effect on static recrystallization. Manganese is known to alter the rate of strain induced precipitation in microalloyed steels [18, 34], although it is generally thought to play only a minor role in retarding recrystallization due to its similar atomic size and diffusion rate to Fe. Silicon may be expected to have a stronger effect based upon its greater size mismatch with Fe.

Chestnut et al. [35] have reported that V has little effect on the static recrystallization kinetics at temperatures where the solute atoms are in solution. It is also known that V gives very little retardation by solute drag [36,37]. Irvine et. al [31] found little effect of 0.015% V addition on static recrystallization kinetics. Cordea and Hook [38] observed some retardation of recrystallization in 0.059% V steels at temperatures below 925°C. Korchynsky and Sturt [39] also reported that retardation of static recrystallization is less in V steel than in Nb steel.

2.1.1.7. Statically Recrystallized Grain Size

Most equations for statically recrystallized grain size are a function of initial grain size and strain, but there are conflicting observations by researchers on the effect of strain, which has been seen to have both a strong and a weak effect on the grain size [10]. Some workers have also reported a dependence on temperature and strain rate, albeit a weak one [40,41]. The equation proposed by Sellars [9] is of the following form:

$$d_{rex} = B_3 D_o^{n_4} \epsilon^{n_5} \dots\dots\dots 2-8$$

where B_3 , n_4 , and n_5 are constants.

2.1.1.8. Metadynamic Recrystallization

If the critical strain for dynamic recrystallization is surpassed during deformation, the recrystallization continues statically when the specimen is unloaded. This process is called metadynamic recrystallization (or post dynamic, static recrystallization) and does not involve an incubation time, since some nuclei are already present upon termination of the deformation.

The kinetics of metadynamic recrystallization are rapid and often completion occurs during quenching after deformation [6]. Although an Avrami-type equation is generally used to describe recrystallization processes involving nucleation and growth, metadynamic recrystallization has also been successfully described using an Avrami equation, even though it does not involve nucleation [42-44]. The fraction recrystallized, X , is modeled using an equation of the form:

$$X = 1 - \exp \left(-A_2 \left(\frac{t}{t_{50}} \right)^{n_2} \right) \dots\dots\dots 2-9$$

where A_2 and n_2 are constants

The time for 50% recrystallization, t_{50} , has been modeled using an equation of the form [9]:

$$t_{50} = B_2 \dot{\epsilon}^{n_3} \exp\left(\frac{Q_{rec}}{RT}\right) \dots\dots\dots 2-10$$

where B_2 and n_3 are constants.

Kemp et al. [43] used an expression similar to equation 2-10 except that the Zener-Hollomon parameter; Z was used instead of the strain rate. Metadynamic recrystallization has been shown to always go to completion in times significantly shorter than the interpass times of industrial hot rolling schedules [10].

The difference between static recrystallization and metadynamic recrystallization can be seen from the dependence of the recrystallization rate on the deformation parameters. Static recrystallization kinetics is strongly dependent on strain and temperature, and somewhat less so on strain rate. The dynamic or metadynamic recrystallization kinetics, however, are highly sensitive to strain rate, less so on temperature, and not at all dependant on strain.

2.1.1.9. Metadynamically Recrystallized Grain Size

The grain size for a given steel composition is dependent only on Z , similar to the case of dynamically recrystallized grains:

$$d_{mdrx} = B_7 Z^{n_6} \dots\dots\dots 2-11$$

where B_7 and n_6 are constants.

The metadynamic grain size has been found to be just over one and a half times the dynamic grain size present at the completion of deformation [10]. Nevertheless, these current equations suggest that it is possible to use metadynamic recrystallization to obtain very fine austenite (and therefore ferrite) grain sizes, significantly finer than can be obtained from static recrystallization, by increasing Z [10].

2.2 The Effect of Alloying Elements on Microstructural Evolution During Hot Deformation

2.2.1. Carbon

It is known that composition plays an important role in the metallurgical events affecting the evolving microstructure, but the extent to which C influences these processes is not always clear. It has been suggested that C changes the activation energy for the self-diffusion of Fe in austenite [45].

Collinson et al. [46-48] studied the effect of C content on the flow strength, and the static and dynamic recrystallization behavior of C-Mn steels with C contents ranging from 0.0037 to 0.79 wt%. It was observed that the C content had a complex effect on the flow strength of austenite. Increasing C reduced the flow strength by up to 30% under conditions of low strain rates and high temperatures. At the high strain rates and low temperatures typical of hot rolling, increasing C resulted in increases in the flow stress of over 100% at low strains. Wray [49] has reported that increasing C content of plain carbon steels decreases the work hardening rate when strained in the temperature range 850 to 1300 °C. This causes a lowering of the flow stress at a rate of about 13 MPa per wt pct C at a strain of 0.1. The decrease in work hardening is probably due to enhanced dynamic recovery, which agrees with the reported expansion of the austenite lattice and increase in Fe self-diffusivity.

Under conditions of multiple peak dynamic recrystallizations in low carbon steels, the addition of C reduced both the amplitude and duration of the cycling. Under single peak dynamic recrystallization conditions, the low carbon steel showed a continuous increase in the critical strain for the initiation of dynamic recrystallization as the strain rate of testing was increased and the temperature reduced. For the high carbon steel the critical strain for dynamic recrystallization increased up to a strain 0.7 and then remained constant, despite further reduction in the temperature or increases in the strain rate. Lx et al. [50] found that increasing the C above 0.4 wt % dramatically reduces the peak strain for the initiation of dynamic recrystallization at a high Zener-Hollomon parameter. Some work has shown that it may be much easier to initiate dynamic recrystallization in high carbon steels in high-speed rolling mills than previously thought [51]. Figure (2-4) illustrates that low carbon steels show a similar dependence with Z as expressed by equation 2-1, but for medium and high carbon steels, there appears to be no effect of Z beyond a critical value. This critical value of Z is exceeded in the latter passes during rolling of most small diameter rod and bar products.

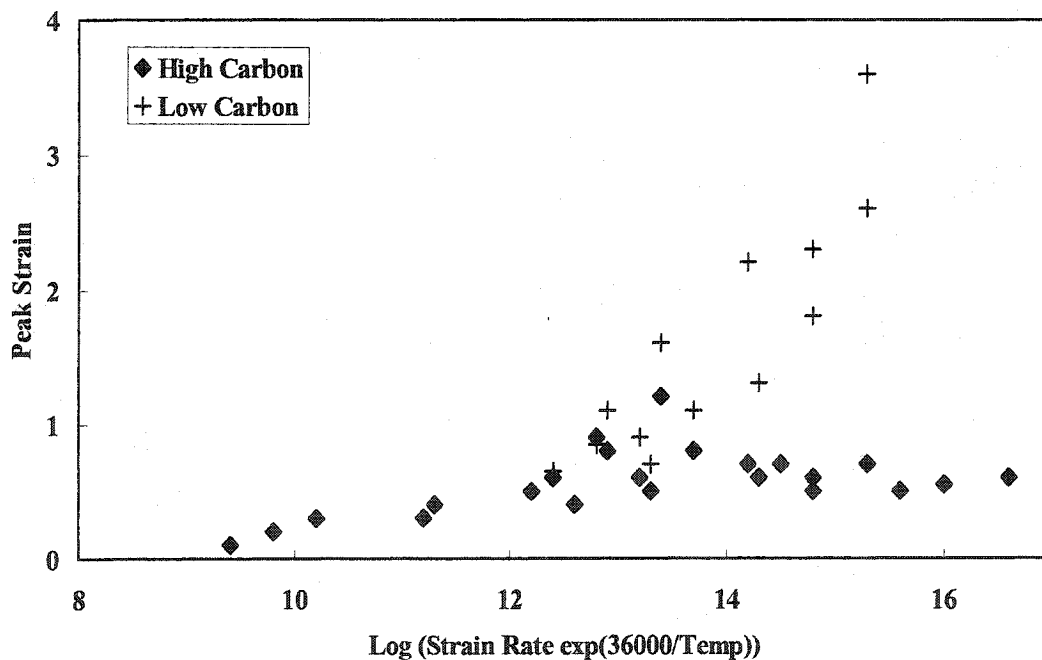


Figure (2-4) Variation in the peak strain with Z for high and low carbon steels [51].

Jaipal et al. [17] conducted compression studies on two different steels with varying C (0.15 and 0.62 wt % C) at several temperatures and strain rates. At high temperatures and low strain rates, increasing C content reduces the peak stress of steel. However, at low temperatures and high strain rates, increasing C increases the peak stress. They found also that for low carbon (0.15%C) steel the strain rate sensitivity, m , is lower at all temperatures than for high carbon (0.62%C) steels.

2.2.2 Effect of Other Alloying Elements in Solid Solution on Recrystallization

Le Bon et al. [52] reported that the retardation of recrystallization observed in Nb steel could not be accounted for by precipitation at higher temperatures. It was suggested that Nb in solid solution caused this delay by solute drag on the migrating boundaries. Floros [53] found that Al, Mo, Nb, and V in solution retard the dynamic and static recovery and recrystallization of austenite after high temperature deformation. The strongest effect is due to Nb followed in decreasing order by that of Al, V and Mo.

The retarding effects of the alloying elements in solid solution have been attributed to the following:

1. Solute addition decreases the stacking fault energy of the matrix leading to an increase in the dislocation density and to a more homogeneous distribution [54].
2. The solute atoms interact with the dislocations obstructing their rearrangement for subcell formation, this process being related to nucleation [55].
3. A solute drag effect on the moving recrystallization grain boundaries [56].

2.2.3. Effect of Alloying Elements as Precipitates

Strain-induced precipitation can affect both the nucleation and the growth process of recrystallization by the following mechanisms:

1. The stabilization of the substructure by fine strain-induced precipitates inhibits the nucleation process.
2. The pinning effect of precipitates on grain boundaries hinders their migration.

It is well established that precipitation of Nb (C,N) in austenite plays an important role in retarding recrystallization [56]. The kinetics of precipitation has been studied in both undeformed and deformed austenite by a number of workers. Vanadium is known to produce effects similar to that of Nb. However, V(C,N) has a much higher solubility than the corresponding Nb precipitates. Hence, the retardation effect is more pronounced at temperatures below 950 °C [54,57,58]. VN has the lowest solubility of the V precipitates, and therefore is the main precipitate that forms. If there is V in excess, then VC can be formed [59]. Chestnut et al. [35] reported that the V has little effect on static recrystallization kinetics at temperatures where the solute atoms are in solution.

2.3. Pearlite Formation

In the steels of interest in this work, the main microstructural constituent is pearlite.

It is important to note that pearlite is not a single phase; the phases in it are ferrite and cementite. Pearlite is the name of the microstructural constituent that consists of alternating lamellae of the two phases. Pearlite is generally considered to be a product of

the decomposition of austenite by a diffusional process. Thus, the transformation procedure is divided into stages: nucleation and growth.

The initiation process for the development of a pearlitic microstructure entails the formation of neighboring nuclei of ferrite and cementite on an austenite grain boundary. Supposing that initially only one nucleus of cementite forms on this boundary, this region will be locally rich in C, which it has obtained from the immediate surroundings. This then reduces the C content on either side of the cementite nucleus and encourages the adjacent nucleation of ferrite, as shown in Figure (2-5). If this occurs and the cooperative process continues, adjacent nuclei of alternating ferrite and cementite are formed. These can then grow by a relatively short-range diffusion process in which C diffuses parallel to the reaction front, from in front of the growing ferrite to the growing cementite. More importantly, the diffusion distance does not increase with time, as would be the case for a continuous precipitation process. This plausible progression leads to the transformation of austenite to a lamellar product that has a specific spatial orientation in which the ferrite and cementite phases are parallel to each other within a colony region. In reality, for each colony of pearlite, the lamellae are mostly parallel and are frequently curved. However, different pearlite colonies have different lamellae orientations, and, as the transformation progresses, neighboring colonies of lamellae join together and continue to advance into the austenite, such that when the transformation occurs at low degrees of undercooling the colony groups advance by a boundary that is roughly spherical in shape, leading to the formation of a pearlite nodule. Eventually, as the nodules continue to grow, they impinge on one another to complete the transformation. If the temperature at which the transformation is occurring is decreased, such that the undercooling enables the nucleation process to become so rapid that all of the grain boundaries are consumed very early in the transformation, the pearlite nodules are then observed to be in contact along the prior-austenite boundaries as a continuous cementite network.

This also exhibits an apparently wide range of interlamellar spacing from colony to colony because the intersection of the polishing plane and the pearlite colonies occurs

at different angles. As the interlamellar spacing is a reflection of the diffusion kinetics at the transformation [60], with decreasing transformation temperature from 700 to 500°C, the lamellar spacing in the pearlite decreases.

As is expected in diffusional transformation, the pearlite transformation start temperature decreases with increasing cooling rate. A fully pearlitic steel rod is heat treated by a process known as patenting. During the patenting, the rod is transformed at a low temperature by passing it through a salt bath at this temperature. This develops a microstructure with very fine pearlite interlamellar spacing because the transformation takes place at the nose of the continuous cooling transformation.

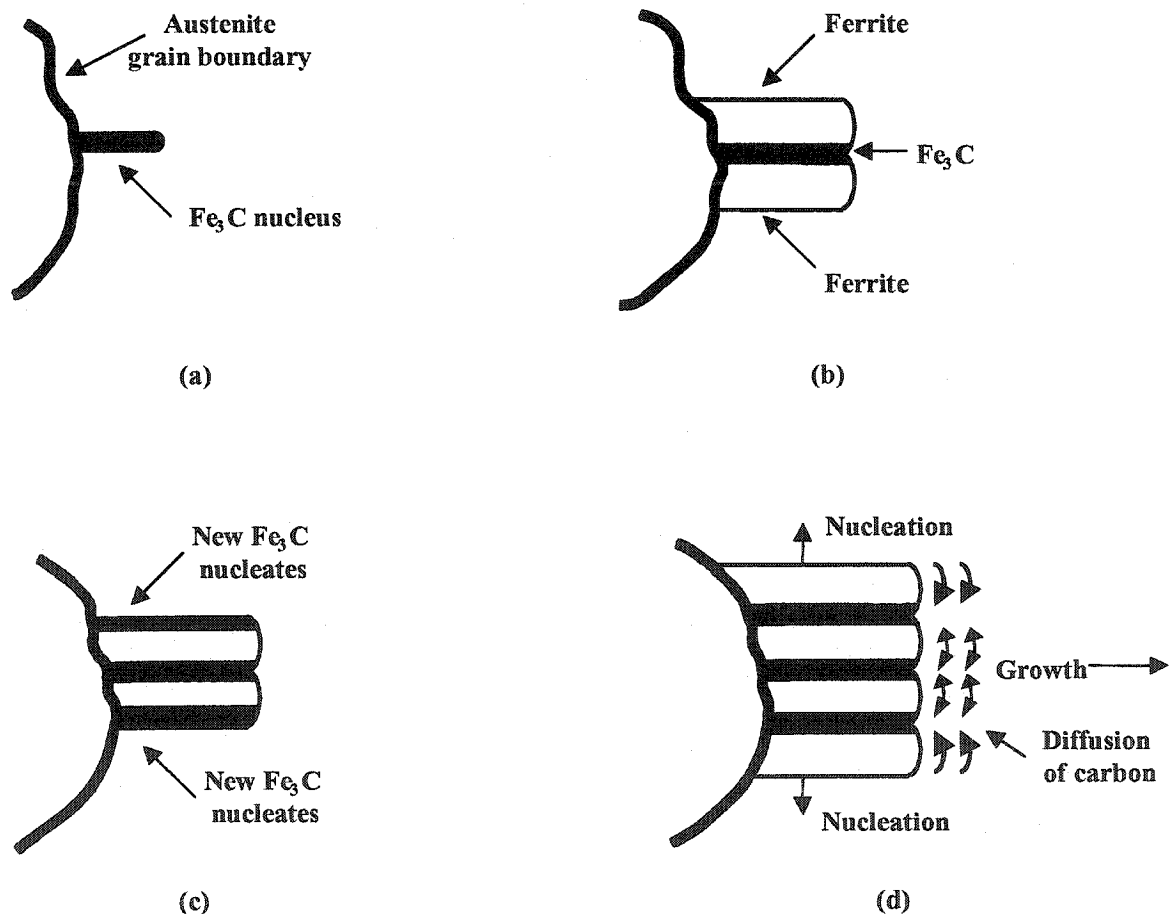


Figure (2-5) Schematic representation of pearlite formation by nucleation and growth; (a) through (d) indicate successive steps in time sequence.

2.4. Mechanical Properties of Pearlitic Steels

The quantitative relationships between microstructure and mechanical properties, which have already been described for ferrite-pearlite structures, apply to steels less than about 0.25% C. The most important structural characteristic of ferrite is its grain size. Grain refinement can both improve the strength and reduced the impact transition temperature. The effect on strength is expressed as the Hall-Petch equation:

$$\sigma_y = \sigma_i + K_y d^{-1/2} \dots\dots\dots 2-12$$

where σ_y is the yield stress, σ_i is the friction stress opposing dislocation movement, K_y is a constant and d is the grain size. The friction stress is dependent on temperature, strain rate, solid solution strengthening, dislocation strength and texture [3].

The medium and high carbon steels have much higher pearlite content; the key microstructural characteristics of pearlitic steels are illustrated in Figure (2-6).

The main factor influencing the strength of pearlite is the interlamellar spacing [58]

$$\sigma_y = \sigma_o + K_y S^{-1/2} \dots\dots\dots 2-13$$

where σ_o is the friction stress, K_y is a constant and S is the interlamellar spacing. The σ_o term is again influenced by the factors described above for σ_i .

Hyzak and Bernstein [61] have suggested another equation, which also includes the pearlite colony size and prior austenite grain size.

$$\sigma_{ys} = 2.18 S^{-1/2} - 0.4P^{-1/2} - 2.88 d^{-1/2} + 52.30 \dots\dots 2-14$$

where P is the pearlite colony size and d is the prior austenite grain size.

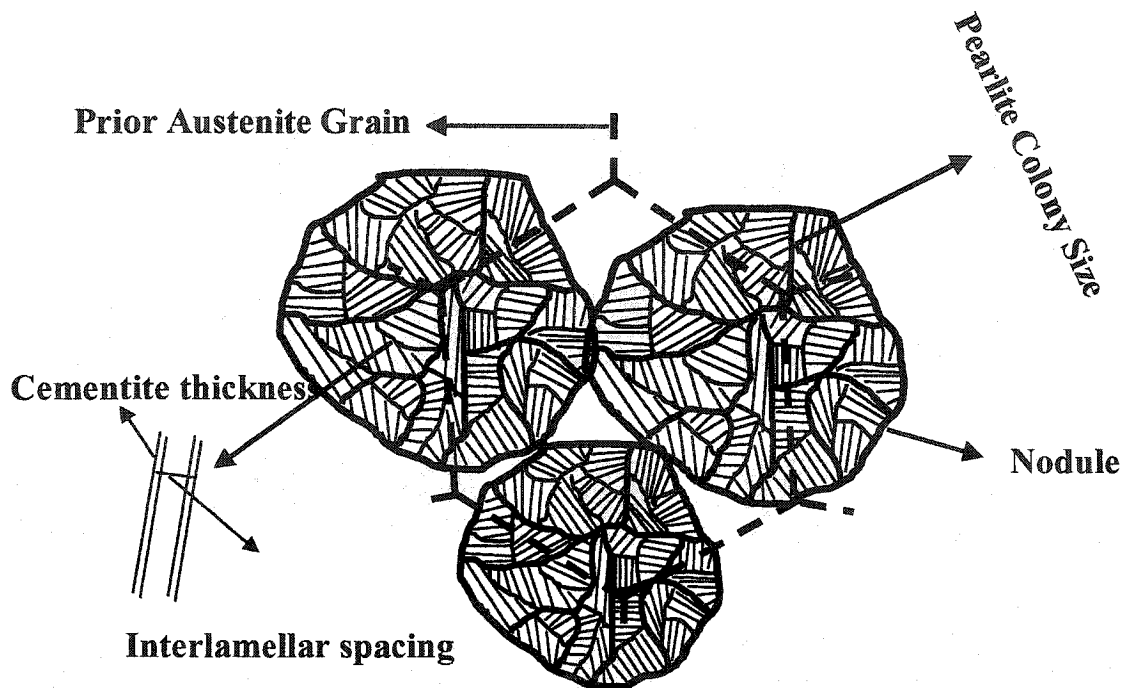


Figure (2-6) Schematic diagram illustration of pearlite morphology

The nodule size is controlled by the austenite grain size, so that the coarser the prior austenite grain size, the larger is the nodule size [62-65]. Pickering et al [66] have reported that the colony size depends on the transformation temperature in a similar way to the interlamellar spacing, i.e. the lower the transformation temperature the smaller is the colony size, which however, is dependent of the prior austenite grain size. Nevertheless, the prior austenite grain size influences the way in which the colonies are arranged. However, it has been shown that the yield stresses of pearlite, and also the ultimate tensile strength, are related only to the pearlite interlamellar spacing through a relationship of the Hall-Petch type, although various authors propose different values for the parameters of the relationship, including the exponent [61, 63, 66-68].

Steels with a high tensile strength are produced with high volume fraction of pearlite, but the toughness and ductility of steels decreases with increasing pearlite content and with a decrease in the interlamellar spacing, which in turn decreases with increasing carbon content. In order to obtain the highest toughness and ductility with a given strength it is desirable to keep the pearlite content to minimum and the interlamellar spacing as high as possible. This can be achieved by increasing the strength of the ferrite through the precipitation of V(C,N), although precipitates also tend to reduce toughness. When the highest strengths are required however, a combination of high pearlite content high carbon steels and V(C,N) precipitation is employed.

The ductility can be improved by refining the austenite grain size [69,70]. The carbides, mainly the cementite distribution, play part in pearlitic steels. The carbide distributions vary from spherical to lamellar pearlitic cementite with a spheroidized pearlite having better ductility than an un-spheroidized one [71]. Ductility, as measured by reduction in area (R_a) varied with microstructure from 10 pct to 50 pct, and has been modelled by the following regression equation [61]:

$$R_a = 1.24 \times 10^{-1} S^{-1} + 2.66 \times 10^{-1} P^{-1} + 1.85 d^{-1/2} - 4.7 \times 10^1 \dots\dots\dots 2-15$$

Examination of the regression coefficient indicates that the prior austenite grain size has the greatest influence on ductility, with pearlite spacing having a more modest effect and colony size having little effect.

2.4.1. Effect of Alloying on Mechanical Properties of High Carbon Steels

The effects of microalloying in high carbon steels tend to be more complex than for low carbon steels, because of the presence of pearlite. Nevertheless, some of the metallurgical principles that proved so effective in providing an understanding of the low carbon microalloyed steels can also be applied to high carbon microalloyed steels.

2.4.1.1. Vanadium

Vanadium microalloying has been found to increase the tensile strength of high carbon steels through microstructure refinement and precipitation strengthening. The refinement effect of V microalloying is due to the inhibition of austenite grain growth, as a result of the precipitation of VN in austenite during hot rolling [72] for V levels between 0.05-0.2 %V in steels containing 0.6-0.8 %C. According to Pickering, the N dissolved in the ferrite is greatly decreased, which further improves the toughness [73]. Strengthening increments of 100-150 MPa in these steels are also achieved by the precipitation of VC and VN in the regions of pearlite and any proeutectoid ferrite during or after the transformation from austenite [73]. During the isothermal transformation there is strong tendency for V to partition away from the growing ferrite and to form VC. The formation of fine V-rich carbonitride particles by interphase precipitation produces a significant increase in strength over that produced by other strengthening factors in ferrite-pearlite microstructures, such as pearlite volume fraction and ferrite grain refinement [68,74].

The solubility of V(C,N) in austenite and ferrite is such that V will be completely dissolved even at low austenitising temperatures (900°C). Since the solute drag effect on austenite grain boundaries is also low, V hardly affects the hot deformation process but rather precipitates during cooling in ferrite, thereby increasing the strength level of the steel.

2.4.1.2. Nitrogen

Nitrogen has certain beneficial effects, which in recent years, have led to the development of different steels containing enhanced N. In almost all cases the beneficial effects of N are the result of interaction with the alloying elements present. To understand the effect of N in steel, as opposed to the effects of C, both of which are

interstitial solutes, the much-increased solubility of N in the solid state, compared with carbon must be appreciated. In addition the nitrides, such as VN, NbN and TiN are much more stable than the corresponding carbides and are thus less soluble than the carbides. Hence nitrides often form small particles, which are slower to grow than the alloy carbides.

The effect of nitrogen on V precipitation strengthening can thus be attributed to the following:

- (i) Nitrogen increases the possibilities of strain-induced precipitation in austenite [75,76] because of the lower solubility of VN compared with VC.
- (ii) Nitrogen increases the volume fraction of precipitates resulting from the decreased solubility of VN in ferrite compared with VC [77,78].
- (iii) Vanadium nitride remains coherent longer than VC [79] owing to its smaller misfit with ferrite.
- (iv) Nitrogen refines the size of interphase precipitates [79].
- (v) The dislocation pinning action of V (CN) increases as N content increases [80].

In pearlitic steels, increasing the N content from 0.001% to 0.006% increases the UTS by 130 MPa [81]; an increase from 0.007 to 0.015% has also been found to increase the UTS 50 MPa [82]. This has been attributed to the production of finer precipitates.

Sage [83] showed that the greatest effect of N is found in the high carbon, high manganese steels in which increasing the N from 100 ppm to 180 ppm raised the tensile strength by 40 MPa largely due to strengthening of the pearlite through precipitation of V (CN) in the laths of the pearlite.

2.4.1.3. Silicon

High Si produces solid solution hardening in proeutectoid and pearlitic ferrite and decreases cementite thickness at constant Interlamellar Spacing (S) (dilution of pearlite), therefore increasing toughness [84]. Increasing the Si content from 0.36 to 0.86% (in a 0.61C-0.11V-.017N steel) resulted in a decrease in S from 370 to 340 μm and a decrease in the cementite lath thickness from 0.038 to 0.035nm [69]. It has been concluded that Si inhibits carbide, particularly Fe_3C , formation at the ferrite-martensite interface [85, 86]. According to other work [87, 88], Si delays the formation of pearlite and accelerates the ferrite reaction. The ejected C enriches the austenite [89-92] helping to form martensite as a final transformation product. A further alternative is that the Si addition simply increases the solubility of C in the ferrite, decreasing the driving force for carbide formation in this way. Silicon had relatively little effect in promoting the formation of martensite, it was also shown to be less effective than Cr in refining the interlamellar spacing.

Tarui et al. [93] showed that increasing the Si content from 0.2 to 1.5% in a eutectoid carbon steel improved yield and tensile strength. A large portion of the strengthening that occurs as a result of the Si addition is again due to the solid solution strengthening of pearlitic ferrite as shown in Figure (2-7). It can be seen from Figure (2-8) that Si has a significant effect on the interlamellar spacing and strength, as noted above.

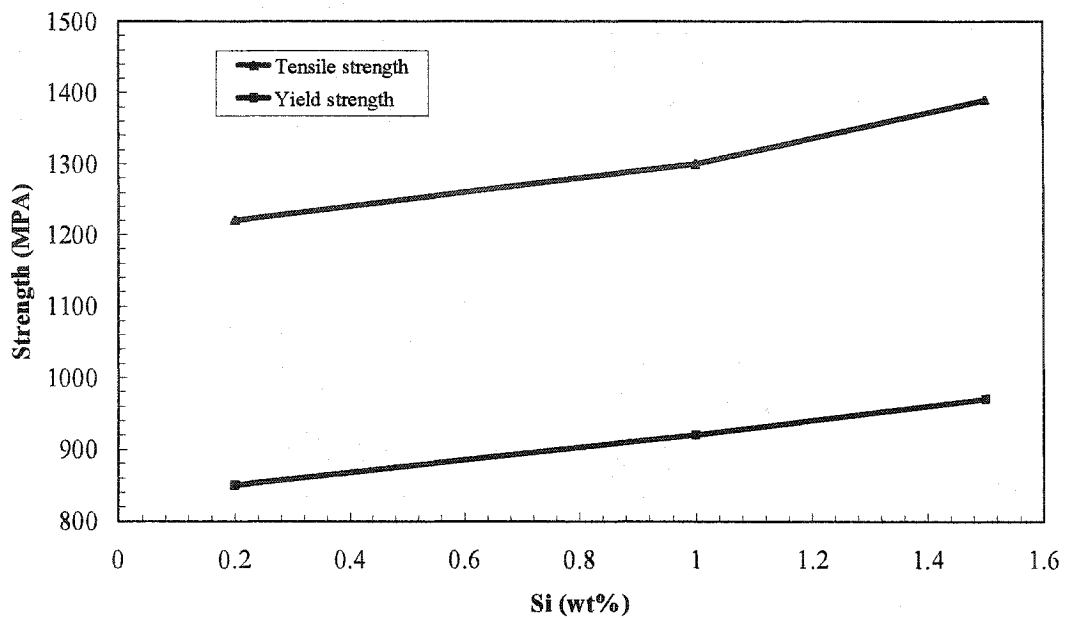


Figure (2-7) Yield and tensile strength plotted against Si content [93].

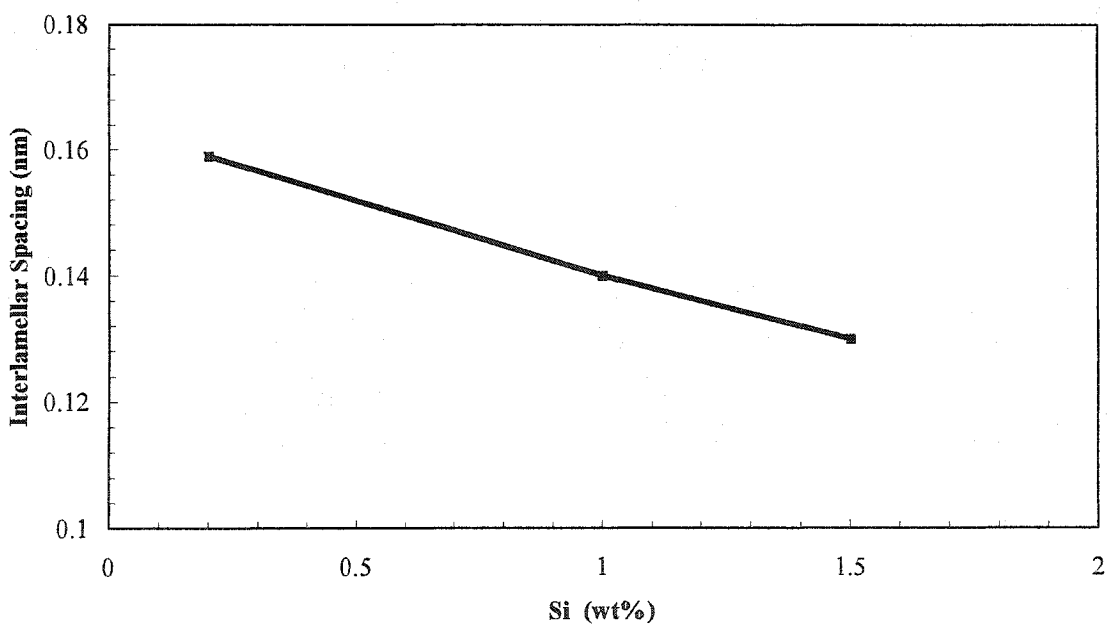


Figure (2-8) Interlamellar spacing plotted against Si content [93]

2.4.1.4. Manganese

For V steels the effect of the Mn on the activity of V is especially important. Manganese is known to increase the activity coefficient of V and at the same time decrease the activity coefficient of C. An increase of Mn content leads to an increase in the solubility of V in austenite at high temperature. This, in combination with the toughness increase due to the dilution of pearlite caused by the added Mn, produces an increase in tensile strength for the same toughness. Dilution of the pearlite can be achieved by increasing the cooling rate in the transformation range as well as increasing the alloying content. Lagneborg et al. [94] have also shown that the direction of the change in strength and toughness due to increasing cooling rate is about the same as for added Mn and reduced C; i.e. the strength increases at a constant toughness.

Manganese has a complex effect on toughness because the beneficial effects of Mn in causing ferrite grain refinement, pearlite colony size refinement and pearlite dilution, are offset by the detrimental effects of Mn in increasing the volume fraction of pearlite and decreasing the interlamellar spacing. Consequently, in general terms, Mn has little overall effect on toughness, but does increase the strength.

CHAPTER 3

3. Experimental Techniques

Five steels were used in the present work to investigate the dynamic, static and metadynamic recrystallization behavior of plain carbon and microalloyed eutectoid steels, and to develop mathematical expressions that can be incorporated into models for the prediction of microstructural evolution in microalloyed hypereutectoid steels during hot deformation. The effect of alloying and processing on the mechanical properties is also explored. This chapter focuses on describing and illustrating the instrumentation and experimental setups utilized. They are categorized as follows: experimental materials, experimental equipment, thermomechanical processing, mechanical properties and metallography.

3.1. Experimental Materials

3.1.1. Steel Compositions

The chemical compositions of the five steels used are listed in **Table 3-1**. Two plain carbon steels (D and E) were used as reference steels. These had slightly lower and higher carbon content (0.71% C and 0.91% C), and were provided by IVACO Rolling Mills (L'Orignal, Ontario, Canada). Three microalloyed steels of varying Si, V and N content were prepared at CANMET Materials Technology Laboratory (Ottawa, Ontario,

Canada), using vacuum melting. In this work, V has been chosen as the key microalloying element rather than Nb, since it is more likely to precipitate in ferrite, leading to more effective precipitation strengthening. In addition, Si additions are being investigated since it has been linked with decreasing pearlite interlamellar spacing, leading to possible improvements in drawability. Steel A has low Si (0.23%) and medium V (0.17%), steel B has high Si (1%) and low V (0.078%) and steel C has medium Si (0.78%) and high V (0.26%).

Table 3-1. Chemical composition of experimental steels (wt%)

<i>Composition</i>	<i>A</i>	<i>B</i>	<i>C</i>	<i>D</i>	<i>E</i>
<i>C</i>	1.1	1.0	1.08	0.71	0.91
<i>Si</i>	0.23	0.99	0.78	0.22	0.21
<i>Mn</i>	0.63	0.77	0.75	0.68	0.49
<i>Cr</i>	0.04	0.066	0.049	0.05	0.04
<i>Ni</i>	0.038	0.039	0.039	0.07	0.07
<i>Cu</i>	0.036	0.037	0.037	0.04	0.02
<i>V</i>	0.17	0.078	0.26		
<i>P</i>	0.010	0.0086	0.009	0.006	0.008
<i>S</i>	0.007	0.008	0.009	0.005	0.005
<i>N</i>	0.007	0.013	0.0058	0.003	0.0031

3.1.2 Specimen Preparation

The hot rolled plates were machined into cylindrical compression specimens, 11.4 mm in height and 7.5 mm in diameter, with their longitudinal axes parallel to the rolling direction. These dimensions were chosen based on studies, which found that an aspect ratio of 1.5 promoted homogeneous deformation during compression testing [95].

3.2. Experimental Equipment

The hot deformation experiments were performed on a computerized material testing machine set up for hot compression testing.

3.2.1. Compression Testing Apparatus

The compression testing machine (Figure (3-1)) is built around an MTS (Materials Testing System) Model 810 uniaxial testing machine, which consists of a load frame, rated at 25 kN, and a closed loop hydraulic power supply with computerized control system. After the completion of a test, the load and displacement data are transferred to a personal computer for analysis.

The temperatures tests are attained with a Research Incorporated radiant furnace, interfaced with a computer control system, which is used to generate commands, record data and perform real-time decision making during tests. Compression anvils are attached to the frame of the MTS by means of water-cooled steels supports as shown in Figure (3-1). The compression anvils were made of TZM alloy (molybdenum based alloy containing a dispersion of 0.5% Ti and 0.08% Zr oxides), which has high strength and creep resistance properties at elevated temperatures.

For the compression tests, thin sheets of mica (50 to 80 μm thick), separated by a layer of boron nitride powder, were placed between the faces of the compression specimens and the anvils in order to maintain uniform deformation, and to avoid quenching problems due to sticking. To minimize oxidation, the specimen and anvils were enclosed in a quartz tube sealed with O-rings in which a high purity argon atmosphere was maintained. Quenching the sample was done by a lever, through a hole, that was made in the lower support between the inside wall of the quartz tube and the

lower anvil. The opening is kept closed throughout the experiment, and opened when the specimen is to be quenched. This mechanism allows for quenching specimens within one second.

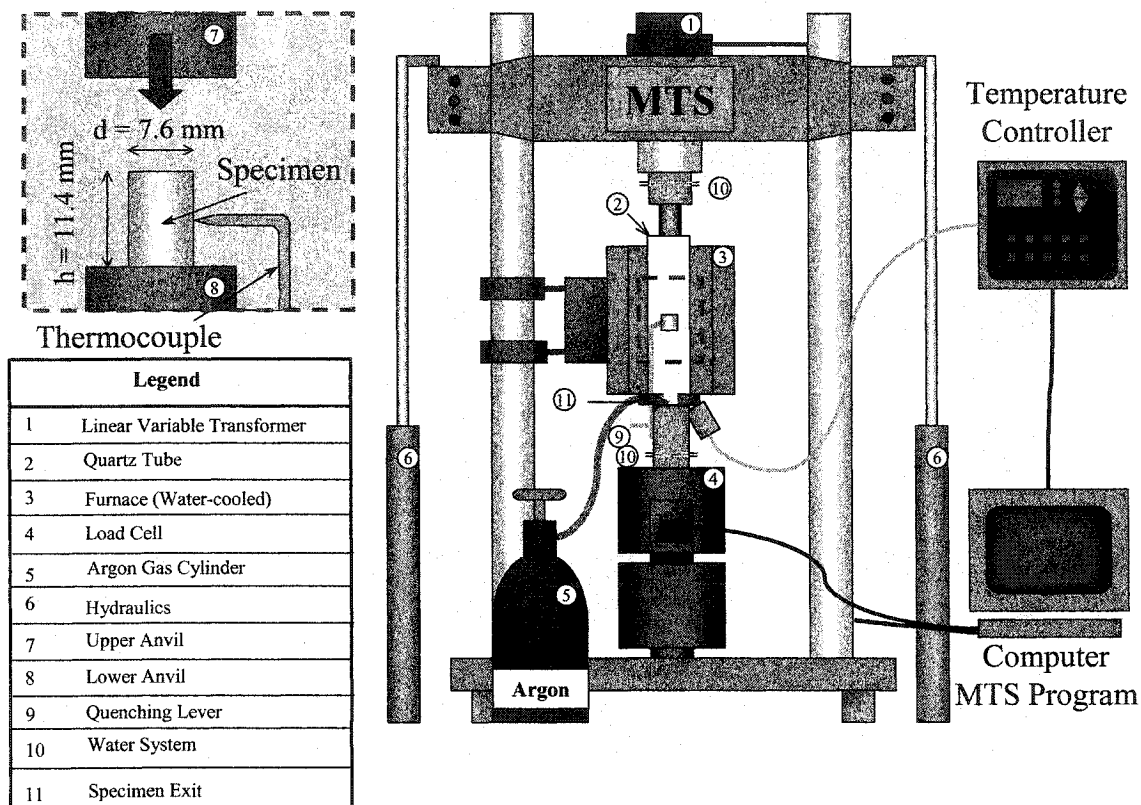


Figure (3-1) Schematic cross-section through the compression testing equipment.

3.2.2. Furnaces

In order to heat the specimens for the compression tests, a radiant furnace equipped with a 16 kW power supply was mounted on the MTS machine. The furnace is attached to the MTS load frame and controlled by a Micristar digital furnace programmer. The furnace is comprised of four-tungsten filament lamps, and four mirror finished elliptical reflectors of aluminum, positioned symmetrically about the center. The

temperature measurement of the specimens was performed using a K-type Chromel-Alumel thermocouple placed in contact with the specimen.

A salt bath for quenching, as shown in Figure (3-2) was used to isothermally transform the austenite (550, 580 and 620 °C).

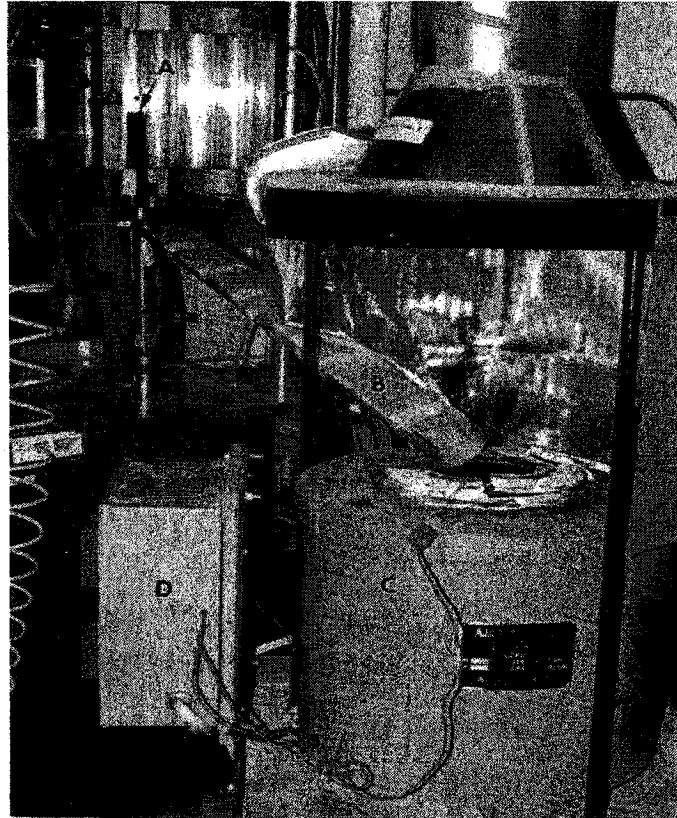


Figure (3-2) Quenching system, (A) lever arm, (B) quench chute, (C) salt bath and (D) furnace digital controller.

3.2.4. Constant Strain Rate Testing

All the compression tests were carried out under constant strain rate conditions. The compression mode, instead of the tension mode, was used because it avoids the

heterogeneous flow due to necking. True strain rate testing requires a continually changing actuator velocity. This was determined as follows:

In a compression test, an increment of true strain in a specimen deformed from an initial height h is given by:

$$d\varepsilon = \frac{dh}{h} \dots\dots\dots 3-1$$

By differentiating with respect to time t , the true strain rate in compression is obtained:

$$\dot{\varepsilon} = \left(-\frac{1}{h}\right) \frac{dh}{dt} \dots\dots\dots 3-2$$

where dh/dt is the rate of change of specimen height.

To run a constant true strain rate test, the specimen must be deformed at a rate which is proportional to its instantaneous height, h :

$$\frac{dh}{dt} = -\dot{\varepsilon}h \dots\dots\dots 3-3$$

By integrating the above equation and setting $h = h_0$ at $t = 0$, the following relation is obtained:

$$h = h_0 \exp(-\dot{\varepsilon}t) \dots\dots\dots 3-4$$

The instantaneous height is also the position of the MTS actuator. With a computer controlled system, true strain rate tests are produced by dividing the entire

deformation time into n steps ($n = 50$ in the present test) with intervals D_i , so that the instantaneous height of the deformation specimen (or the position of the MTS actuator) at time i can be expressed as:

$$h_i = h_0 \exp(-\dot{\epsilon}_i \Delta t) \dots\dots\dots 3-5$$

During testing, load and displacement data points were recorded and then converted into true stress and true strain by the following equations:

$$\sigma_i = \frac{\text{load}}{A_i} \dots\dots\dots 3-6$$

$$\epsilon_i = -\ln \left(\frac{h_i}{h_0} \right) \dots\dots\dots 3-7$$

where A_i is the instantaneous sample cross section, which was calculated as $A_i = A_0 h_0 / h_i$. Here A_0 and h_0 are the initial cross sectional area and height of the specimen, respectively, and h_i is the instantaneous height of the specimen.

3.3. Thermal Cycles and Deformation Schedule

3.3.1. Solution Treatment

The specimens were heated at a constant rate of $1.5^\circ\text{C}\cdot\text{s}^{-1}$ to 1200°C at hold at this temperature for 20 minutes as the first step of each separate test, partly to ensure dissolution of the VN and VC precipitates present in the initial microstructure, so that they can reprecipitate during later cooling and/or processing, and partly because this is a typical reheating temperature in a steel rolling mill. To determine the temperature that dissolves the V prior to deformation testing, the following equations were used [96]:

$$\log [V][C] = -\frac{9500}{T} + 6.72 \quad \dots\dots\dots 3-8$$

$$\log [V][N] = -\frac{8330}{T} + 3.40 \quad \dots\dots\dots 3-9$$

where the alloying concentration terms are in weight percent and the temperature is in Kelvin. Table 3-2 gives the dissolution temperatures calculated for the three steels used in this study.

Table 3-2 Calculated solution temperatures of the steels

<i>Steels</i>	<i>Temperature of solubility of VN (°C)</i>	<i>Temperature of solubility of VC (°C)</i>
<i>A</i>	1044	1000
<i>B</i>	1029	940
<i>C</i>	1050	1033

3.3.2. Single Hit Compression Testing Schedule

These tests were conducted to determine the dynamic recrystallization characteristics. After the reheating temperature was decreased at a rate of $1^{\circ}\text{C}\cdot\text{s}^{-1}$ to the test temperature (900, 950, 1000, 1050°C) and held for 5 minutes to homogenize the temperature within the specimen. The specimen was deformed isothermally at strain rates of 0.01, 0.1 and 1s^{-1} , followed by quenching, as shown in Figure (3-3).

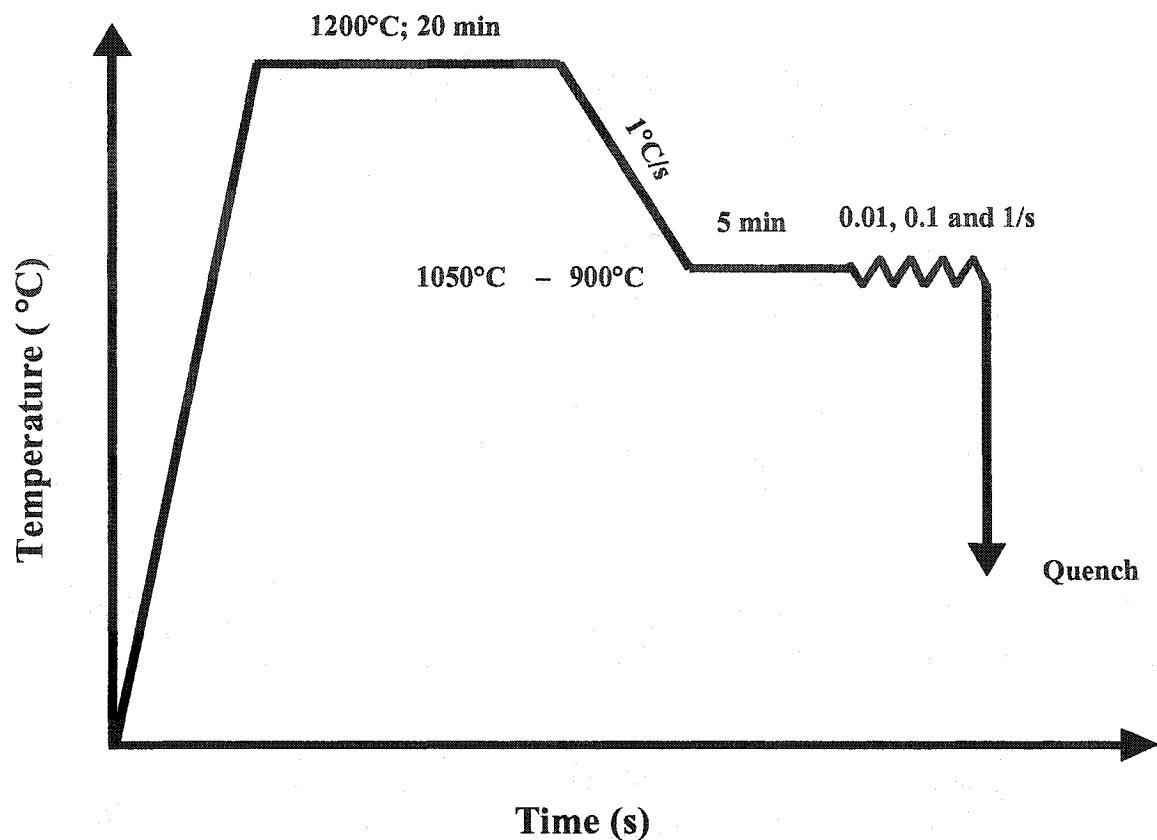


Figure (3-3) Schematic illustration of the TMP schedule for characterizing dynamic recrystallization.

3.3.3. Double Hit Compression Tests

To study the progress of static and metadynamic recrystallization during finish rolling, several sets of double hit compression tests were performed. After reheating, the specimens were then slowly cooled ($1^{\circ}\text{C}\cdot\text{s}^{-1}$) to the test temperature (Figure (3-4)). After holding at the test temperature for 5 minutes, the first deformation was applied. Testing was interrupted at the strains ranging from the critical strain for static recrystallization up to the steady state strain for strain rates of 0.01, 0.1 and 1s^{-1} and temperature range 900 to 1050°C . After unloading, the specimen was held at the test temperature for a time

between 0.1 to 500 seconds and then the specimen was reloaded to the same level of strain followed by water quenching.

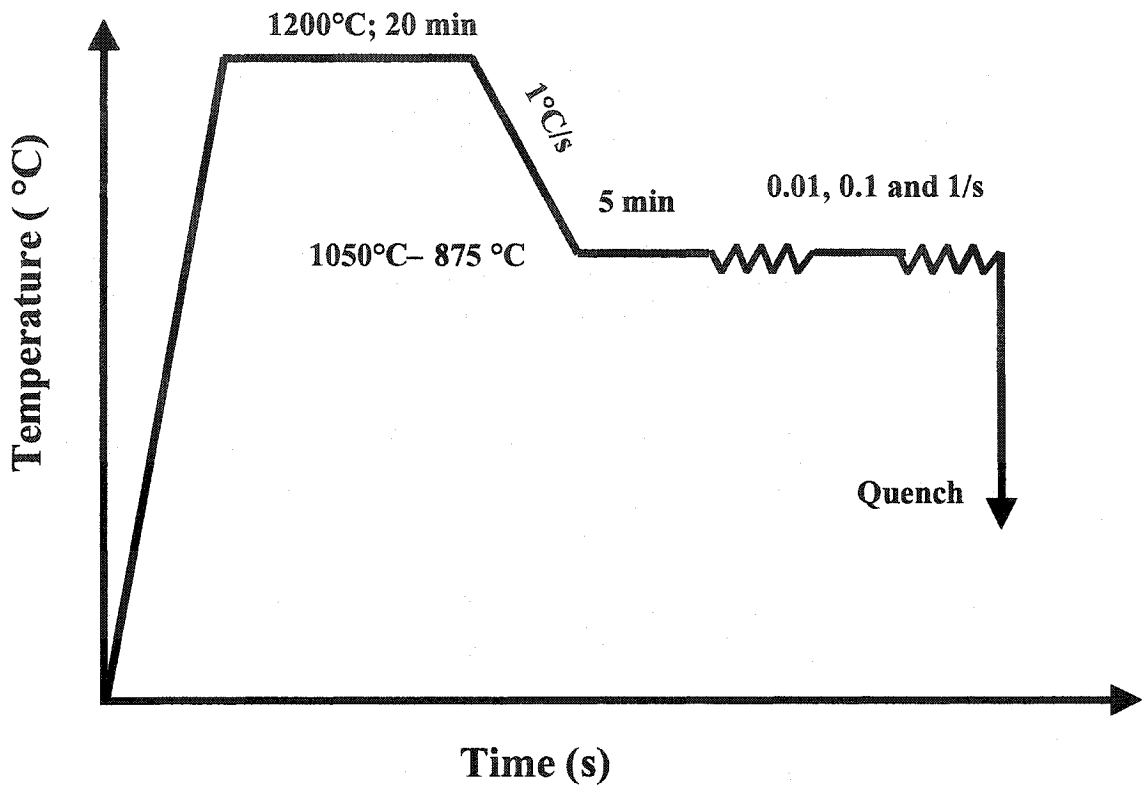


Figure (3-4) Schematic illustration of the TMP schedule for characterizing static and metadynamic recrystallization.

3.3.4. Measuring the Softening

The interrupted deformation method is based on the principle that the yield stress at high temperatures is a sensitive measure of structural changes. In this work, the 0.2% offset yield strength was used to determine the softening due to metadynamic and static recrystallization, as shown in Figure (3-5). The fractional softening, X, is measured by:

$$X = \frac{[\sigma_m - \sigma_2]}{[\sigma_m - \sigma_1]} \times 100 \% \dots\dots\dots 3-10$$

where: σ_m is the flow stress at the interruption

σ_1 is the offset stress (0.2%) at the first hit

σ_2 is the offset stress (0.2%) at the second hit

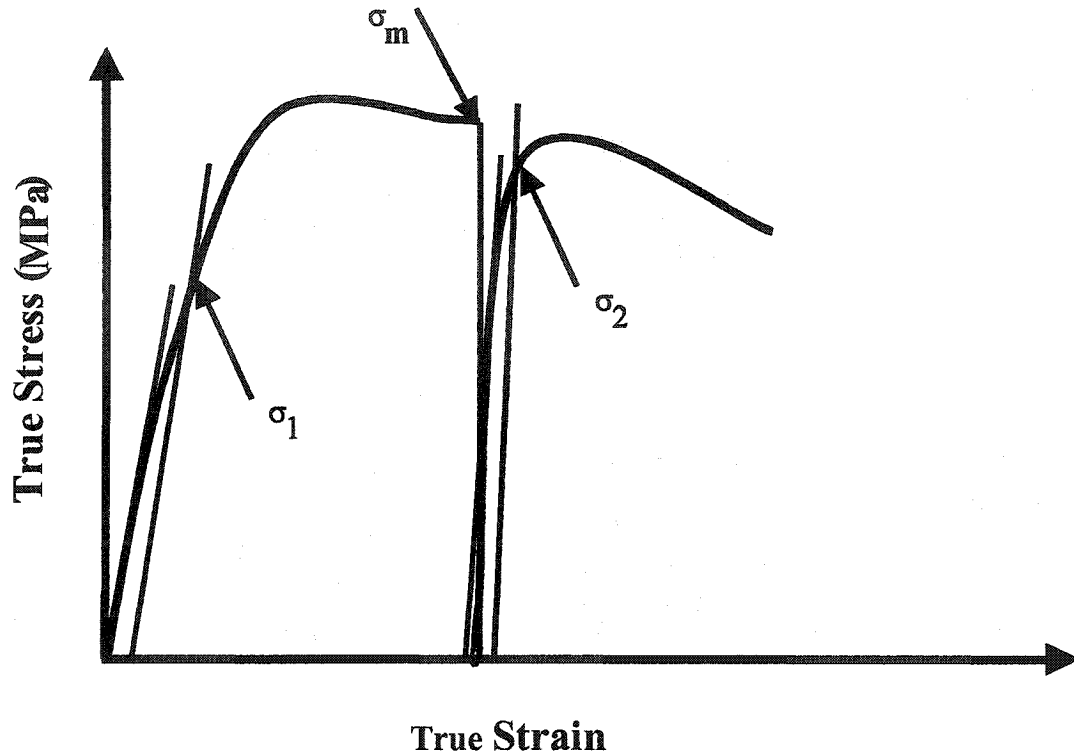


Figure (3-5) Measurement of the softening by the 0.2% offset method.

3.3.5. Continuous Cooling Compression Testing Procedure

For the purpose of characterizing the transformation temperatures of austenite-to-pearlite, continuous cooling compression (CCC) testing was performed. This utilizes the concept of changes in flow behavior that accompany changes in phases. Figure (3-6) shows a typical CCC test schedule, which is defined in terms of temperature and time. The specimen was reheated and then cooled at a constant $1^{\circ}\text{C}\cdot\text{s}^{-1}$ cooling rate. When the temperature reached 850°C , continuous deformation at a constant strain rate of 0.001s^{-1}

was applied to the specimen during cooling. The true strain and true stress were calculated from the data generated during deformation.

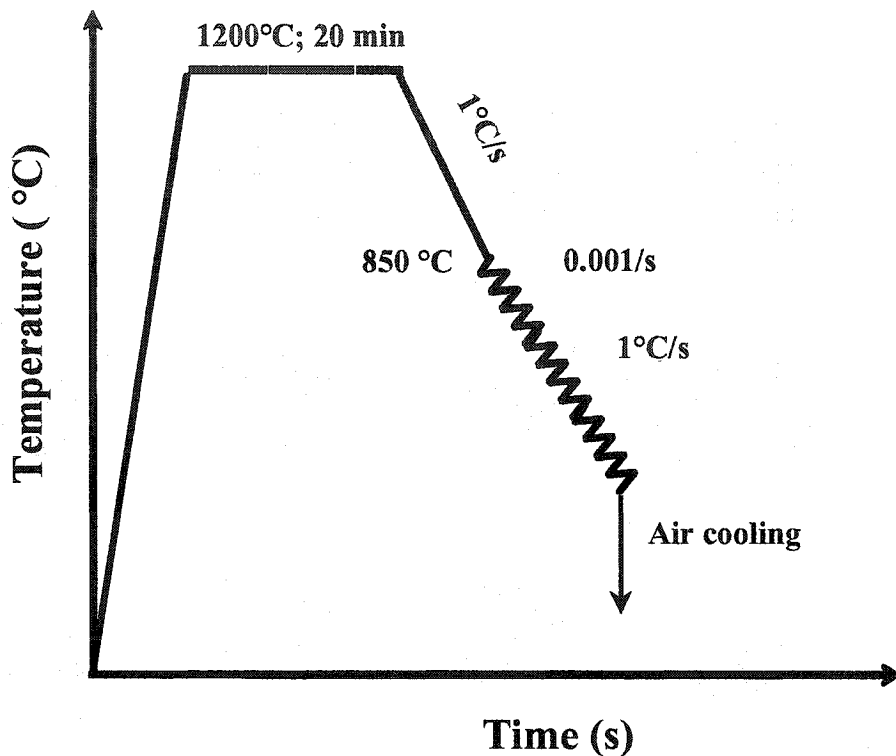


Figure (3-6) Continuous Cooling Compression (CCC) test schedule.

3.3.6. Mechanical Property

3.3.6.1. Heat-treated Specimens

The specimens were austenitized for 20 minutes at 1200 and 900°C to produce a coarse and a fine austenite grain size. The specimens were isothermally transformed at 550, 580 and 620°C in a molten salt bath for 10 minutes; this was designed to produce a range of interlamellar spacings. After transformation the specimens were water quenched.

3.3.6.2. Deformed Specimens

The specimens were austenitized for 20 minutes as before at 1200 and 900°C. At these temperatures, compression testing was performed at a strain rate of 0.01s^{-1} and was interrupted at a strain of 0.1, which is below the critical strain required for dynamic recrystallization with an interpass time of 5 minute. The specimens were immediately isothermally transformed, as per the heat-treated specimens, and water quenched.

3.4. Mechanical Property Measurements

3.4.1. Shear Punch Test

The mechanical properties at room temperature were measured using a shear punch test method [97]. This technique was selected since the compression specimens were too small for the usual tensile testing. The shear punch apparatus (Figure (3-7)) consists of a punch and a die. The centers of the punch and die were exactly aligned. Testing was carried out on the MTS previously described. The specimens were cut transversely to give 2-3 rectangular slices, which were ground with 600 grit SiC paper to a final thickness 300-350 μm . The specimens sheet was fixed between the die and a washer. The latter of which prevented the specimen from moving during punching. A flat tip tool was driven through the specimen, punching a 1.5 mm circular diameter from it. Meanwhile, the force-displacement data were recorded by means of a load cell and displacement transducer.

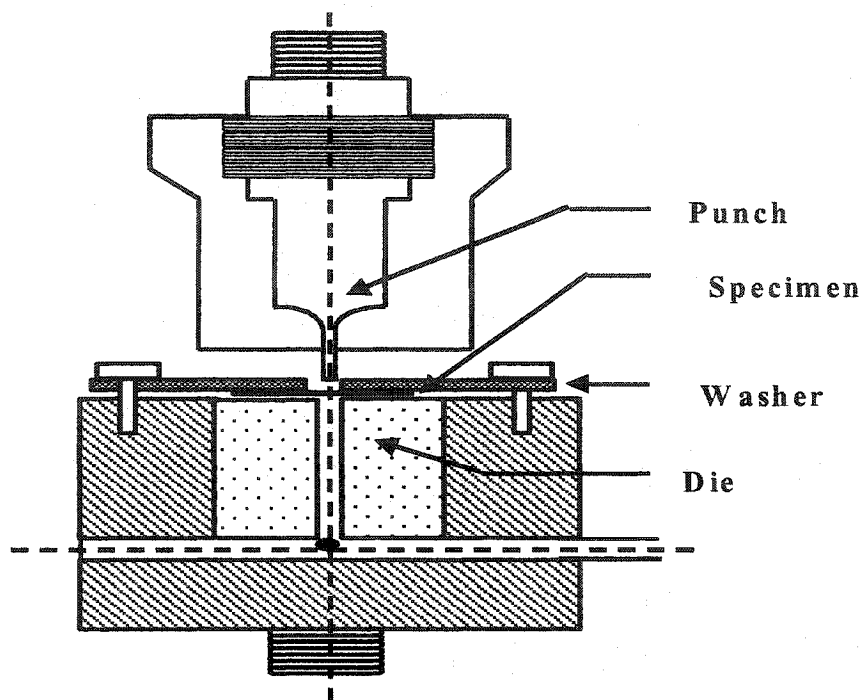


Figure (3-7) Schematic illustration showing the shear punch unit.

3.4.2. Data Manipulation

In order to calibrate the shear-punch data with the standard tensile data, a series of shear punch and uniaxial tensile tests were performed at room temperature. A typical example of a force-displacement curve produced by the shear punch is shown in Figure (3-8). It is apparent that this deformation possesses all the features of a force-displacement curve produced in uniaxial tension. These include an elastic zone, a deviation from elasticity, a plastic zone, a load maximum necking and final fracture.

Lucas et al. [98] have suggested that the force at deviation from linearity, P_y , and the maximum force, P_m , correlate well with the uniaxial yield and tensile strengths, respectively, according to the following empirical equation:

$$\sigma_{eff} = \frac{P - P_f}{2\pi r t} = C\sigma \dots\dots\dots 3-11$$

where P is the yield or maximum load, σ is the corresponding yield or maximum stress in tension, P_f is the friction load, r is the punch radius, t is the specimen thickness, and C is the correlation factor.

By means of this correlation factor, the calculated effective stresses can be translated in to uniaxial tensile stresses. This can be obtained by taking the slope of the best-fit regression between these two parameters for standard materials or for materials whose uniaxial yield and tensile strengths are known.

The total elongation is determined by the following empirical equation where El_{total} is the total elongation and d_f is the displacement at failure.

$$El_{total} = \frac{d_f}{t} \dots\dots\dots 3-12$$

It should be mentioned that this equation was originally derived for the reduction of area at fracture. However, in this work, correlation of the punch data with uniaxial tension results showed that the (d_f/t) ratio corresponded to the total elongation at fracture.

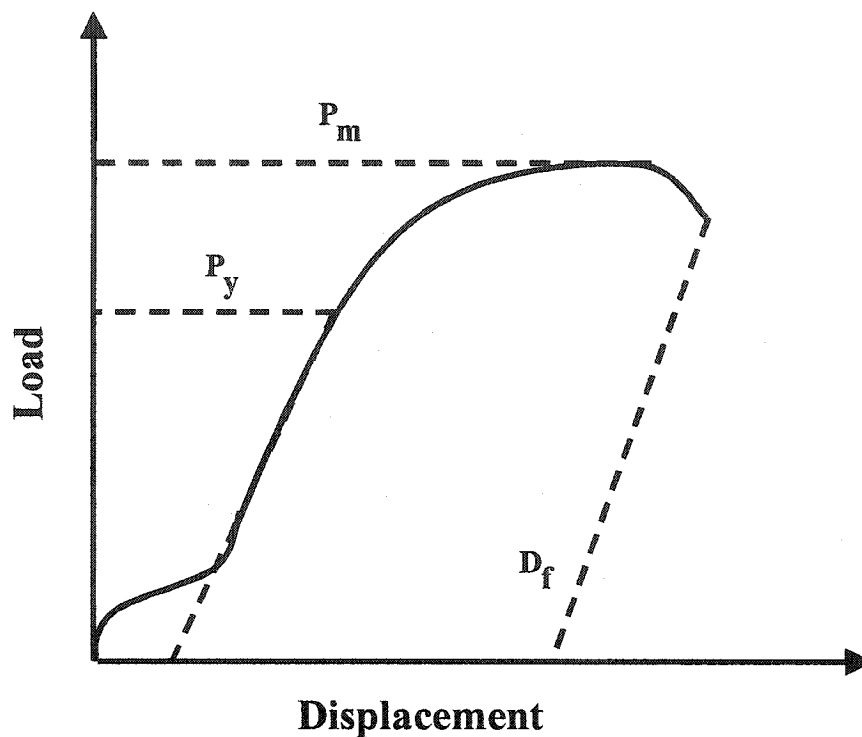


Figure (3-8) A typical load-displacement curve for steels.

In order to calibrate shear punch data with standard tensile data, a series of shear punch and uniaxial tension tests was performed at room temperature. In general, more than eight shear punch tests and five tensile tests were performed for each material.

By applying the above correlation, it was found that, for the yield data (Figure (3-9)) $C = 0.54$, and for the maximum load data (Figure (3-10)), $C = 0.64$. The 95% confidence interval on the predicted stress for a given P is $\pm 8\%$ of σ_y for yield and $\pm 6\%$ of σ_{UTS} for ultimate tensile stress.

Shear punch data have also been used to determine the ductility of material by correlating the ratio D_f/t from shear punch tests with either the reduction of area [99] or total percent elongation [100]. For the materials tested, the latter correlation best fits the shear punch data as shown in Figure (3-11).

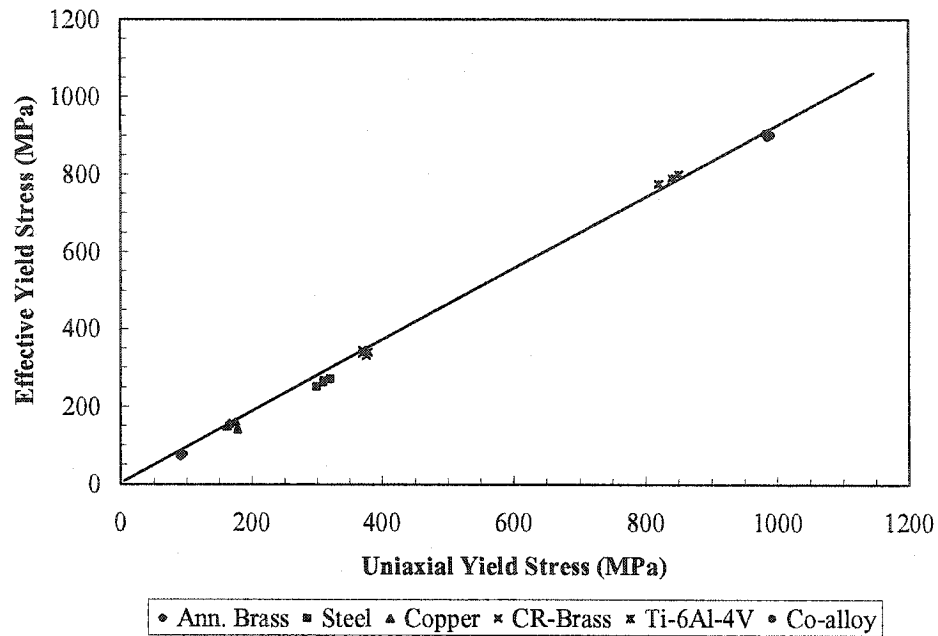


Figure (3-9) Comparison of the shear yield data with yield strength from uniaxial tensile data. The solid line is the regression line for the yield data.

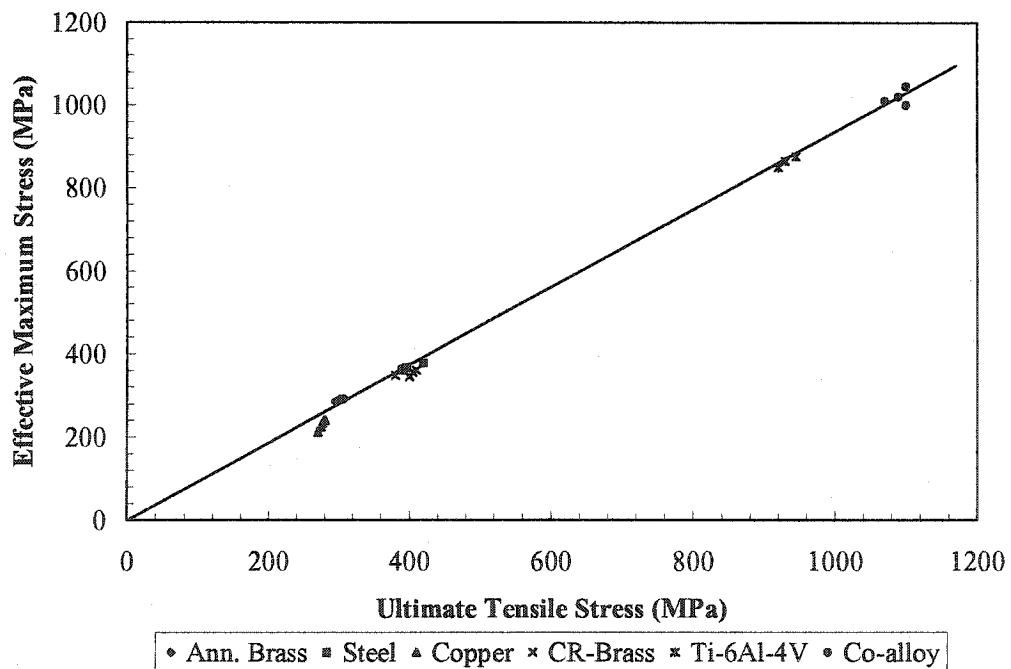


Figure (3-10) Comparison of the ultimate tensile strength determined by the shear punch and uniaxial tensile data. The solid line is the regression line for the maximum load data.

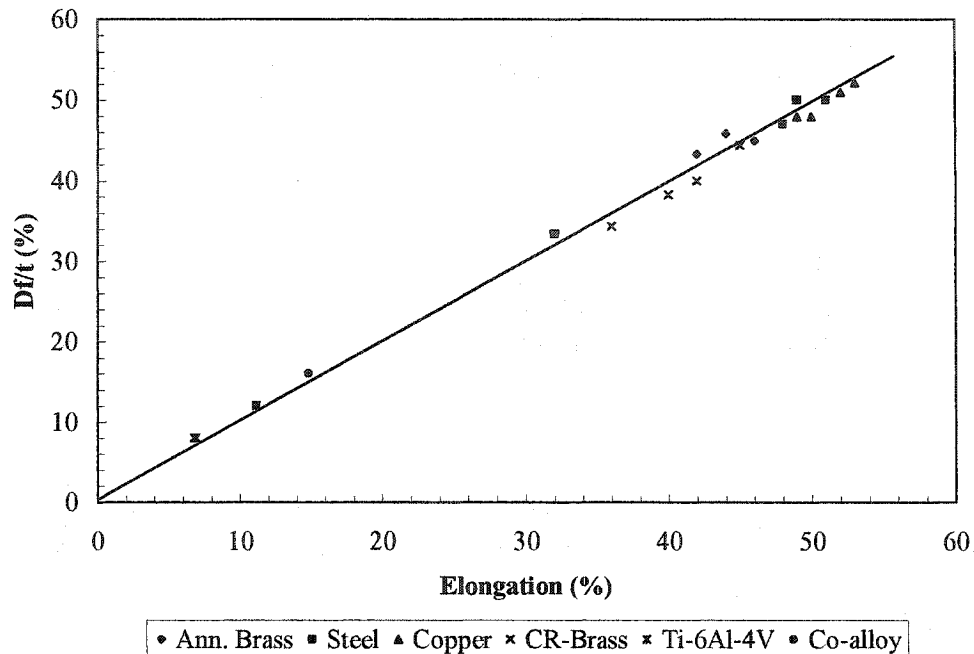


Figure (3-11) Comparison of D_f/t with percent elongation measured in uniaxial tension.

The solid line is the regression line for the ductility data.

3.5. Metallography

3.5.1. Optical Microscopy

Metallographic preparation of the steel specimens involved mounting in bakelite followed by automated grinding using successively finer silicon carbide papers from 60 to 800 grit. The specimens were then polished with 9, 3 and 1 μm water-based diamond suspensions on short nap cloths with an alcohol-based lubricant. To reveal the prior-austenite grain boundaries, the austenitized and quenched specimens were etched by immersing in a solution containing 4 drops HCl, 10 drops wetting agent Teepol and 100 ml saturated aqueous picric acid that was heated to 80°C. It is noteworthy to mention that during etching the specimens were swabbed regularly with cotton wool to remove dark deposits from forming due to the chemical attack. The prior-austenite grain size of

the specimens was then determined from light optical micrographs by the intercept method [101].

3.5.2. Field Emission Scanning Electron Microscopy (FE-SEM)

Field Emission Scanning Electron Microscopy FE-SEM is a high-resolution imaging technique that provides topographic and structural information in plan view or within the cross-section. Used in conjunction with X-Ray microanalysis by an Energy Dispersive Spectroscopy (EDS), the FEG-SEM can qualitatively and quantitatively analyze the elements present in a selected area of a secondary or backscattered electron image.

To reveal and characterize the fine precipitates in the microalloyed steels, an imaging technique capable of achieving good resolution and contrast at a magnification of roughly 100,000x is necessary. For such applications, the selection of an appropriate detector is a significant factor in determining how charging, contrast and contamination will occur. In this work, the Hitachi S-4700 FEG-SEM was used with a mixed detection system using the lower and upper detectors. A feature of this microscope is the Snorkel lens with the ExB filter, which can be used to select a mix of electrons reaching the upper detector. In this work, the upper detector was used for its high resolution and high signal to noise ratio ability for secondary electron imaging. The system can be adjusted, with the voltage bias, to give images consisting of pure secondary electrons to pure backscattered electrons, and anywhere in between. This provides great flexibility in overcoming charging and in optimizing imaging contrast.

For microalloyed steels, the usual approach for fine precipitate characterization is transmission electron microscopy. However, TEM specimen preparation (foils or carbon replicas) is much more involved than that for FE-SEM specimens. Moreover, for steels

with considerable levels of pearlite, both thin foil and extraction replica preparation are problematic, since cementite is not easily attacked by the etchants that attack ferrite.

It is noteworthy that application of the FE-SEM for magnetic materials, such as the microalloyed steels used in this work, is problematic in that the electromagnetic field around the electron beam column results in the vertical shifting of the specimen. Thus, a clamping device was designed and utilized for rigid fixing of the specimen to the sample holder.

3.5.3. Quantifying Pearlite

A series of photographs was taken of each surface; from these, the nodule size was readily determined using the linear intercept method. The delineated pearlite nodules were then measured from a series of light optical micrographs using the linear intercept method in which the mean linear intercept, \bar{l} , was the average size of the nodules and computed as

$$\bar{l} = \frac{l}{MN} \dots\dots\dots 3-13$$

Where l is the total line length employed, M is the magnification of the micrograph, and N is the number of nodule boundaries intersected by the test line.

All samples were examined in the FE-SEM to measure the interlamellar spacing of the pearlite. The samples were ground and polished to a fineness of 1 μm , and were etched in 4% nital. The mean true spacing was determined using a method similar to that recommended by Underwood [102]. Specifically, concentric circular test lines were superimposed over the FE-SEM image, and the number of intersections of cementite lamellae was counted to give the mean intercept spacing, \bar{b} :

$$\bar{b} = \frac{L}{N} \times \frac{1}{M} \dots\dots\dots 3-14$$

where

L is the total length of line used

N is the total of cementite lamellae intersected

M is the magnification

Each value of \bar{b} involved measurements of at least average 30 pearlite colonies fields of view and a total of not less than 2000 intersections. The mean intercept spacing was then used to calculate the mean true spacing, S_o , using the following relationship [103]:

$$S_o = \frac{\bar{b}}{2} \dots\dots\dots 3-15$$

The colony size was measured by optical microscopy, again by obtaining the mean linear intercept.

CHAPTER 4

The purpose of the present research was to study the effect of silicon and vanadium alloy additions on pearlitic steels with respect to (i) dynamic, metadynamic and static recrystallization and (ii) as-hot rolled structure and properties.

This chapter starts with an analysis of the reheated austenite grain size. This is followed by a presentation of the results concerning the continuous stress-strain curves. Then, the softening results of static and metadynamic recrystallization and the effect of the deformation parameters are described. Microstructures related to the mechanical tests described above are introduced. Finally, the mechanical properties results are related to the microstructure.

4.1. Reheated Austenite Grain Size

Since the austenite grain size of steel is an important factor in determining its response to heat treatment and mechanical properties, it was necessary to determine this for the different steels compositions. Individual specimens were reheated to austenitization temperatures 1200, 1100, 1000 and 900°C and held for 20 minutes before quenching. The austenite grain size was well delineated, as can be seen in Figures ((4-1) and (4-2)). As shown in Figure (4-3), in general, the grain size increases with increasing austenitising temperature. The inhibiting effect of V and Si additions leads to distinctly finer prior austenite grain size. As the V contents increased, the austenite grain size decreases, as shown by comparing steels A to C. The grain size decrease, however, also corresponds to a decrease in the C content.

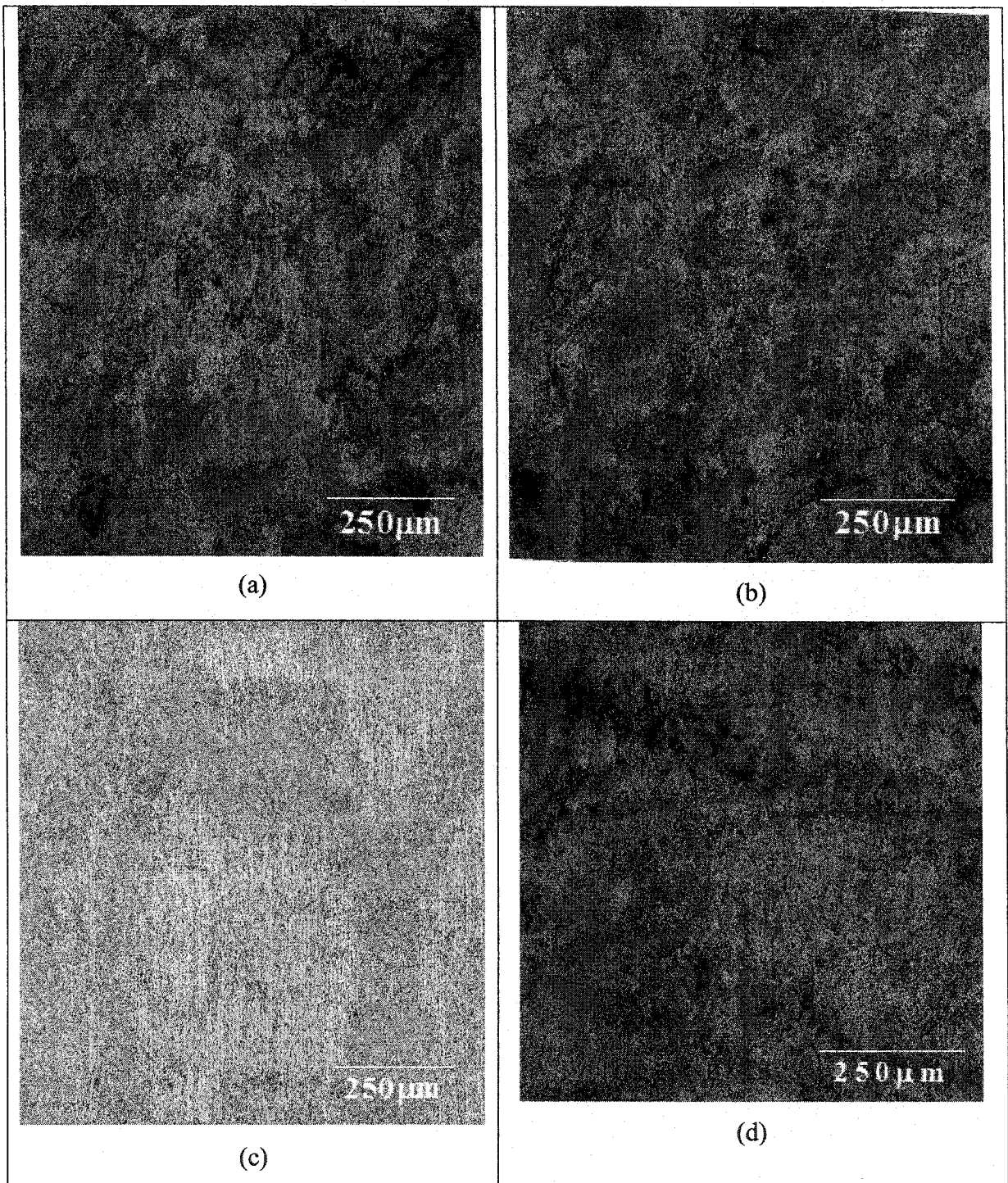


Figure (4-1) Reheated austenite microstructures of the A steel: (a) 1200°C, (b) 1100°C
(c) 1000°C and (d) 900°C.

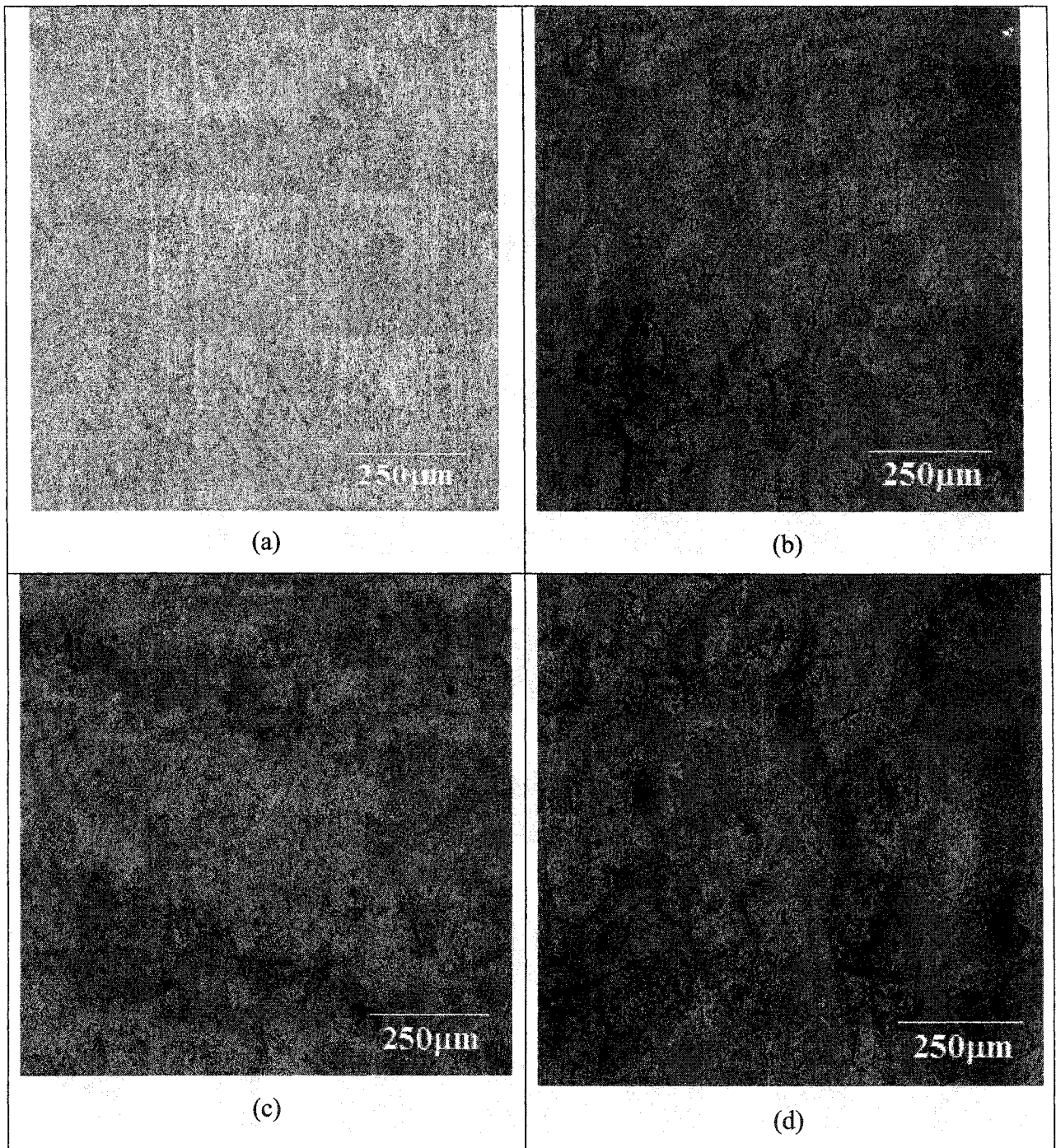


Figure (4-2) Reheated austenite microstructures for four steels at 1000°C: (a) A, (b) B (c) C and (d) E.

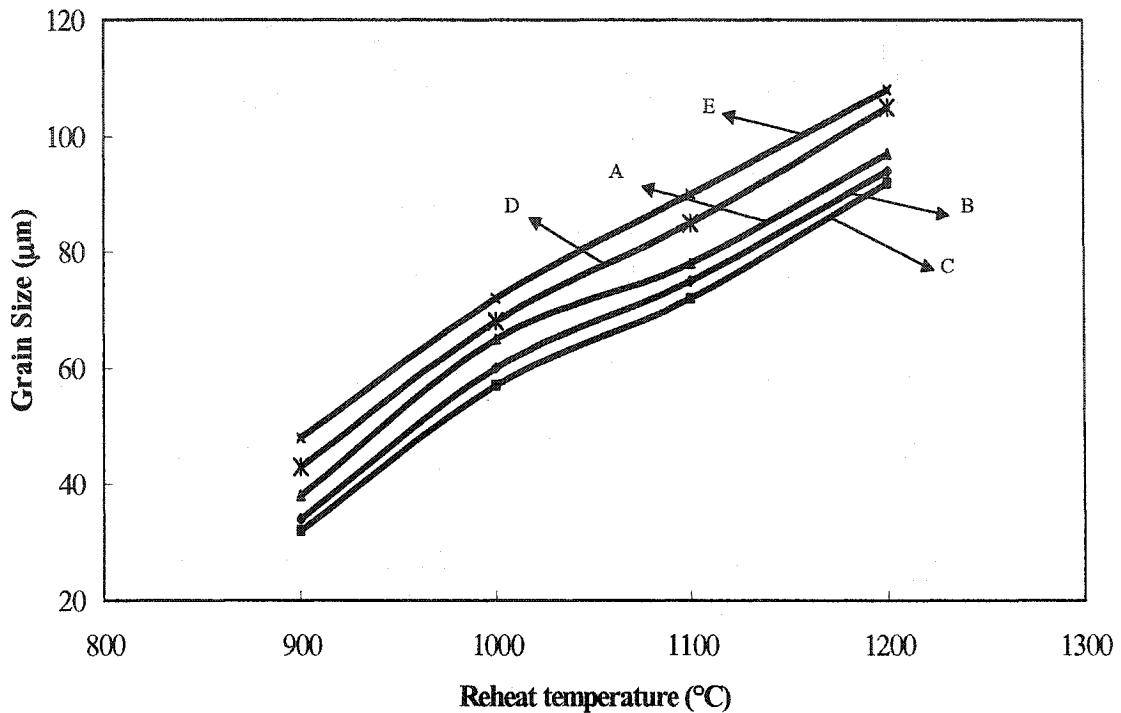


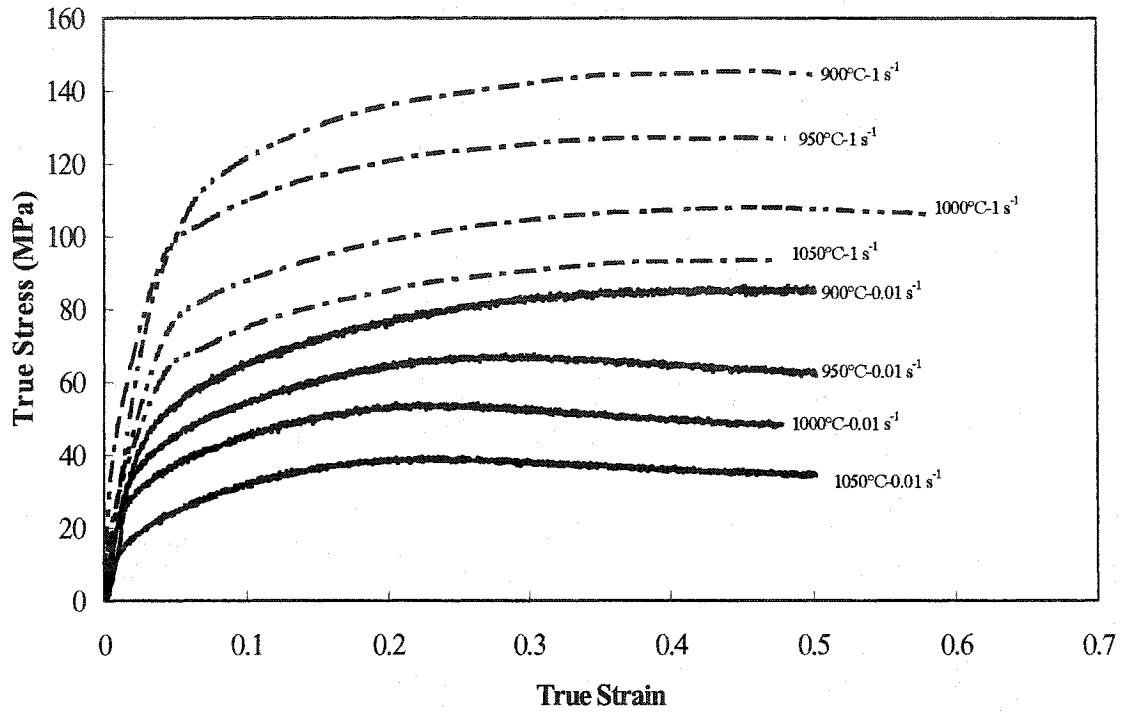
Figure (4-3) Effect of austenitizing temperature on prior austenite grain size.

4.2. Flow Curves

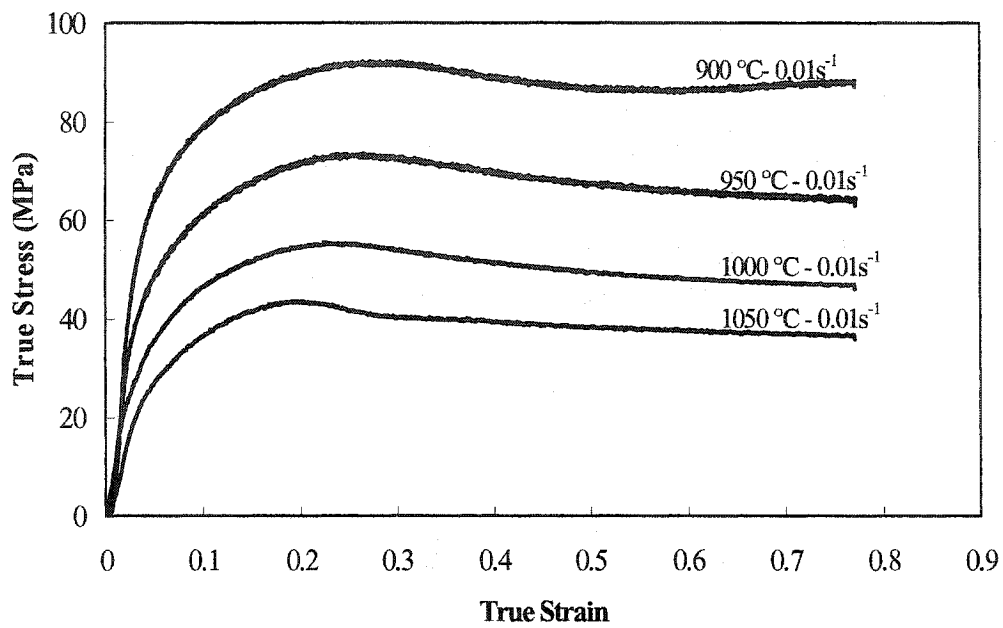
4.2.1. Single Hit Flow Curves

The flow curves obtained for the five steels deformed to a strain of 0.7 were plotted for the deformation temperatures (900°C-1050°C) for various strain rates. All flow curves displayed a rapid initial increase to a stress maximum, characterized by a peak strain and peak stress, followed by a gradual fall to a constant stress level (steady state stress). Examples of the flow stress/strain curves are given in Figure (4-4) for steels A, B, C, D and E. As expected, with decreasing deformation temperature the values of peak strain, peak stress and steady state stress increased. Cyclic flow behavior, associated with grain *coarsening* during dynamic recrystallization, was found at 1050°C at strain rate $0.01s^{-1}$ (Figure 4-4d). Below 1000°C only single peak behavior

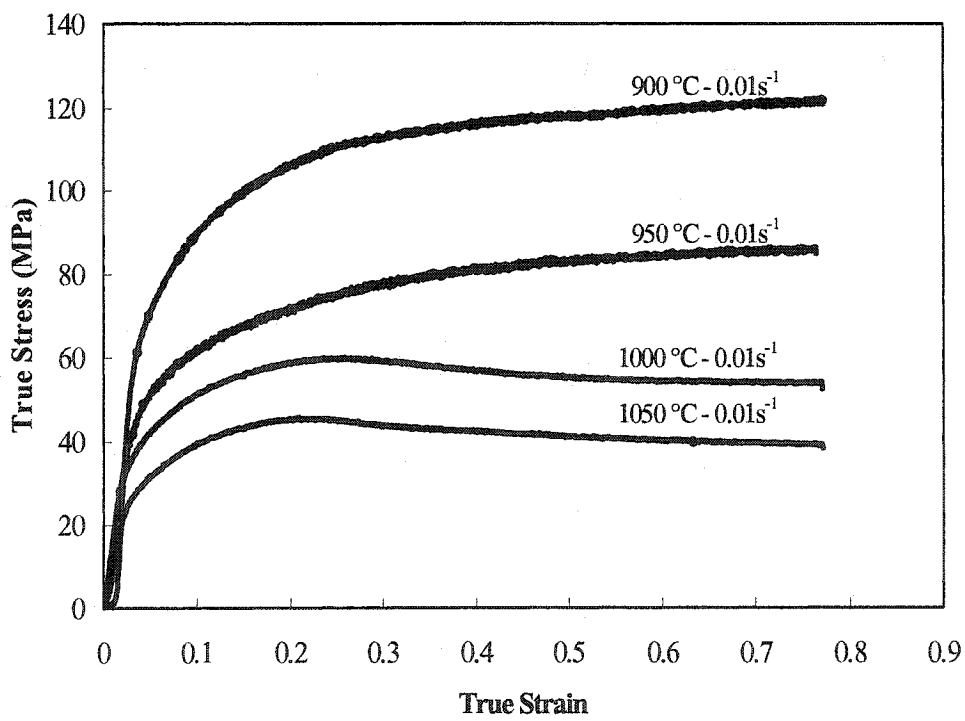
characteristic of grain *refining* during dynamic recrystallization can be seen. As mentioned in the literature review, increases in strain rate or reductions in temperature favor single peak behavior.



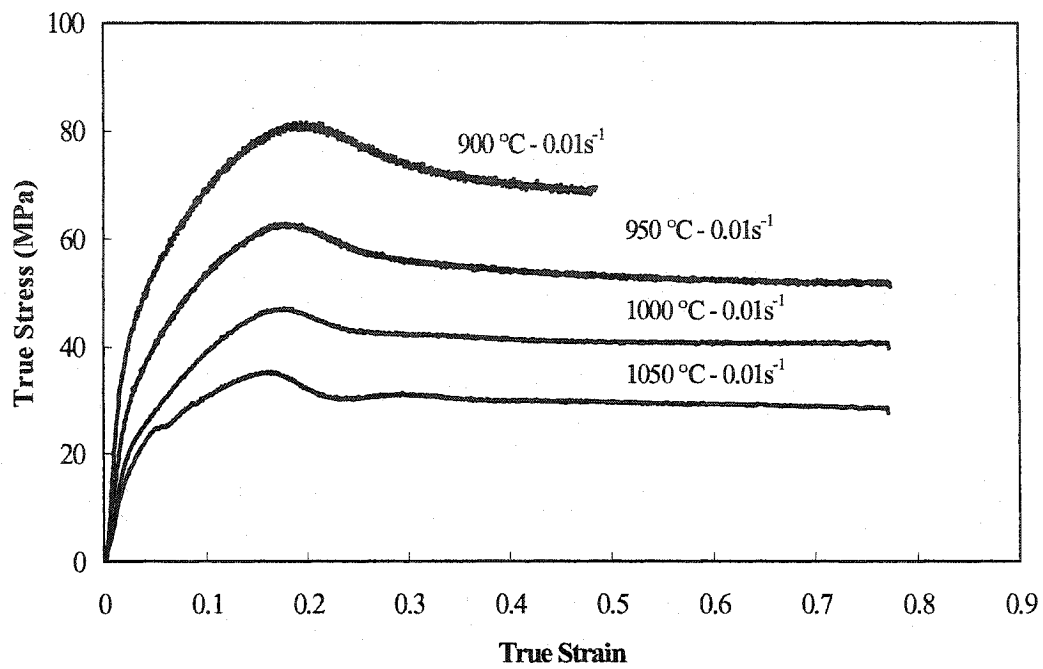
(a)



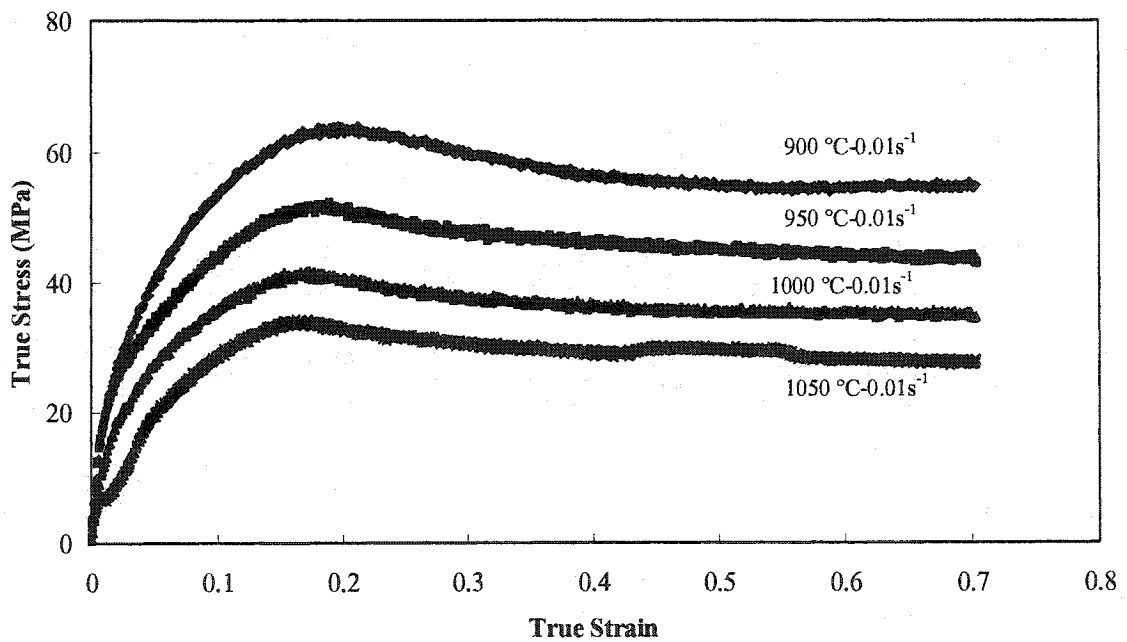
(b)



(c)



(d)



(e)

Figure (4-4) Stress-Strain curves for steels (a) A, (b) B, (c) C, (d) D and (e) E.

4.2.2. Double Hit Flow Curves

Examples of interrupted compression stress-strain curves are displayed in Figures ((4-5), (4-6), (4-7) and (4-8)) for steels A, B, C, and E. Several interrupted compression tests with increasing unloading times are plotted together to demonstrate the effect of the unloading time on the flow curves.

Using the data from the single hit tests, tests were designed to initiate dynamic recrystallization in the first hit, so that metadynamic recrystallization would occur in the unloading (static) period. Interrupted compression stress-strain curves with increasing unloading times are given in Figure (4-5) for steel A. As expected, when the unloading time is short, little softening occurs. As a consequence of the lack of softening, the second hit curve displays little work hardening prior to reaching the dynamic recrystallization peak. When the unloading time is increased, metadynamic recrystallization occurs and diminishes the dislocation density somewhat, leading to increased work hardening on reloading. Note that the peak stress and strain are much smaller after full metadynamic recrystallization because of the grain refinement that has occurred due to dynamic recrystallization. The higher grain boundary area per unit volume increases the recrystallization nucleation rate, since grain boundaries are preferred nucleation sites. This will therefore decrease the peak strain and consequently, the peak stress since less work hardening will have occurred in reaching the peak strain.

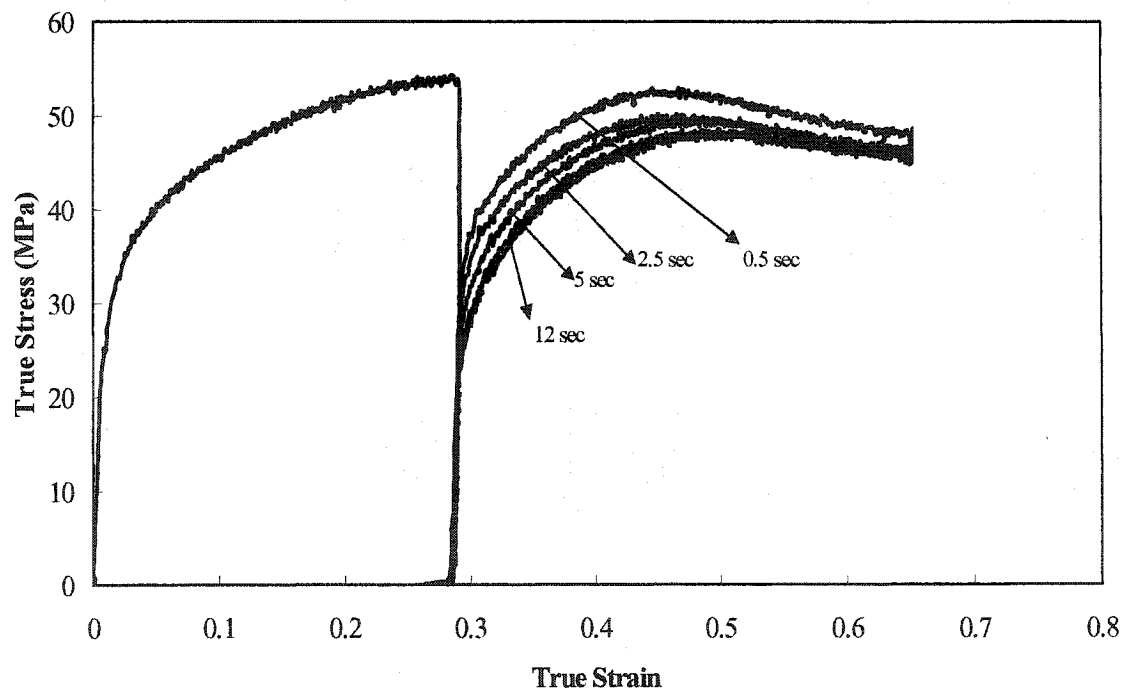
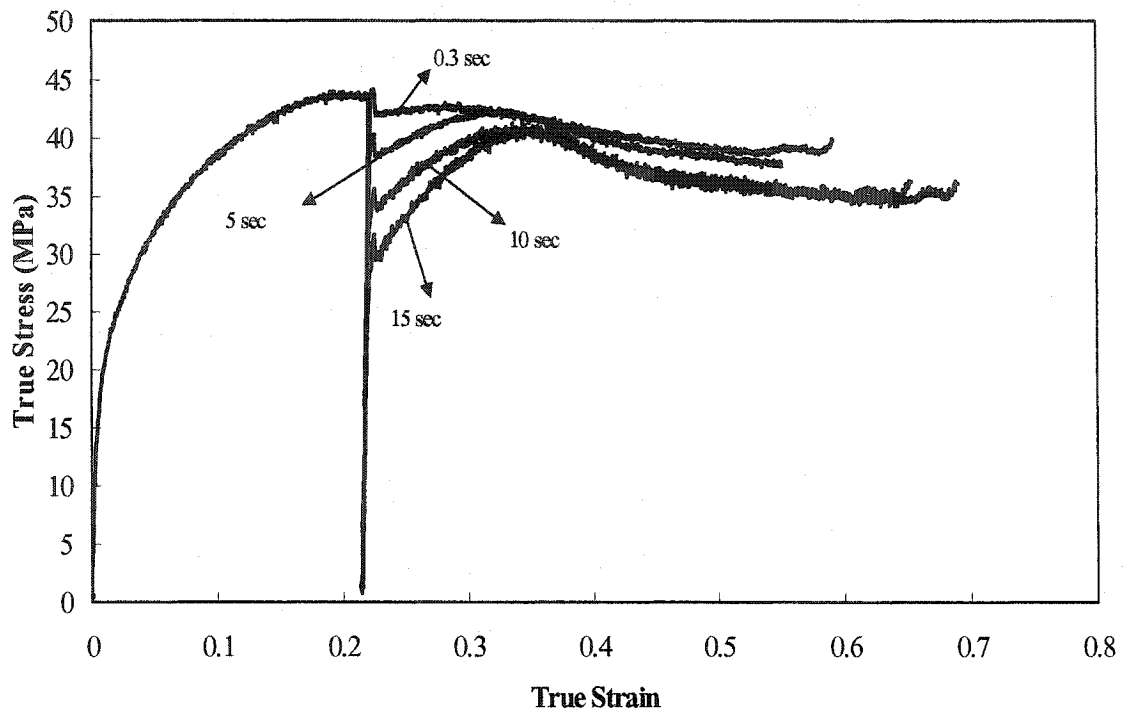


Figure (4-5) Stress-strain curves determined for steel A showing the softening taking place at 1050°C for different unloading times (a) 0.01 s^{-1} and (b) 0.1 s^{-1} .

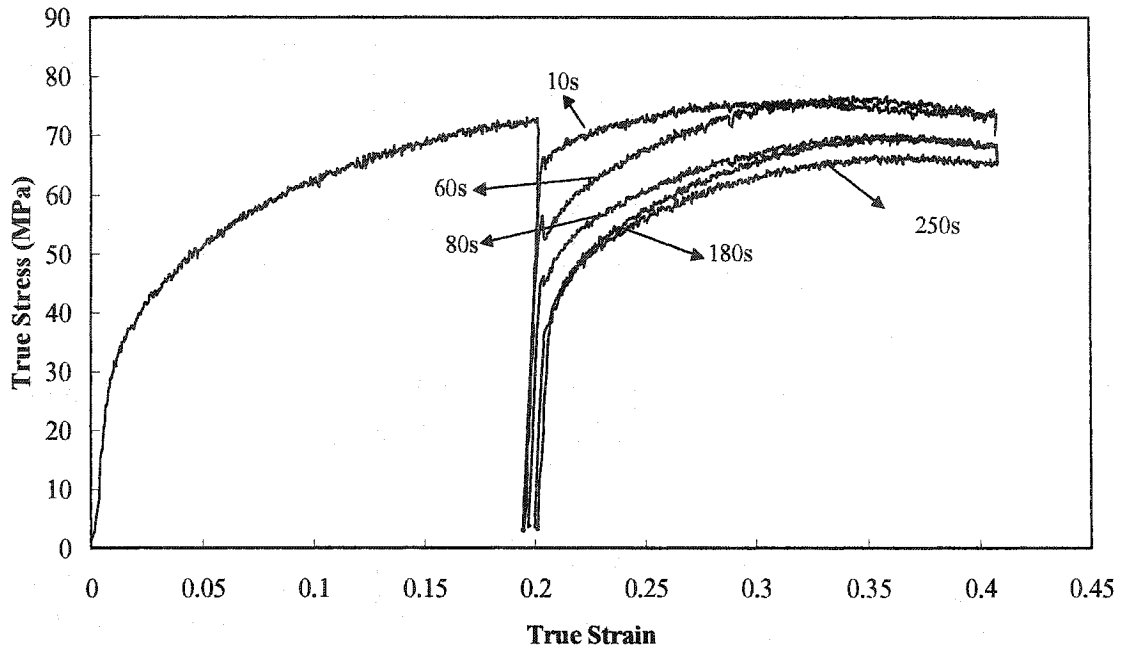


Figure (4-6) Stress-strain curves determined for steel B showing the softening taking place at 925°C for different unloading times at a strain rate 0.01 s^{-1} .

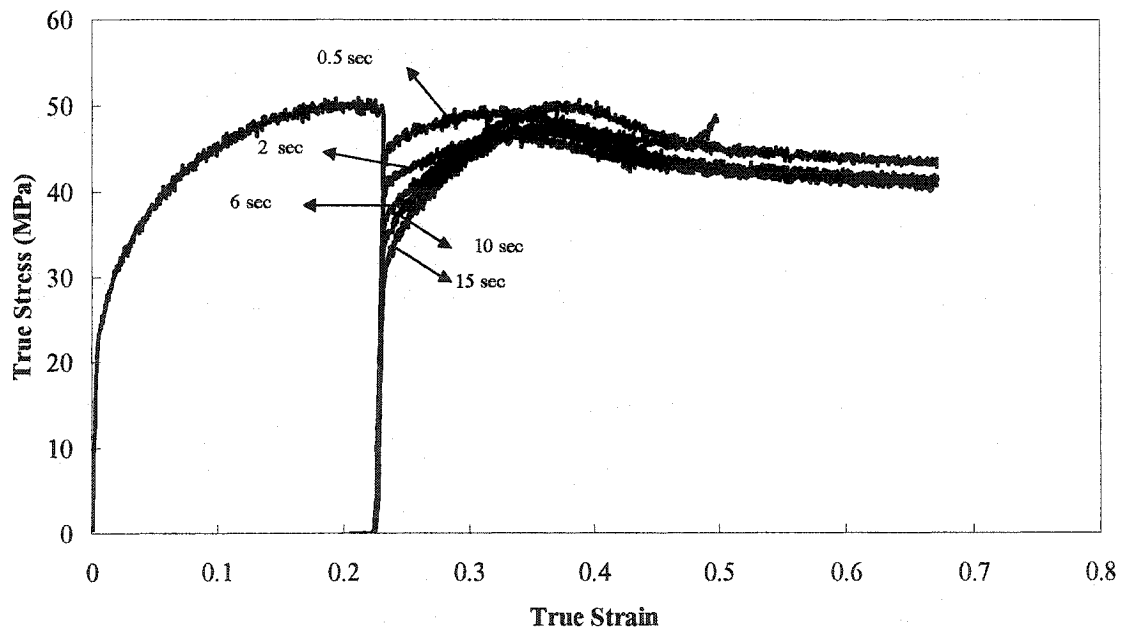
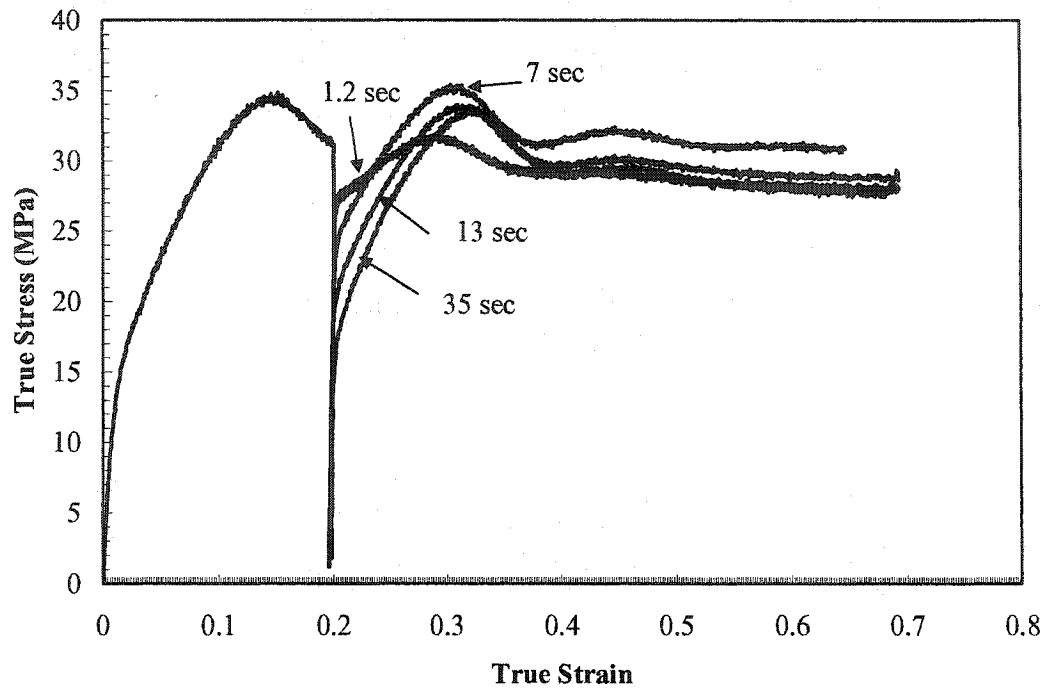


Figure (4-7) Stress-strain curves determined for steel C showing the softening taking place at 1050°C for different unloading times at strain rate 0.01 s^{-1} .



(a)

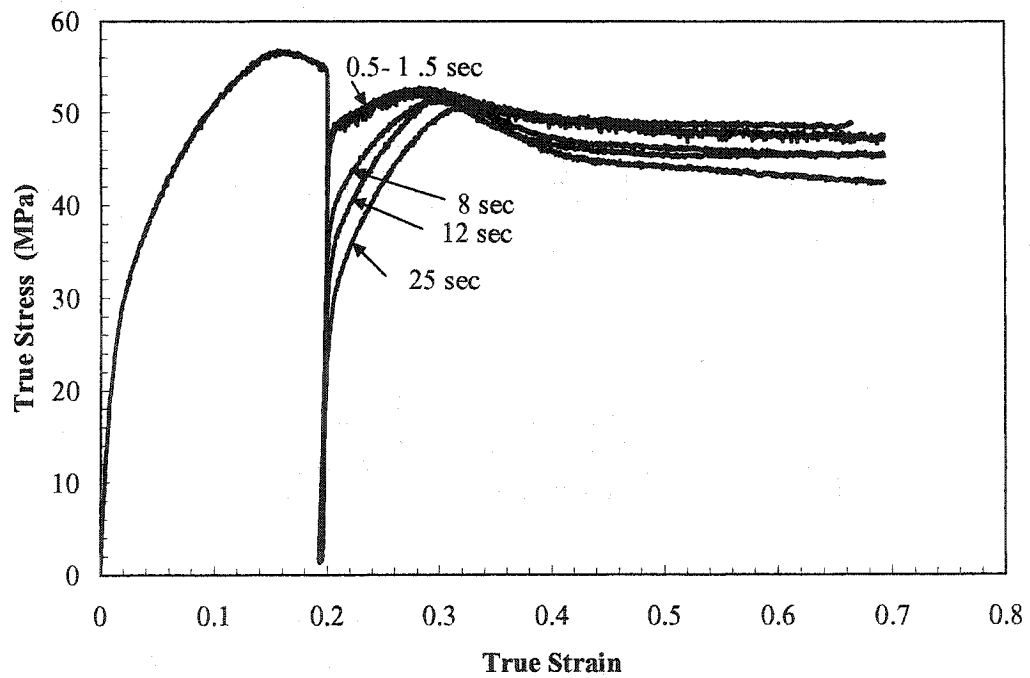


Figure (4-8) Stress-strain curves for steel E showing the softening taking place at (a) 1050°C and (b) 950°C for different unloading times at strain rate 0.01 s^{-1} .

4.3. Continuous Cooling Compression (CCC)

The CCC method is based on the correlation of significant changes in the flow stress versus strain behavior to microstructural changes. Figure (4-9) shows the hypothetical flow stress behavior as a function of temperature during CCC testing conditions where there is no microstructural change. Therefore, under practical conditions, any deviation from a smooth increase in the flow stress with decreasing temperature can be related to a change in the structural characteristics of the material.

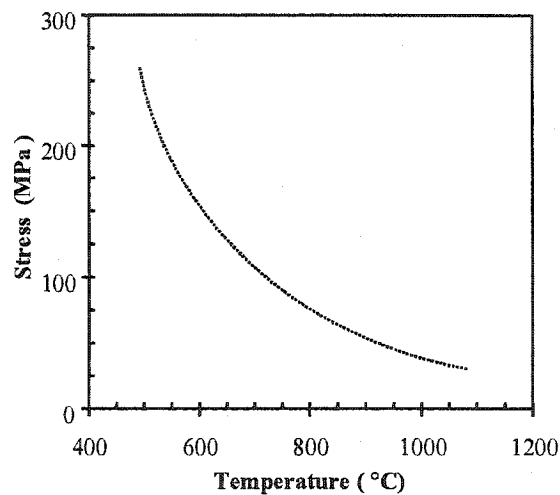


Figure (4-9) Theoretical flow stress behavior during CCC testing.

For the steels A, B, C and E, the CCC true stress-strain curves, given in Figure (4-10), were observed to exhibit an overall increase in the flow stress with increasing strain and decreasing temperature with specific deviations occurring at different temperatures and flow stress levels that reflected the compositional differences in these microalloyed steels. In particular, the addition of V and Si (steels A, B, C versus E) was determined to significantly increase the flow stress levels in these steels, especially at temperatures below 800°C. This flow stress increase may be related to the solute drag and solid solution strengthening effects of V and Si that have been noted to retard dynamic recovery [104,105]. Additionally, for each flow stress-strain curve, two deviations or

inflection points were observed, which could be related to the Ar_3 and Ar_1 temperatures. The first deviation in Figure (4-10), characterized by a stress drop and negative slope in the flow stress-strain curve, indicated that the material became softer and corresponds to the start temperature for the transformation of austenite to pearlite (Ar_3), as the latter is softer than the parent phase at any given temperature [104,106]. As shown in Figure (4-10), a second deviation, which occurred at a strain of 0.3 ± 0.05 , was characterized by a change back to a positive slope in the stress-strain curve, inevitably due to the completion of the austenite transformation (Ar_1) that then produces a rapid increase in the strengthening rate after the first deviation.

From the CCC results, the transformation start temperatures (Ar_3) were obtained to be about 620, 630, 645 and 600°C for steels A, B, C and E, respectively. Steel C was determined to have a higher Ar_3 (i.e. faster austenite to pearlite transformation kinetics) as compared to steels A, B and E, most likely due to the highest V content and relatively high Si level (~0.8%) in the former material. Hence, from the CCC curves it is evident that V and Si additions, either separately or in combination, can have a noticeable effect on the transformation temperature in microalloyed steels. Based on these transformation temperature findings, the salt bath conditions of 550, 580 and 620°C were selected to investigate the evolution of the pearlitic microstructure with thermal processing.

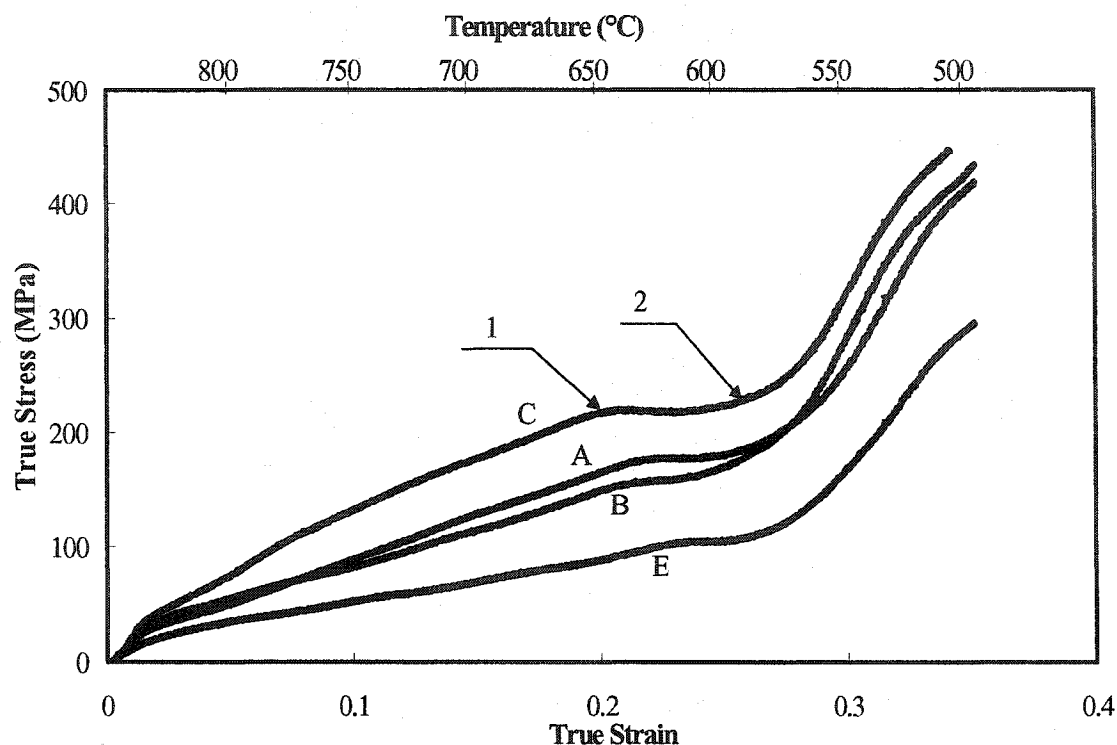


Figure (4-10) True stress-strain curves of steels A, B, C and E obtained by continuous cooling compression testing. Arrows labeled 1 and 2 represent the first and second deviations.

4.4. Microstructural Results

Quenches were performed after selected continuous deformation tests. Examples of microstructures obtained are presented here.

4.4.1. Dynamically Recrystallized Grain Size

4.4.1.1. Vanadium and Silicon Steels

Dynamically recrystallized structures were quenched within the steady state at different temperatures. Examples are presented in Figure (4-11) for steel A. The

microstructure appears to be composed of small equiaxed grains, intermediate grains and deformed elongated grains.

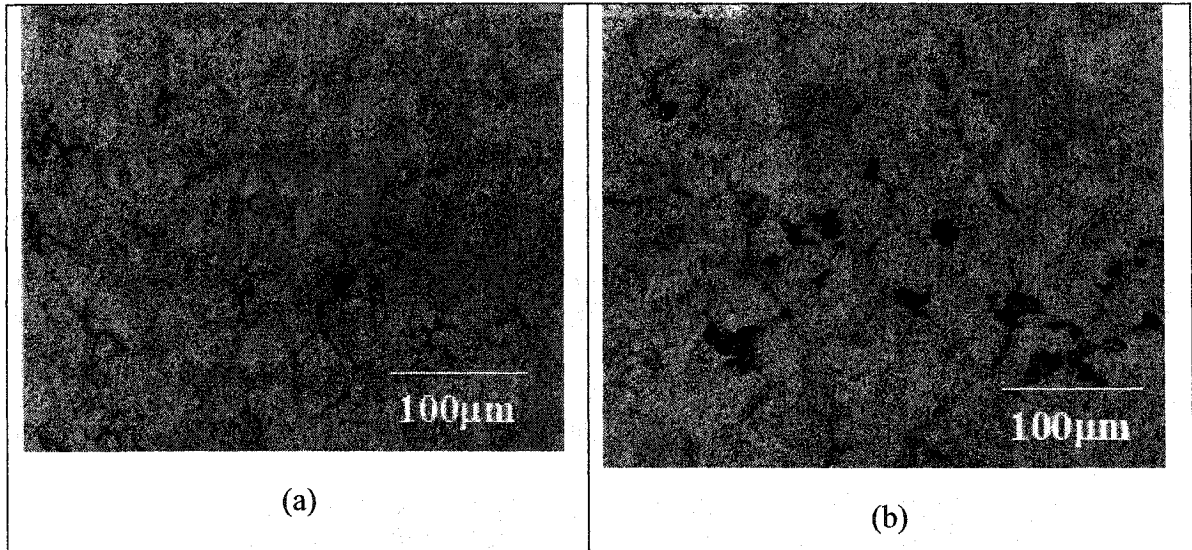


Figure (4-11) Dynamically recrystallized microstructure of steel A deformed (a) 950°C at strain rate = 1s^{-1} and (b) 1000°C at strain rate = 1s^{-1} .

The change in dynamically recrystallized grain size with $\ln(Z)$ for the V and Si steels is plotted in Figure (4-12). It is interesting to note that with increasing V and Si content the dynamically recrystallized grain size decreases. It should be mentioned that, in these steels other elements are also changing; in particular, the Si content of A and D are the same and C and B have an increasing amounts of Si respectively. But it is believed that these would not as strongly influence the dynamically recrystallized grain size. The greater stability of VN leads to its preferential precipitation over VC, particularly at higher temperatures. In enhanced N steels there is still sufficient N to cause the formation of V (CN) to precipitate during and after austenite transformation [107,108]. This is probably leading to the finer dynamically recrystallized grain size, although the mechanism is not clear at this time.

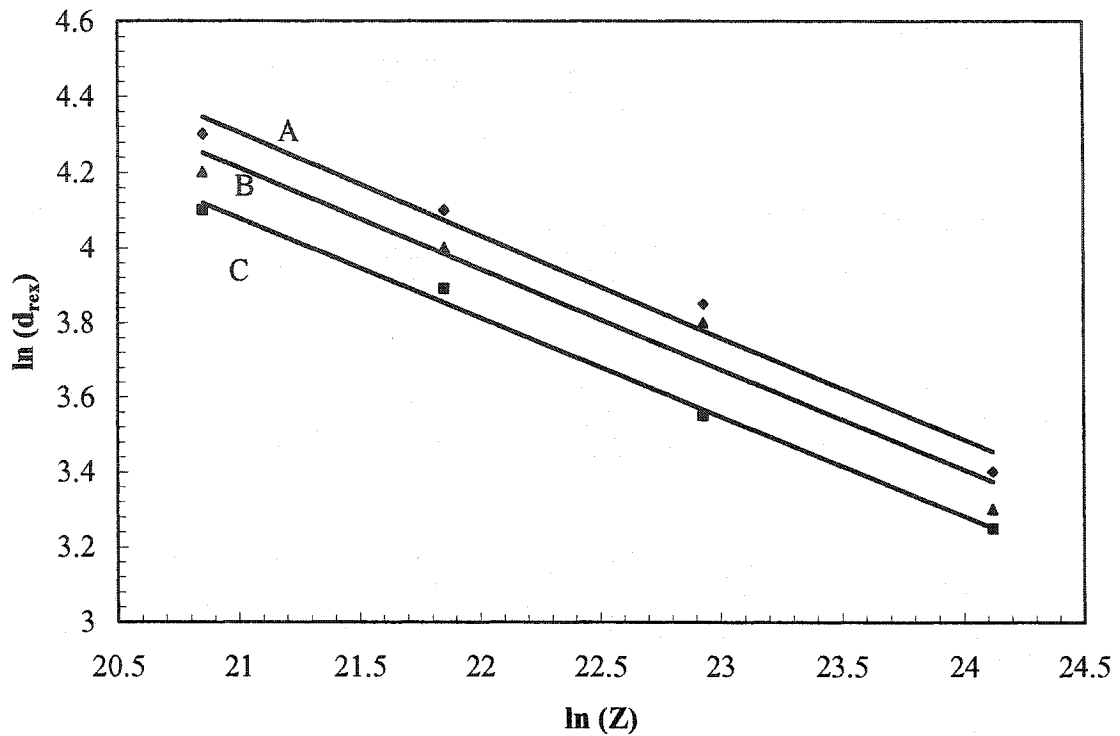


Figure (4-12) Dynamically recrystallized grain size for V and Si steels.

The effect of V and Si on the dynamically recrystallized grain size was determined by fitting a linear regression to the experimental results. The equation for the dependence of recrystallized grain size during deformation temperature and strain rate was determined as given Eq. 2-4. The dependence of B in Eq. 2-4 on V and Si concentrations can now be determined, as shown in Figure (4-13), leading to the following linear relation

$$d_{rex} = [-0.57[V + Si] + 2.4] \times 10^4 Z^{-0.27} \dots\dots 4-1$$

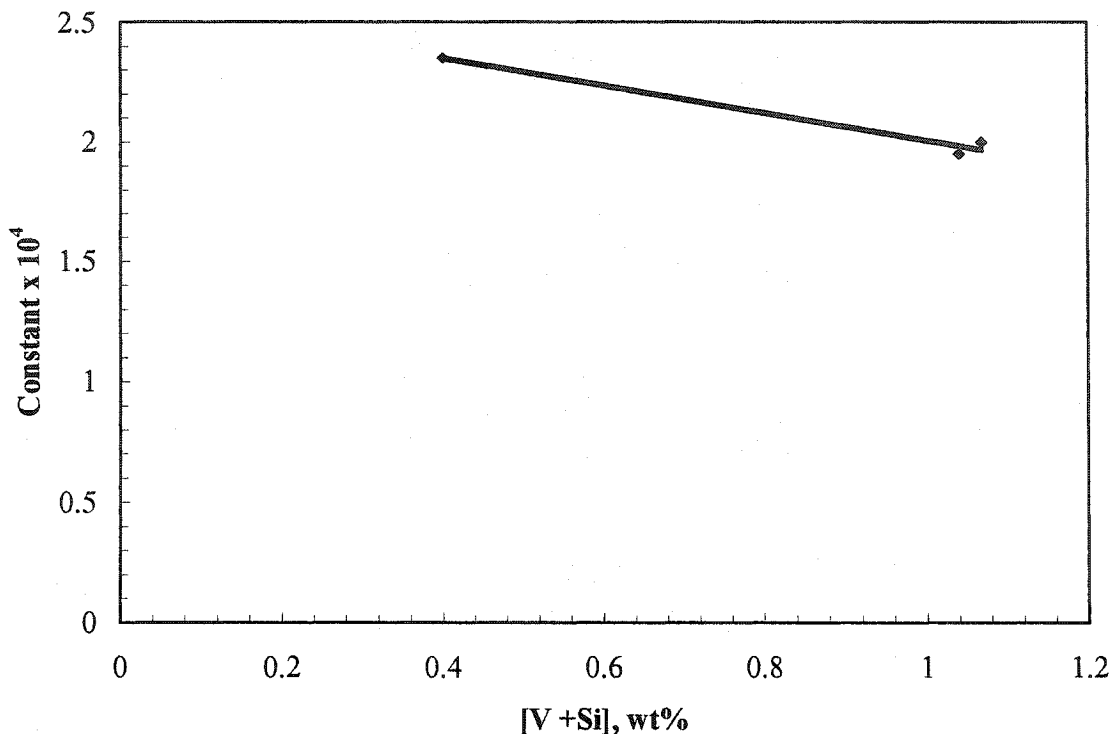


Figure (4-13) Effect of V and Si on the constant B_{rex} .

4.4.1.2. Hypereutectoid Steel

Dynamic recrystallization is expected to produce significant grain refinement resulting in single peak stress-strain curves for nearly all industrial deformation conditions. Full dynamic recrystallization and a constant mean grain size characterize the steady-state region. The fully dynamically recrystallized grain size has been found in this work to be dependent only on the Zener-Hollomon parameter, Z and is given by

$$d_{rex} = 1.7 \times 10^4 Z^{-0.22} \dots\dots\dots 4-2$$

The Zener-Hollomon exponent that was found (0.22) was in good agreement with the values (0.15 to 0.27) observed by other workers [109-112]. From the present results,

the average of 1.7×10^4 for this steel compares with that of 1.6×10^4 proposed by Hodgson [112].

4.4.2. Metadynamically Recrystallized Grain Size

4.4.2.1. Vanadium and Silicon Steels

In this part of the investigation, quenches were performed at the end of each test. The effect of strain rate and temperature on the metadynamically recrystallized grain size is presented in this section. Examples of metadynamically recrystallized microstructures are shown in Figure (4-14) for steel B. As the temperature was decreased, a finer metadynamic microstructure was obtained. The effect of increasing strain rate also led to a finer grain size (Figure (4-15) for steel C).

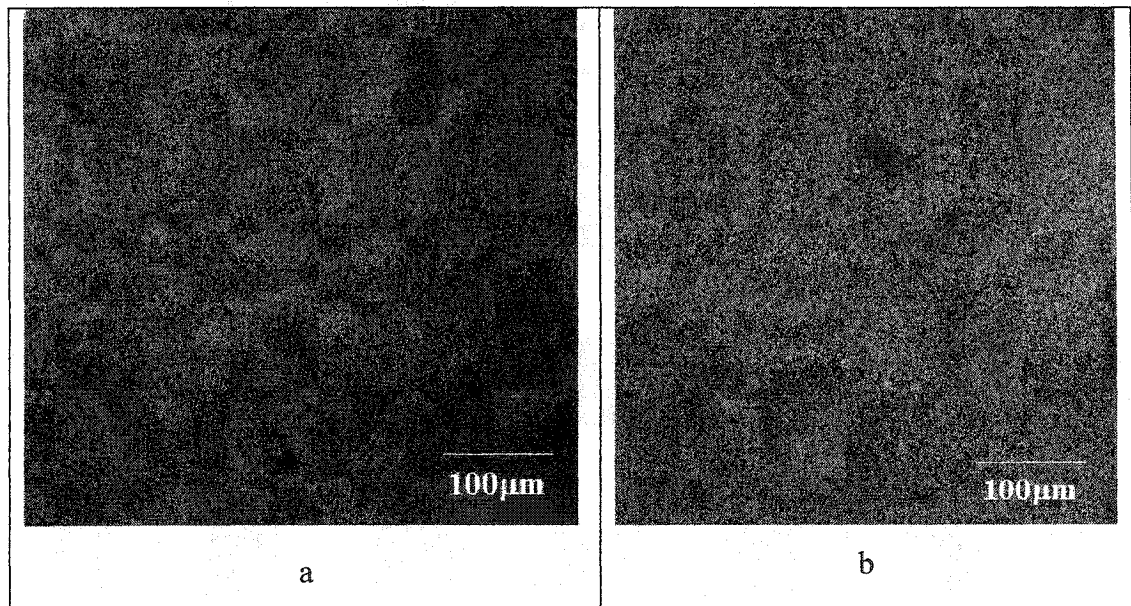


Figure (4-14) Metadynamically recrystallized microstructures in the B steel after deformation strain rate = 0.1 s^{-1} (a) 1050°C and (b) 1000°C .

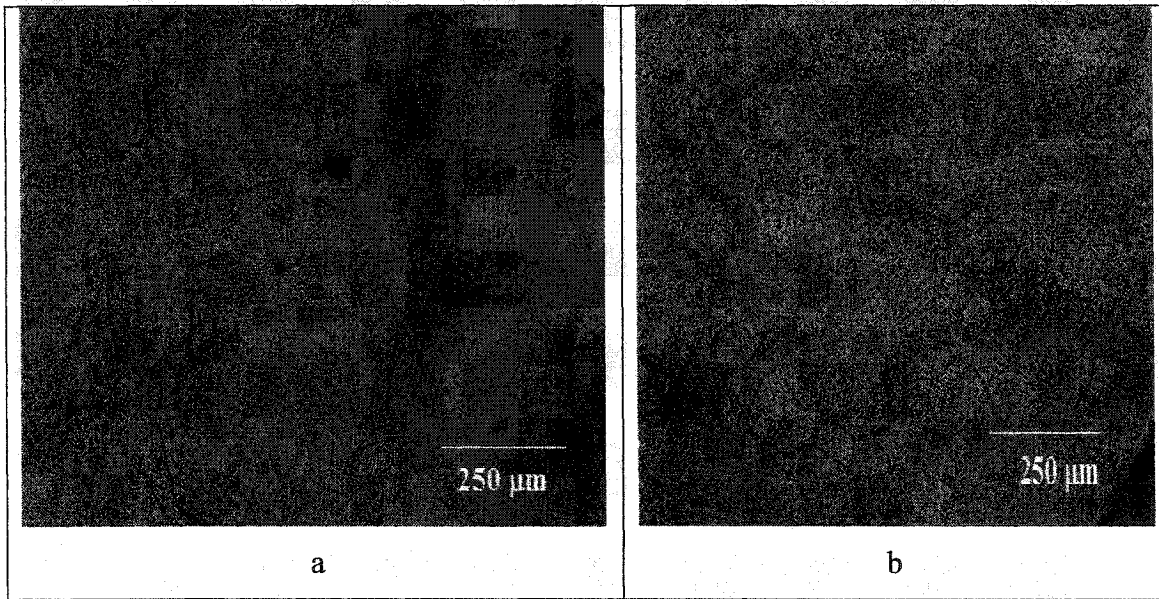


Figure (4-15) Metadynamically recrystallized microstructures in the C steel after deformation at 1050°C (a) 0.1s^{-1} and (b) 1s^{-1} .

The grain size after full metadynamic recrystallization was measured under different conditions. The change in recrystallized grain size with $\ln(Z)$ for the V and Si steels is plotted in Figure (4-16). The dependence of B in Eq. 2-11 on V and Si concentration can now be determined, as shown in Figure (4-17), leading to the following linear relation

$$d_{rex} = [-0.54[V + Si] + 2.8] \times 10^4 Z^{-0.27} \dots\dots\dots 4-3$$

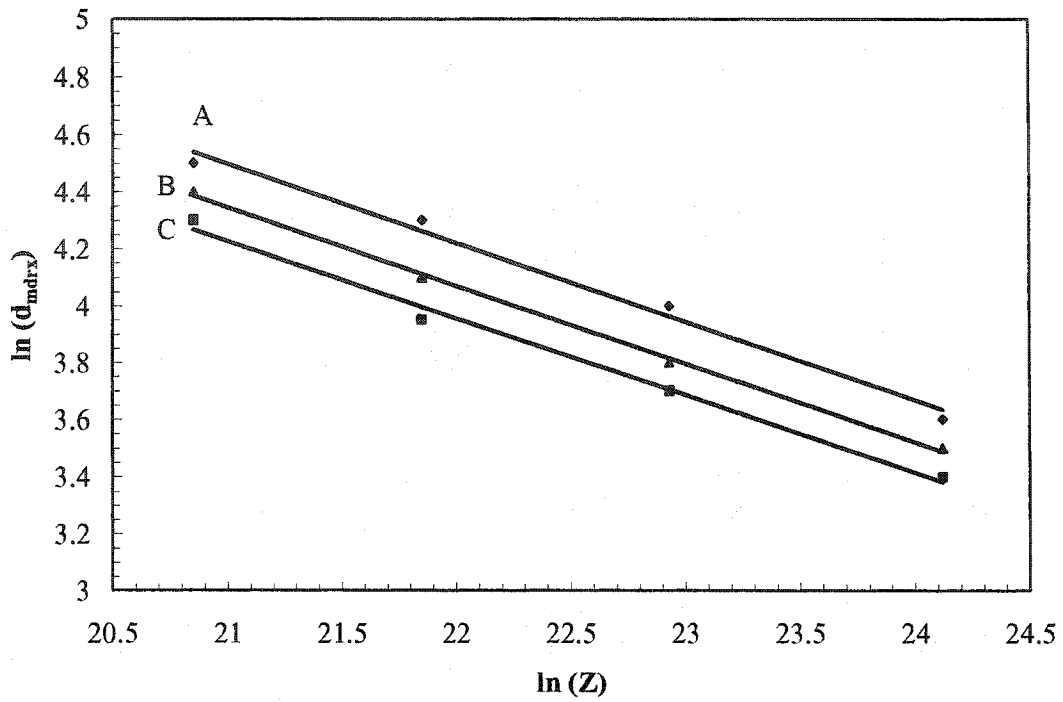


Figure (4-16) Grain size (MDRX) for V and Si steels.

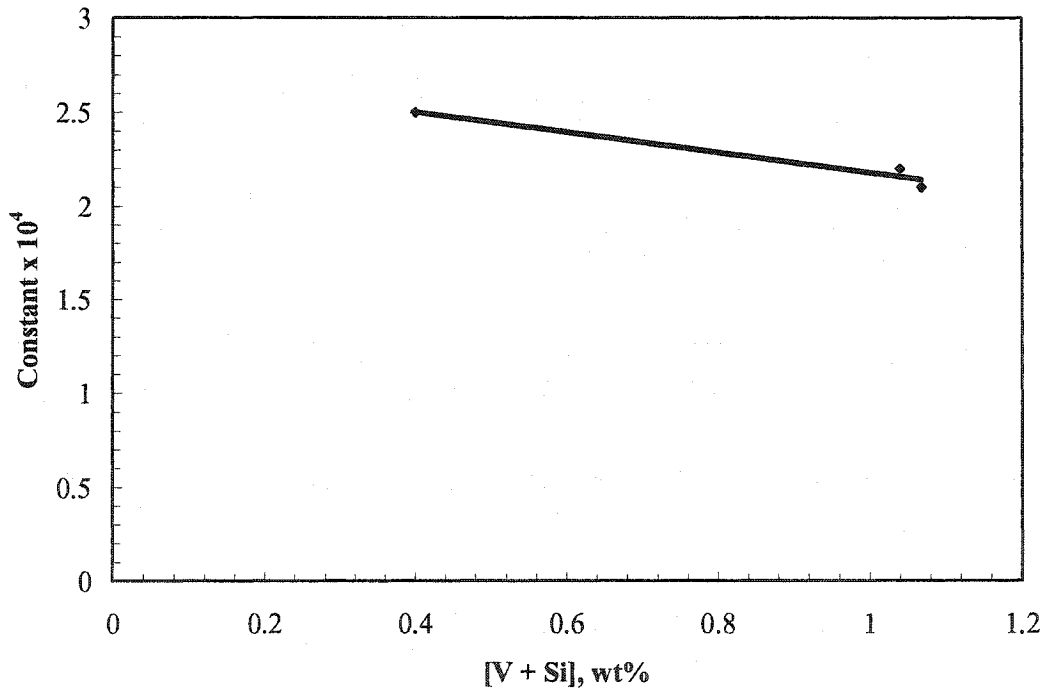


Figure (4-17) Effect of V and Si on the constant B_{mdrx} .

4.4.2.2. Hypereutectoid Steel

As for the other steels, the metadynamically recrystallized grain size of the C-Mn steel depends on the Zener-Hollomon parameter

$$d_{m\text{drx}} = 2.55 \times 10^4 Z^{-0.22} \dots\dots\dots 4-4$$

The parameter $\ln(d_{m\text{drx}})$ was plotted as a function of $\ln(Z)$, as shown in Figure (4-18). The Zener-Hollomon exponent was found to be 0.22 (for full softening after metadynamic recrystallization), and is in good agreement with values of (0.15 to 0.27) reported in previous investigations for plain carbon steel [109-115]. From the present results, the average of 2.55×10^4 for this steel compares with that of 2.6×10^4 reported by Hodgson [112].

From the equations proposed for dynamic and metadynamic grain size, the metadynamically recrystallized grain size is about 50% higher than the dynamically recrystallized grain size.

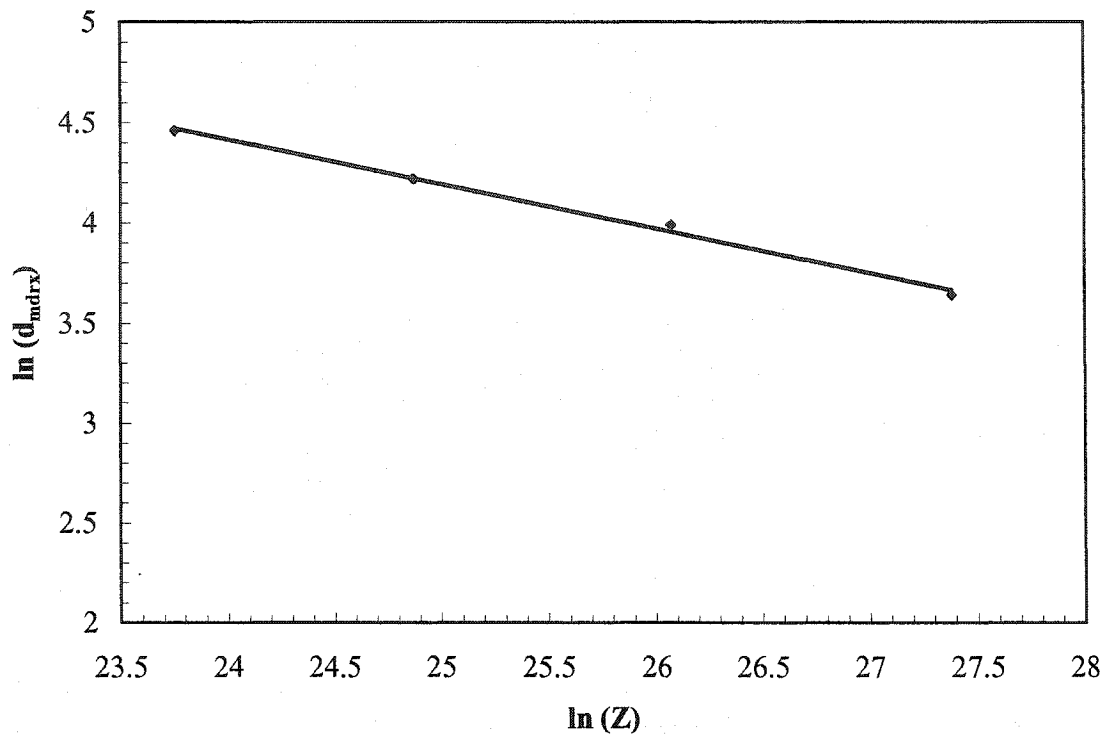


Figure (4-18) $\ln(d_{\text{mdrx}})$ plotted as function of $\ln(Z)$.

4.4.3. Statically Recrystallized Grain Size

4.4.3.1. Vanadium and Silicon Steels

Examples of statically recrystallized microstructures are shown in Figure (4-19) for steels A and C.

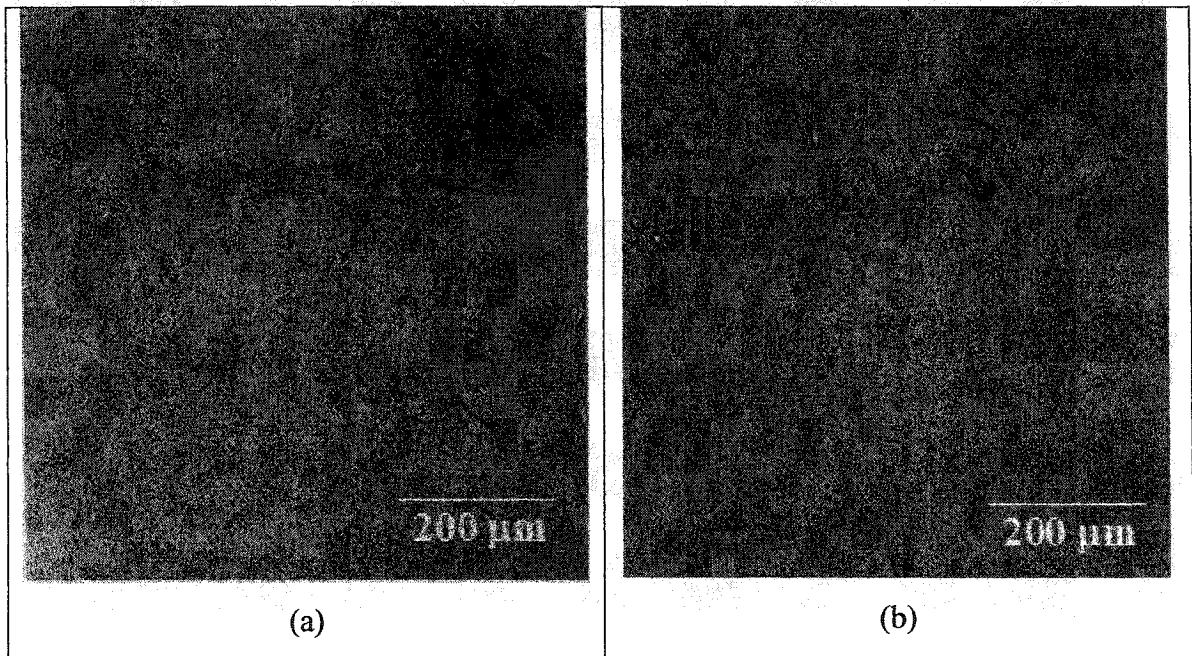


Figure (4-19) Statically recrystallized microstructures after deformation at 1050°C at strain rate 0.1s^{-1} (a) steel A and (b) steel C.

The three steels employed in this investigation exhibited finer grain sizes than those predicted for plain carbon steel (Figure (4-20)). An expression for the statically recrystallized grain size, d_{SRX} , was generated as follows, using the form reported by Sellars [9]. The dependence of B in Eq. 2-8 on the silicon and vanadium concentrations can now be determined, as shown in Figure (4-21), leading to the following linear relation:

$$d_{SRX} = [-0.15 [V + Si] + 0.70] d_0^{0.67} \varepsilon^{-0.5} \dots\dots\dots 4-5$$

The strain exponent for this work was found to be -0.5 .

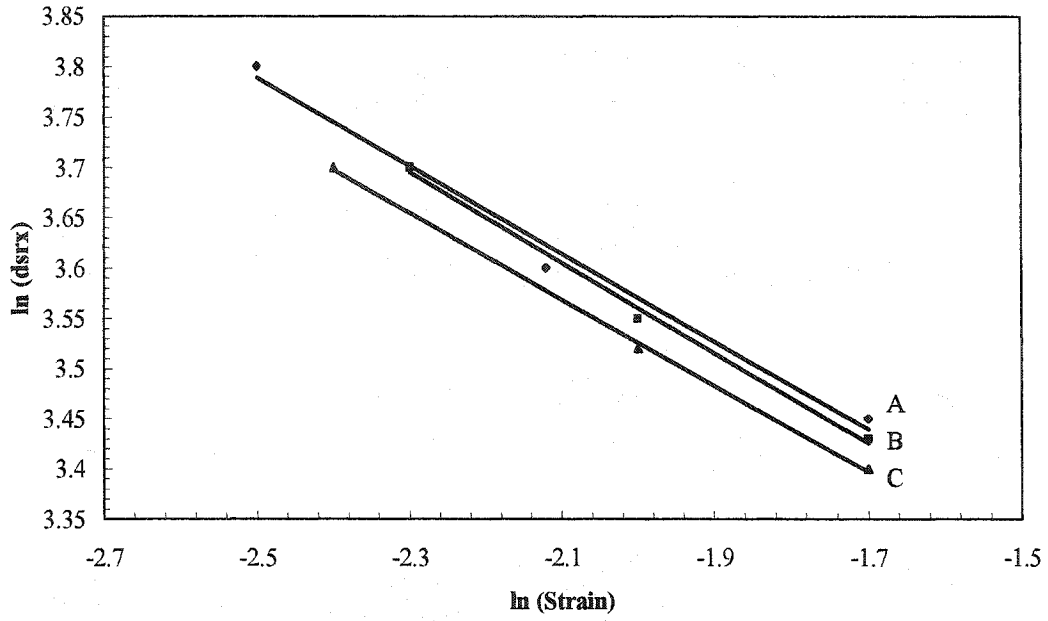


Figure (4-20) $\ln(d_{srx})$ plotted as function of $\ln(\text{strain})$.

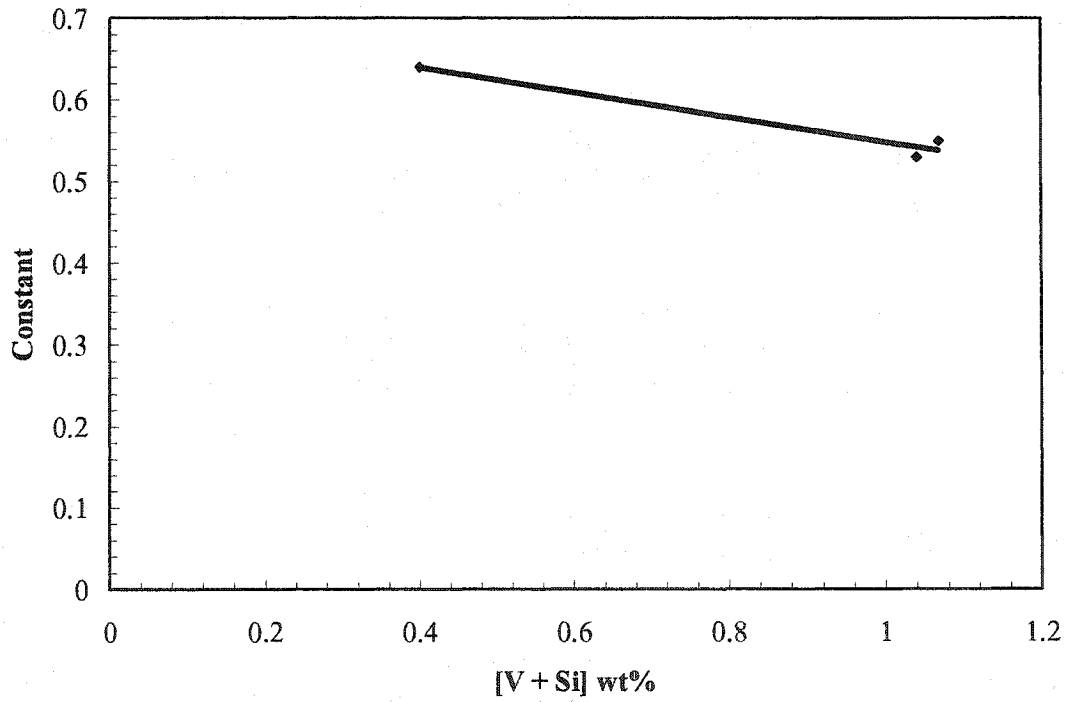


Figure (4-21) Effect of V and Si on the constant B_{srx} .

4.4.3.2. Hypereutectoid Steel

The statically recrystallized grain size increases with the initial grain size and decreases with increasing applied strain and there is no effect of temperature.

$$d_{srx} = 0.3 d_o^{0.67} \epsilon^{-0.9} \dots\dots\dots 4-6$$

The exponent from the current experimental data was determined to be (Figure (4-22)) -0.9 , compared well with the value of -1.0 reported previously by Sellars [9] from published data. Moreover, Suehiro et al. [116] was observed no effect of composition on the recrystallized grain size for C from 0.1 to 0.8.

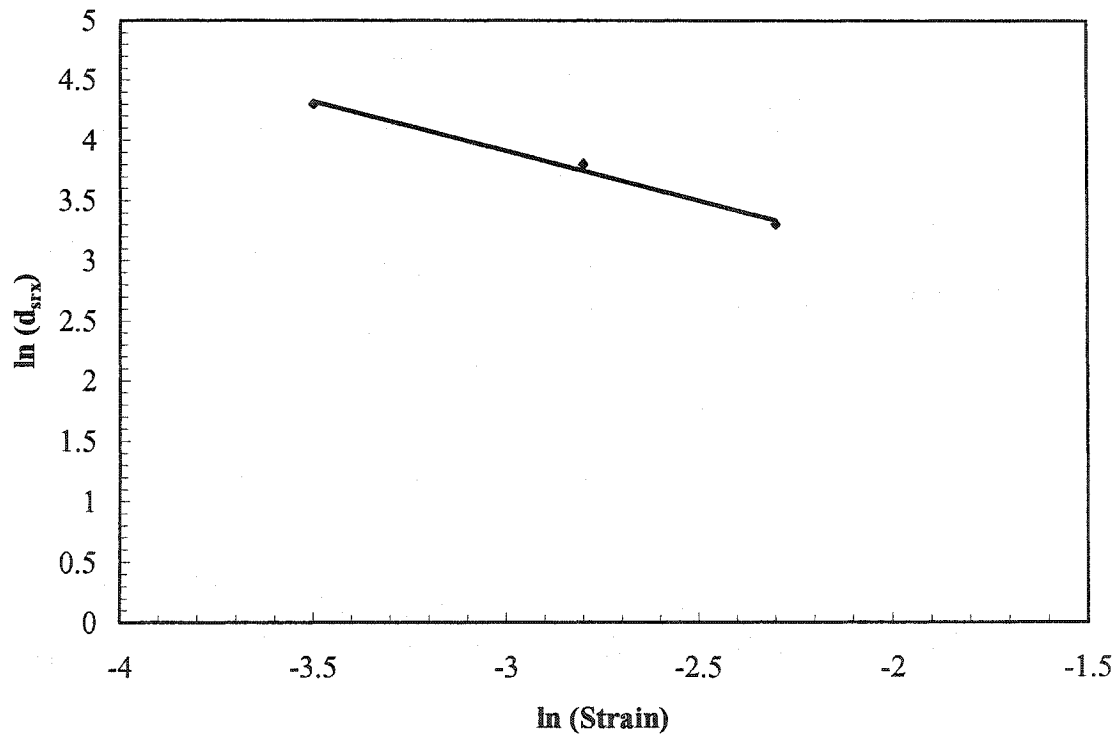


Figure (4-22) $\ln(d_{srx})$ plotted as function of $\ln(\text{strain})$.

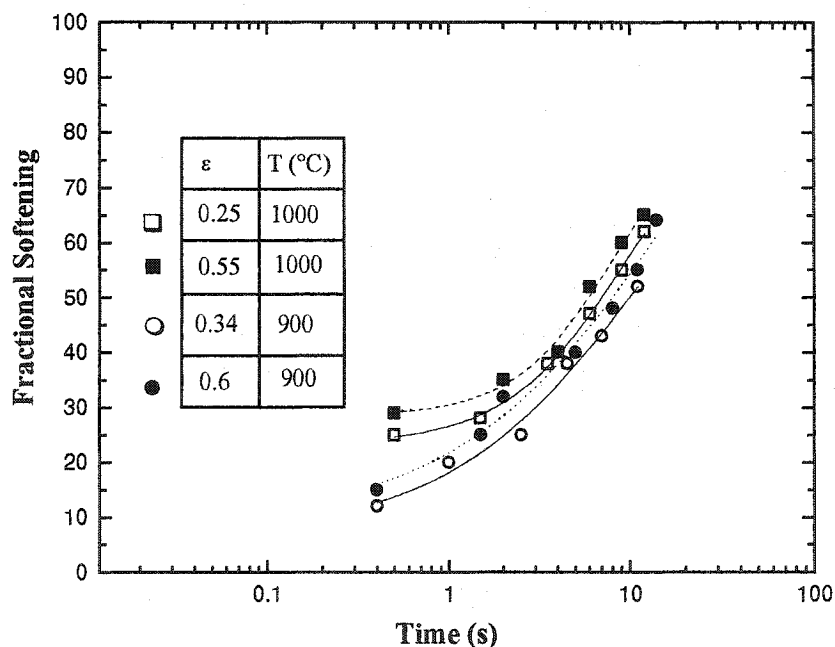
4.5. Metadynamic Recrystallization Characteristics

Once the critical strain for dynamic recrystallization is surpassed during deformation, the dynamically recrystallized nuclei continue to grow when the specimen is unloaded. This process is called metadynamic recrystallization and does not involve an incubation time, since the nuclei are already present upon termination of the deformation.

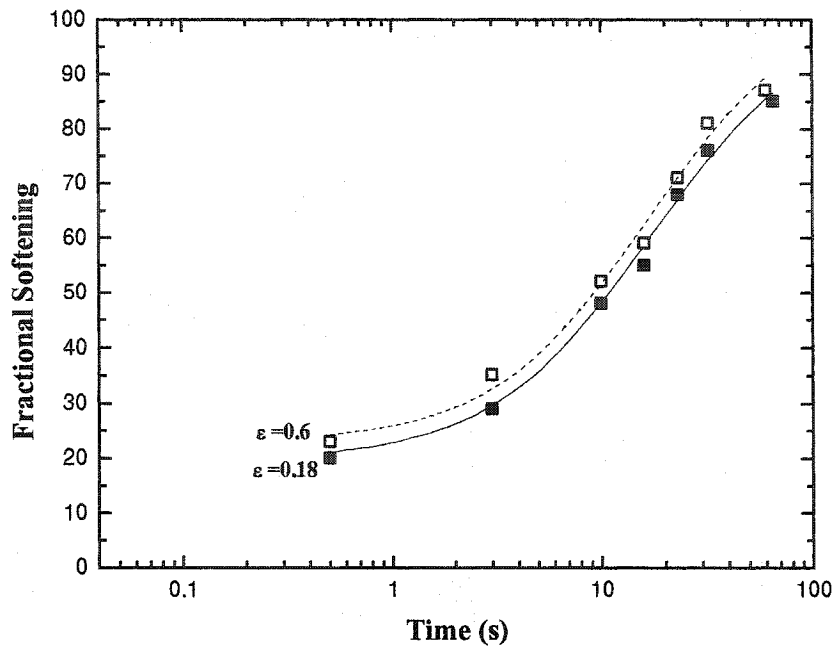
4.5.1. Effect of Deformation Parameters on the Metadynamic Softening

4.5.1.1. Strain

The softening curves shown in Figure (4-23), which are typical of all the steels tested, indicate that, above the critical strain for dynamic recrystallization, strain has little influence upon the fractional softening of metadynamic recrystallization. This observation agrees with that of Hodgson [117], Roucoules et al. [118] and Bai [119].



(a)



(b)

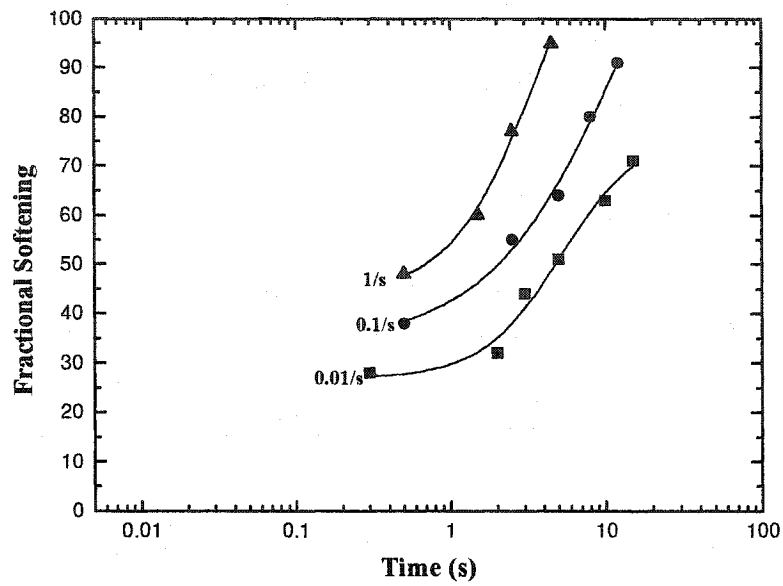
Figure (4-23) Effect of strain on softening in steels (a) A, (b) E.

4.5.1.2. Strain Rate

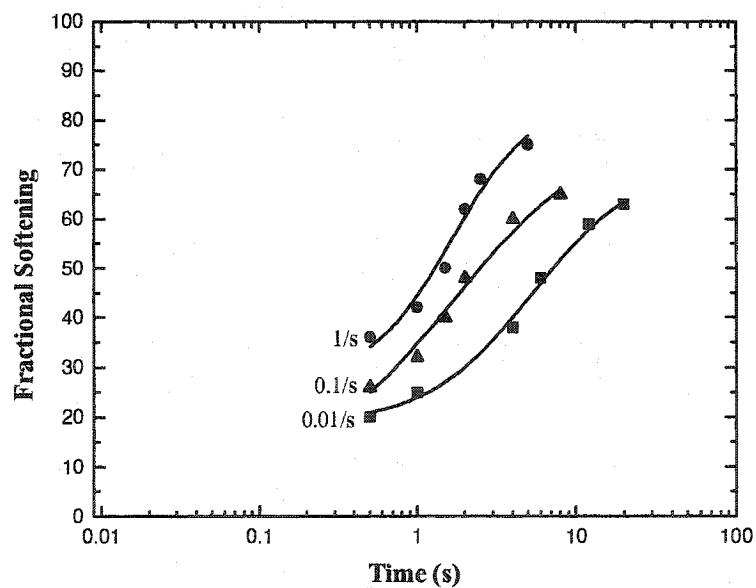
In general, increasing the strain rate increases the flow stress, since less time is available for dynamic recovery. As well, there is a decrease in the subgrain size, and these two effects lead to an increase in the stored energy. Therefore, with increasing strain rate, the driving force for recrystallization will increase, and the recrystallization kinetics will be faster.

The effect of strain rate was investigated over the range 0.01s^{-1} to 1s^{-1} at 1050°C . The measured fractional softening is plotted as a function of the logarithm of the holding time as shown in Figure (4-24) for the A, B and C steels. For all the steels, these plots have the beginnings of a sigmoidal appearance, and, as anticipated, the recrystallization

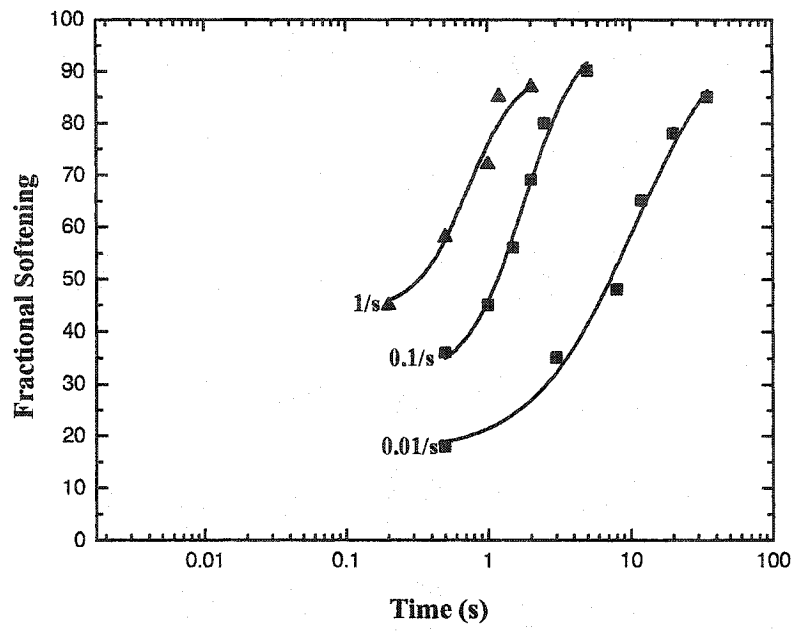
rate increases with increasing strain rate. For example, in steel A the time for 50 % softening decreases from about 5s to less than 1s as the strain rate is increased from 0.01s^{-1} to 1s^{-1} . The present observations are in good agreement with those reported by Hodgson [117] and Roucoules [42].



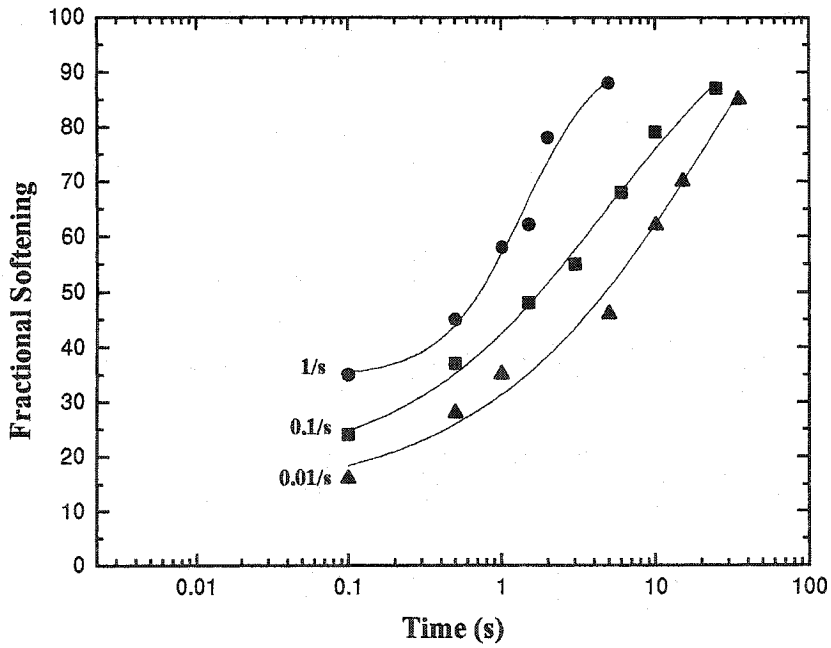
(a)



(b)



(c)



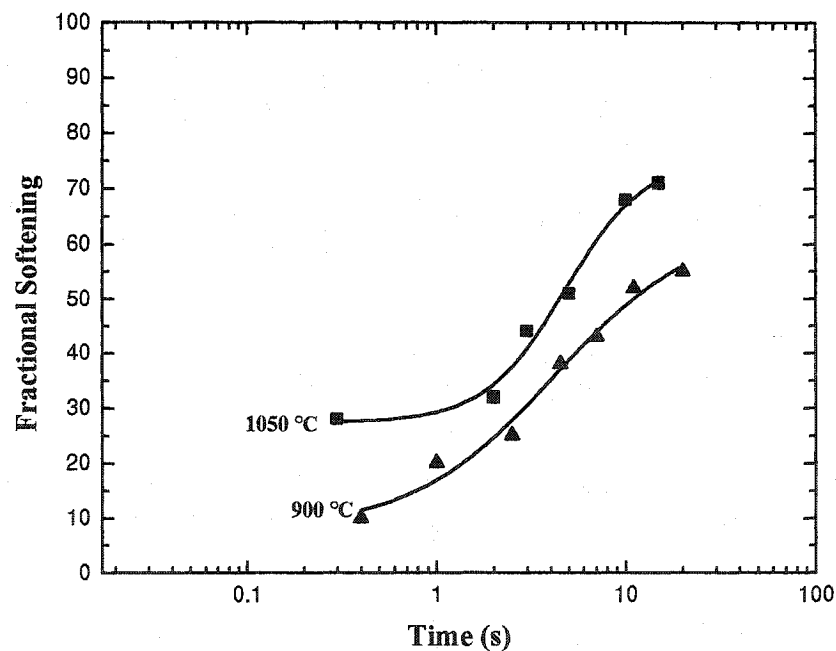
(d)

Figure (4-24) Effect of strain rate on softening in steels (a) A, (b) B and (c) C, and (d) E.

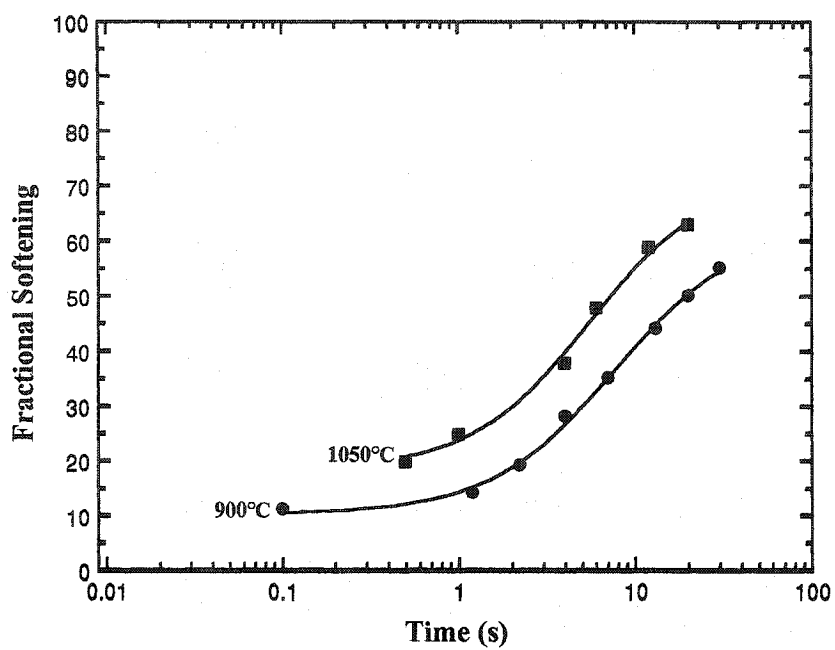
4.5.1.3. Deformation Temperature

The effect of deformation temperature on softening by metadynamic recrystallization is shown in Figure (4-25) for the A, B, C and E steels, respectively. In this case, the strain rate was held constant, while the deformation temperature was varied. These softening curves are also sigmoidal in appearance. These curves show that the rate of softening increases with increasing temperature.

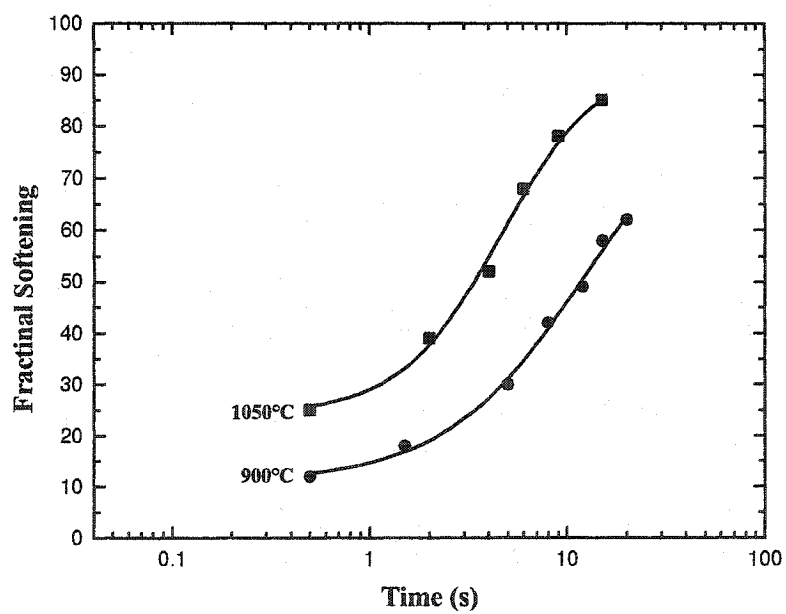
For example for steel E (Figure (4-25d), at a holding time of 10 s, the fraction of metadynamic recrystallization attained in this steel increased from about 25% at 900°C to 35% at 950°C, to 50% at 1000°C, and to 70% at 1050°C. This effect is due to the increasing mobility of the recrystallizing grain boundaries [120].



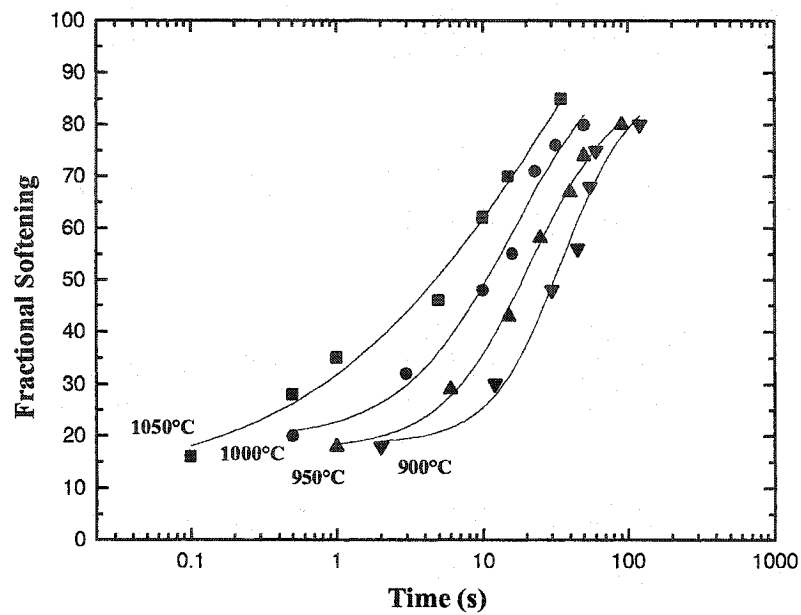
(a)



(b)



(c)



(d)

Figure (4-25) Effect of temperature deformation on softening in steels (a) A, (b) B and (c) C, and (d) E.

4.5.1.4. Initial Grain Size

The kinetics of metadynamic recrystallization is not markedly affected by the initial grain size. This is because the majority of the metadynamic recrystallization nuclei are formed during deformation. The density of these dynamically formed nuclei and the steady state flow stress attained at high strains after full dynamic recrystallization are independent of the initial austenite grain size.

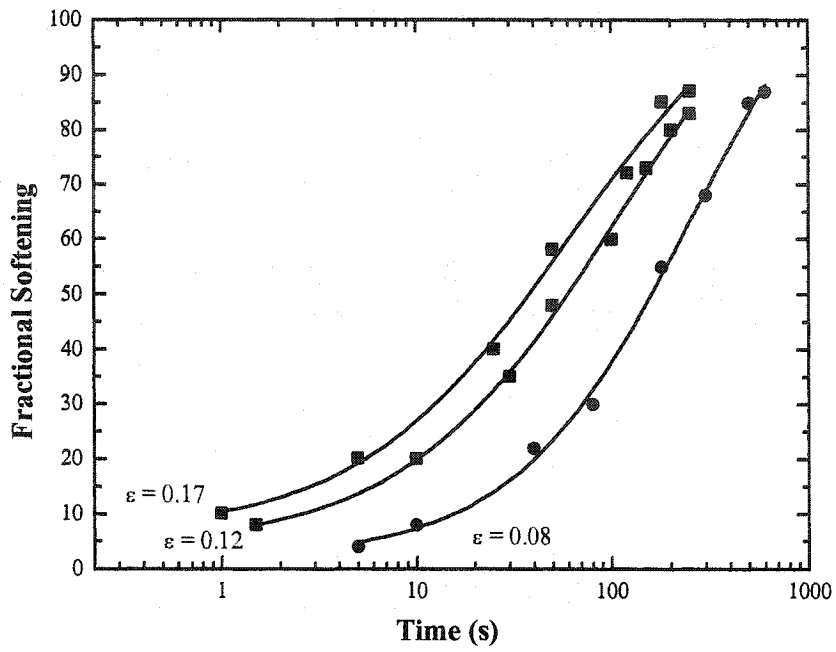
4.6. Static Recrystallization Characteristics

4.6.1 Effect of Deformation Parameters on the Softening

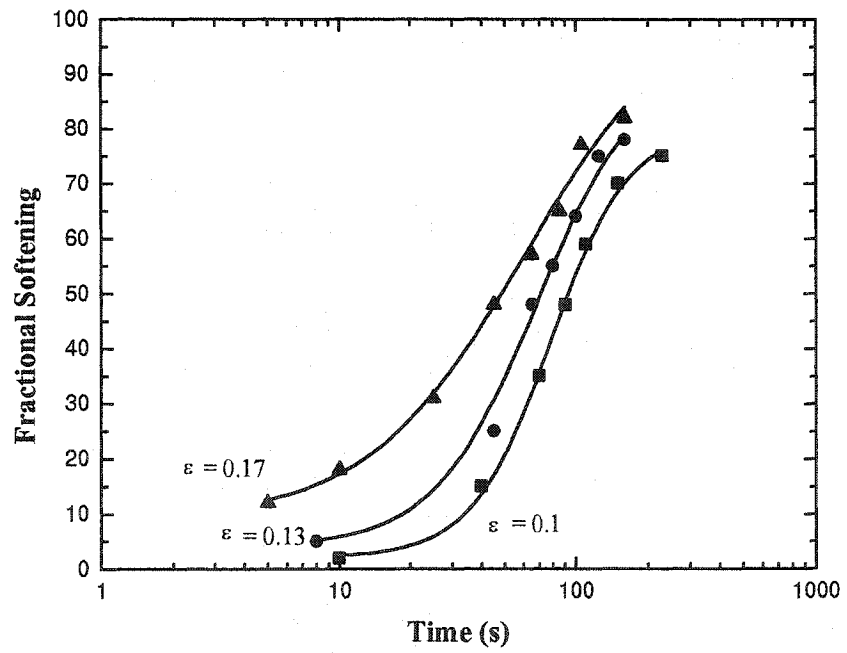
4.6.1.1. Strain

The static softening fraction as a function of time for all three strain conditions is shown in Figure (4-26) for steels A, B, C and E. In these tests, reheating temperature of 1200°C and a holding of 20 minute were used to produce the initial grain size. Then, the specimens were cooled to 1050°C and deformed to different strains at constant strain rate. It can be seen that the higher the strain, the faster the recrystallization rate. This can be attributed to the higher dislocation density generated by the increased deformation, which results in a greater driving force for static recrystallization. In all cases there appears to be smooth sigmoidal softening, with no evidence of a multistage softening reaction. Recovery occurs at a very slow rate until about 25% softening is attained, and then recrystallization takes over and proceeds more rapidly. Recovery tends to be slower than recrystallization, because in the latter, movement of new grain boundaries is a more rapid way to remove dislocations than dislocation-dislocation interaction. However, the nucleation of these crystals is slower than recovery because a critical nuclei size has to be attained before recrystallization can progress.

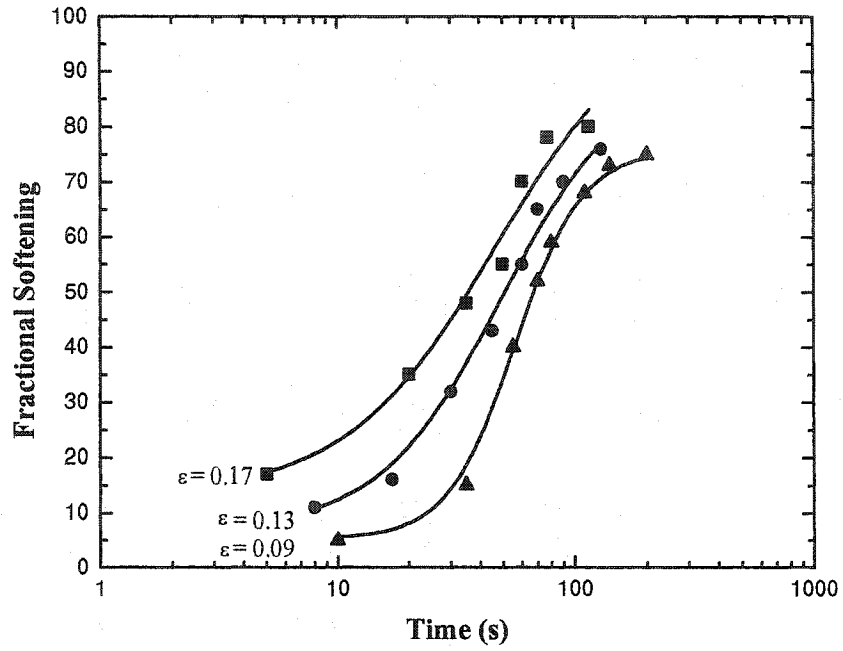
For example in steel E (Figure (4-26d)), it can be seen that full recrystallization, occurs in less than 100s for a strain of 0.1. Halving the strain leads to an increase in time of approximately a factor of 5 to reach the same level of softening.



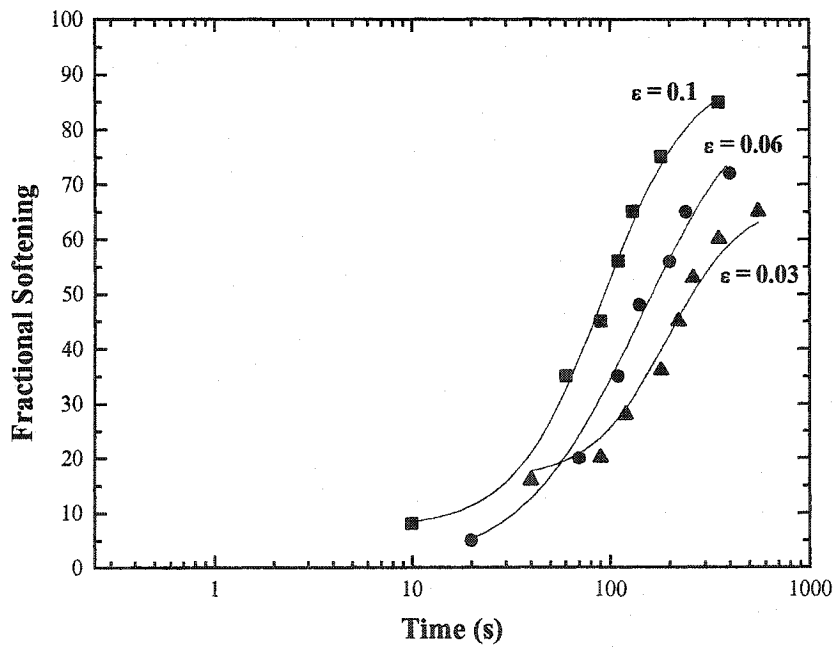
(a)



(b)



(c)



(d)

Figure (4-26) Effect of strain on softening in steels (a) A, (b) B (c) C and (d) E.

4.6.1.2. Strain Rate

For the kinetics of static recrystallization, the influence of strain rate on static recrystallization, as shown in Figure (4-27), which is typical of all the steels tested, is less than the influence of the other variables (temperature, strain). However, the recrystallization kinetics is significantly accelerated when the strain rate is increased. The results given here are in agreement with previous investigations [9,112,117,121,122]. Again, for example in steel E (Figure 4-28) for 50% softening at a strain rate of 0.01s^{-1} the required hold time is 80s, compared to 60s when the strain rate is increased to 1s^{-1} .

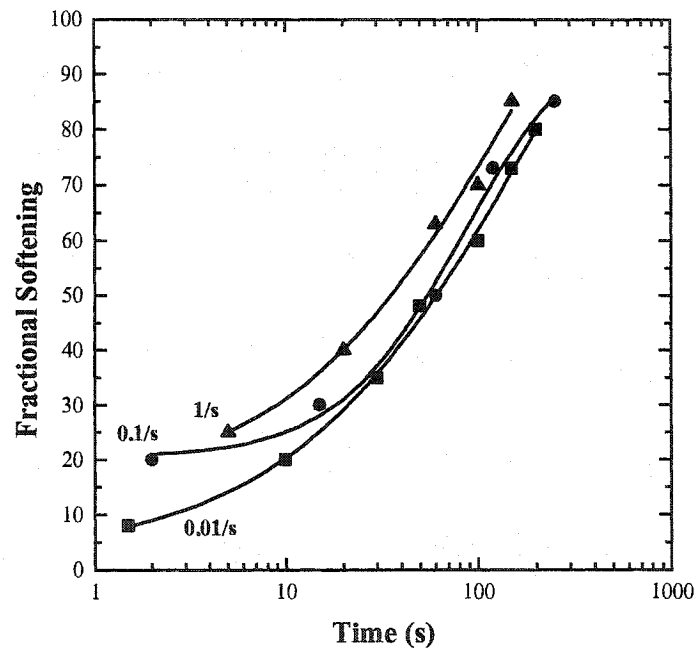


Figure (4-27) Effect of strain rate on softening in steel A.

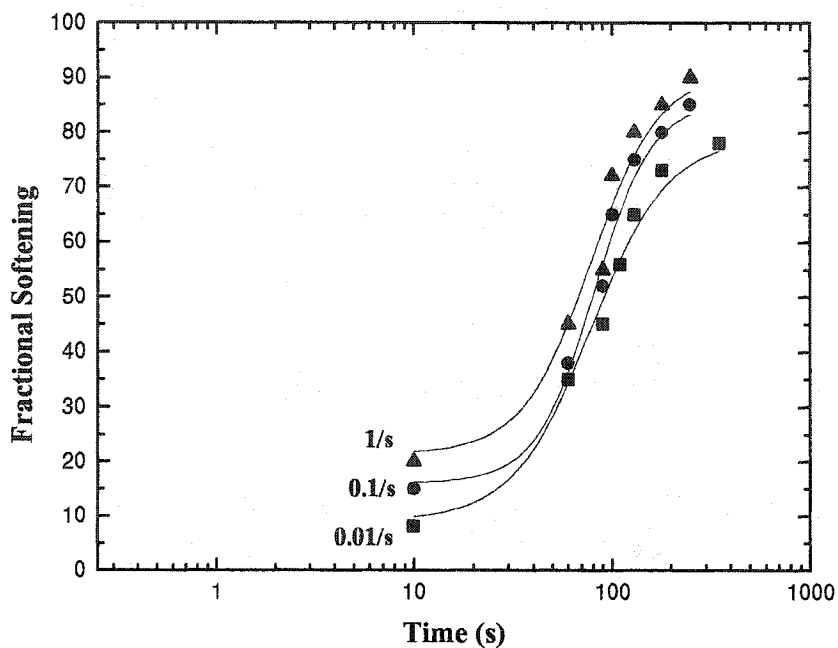


Figure (4-28) Effect of strain rate on softening in steel E.

4.6.1.3. Deformation Temperature

4.6.1.3.1. Hypereutectoid Steel

It was demonstrated that the softening and recrystallization rate become faster as the test temperature is increased. This is due to the enhanced boundary diffusivity and thus mobility at higher testing temperature and also due to the increased driving force for recrystallization [120]. It is clear from Figure (4-29) that the recrystallization kinetics is enhanced as the temperature is increased for static recrystallization.

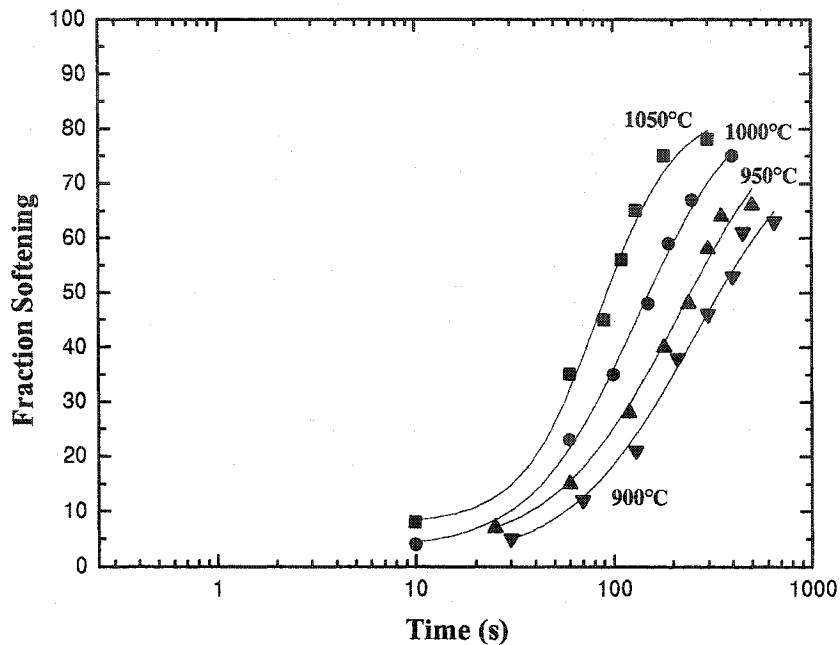


Figure (4-29) Effect of deformation temperature on softening in steel E.

4.6.1.3.2. Vanadium and Silicon Steels

Figures ((4-30), (4-31) and (4-32)) show the statically recrystallized fraction for steels A, B and C, respectively, at temperatures between 1100 and 875°C. The steels behaved similarly. It is evident that at 1100, 1050 and 1000°C, the softening curve follows the Avrami equation, i.e. it has a conventional sigmoidal appearance. The curves corresponding to 950-875°C display a plateau probably caused by the formation of V precipitates, which momentarily block the progress of recrystallization. The appearance of these plateaus is similar to those observed in all the microalloyed steels (containing V, Ti and Nb) studied by Medina [123,124]. It is also likely that Si plays a role in retarding recrystallization due to its atomic size mismatch with Fe [125,126] (this should be

apparent in the curves before precipitation takes place). However, recrystallization eventually resumes, probably due to precipitate coarsening.

This means that before and after the plateau, *i.e.* before and after the precipitation, the recrystallization kinetics obey Avrami's Law. The start and finish of the plateaus correspond approximately with the start and finish of strain-induced precipitation. These temperatures can then be used to generate precipitation-temperature-time diagrams, as will be seen below in more detail.

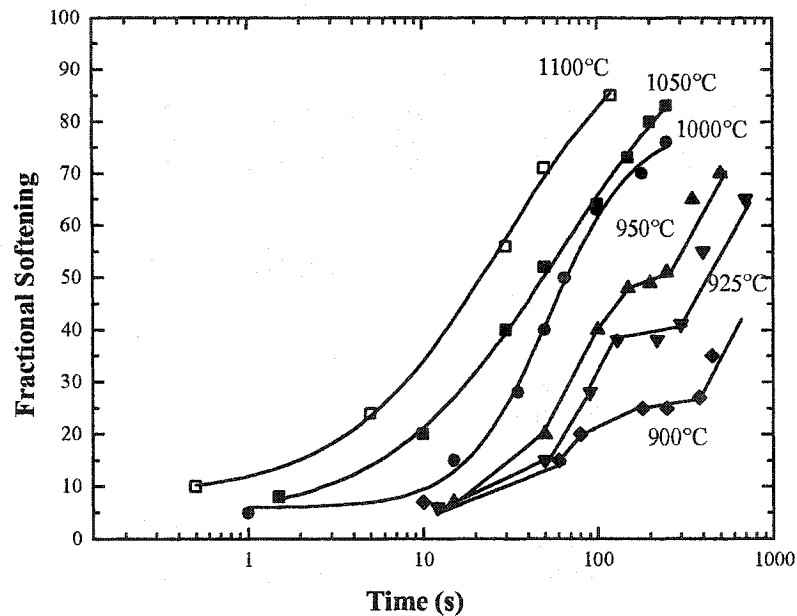


Figure (4-30) Effect of temperature on static softening kinetics for steel A at a strain rate of 0.01s^{-1} .

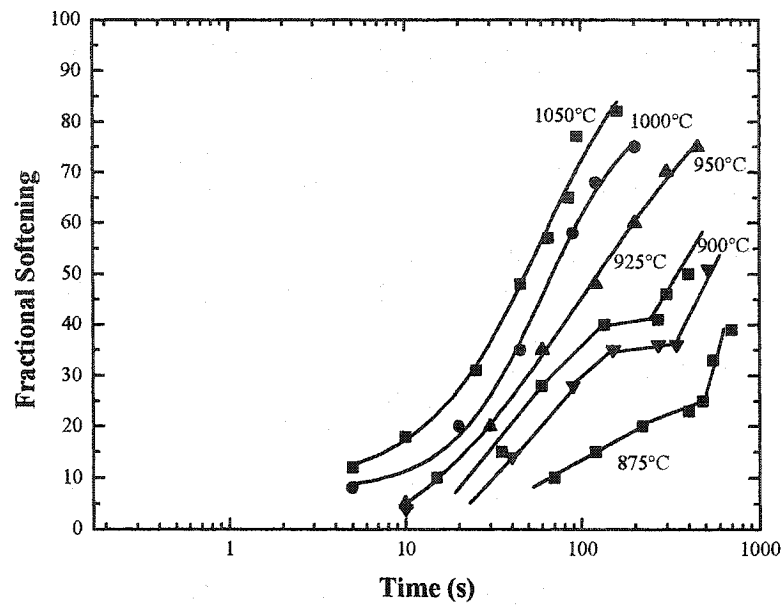


Figure (4-31) Effect of temperature on static softening kinetics for steel B at a strain rate of 0.01s^{-1} .

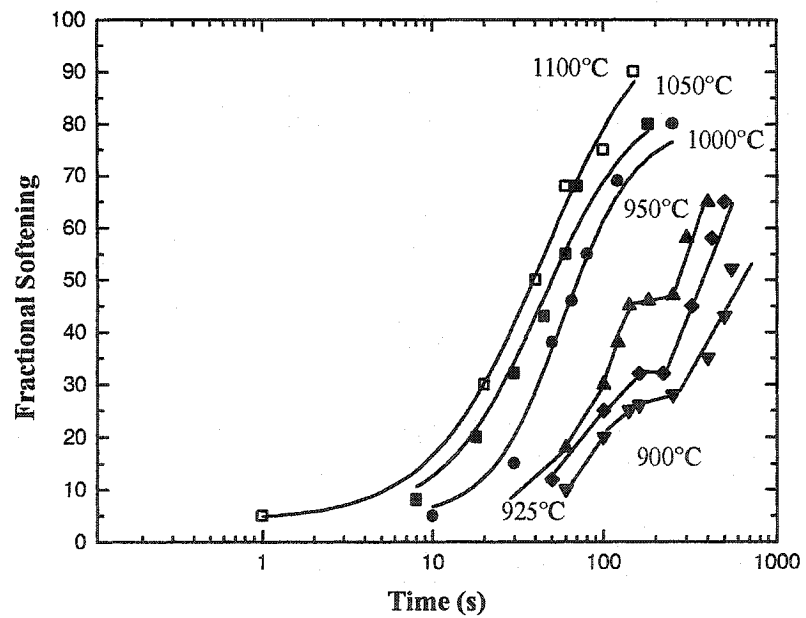


Figure (4-32) Effect of temperature on static softening kinetics for steel C at a strain rate of 0.01s^{-1} .

Medina et al. [127] have reported that at the end of the plateau it is still possible to find a certain number of precipitates of the same average size as most of those found at the start of the plateau. They found that the volume of small sized precipitates decreases from the start to the end of the plateau because precipitation becomes overlapped with coalescence or coarsening of precipitates, until the volume fraction of the smallest precipitates is insufficient to continuously inhibit recrystallization.

4.6.1.4. Initial Grain Size

The effect of initial grain size on the fractional softening of static recrystallization is shown in Figure (4-33), which is typical of all the steels tested. In this case, the strain rate and deformation temperature were held constant, while the reheat temperature was varied from 1200°C–1000°C. In general, the austenite grain sizes increased with increasing reheat temperature. It is clear that as the grain size decreases the rate of recrystallization increases markedly. This is because smaller grains have a large grain boundary area per unit volume, which leads to an increase in the density of potential nucleation sites for static recrystallization.

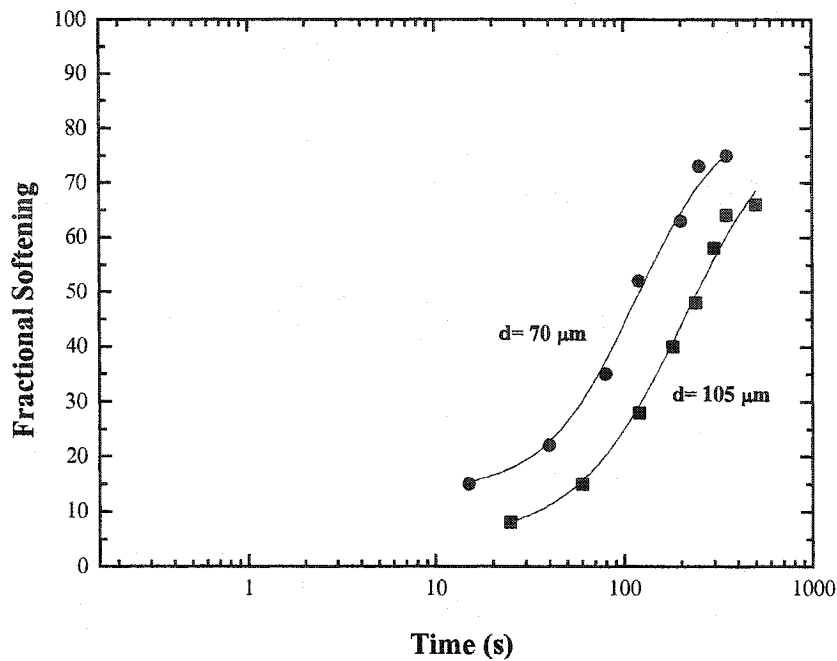


Figure (4-33) Effect of initial grain size on softening.

4.6.2. Precipitation Time Temperature Diagrams

The strain-induced precipitation-time-temperature diagrams, obtained from the plateaus of the kinetics data are presented in Figures ((4-34) and (4-35)) for precipitation start (P_s) and finish (P_f) times, respectively. It can be seen that there is an increasing separation of the P_s times with increasing temperature (with the times being very close at 900 °C). This latter is consistent with the results of another investigation [128]. The P_f times follow a similar behavior, but the times are slightly more separated than the P_s curves at the lower temperatures. It can be observed that the nose temperature, which corresponds to the temperature at which precipitation occurs in the minimum time, depends on the Si and V concentrations. As this content increases the nose temperature increases as can be seen in Table 4-1. It can be seen that the nose of the curve for steel C is higher than 950°C, but the nose of the curves for steels A and B are very close

(930°C). It can be also seen that, as the product of the V and Si concentration decreases, the upper part of these curves is shifted to lower temperatures and longer times. This is due to the difference in the chemical driving force for precipitation. Higher concentrations of the precipitate forming elements produce higher driving forces at a given temperatures and therefore accelerate the precipitation kinetics.

Table 4-1 Nose temperature for steels A B and C

<i>Steels</i>	<i>Nose temperature °C</i>	<i>Time sec</i>
A	930	160
B	920	135
C	<950	115

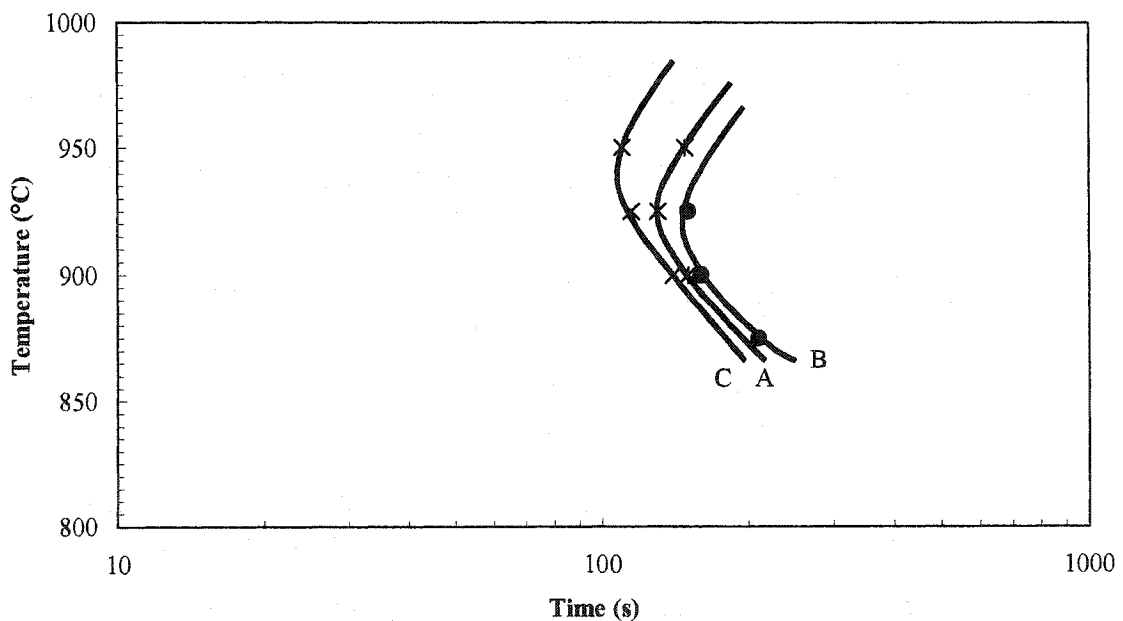


Figure (4-34) Precipitation start temperature time curves, P_s , for steels A, B and C acquired by the present double compression technique at a strain rate of $0.01s^{-1}$.

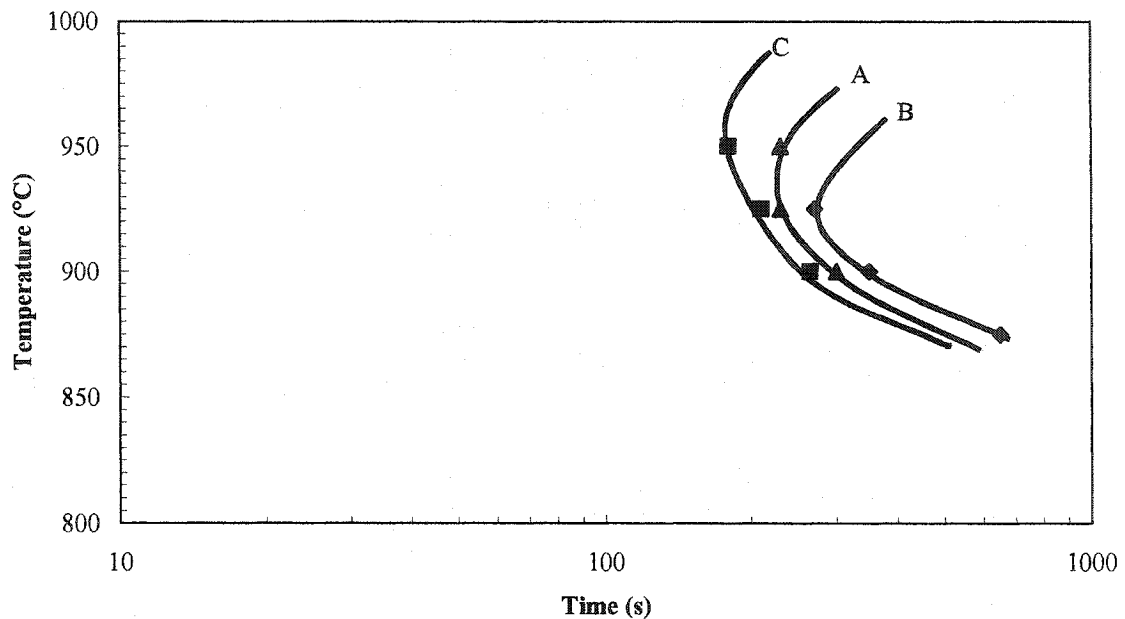


Figure (4-35) Precipitation finish temperature time curves, P_f , for steels A, B and C acquired by the present double compression technique at strain rate $0.01s^{-1}$.

4.7. Effect of Thermomechanical Variables on Pearlite Characteristics

4.7.1. Effect of Heat Treatment

4.7.1.1. Hypereutectoid Steel

From the microstructures of the heat-treated vanadium-free steel E at the different temperatures, the evolution the prior-austenite grain structure characteristics was examined for the influence of the thermal processing conditions, as illustrated in the optical micrographs given in Figure (4-36). Increasing the reheat temperature was observed to increase not only the prior-austenite grain size, as delineated previously, but also the thickness of the grain boundary cementite network that was observed to form unconditionally in steel E for all the heat treatments examined in this work. As given in Table 4-2, the progressive increase in the thickness of the cementite network with increasing reheat and transformation temperatures may be related to the increased

kinetics for grain boundary cementite formation at higher temperatures. Moreover, with increasing reheat temperature there is an increase in the prior-austenite grain size, as given in Figure (4-3), that may assist the growth of the cementite network through a reduction in the overall grain boundary area available for proeutectoid cementite formation. This is exemplified through the austenitizing condition at the lower reheat temperature of 900°C, Figure (4-36a-c), where the prior-austenite grain size was 48 μm , which resulted in a thinner layer of grain boundary cementite as compared to reheating to 1200°C, as shown in Figure (4-36d), where the grain size was more than double (110 μm).

Table 4-2 Thicknesses of the cementite network

<i>Heat treatment (°C)</i>	<i>Transformation Temperature (°C)</i>	<i>Non-deformed</i>
1200	620	25.5 μm
	580	20.5 μm
	550	16.8 μm
900	620	19.9 μm
	580	19.9 μm
	550	14.0 μm

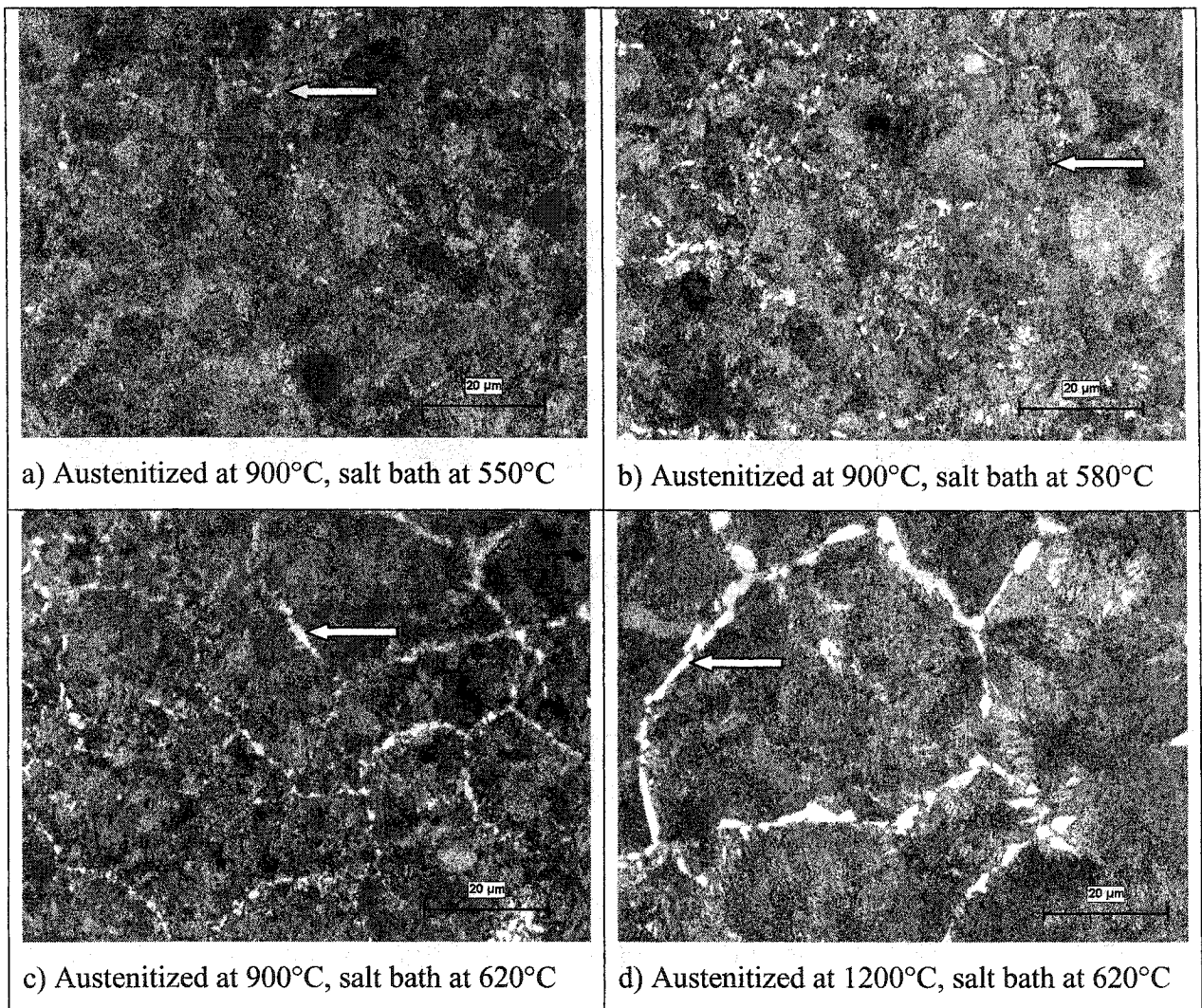


Figure (4-36) Optical micrographs showing the microstructure of the steel E.

4.7.1.2. Vanadium and Silicon Steels

The addition of microalloying elements to a hypereutectoid steel with a low or high Si content was observed to prevent the formation of a thick continuous cementite layer at the prior-austenite grain boundaries, as illustrated in the optical micrographs given in Figure (4-37) for steel A. Specifically, the nature of the grain boundary cementite for the microalloyed steels was considerably difficult to examine even from the general microstructural observations performed using a FE-SEM at relatively low

magnifications (3,000x), as shown in Figure (4-38). In fact, low voltage imaging was employed on a FE-SEM at high magnifications (20,000x) to ascertain the presence of the grain boundary cementite particles as depicted in Figure (4-39).

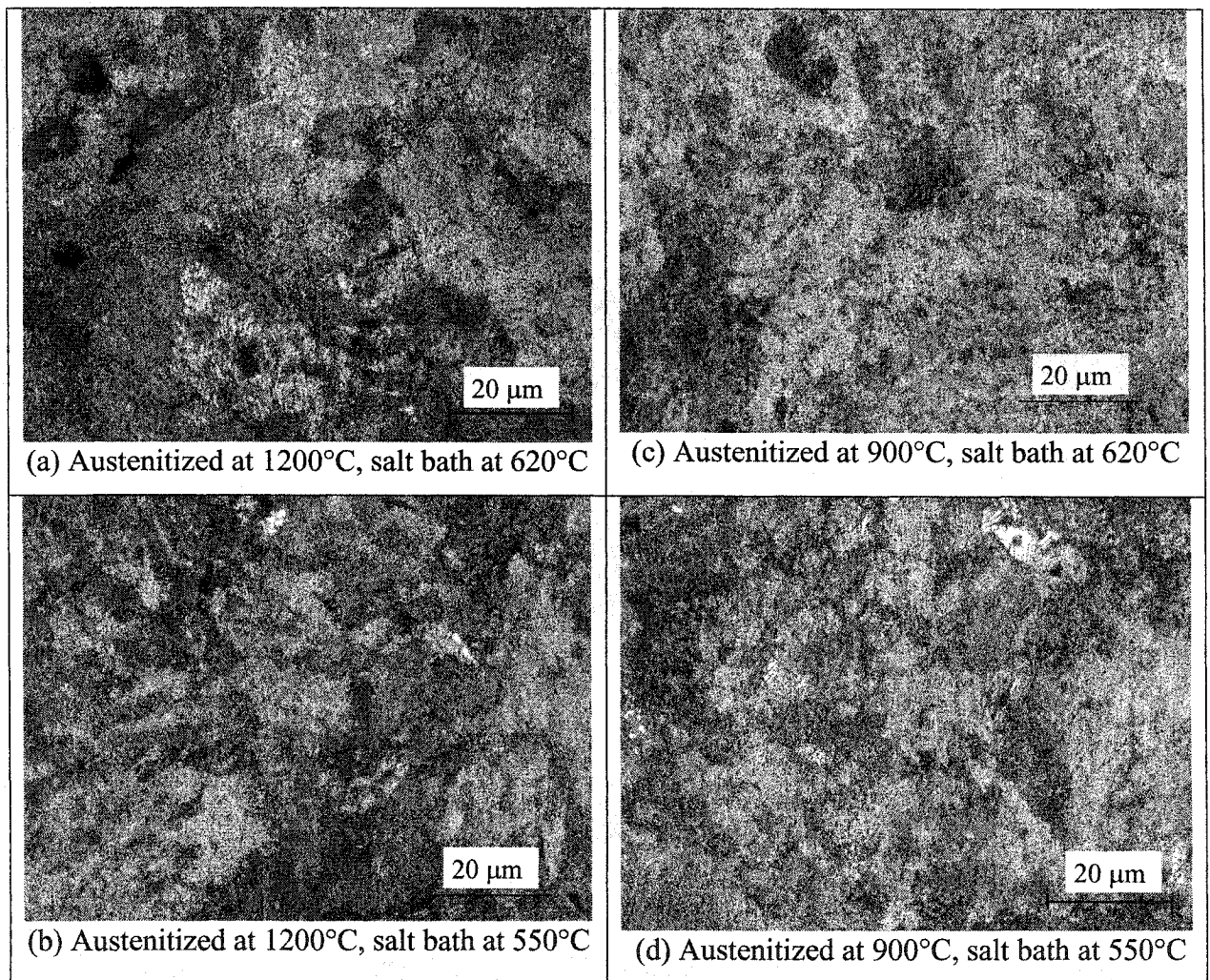


Figure (4-37) Optical micrographs showing the microstructure of the steel A.

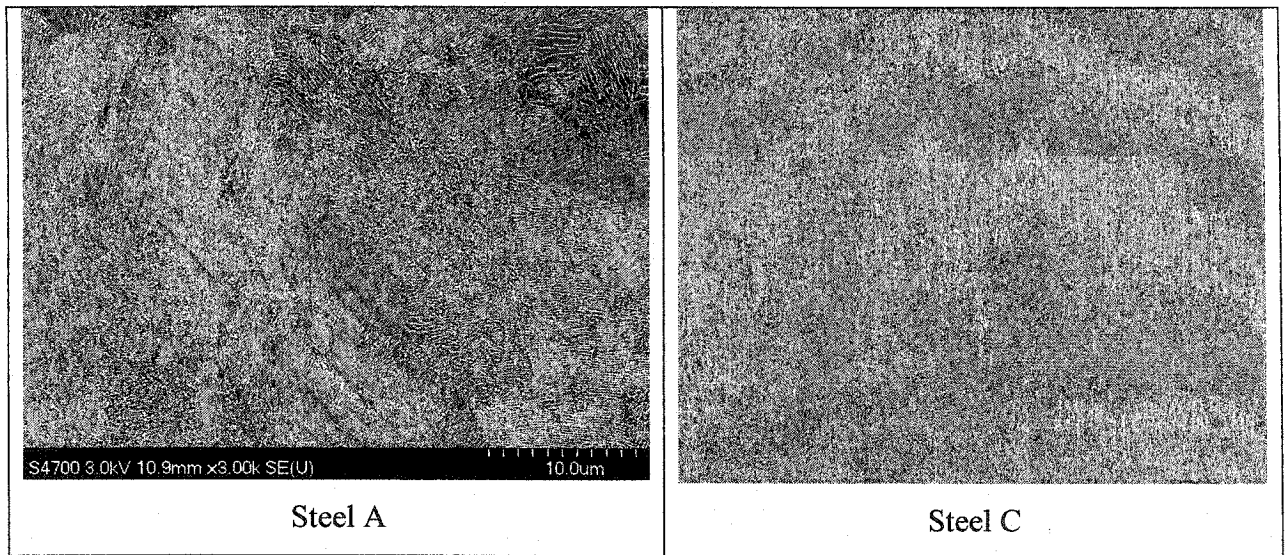


Figure (4-38) FE-SEM images showing the microstructure of steels A and C austenitized at 1200°C and transformed at 620°C.

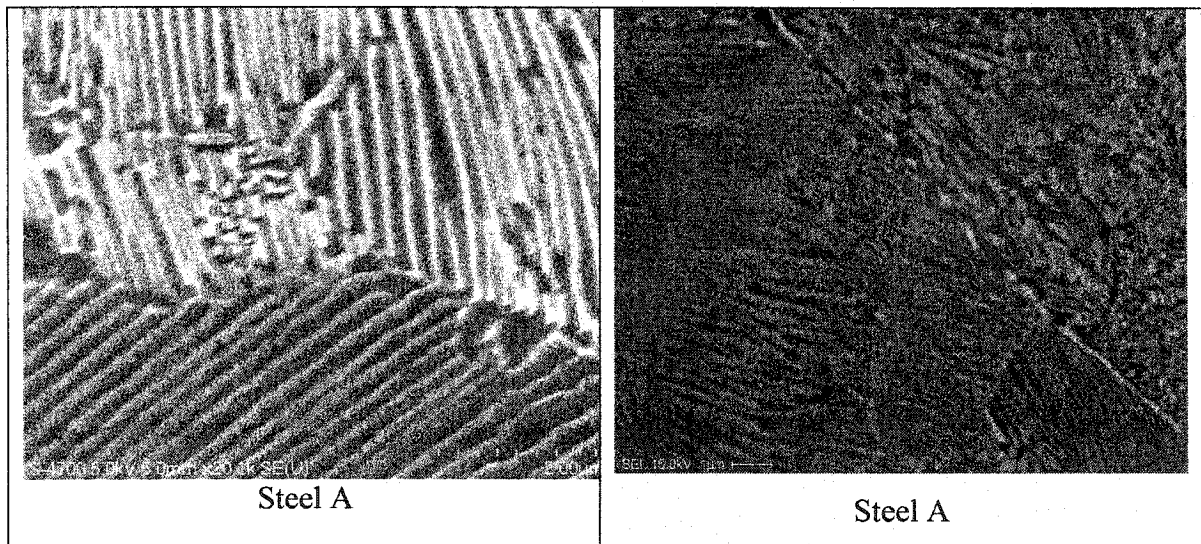


Figure (4-39) Low voltage imaging using a FE-SEM at higher magnifications to show the grain boundary cementite particles in steel A austenitized at 1200°C and transformed at 620°C.

The effects of the various heat treatments on the microstructural parameters are given in **Tables 4-3, 4-4, 4-5, and 4-6** for steels A, B, C and E. The interlamellar spacing of the pearlite was found to increase with increasing transformation temperature and prior austenite grain size. Also, in the steels alloyed with V and Si (A, B, C), the interlamellar spacing was smaller than that of steel E. This finding is consistent with the results of other investigations [84,129-131]. As the interlamellar spacing in steel A was smaller than that of steel E at the same transformation temperature; it can be concluded from this difference in the interlamellar spacing that additions of V decrease the interlamellar spacing at constant transformation temperature. It can also be noticed that steel B, which had a higher Si content and a lower V level, produced finer interlamellar spacing when compared with steel E under the same conditions. The additional refinement in steel C can be attributed to the effects of the higher V level and intermediate Si content.

The effect of the transformation temperature on the pearlite colony size is also shown in **Tables 4-3, 4-4, 4-5, and 4-6**. It is evident that the pearlite colony size is dependent on the transformation temperature, but not on the prior austenite grain size.

In these tables, the lamellar cementite thickness was calculated as a function of interlamellar spacing and C content in the pearlite according to [132]:

$$t_c = \frac{S \times 0.15(\text{wt} \% C)}{V} \dots\dots\dots 5-44$$

where t_c is cementite thickness, S is interlamellar spacing, V is the volume fraction of pearlite, and wt% C is the carbon content in the steels. The cementite plate thickness, t_c , thus decreases as the interlamellar spacing decreases. As the interlamellar spacings of steel A transformed at 620°C, steel B transformed at 620°C, steel C transformed at 620°C and steel E transformed at 580°C are all 0.15 μm , the cementite thickness of steel A is larger than that of steels B, C and E. Moreover, at the same interlamellar spacing, an increase in the C content results in the increase in the cementite thickness.

The nodule size appears to be controlled by both the transformation temperature and prior austenite grain size: a higher transformation temperature and a coarser prior austenite grain size give a larger nodule size.

Table 4-3 The effect of heat treatment on the microstructure of steel A

Heat treatment (°C)	AGS (μm)	TT (°C)	S (μm)	P (μm)	t _c (μm)	N (μm)
1200		620	0.18 ±0.04	7.5 ±0.4	0.029	34 ±5
	97	580	0.16 ±0.03	5.5 ±0.3	0.026	27 ±4
		550	0.14 ±0.02	4.8 ±0.5	0.023	23 ±3
1100		620	0.17 ±0.03	7.2 ±0.2	0.028	27 ±6
		580	0.14 ±0.02	5.2 ±0.4	0.023	22 ±5
	78	550	0.13 ±0.03	4.7 ±0.3	0.021	17 ±4
1000		620	0.15 ±0.02	7.1 ±0.5	0.025	21 ±3
		580	0.135 ±0.02	5.0 ±0.3	0.022	18 ±3
	65	550	0.125 ±0.02	4.5 ±0.4	0.020	15 ±4
900		620	0.12 ±0.02	6.9 ±0.5	0.020	17 ±3
	38	580	0.11 ±0.01	4.8 ±0.4	0.018	14 ±2
		550	0.10 ±0.01	4.3 ±0.3	0.017	12 ±2

Austenite grain size AGS; Transformation Temperature TT; Interlamellar spacing S; Pearlite colony size P; Cementite thickness t_c; Pearlite nodule size N

Table 4-4 The effect of heat treatment on the microstructure of steel B

Heat treatment (°C)	AGS (μm)	TT (°C)	S (μm)	P (μm)	t _c (μm)	N (μm)
1200		620	0.16 ±0.03	7.3 ±0.4	0.024	29 ±5
	94	580	0.14 ±0.02	5.2 ±0.2	0.021	26 ±4
		550	0.12 ±0.03	4.5 ±0.3	0.018	22 ±4
1100		620	0.15 ±0.03	7.1 ±0.4	0.023	25 ±3
		580	0.13 ±0.03	5.0 ±0.3	0.020	22 ±3
	75	550	0.12 ±0.02	4.4 ±0.4	0.018	20 ±3
1000		620	0.14 ±0.02	6.9 ±0.5	0.021	22 ±3
		580	0.12 ±0.02	4.8 ±0.5	0.018	18 ±4
	60	550	0.11 ±0.02	4.4 ±0.4	0.017	16 ±4
900		620	0.11 ±0.02	6.8 ±0.4	0.017	15 ±4
	34	580	0.10 ±0.01	4.7 ±0.5	0.015	13 ±3
		550	0.09 ±0.01	4.1 ±0.4	0.013	10 ±3

Table 4-5 The effect of heat treatment on the microstructure of steel C

Heat treatment (°C)	AGS (μm)	TT (°C)	S (μm)	P (μm)	t _c (μm)	N (μm)
1200		620	0.15 ±0.03	7.2 ±0.5	0.024	27 ±5
	92	580	0.13 ±0.02	5.0 ±0.4	0.021	24 ±3
		550	0.12 ±0.03	4.3 ±0.4	0.019	20 ±3
1100		620	0.14 ±0.03	7.0 ±0.3	0.023	24 ±4
		580	0.12 ±0.02	4.8 ±0.4	0.019	20 ±4
	72	550	0.11 ±0.02	4.3 ±0.3	0.018	18 ±3
1000		620	0.12 ±0.03	6.8 ±0.5	0.019	20 ±3
		580	0.11 ±0.02	4.6 ±0.5	0.018	17 ±4
	57	550	0.10 ±0.01	4.6 ±0.4	0.016	15 ±4
900		620	0.11 ±0.01	6.7 ±0.4	0.018	12 ±3
	29	580	0.09 ±0.01	4.4 ±0.3	0.014	9.0 ±3
		550	0.06 ±0.01	4.0 ±0.3	0.009	7.0 ±3

Table 4-6 The effect of heat treatment on the microstructure of steel E

Heat treatment (°C)	AGS (μm)	TT (°C)	S (μm)	P (μm)	t _c (μm)	N (μm)
1200		620	0.22 ±0.03	7.8 ±0.4	0.030	43 ±4
	108	580	0.19 ±0.02	5.9 ±0.5	0.026	34 ±4
		550	0.17 ±0.03	5.2 ±0.3	0.023	25 ±3
1100		620	0.18 ±0.02	7.5 ±0.4	0.025	34 ±4
		580	0.16 ±0.03	5.5 ±0.3	0.022	26 ±5
	88	550	0.15 ±0.02	4.9 ±0.5	0.020	20±4
1000		620	0.17 ±0.02	7.3 ±0.3	0.023	27 ±3
		580	0.15±0.01	5.3 ±0.4	0.020	22 ±4
	70	550	0.14 ±0.02	4.8 ±0.4	0.019	18 ±3
900		620	0.15 ±0.02	7.2 ±0.3	0.021	21 ±3
	48	580	0.13 ±0.02	5.0 ±0.5	0.018	17 ±2
		550	0.115 ±0.01	4.5 ±0.2	0.015	14 ±2

4.7.2. Effect of Deformation on Microstructure

The microstructure of steel E, hot deformed (as described in section 3.3.7) and isothermally transformed at 620 and 550°C, consisted of grain boundary cementite network and pearlite, as shown in Figure (4-40) and **Table 4-7**, and is similar to the structure of the heat-treated specimens. Comparing these results to **Table 4-2**, there is no significant effect of the deformation. As can be seen in **Tables 4-8 to 4-11**, this is partly because the grain size of the prior austenite has not been significantly refined by the deformation. As mentioned above in section (4.4.3) the statically recrystallized grain size is dependent on the strain and initial grain size.

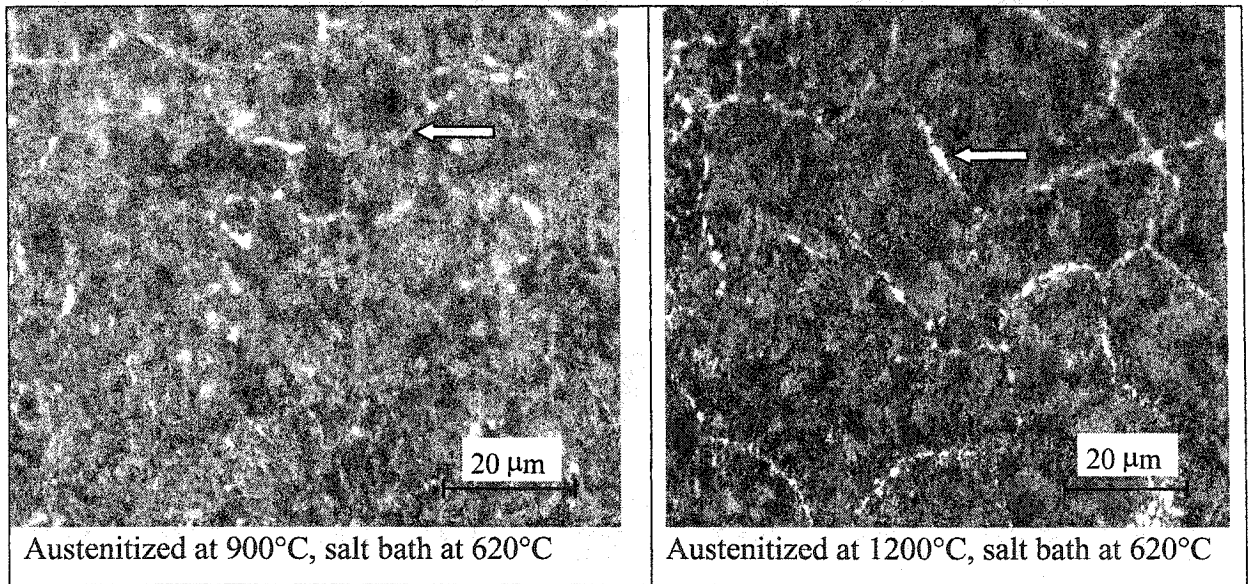


Figure (4-40) Optical micrographs showing the microstructure of steel E.

Table 4-7 Thicknesses of the cementite network

Heat treatment (°C)	Transformation temperature (°C)	Deformed
1200	620	24.0 μm
	580	19.7 μm
	550	16.0 μm
900	620	19.8 μm
	580	15.6 μm
	550	13.0 μm

Table 4-8 The effect of deformation on the microstructure of steel A

Deformation (°C)	AGS (μm)	TT (°C)	S (μm)	P (μm)	t_c (μm)	N (μm)
1200		620	0.15 ± 0.02	6.5 ± 0.3	0.025	28 ± 3
	78	580	0.13 ± 0.02	5.3 ± 0.5	0.021	24 ± 3
		550	0.11 ± 0.01	4.2 ± 0.2	0.018	20 ± 2
900		620	0.10 ± 0.01	6.2 ± 0.6	0.017	15 ± 5
	28	580	0.09 ± 0.02	5.1 ± 0.3	0.015	12 ± 2
		550	0.08 ± 0.02	4.0 ± 0.2	0.013	10 ± 3

Table 4-9 The effect of deformation on the microstructure of steel B

Deformation (°C)	AGS (μm)	TT (°C)	S (μm)	P (μm)	t_c (μm)	N (μm)
1200		620	0.13 ± 0.02	6.3 ± 0.5	0.020	25 ± 4
	76	580	0.11 ± 0.01	5.1 ± 0.4	0.017	20 ± 3
		550	0.09 ± 0.01	4.0 ± 0.2	0.014	18 ± 2
900		620	0.10 ± 0.02	6.2 ± 0.6	0.015	14 ± 4
	25	580	0.08 ± 0.01	4.9 ± 0.5	0.012	10 ± 2
		550	0.07 ± 0.02	3.8 ± 0.3	0.010	8 ± 3

Table 4-10 The effect of deformation on the microstructure of steel C

Deformation (°C)	AGS (μm)	TT (°C)	S (μm)	P (μm)	t_c (μm)	N (μm)
1200		620	0.12 ± 0.02	6.3 ± 0.7	0.019	22 ± 2
	70	580	0.11 ± 0.01	4.9 ± 0.5	0.018	18 ± 3
		550	0.10 ± 0.01	3.9 ± 0.3	0.016	15 ± 2
900		620	0.09 ± 0.01	6.0 ± 0.5	0.015	10 ± 3
	20	580	0.07 ± 0.01	4.8 ± 0.4	0.011	8.0 ± 1
		550	0.06 ± 0.01	3.7 ± 0.5	0.009	6.0 ± 2

Table 4-11 The effect of deformation on the microstructure of steel E

Deformation (°C)	AGS (μm)	TT (°C)	S (μm)	P (μm)	t_c (μm)	N (μm)
1200		620	0.18 ± 0.03	6.8 ± 0.6	0.025	34 ± 5
	85	580	0.16 ± 0.02	5.3 ± 0.3	0.022	28 ± 3
		550	0.14 ± 0.01	4.5 ± 0.5	0.019	22 ± 2
900		620	0.13 ± 0.01	6.5 ± 0.4	0.018	20 ± 3
	32	580	0.11 ± 0.02	5.0 ± 0.3	0.015	16 ± 4
		550	0.10 ± 0.01	4.1 ± 0.5	0.014	13 ± 3

A comparison of the microstructural parameters for the non-deformed specimens with these results shows that the deformed specimens have much finer pearlite structures i.e. interlamellar spacing, pearlite colony size and pearlite nodule size than non deformed ones, as shown in **Table 4-12**.

Table 4-12 Percentage decrease in pearlite microstructural characteristics after at 1200°C

Steels	Transformation temperature °C	% Decrease in interlamellar spacing	% Decrease in pearlite colony size	% Decrease in pearlite nodule size
		$\frac{S_{def} - S_{nondef}}{S_{non-def}} \%$	$\frac{P_{def} - P_{nondef}}{P_{non-def}} \%$	$\frac{N_{def} - N_{nondef}}{N_{non-def}} \%$
A	620	16	15	17
	580	18	7	12
	550	21	14	13
B	620	18	10	13
	580	21	2	23
	550	25	7	18
C	620	20	14	18
	580	15	2	25
	550	20	10	25
E	620	16	15	20
	580	15	11	17
	550	17	15	13

def: deformed

non-def: non-deformed (heat-treated)

4.8. Precipitation Characteristics

Analysis of the isothermally transformed steel E, which did not contain V, showed a well-developed pearlitic structure with continuous lamellar cementite. However for all isothermal transformation temperatures, no precipitates were observed in the interlamellar regions of the pearlitic grains, as shown in Figure (4-41). Alternatively, for the isothermally transformed vanadium steel A, fine precipitates were observed to form exclusively in the ferritic lamellae of the pearlite, as depicted in Figure (4-42). Moreover

the precipitates, which had a spheroidal morphology and ranged in size from 20-30 nm (Figure 4-43), were observed to have an aligned distribution caused by forming in regular arrays that were separated by a spacing of 5-10 nm, as shown in Figure (4-42).

Essentially, the precipitates were aligned perpendicular to the direction of the cementite lamella and their dispersion stopped at any cementite/ferrite interface and restarted in an adjacent ferrite/cementite interface. Hence the cementite phase was the only discontinuity in the development of the particulate arrays as no evidence of precipitation in the cementite was found as shown in Figure (4-43). These observations are consistent with other TEM investigations [133-137] that showed VC precipitation in the ferritic lamellae of the pearlite for V microalloyed steels.

To identify the nature of the particles found in the ferritic lamellae of the pearlitic microstructure in this work, EDX analysis was performed to qualify the elements present as shown in Figure (4-44). Although both V and C were observed, quantification of the particles was hindered by interference from Cr in the steel and low counts for V. Nevertheless, the overall characteristics of these particles suggest that these are VC [72, 138-141], especially since precipitation was only observed to occur in steel A for an isothermal transformation temperature above 580°C as reported in other investigations [142-146].

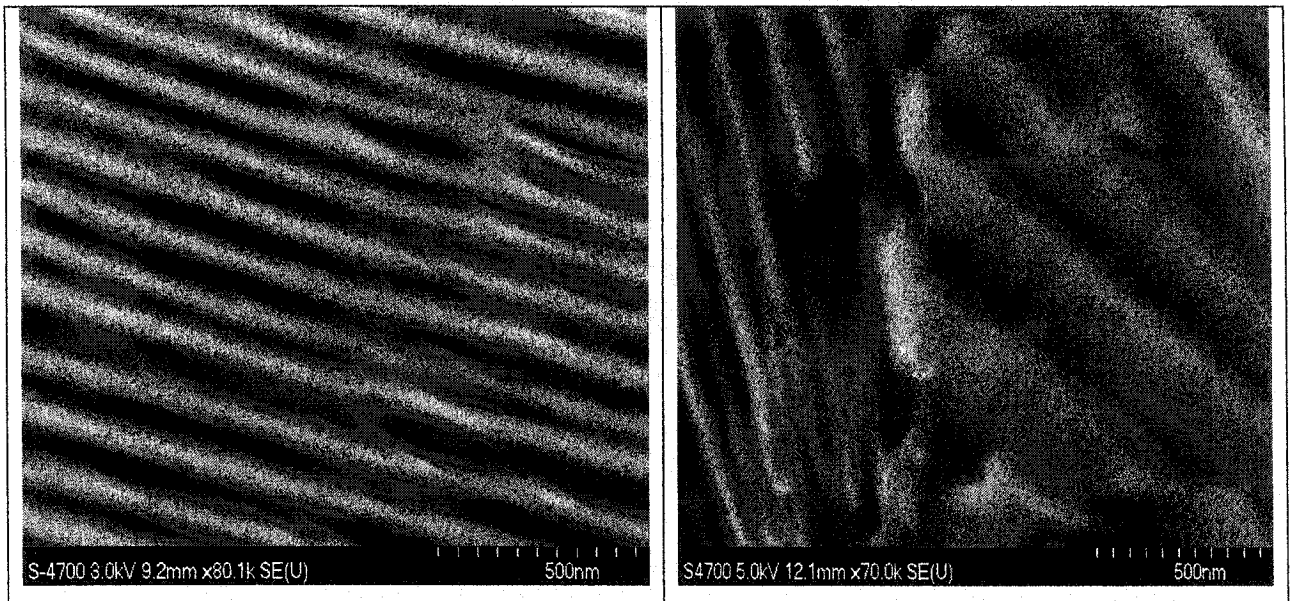


Figure (4-41) FE-SEM micrographs of steel E, isothermally transformed at 620°C for 10 minutes showing ferritic lamellae separated by cementite plates.

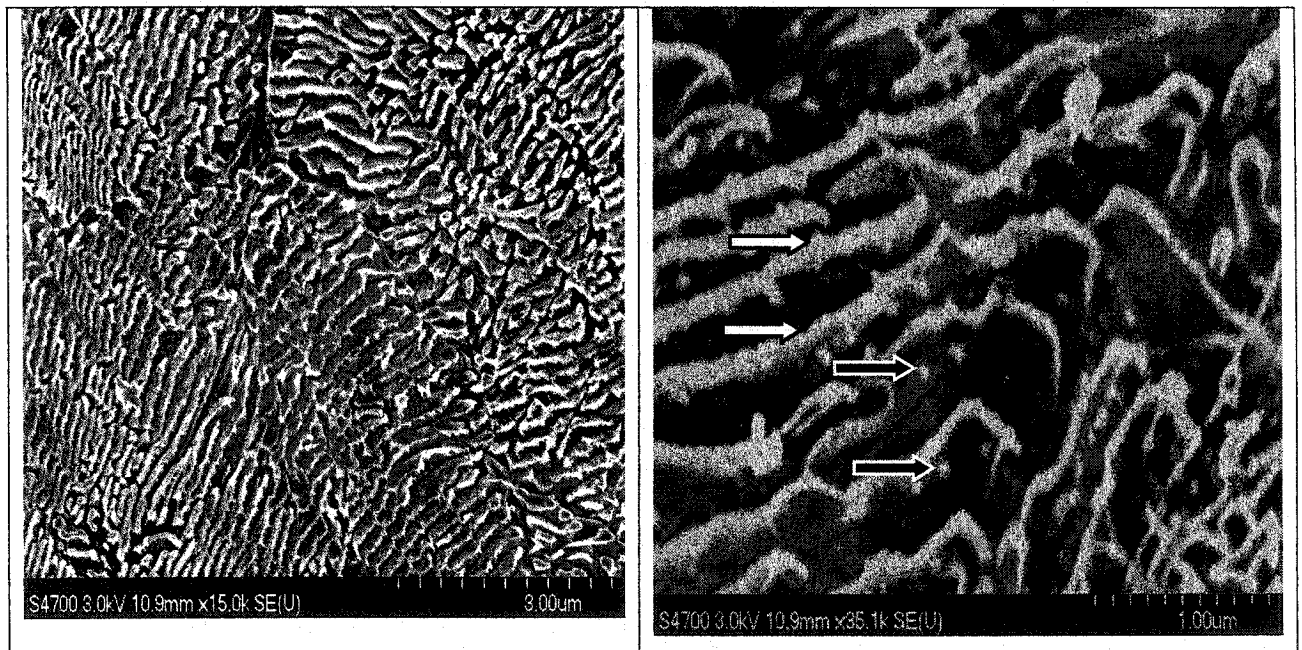


Figure (4-42) FE-SEM micrographs of steel A, isothermally transformed at 620°C for 10 minutes, showing cementite plates (white arrows) and fine precipitates in ferritic lamellae (black arrows).

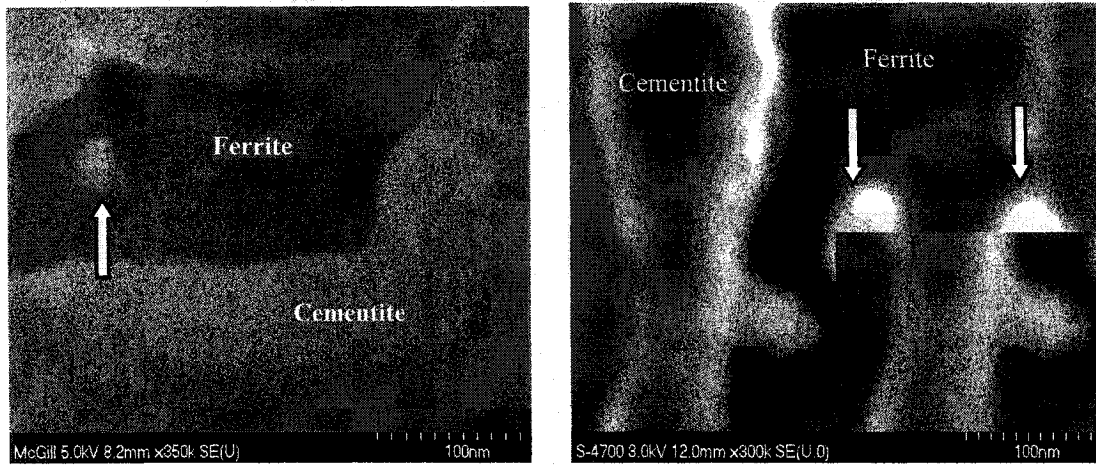


Figure (4-43) FEG-SEM micrographs of steel A showing fine precipitates (arrows) in the ferrite phase and no precipitation in the cementite structure.

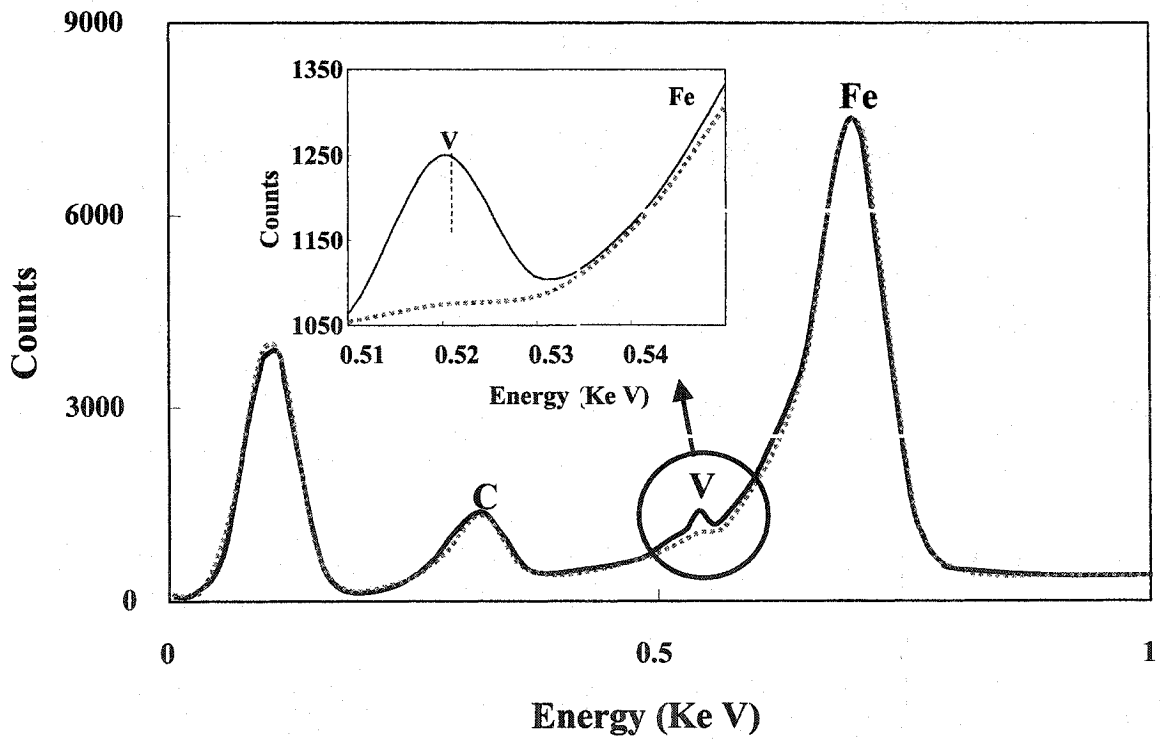


Figure (4-44) EDAX of the precipitate phase in ferrite lamella showing the presence of V and C in the precipitate (solid line) and no vanadium in the ferrite next to the precipitate (dashed line).

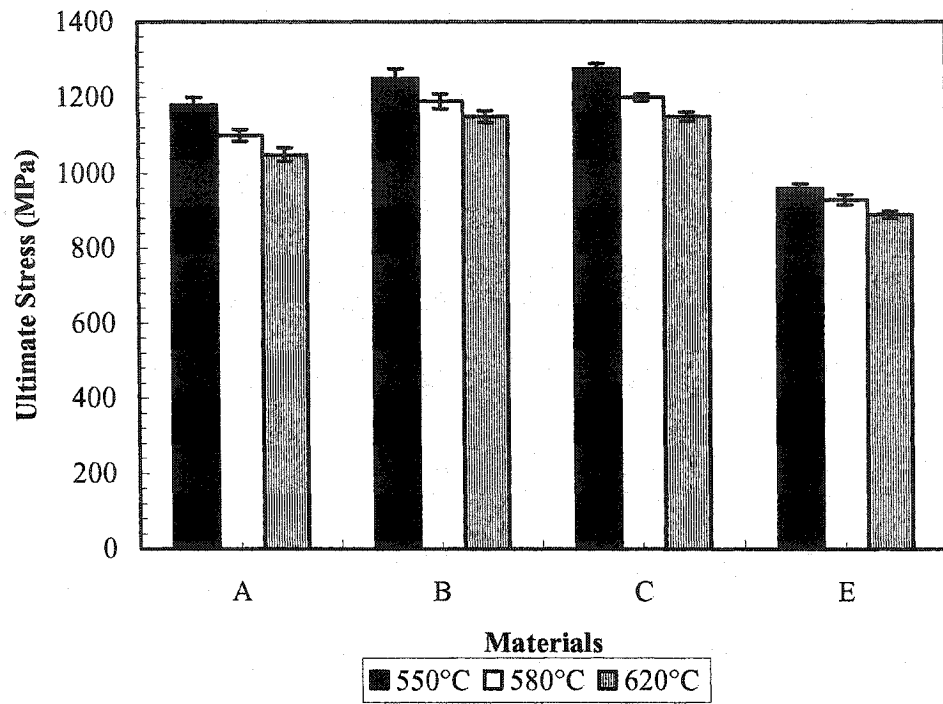
4.9. Mechanical Properties

4.9.1. Heat treated Specimens

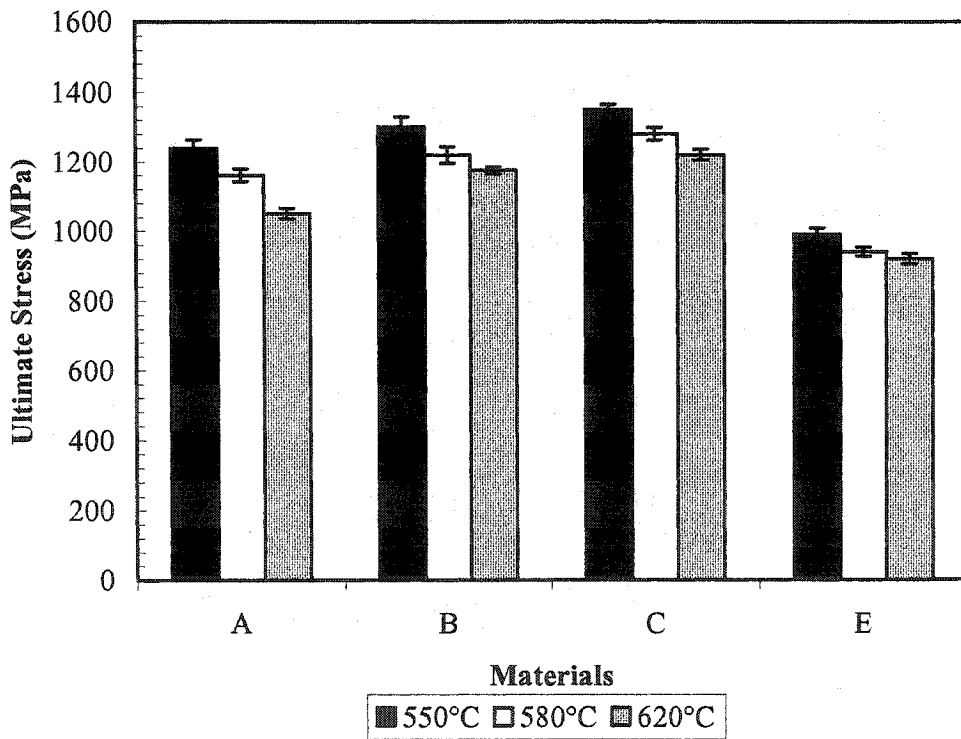
4.9.1.1. Strength

The variation in ultimate stress and yield stress for various isothermal transformation conditions and austenitization temperatures is shown in Figures (4-45) and (4-46). The ultimate stress and yield stress increase with decreasing isothermal transformation and austenitization temperatures in all the steels investigated. This is essentially because the strength of fully pearlitic eutectoid steels is controlled by the pearlite interlamellar spacing [147].

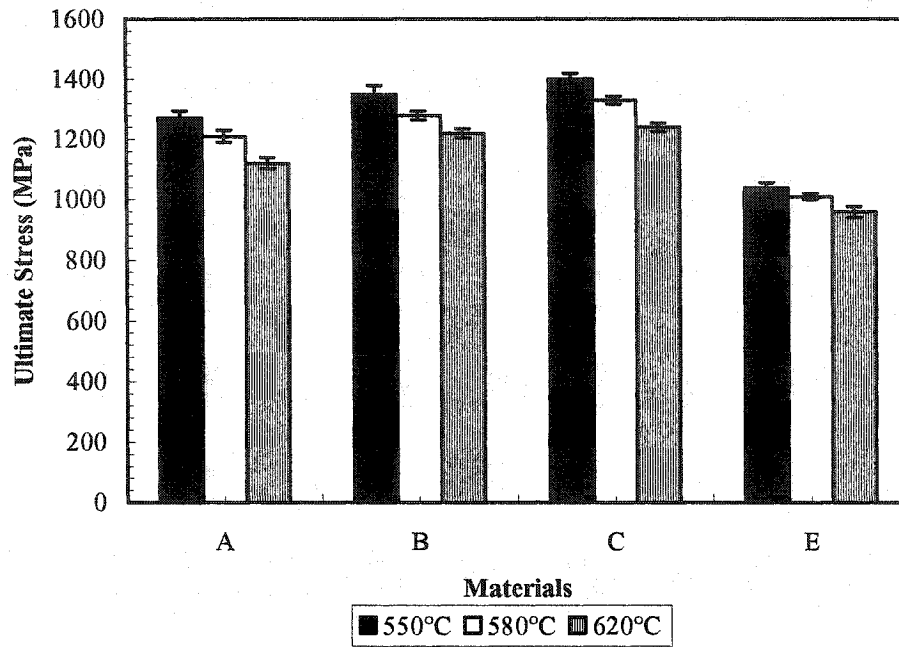
All the alloyed steels had strengths superior to that of the plain carbon, not only because of the interlamellar spacing, but also as a result of i) the improved dispersion of grain boundary carbide, ii) the decreased austenite grain size [147], iii) the V precipitation and iv) the solid solution strengthening effect of Si. Silicon has also been found to promote the precipitation of vanadium carbides, and may therefore lead to more numerous and finer VC. Steel C had the highest strength, which correlates with the highest level of V, as well as the second highest level of Si. Note that steel B, which has a very low level of V but the highest Si level is second only to steel C in strength.



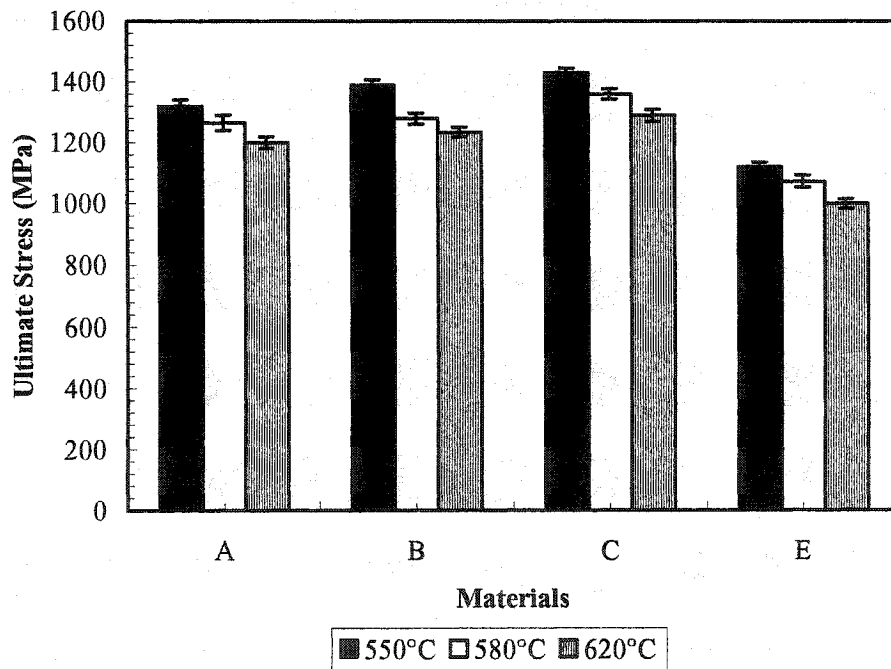
(a)



(b)

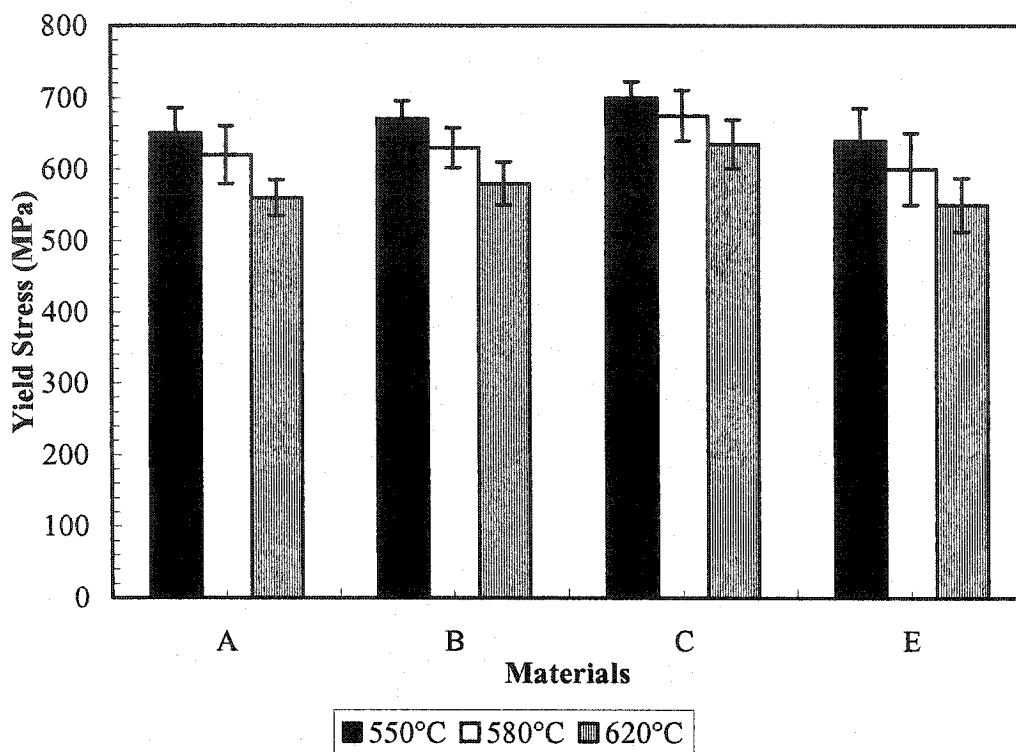


(c)

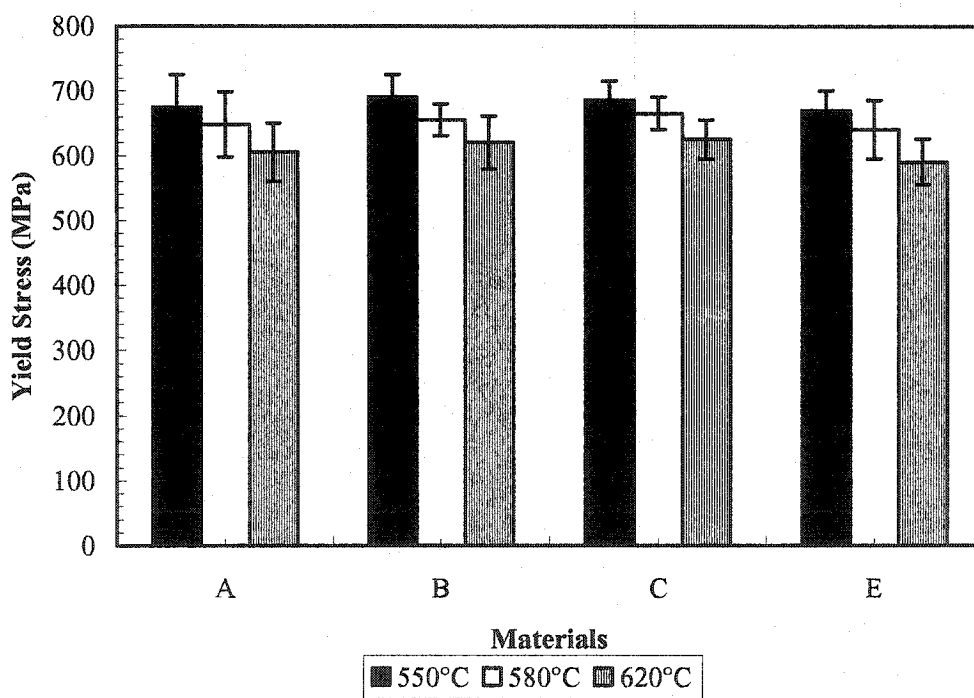


(d)

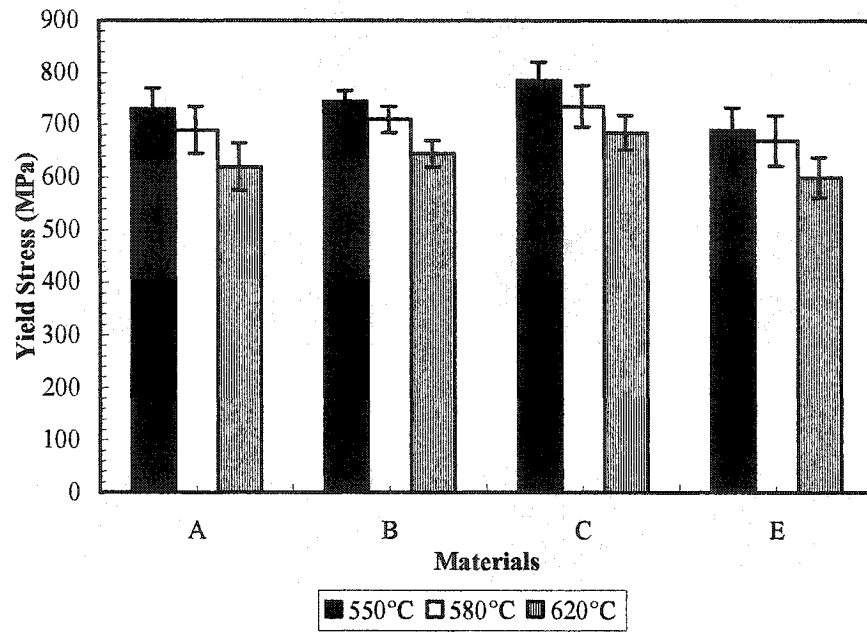
Figure (4-45) Ultimate stress after heat treatment at (a) 1200°C, (b) 1100°C, (c) 1000°C and (d) 900°C.



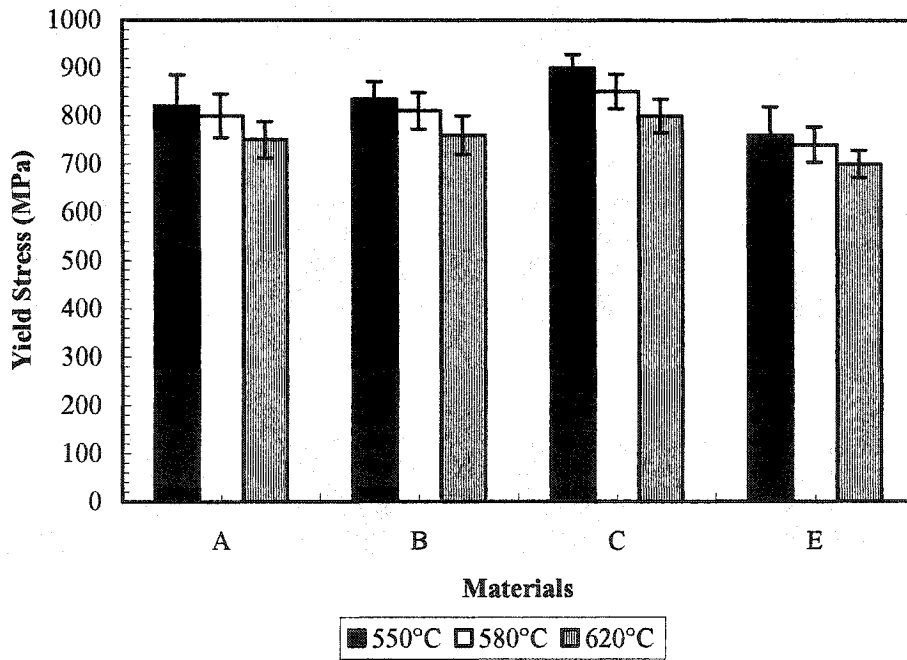
(a)



(b)



(c)



(d)

Figure (4-46) Yield stress after heat treatment at (a) 1200°C, (b) 1100°C, (c) 1000°C and (d) 900°C.

4.9.1.2. Ductility

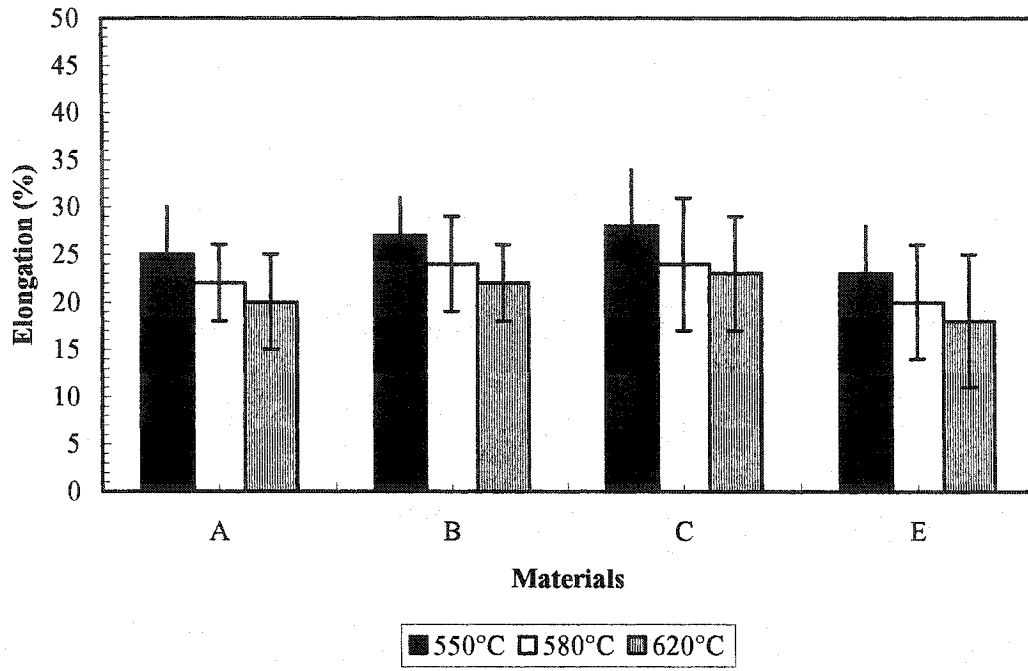
The influence of reheat temperature and transformation temperature on room temperature ductility appears in Figure (4-47) for all steels. It can be seen that the ductility increases with decreasing reheated temperature, i.e. decreasing austenite grain size. Also, increasing the transformation temperature, i.e. increasing the interlamellar spacing and thickness of lamellar cementite, decreases the ductility as shown in Figure (4-48b). It has been found that the refinement of the pearlite colony size can significantly increase the ductility [61]. In fact, **Table 4-13** shows that the strength increases with increasing ductility for all steels with decreasing transformation temperature. This finding is consistent with the results of other researchers [61,148].

Table 4-13 Mechanical properties of steels austenited at 900°C with transformation temperatures

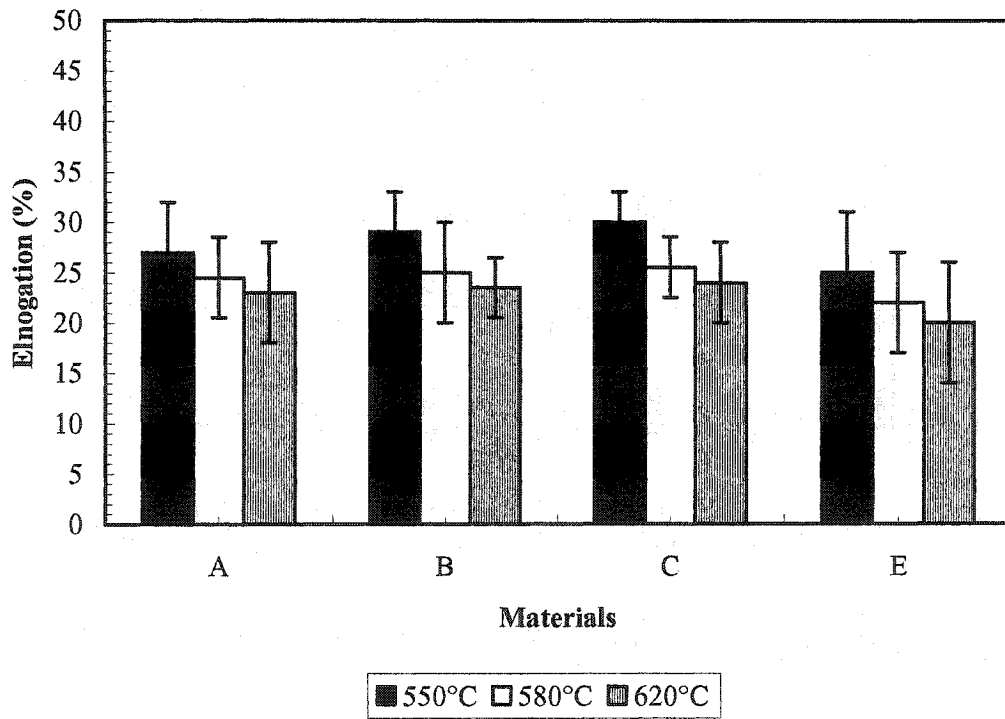
<i>Steel</i>	<i>Transformation Temperature °C</i>	<i>Strength MPa</i>	<i>Elongation %</i>
E	550	1120	29
	580	1073	25
	620	1000	23
Bae et. al. [148]	550	1138	38
	580	1123	37
	590	1050	35
	610	1038	31

4.9.1.3 Formability

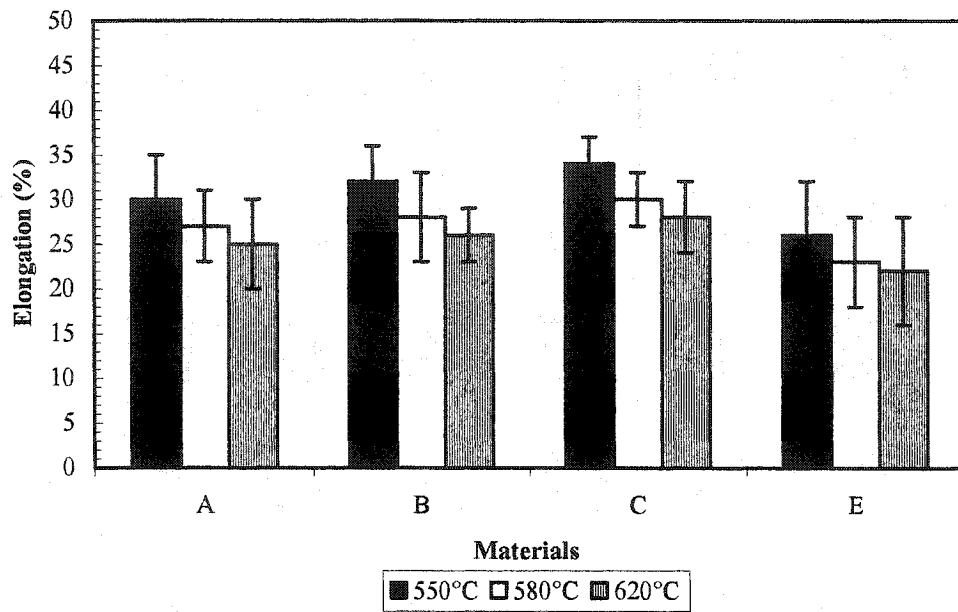
The formability is often taken to be the product of the ultimate stress and total elongation. Figure (4-49) illustrates the plots of formability index as a function of transformation temperature for the steels under investigation. All the steels exhibit their maximum formability index at 550°C.



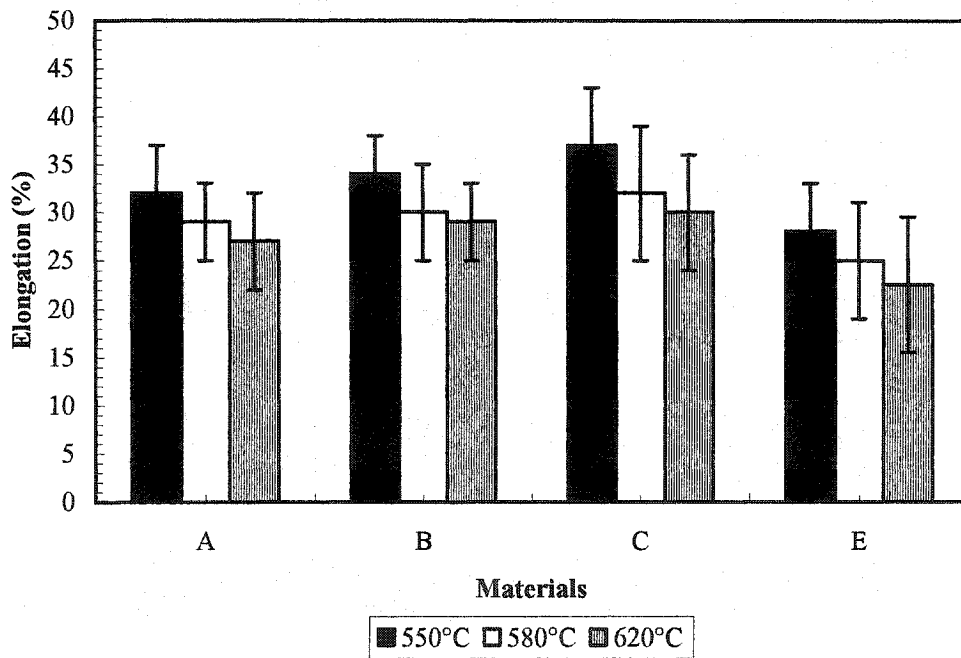
(a)



(b)

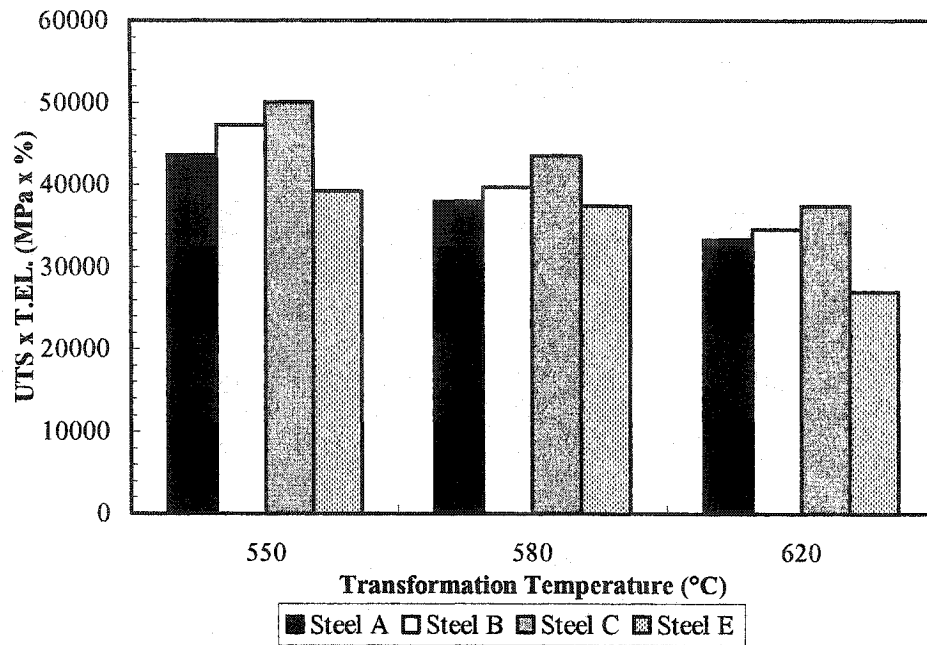


(c)

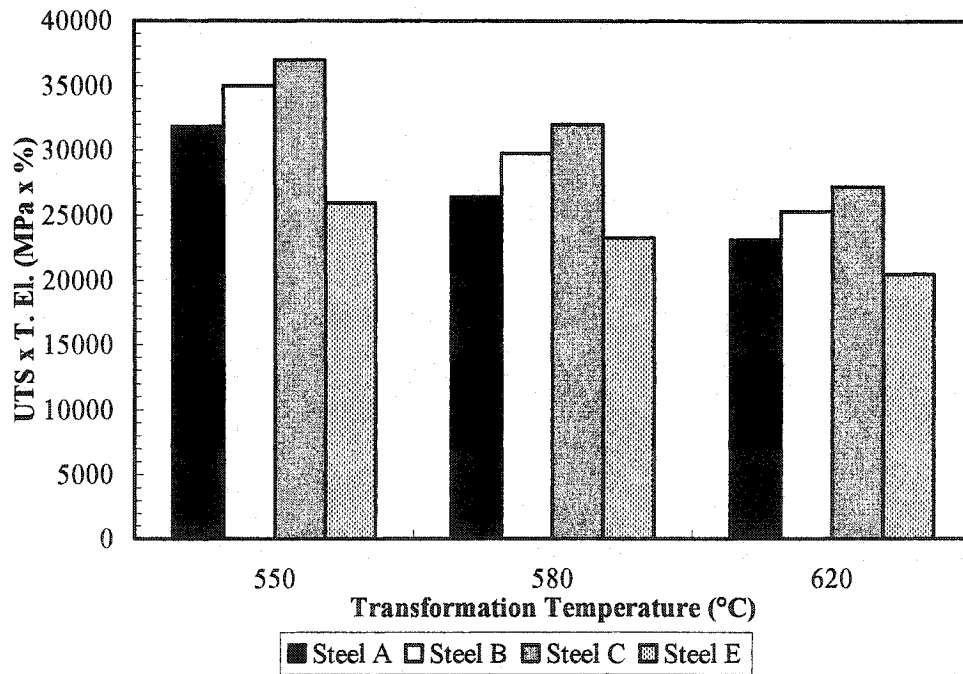


(d)

Figure (4-47) Elongation after heat treatment at (a) 1200°C, (b) 1100°C (c) 1000°C and (d) 900°C.



(a)



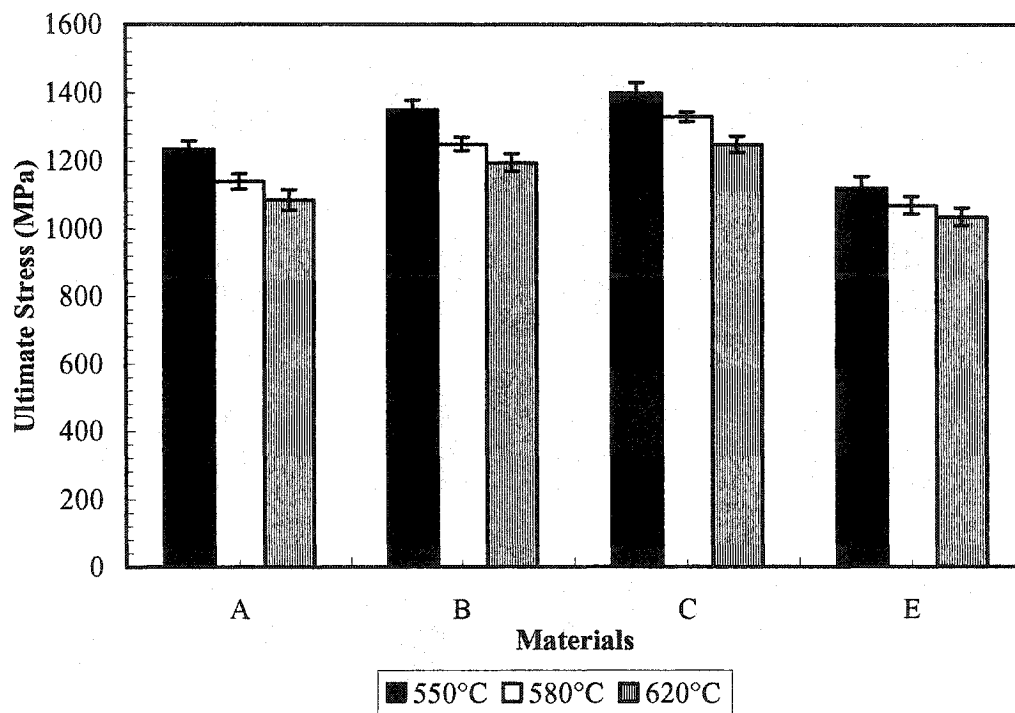
(b)

Figure (4-48) Formability after heat treatment at (a) 900°C, and (b) 1200°C.

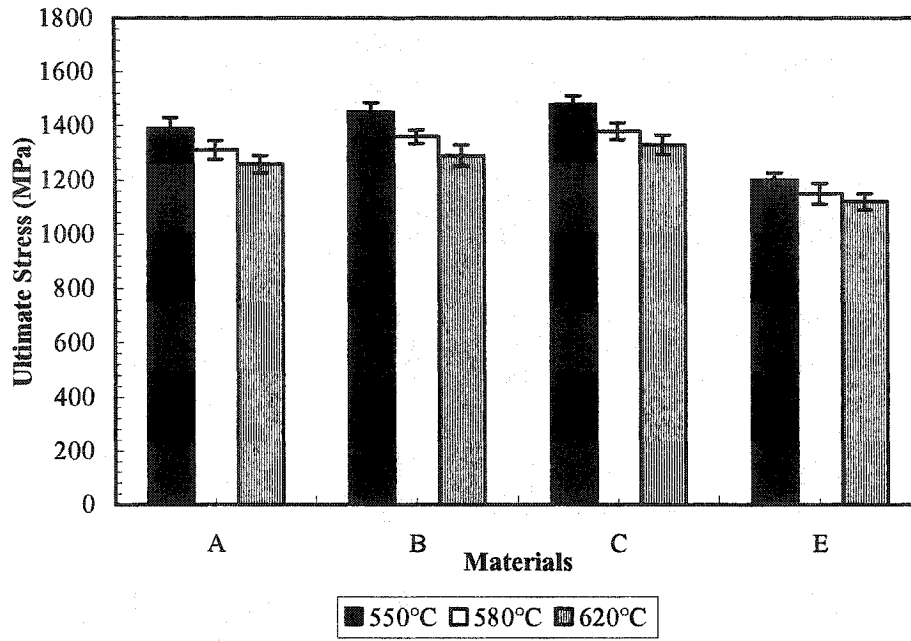
4.9.2. Hot Deformed Specimens

4.9.2.1. Strength

The variations in ultimate stress and yield stress for various isothermal transformation conditions and austenitization temperatures are shown in Figures (4-49 and 4-50) for steels A, B, C, and E. A comparison of these results with those of the previous section indicates that the deformed specimens have about 15% higher strengths than the heat-treated ones. This is mainly due to the refined pearlite structure.

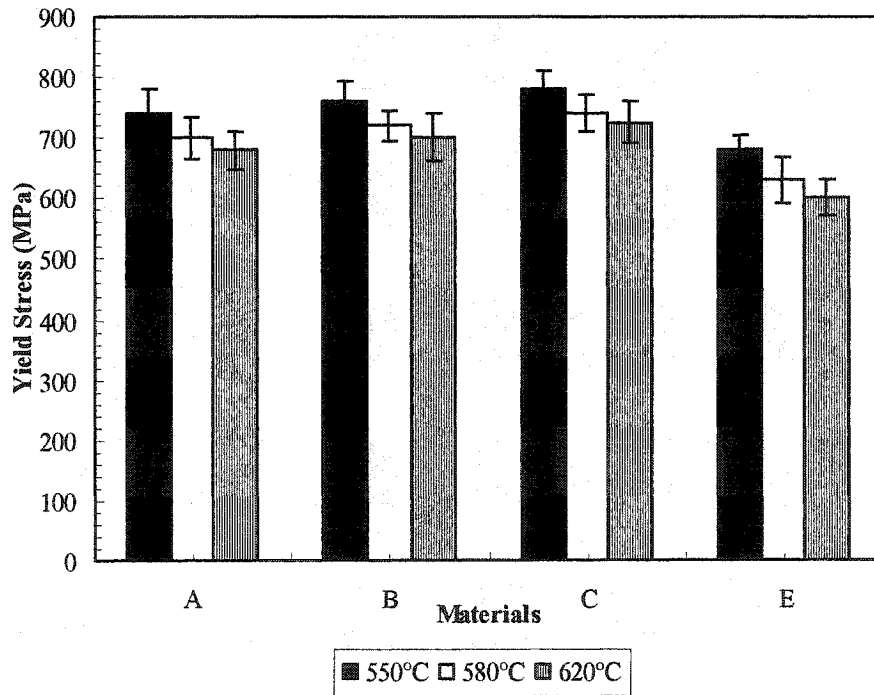


(a)

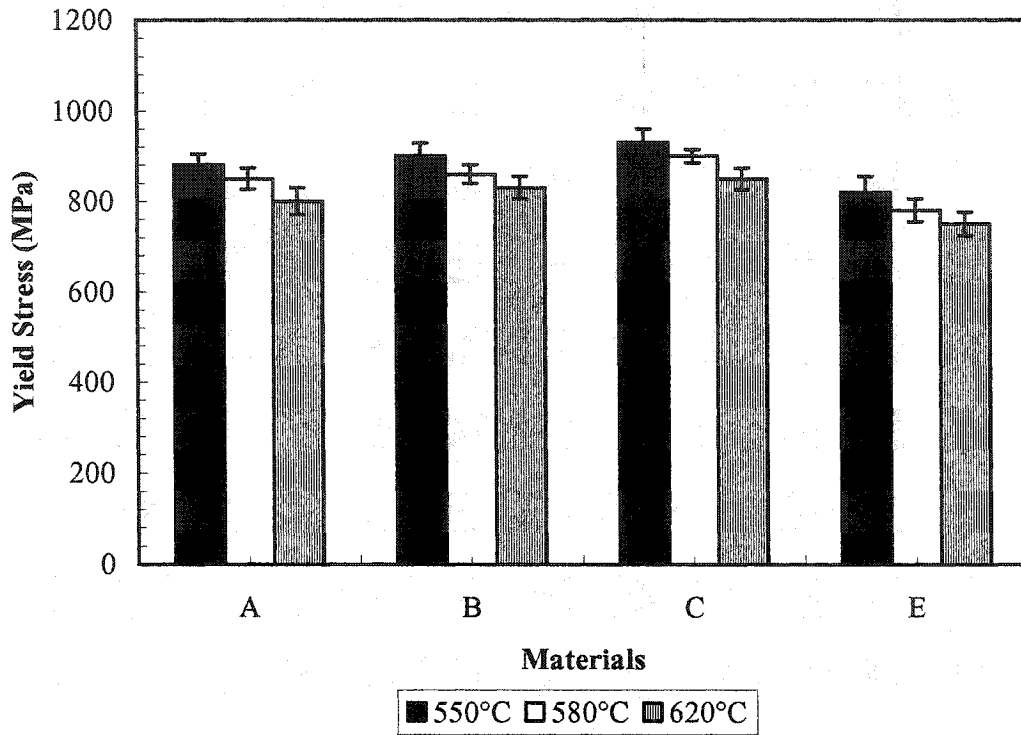


(b)

Figure (4-49) Ultimate stress after deformation at (a) 1200°C and (b) 900°C.



(a)

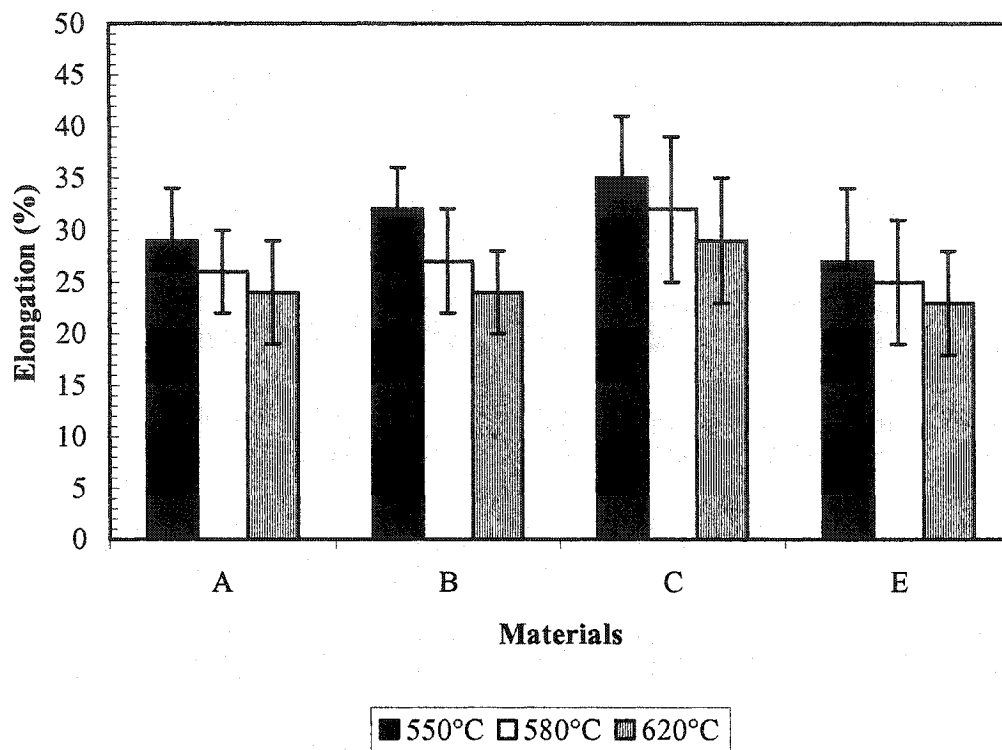


(b)

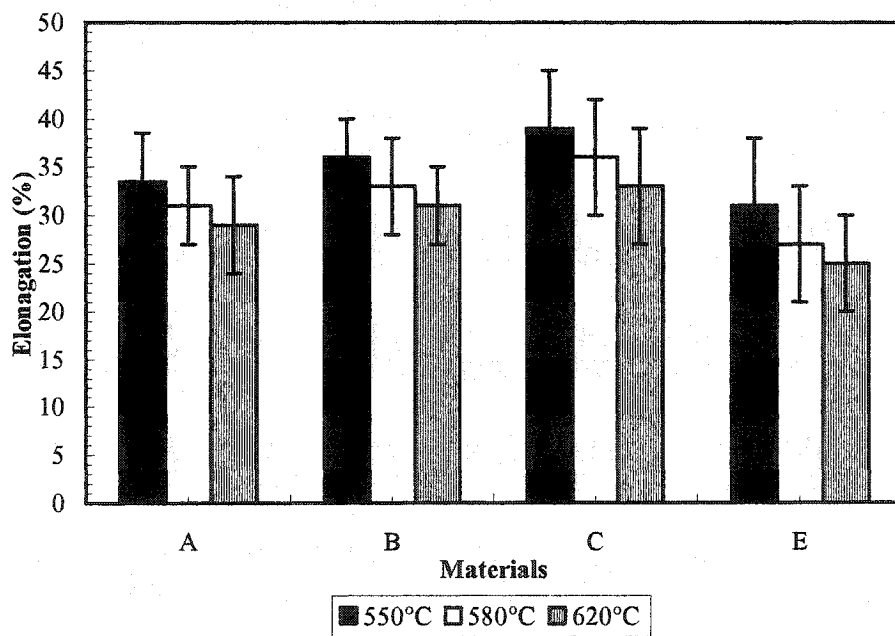
Figure (4-50) Yield stress after deformation at (a) 1200°C and (b) 900°C.

4.9.2.2. Ductility

The variation in the ductility with deformation temperature is plotted in Figure (4-51) for all steels and transformation temperatures. There seems to be no strong effect of hot deformation on the ductility, even though the strength has increased.



(a)

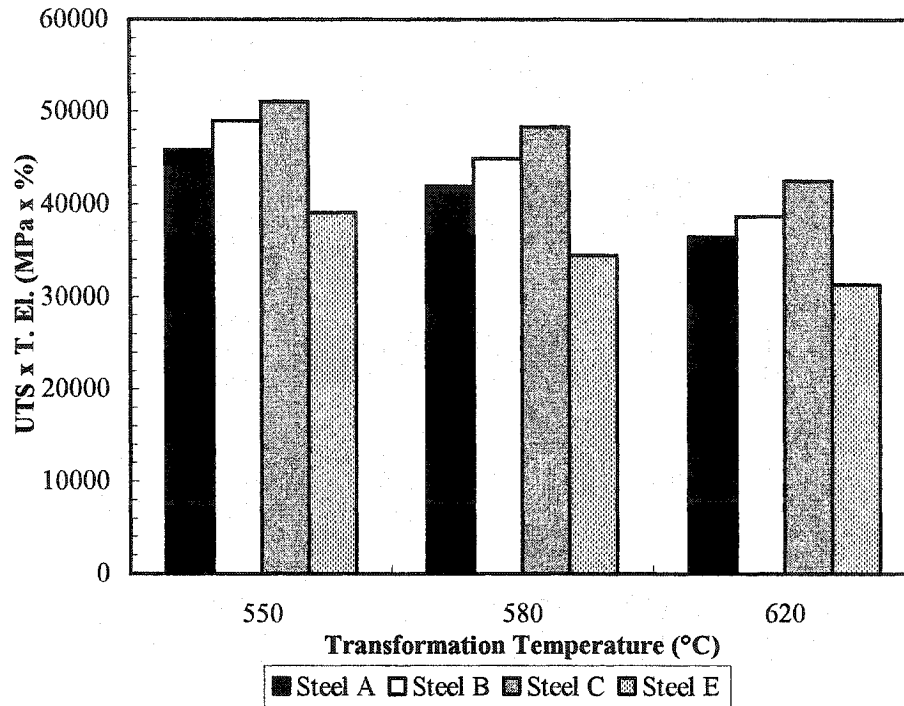


(b)

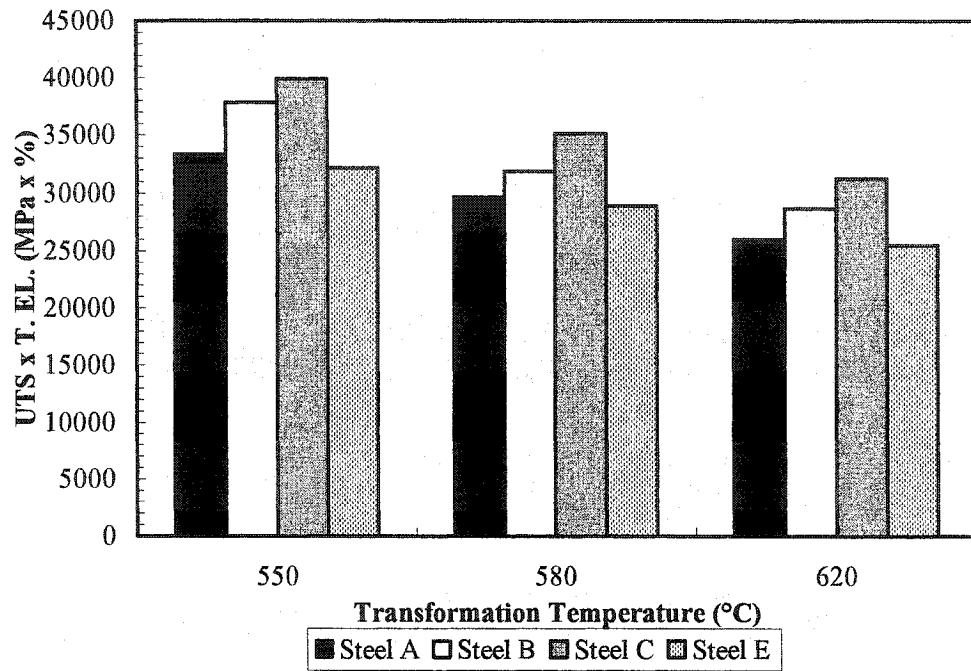
Figure (4-51) Elongation after deformation at (a) 900°C, and (b) 1200°C.

4.9.2.3 Formability

Figure (4-52) illustrates plots of the formability index as a function of transformation temperature for the steels under investigation. Again, all the steels exhibit formability index trends with their maxima occurring at 550°C.



(a)



(b)

Figure (4-52) Formability after deformation at (a) 1200°C, and (b) 900°C

CHAPTER 5

5.1. Dynamic Recrystallization

The objective of this section is to discuss the behavior of the peak strain measured at different strain rates and deformation temperatures. These steels are targeted for rod production, which inevitably involves dynamic recrystallization.

5.1.1. Effect of the Deformation Temperature on the Peak Strain

A plot of the change in the peak strain with inverse temperature is shown in Figure (5-1). The slopes of the peak strain and $1/T$ plots for the steels containing V are approximately equal at higher temperatures and shift to slightly higher values at 950°C (the broken line) for the 0.17 V and 0.078 V steels (i.e. steels A and B). This change or transition in the slope may be attributed to the influence of V (C, N) precipitation on dynamic recrystallization. The solvus temperatures for VC are circled on Figure (5-1). In all cases the transition takes place below 950°C , the solvus temperature.

For steel C, which had an intermediate Si content and the highest V level, the peak strains were higher for than steels A and B at all temperatures. This suggests that another influence of changing Si and V on the peak strain is solute drag. For steel C the

slope transition temperature could not be determined from the flow stress behavior because a peak strain was only present at temperatures below 1000°C. Finally note, in Figure (5-1), in the case of steel D, the reference material (containing no vanadium), the peak strains are much lower and no slope transition temperature can be seen.

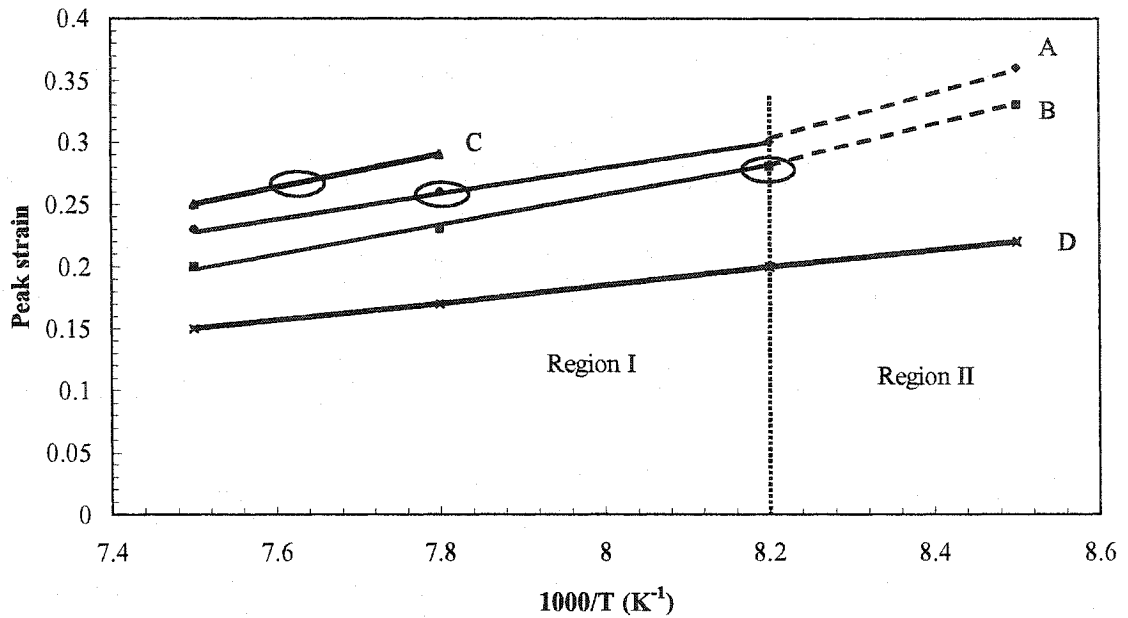


Figure (5-1) Peak strain as a function of the inverse absolute temperature at strain rate 0.01s⁻¹. Solvus temperatures for VC are circled.

5.1.2. Activation Energy of Deformation

Various empirical equations have been proposed to describe the thermally activated process of hot deformation. The one used most frequently is that suggested by Sellars (Section 2.2.1.3.):

$$\sigma_{ss} = A_{ss} \times \left\{ \dot{\epsilon} \exp \left[\frac{Q_{def}}{RT} \right] \right\}^{q_{ss}} \dots\dots\dots 5-1$$

Plotting the steady state stress as a function of the logarithm of the strain rate yields Q_{def} . However, there is another way to evaluate Q_{def} , since the peak strain depends on the Zener-Hollomon parameter according to equation 5-2 [9,149].

$$\varepsilon_p = A_p \times d_o^{0.5} \left\{ \dot{\varepsilon} \exp \left(Q_{\text{def}} / RT \right) \right\}^{q_p} \dots\dots\dots 5-2$$

Thus, plotting the peak strain as a function of the logarithm of the strain rate should also yield Q_{def} . In the present work, Q_{def} was determined in both ways (Figures (5-2) and (5-3)).

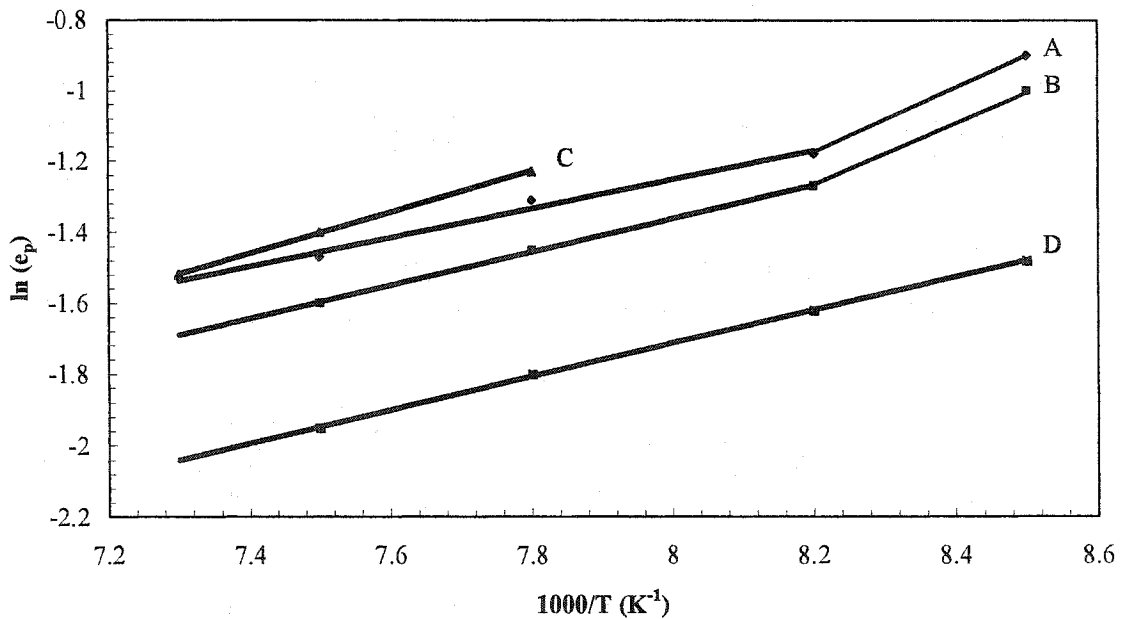


Figure (5-2) Effect of temperature on the peak a strain at strain rate of 0.01s^{-1} .

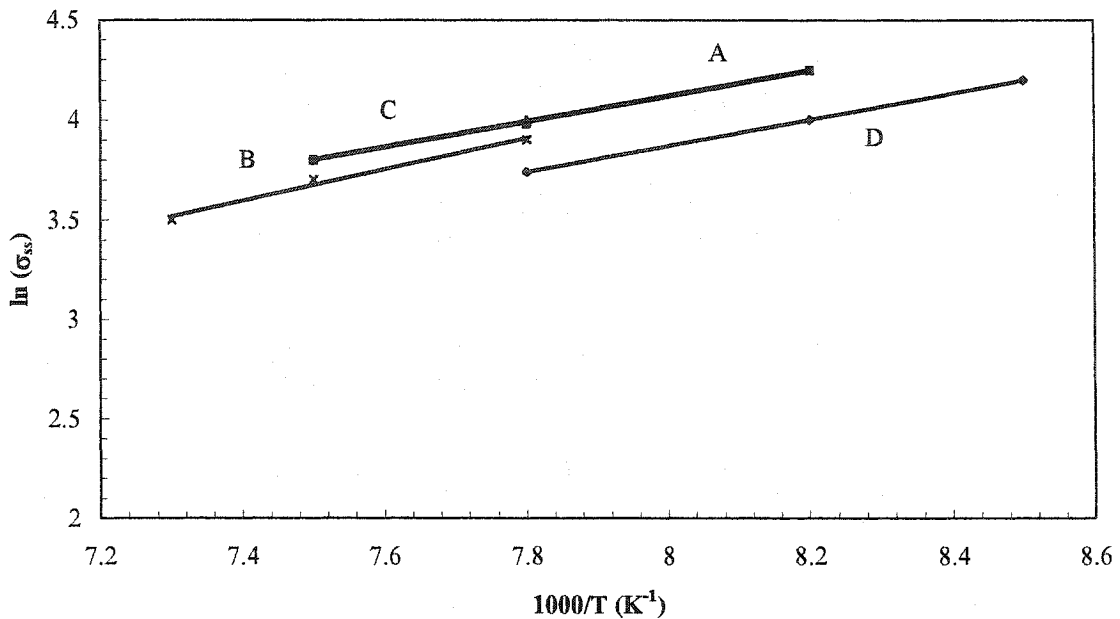


Figure (5-3) Effect of temperature on the steady state stress at a strain rate of 0.01s^{-1} .

The values of A , q and Q_{def} are listed for the various grades in **Table 5-1**. It should be mentioned that the constant, A , is based on the assumption that the peak strain, (ε_p) , depends on the initial grain size according to equation Eq. 5-2. The Zener-Hollomon exponents are in good agreement with the values ranging from 0.125 to 0.175 [150-153] that have been observed by other workers. The peak strain values for vanadium steels are higher than for the C-Mn steels, which agrees with the general finding that the peak strain increases with increasing alloying levels [154,155]. It is clear from the present work that the values of Q_{def} are generally higher when evaluated from the steady state stress (Figure (5-4)). Also the Q_{def} derived from the peak strain increases only slightly with increasing vanadium content. On the other hand, the Q_{def} derived from the steady state stress increased rapidly with increasing vanadium content.

Table 5-1 Values of activation energy for deformation and associated constants for the four steels

Steel	Q_{def} (kJ/mole)		q		A	
	σ_{ss}	ϵ_p	σ_{ss}	ϵ_p	A_{ss}	A_p
A	348	282	0.16	0.15	0.6	9.36×10^{-4}
B	340	280	0.16	0.15	0.78	7.96×10^{-4}
C	386	287	0.17	0.15	0.24	9.7×10^{-4}
D	170	250	0.17	0.16	0.36	7.9×10^{-4}

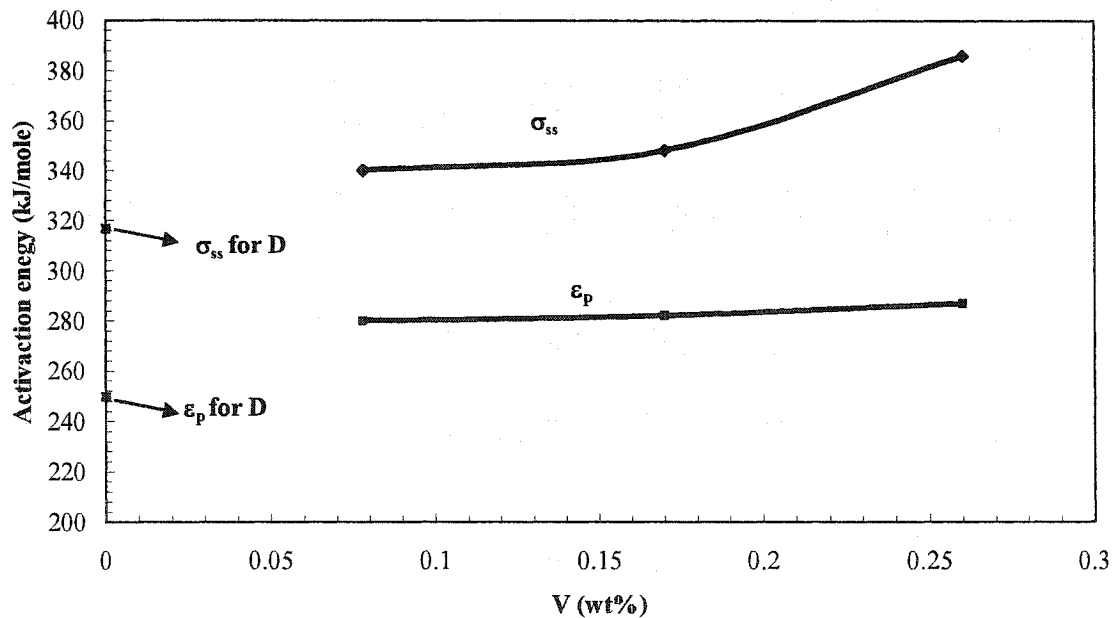


Figure (5-4) Effect of V on activation energy.

The dependence of A_p on the V content can now be determined, as shown in Figure (5-5). Here it can be seen that there is a curved relationship between the peak strain and $\ln[V]$. The final form of equation Eq. 5-2 with the effect of V and Q_{def} derived from the peak strain (instead of the Q_{def} derived from the steady state stress) is the following:

$$\varepsilon_p = (1.479 \ln [V] + 11.782) \times 10^{-4} d_0^{0.5} Z^{0.15} \dots\dots 5-3$$

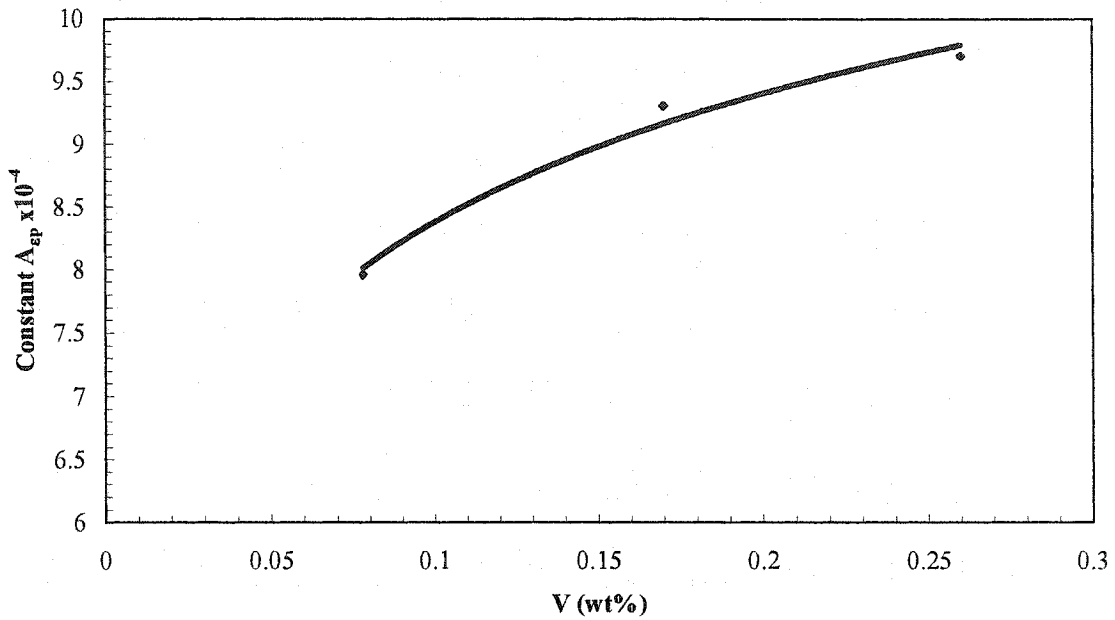


Figure (5-5) Effect of V on the constant A_{ep} .

Predicted and measured values for ε_p are compared in Figure (5-6) and good agreement is displayed.

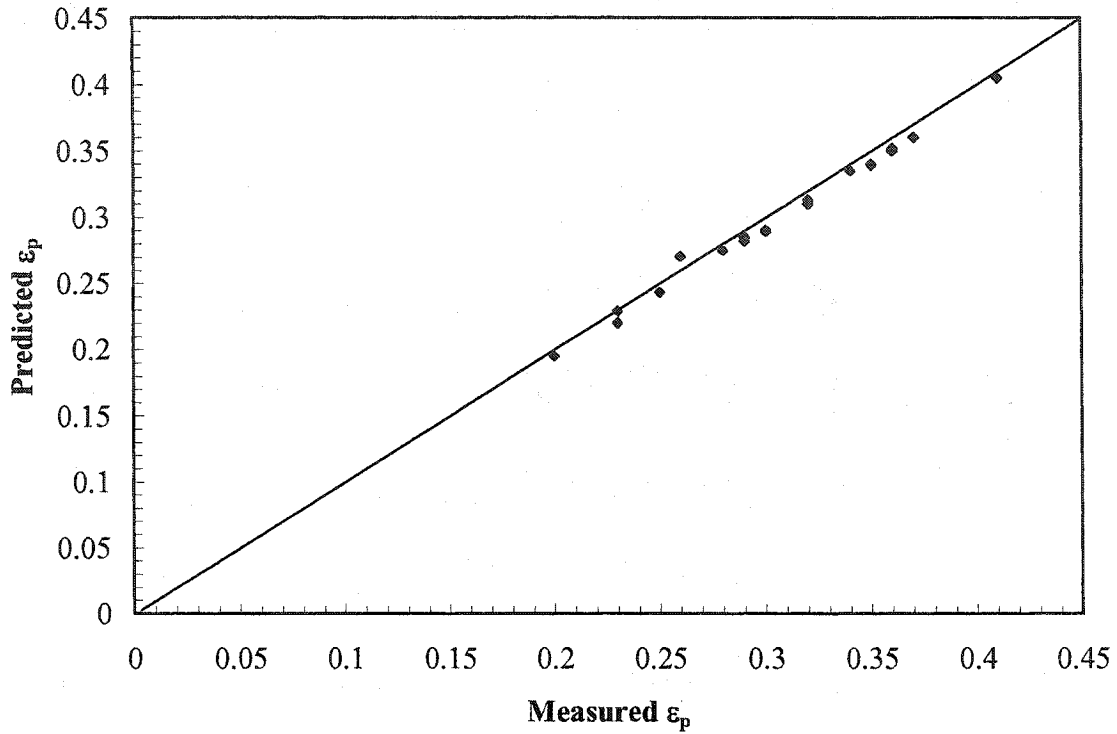


Figure (5-6) Comparison between predicted and measured ϵ_p values using equation 5-3

5.1.3. Comparison of High Carbon Steel with Low Carbon Steel

Using the values determined in this work for the activation energy, and constants A_{ss} and A_p the following equations describing the peak strain and steady state stress are proposed for eutectoid steel

$$\epsilon_p = 7.9 \times 10^{-4} \times d_o^{0.5} \left\{ \dot{\epsilon} \exp \left(\frac{250000}{RT} \right) \right\}^{0.16} \dots\dots\dots 5-4$$

$$\sigma_{ss} = 0.36 \times \left\{ \dot{\epsilon} \exp \left[\frac{317000}{RT} \right] \right\}^{0.17} \dots\dots\dots 5-5$$

Q_{def} was obtained from the gradient of the plots of $\ln \sigma_{\text{ss}}$ against $1/T$. The activation energy for the present steel was determined to be 317 kJ/mol.

To compare our compression results with previous work, as shown in Figure (5-7), the peak strain-temperature behavior was predicted for C-Mn steels using equations derived by previous investigators:

$$\text{CANMET-McGill Model [9]} \quad \varepsilon_c = 6.5 \times 10^{-4} \times d_o^{0.3} \left\{ \dot{\varepsilon} \exp \left(300000/RT \right) \right\}^{0.17} \quad \dots\dots\dots 5-6$$

$$\text{Sellars} \quad \varepsilon_p = 4.9 \times 10^{-4} \times d_o^{0.5} \left\{ \dot{\varepsilon} \exp \left(312000/RT \right) \right\}^{0.15} \quad \dots\dots\dots 5-7$$

It should be mentioned that the peak strain (ε_p) for dynamic recrystallization is usually related to the critical strain of dynamic recrystallization by a factor of 0.65-0.8 [156-158]. Also, both the Sellars and CANMET-model equations are based on torsion test data, whilst the present work employed compression testing. It has been determined that the value of the peak strain determined in torsion is higher (by a factor of ~ 1.3 to 2.5) than the value of the peak strain determined in compression [159,160]. This is because of different contributions of friction, texture change, slip geometry, adiabatic heating, and localization for each technique. However, there is reasonable agreement between the present results and that of the previous investigators.

When determining the peak strain using the CANMET-McGill model Eq. 5-6 the values generated are lower than those determined from equation Eq. 5-7 (Sellars and other workers). However, the CANMET-McGill model values are reasonably close to the experimental data if the CANMET-McGill model predictions are considered as the critical strain (ε_c) instead of the peak strain. The broken curve in Figure (5-7) represents the peak strain values calculated by the CANMET-McGill model when taking the strain

as critical strain values. The peak strain values (represented by the broken curve) are obtained by dividing the critical strain values derived from the CANMET-McGill model by 0.72 (which is the average between 0.65 to 0.8 as the reported conversion factor between the peak strain and the critical strain in the steels [$\epsilon_c = 0.65$ to $0.8 \epsilon_p$]).

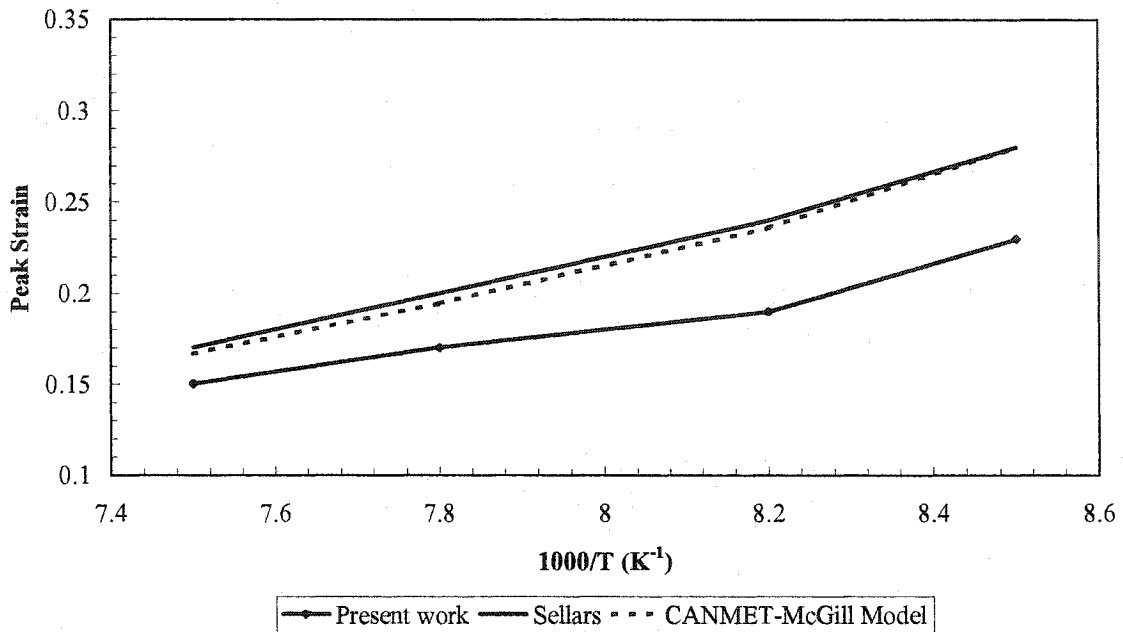


Figure (5-7) Comparison between the present work (Compression), CANMET McGill model and Sellars (Torsion) equation for plain carbon steels.

The dashed curve in Figure (5-8) represents the peak strain values for the present work are obtained by 1.3 (which is the factor of ~ 1.3 to 2.5), i.e. to convert the compression test results to torsion test results. It can be seen that the peak strain values for the present work match the peak strain values for the CANMET McGill model and the Sellars equation.

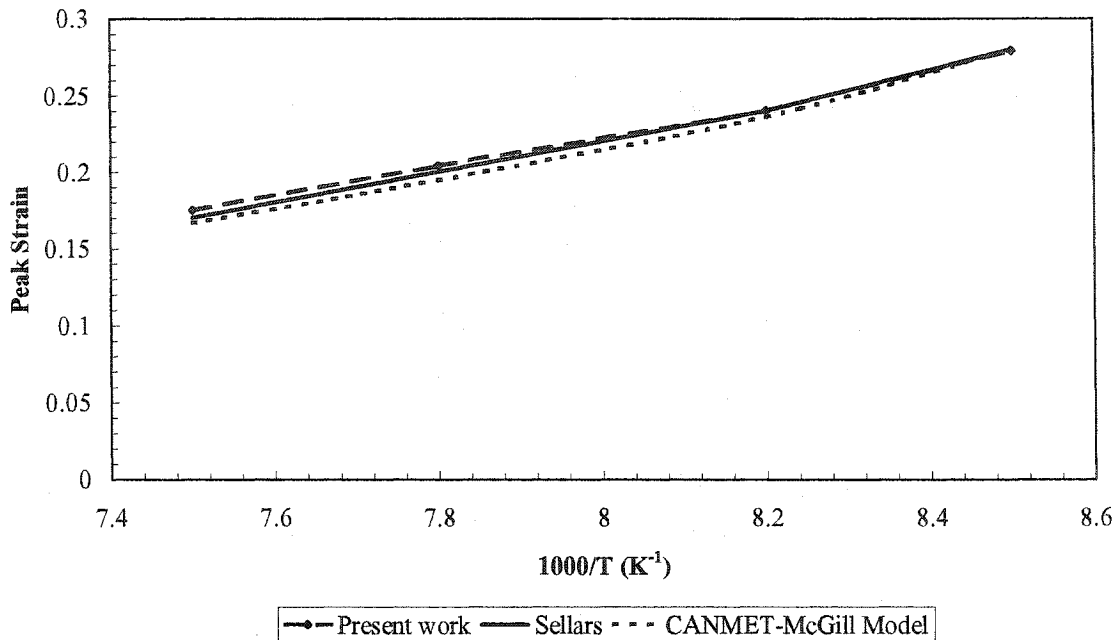


Figure (5-8) Comparison between the present work (the compression values converted to torsion values), CANMET McGill model and Sellars equation for plain carbon steels (Torsion values).

5.2. Static Recrystallization (Microalloyed Steels)

In this section the effect of V and Si on the hot working characteristics of these near eutectoid steels is evaluated and discussed. A convenient way to do this is to model the kinetics of recrystallization and compare the resulting equations with those from the literature for the more conventional HSLA steels.

5.2.1. Modeling the Kinetics of Static Recrystallization

The kinetics of static recrystallization can be described by an Avrami equation of the following form [9,111,113,161]:

$$X = 1 - \exp \left[-0.693 \left[\frac{t}{t_{0.5}} \right]^n \right] \dots\dots\dots 5-8$$

where $t_{0.5}$ is the time needed for a recrystallized a volume fraction of 50%. The expression most widely used for this parameter is:

$$t_{0.5} = A_{srx} \varepsilon^r d_o^q \dot{\varepsilon}^s \exp \left[\frac{Q_{rex}}{RT} \right] \dots\dots\dots 5-9$$

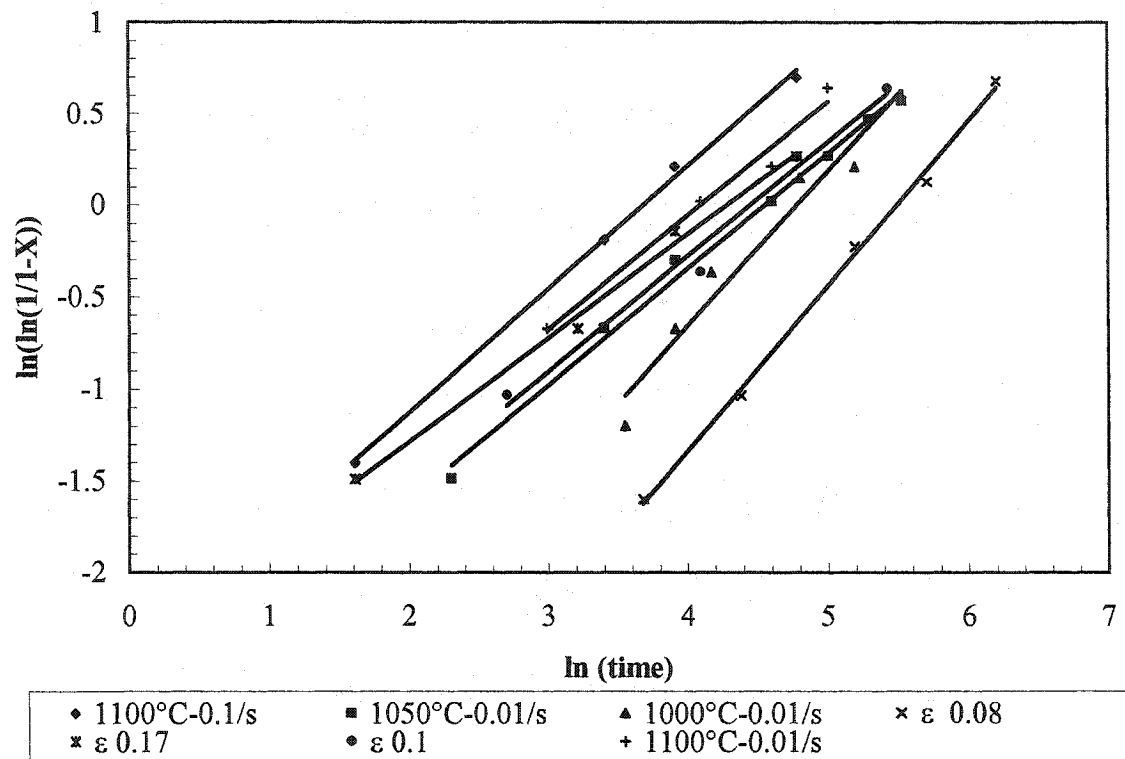
where A_{srx} , n , r , q , and s are material dependent constants, ε is the true strain, $\dot{\varepsilon}$ is the strain rate, Q_{rex} is the apparent activation energy of recrystallization (kJ/mole), T is the absolute temperature (K), R is the gas constant (J/mole K) and d_o is the austenite grain size.

5.2.1.1. Determination of "n"

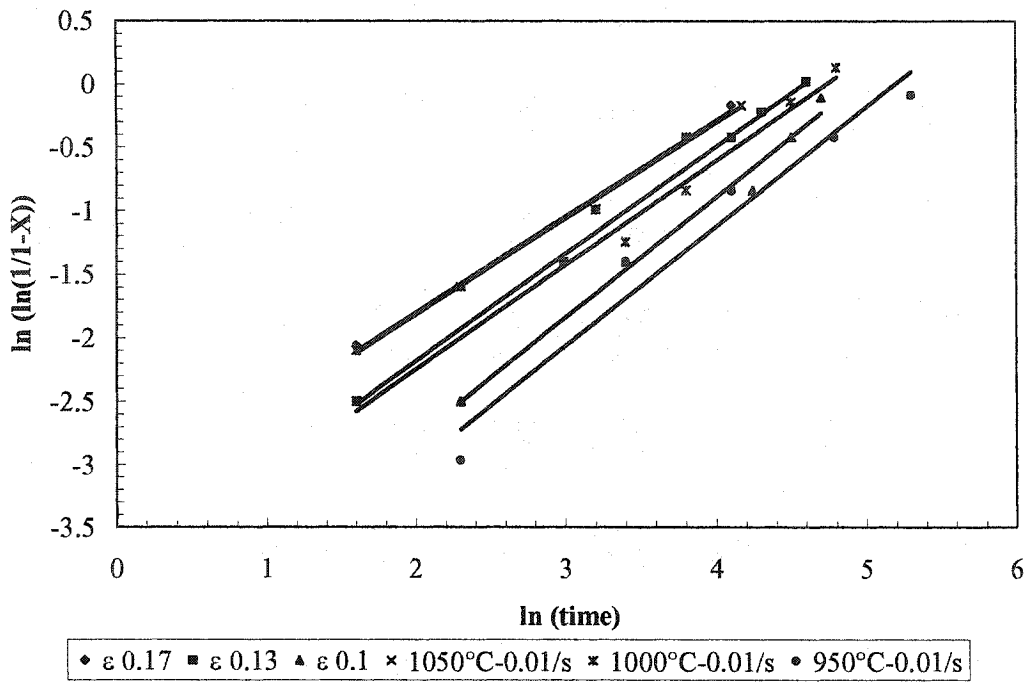
To determine n , the present softening results were plotted as $\ln (\ln (1/(1-X)))$ versus \ln time, as presented in Figure (5-9) for the three steels studied, under different conditions of temperature, strain and strain rate. The average of n value found to be 1 for steels A, B, C, which is within the range of values of 1 to 2 observed by other workers [111,123,161-164]. Typical the value of n is not strongly affected by chemical composition, but it has been reported to increase with decreasing temperature and to decrease from 2 to 1 when the grain size increases from 104 to 530 μm [162,163]. Barraclough and Sellars have suggested that such variations in n could result from differences in the grain size distribution [162].

Differences in the results concerning the time exponent n can also be attributed to the different models of deformation employed by different authors. Sellars has pointed

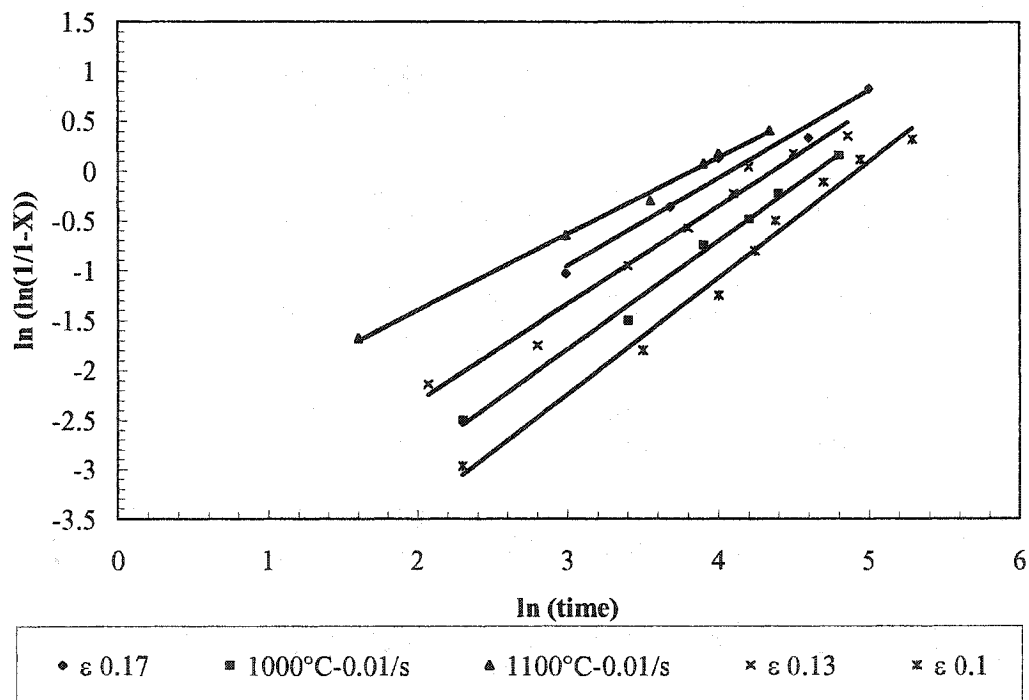
out that much of the discrepancy can result from differences in the methods of observation, i.e., mechanical testing versus the direct measurement of recrystallization by metallographic. The type of mechanical test used to evaluate the softening can be another cause of these differences.



(a)



(b)



(c)

Figure (5-9) Dependence of $\ln(\ln(1/1-X))$ on $\ln(\text{time})$ for steels A, B and C.

5.2.2. Determination of the Dependence of $t_{0.5}$ on the Deformation Parameters

5.2.2.1. Effect of Strain

The effect of strain on $t_{0.5}$ was estimated at constant temperature and strain rate. Under these conditions, $t_{0.5}$ was found to have a power dependence on strain rate:

$$t_{0.5} \propto \varepsilon^r \dots\dots\dots 5-10$$

The strain exponent, r , can be obtained from the $\ln(t_{0.5})$ versus $\ln(\text{strain})$ plots as shown in Figure (5-10). These curves exhibit very similar slopes. The average value of -2 for the exponent r was in good agreement with values of -2 to -4 observed by other workers [113,153,164-168].

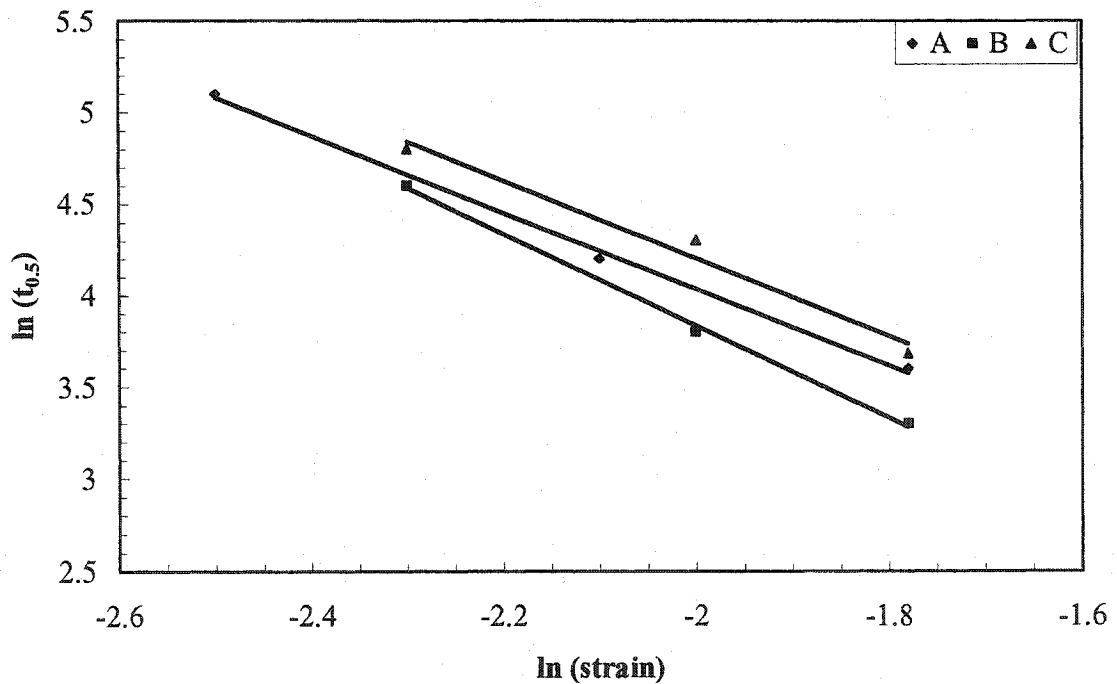


Figure (5-10) Effect of strain on the static $t_{0.5}$.

5.2.2.2. Effect of Strain Rate

The effect of strain rate on $t_{0.5}$ was estimated at constant temperature and strain. Under these conditions, $t_{0.5}$ has a power dependence on strain rate (equation 5-9) and the exponent s was found to be 0.4. This shows that the influence of strain rate on static recrystallization kinetics is lower than the influence of the other variables (temperature, strain and grain size), but it is not insignificant. A typical dependence of $t_{0.5} \propto \dot{\epsilon}^s$, where s , which appears to depend on the alloy, varies between 0.4-0.5 for different materials, has been reported [163,169-172].

5.2.2.3. Activation Energy of Deformation

The activation energy was obtained from plots of $\ln t_{0.5}$ as a function of $1000/T$, where the slope is Q/R . Figure (5-11) shows the graphs for all the steels. For the V microalloyed steels, there are clearly two activation energies, one at low temperatures and one at high temperatures. The temperature at which the transition from high to low activation energy occurs is also shown. Steel B, which has a much lower V content than the other steels, has the lowest transition temperature. Also shown in **Table 5-2** is steel E, the hypereutectoid steel with no V and a conventional level of Si. It can be seen that without V the activation energy is constant over the investigated compositional range. These observations suggest that the change in activation energy mirrors the transition from V in solid solution to V precipitation.

The values of the activation energy are listed for the various grades in **Table 5-2**. Comparing these to the solubility temperatures of **Table 3-2**, it can be seen that, for steel B, the transition temperature (946 °C) is slightly above the solubility of VC, but well below that of VN. For steels A and C, the transition temperature (about 977 °C), is below the solubilities of both precipitate compounds. It can be seen that without V (steel E) the activation energy is constant over the investigated range. In the higher temperature

range, (i.e. assuming V to be in solid solution) an average value of 300 kJ/mole for the V containing steels was calculated. The activation energy for the plain carbon hypereutectoid steel E was determined to be 270 kJ/mole. This seems to indicate that there is an effect of V and possibly Si in solid solution.

Table 5-2 Activation energies for hot deformation

Steel	Q high temperature	Q lower temperature
A	305	415
B	290	475
C	310	478
E	270	-

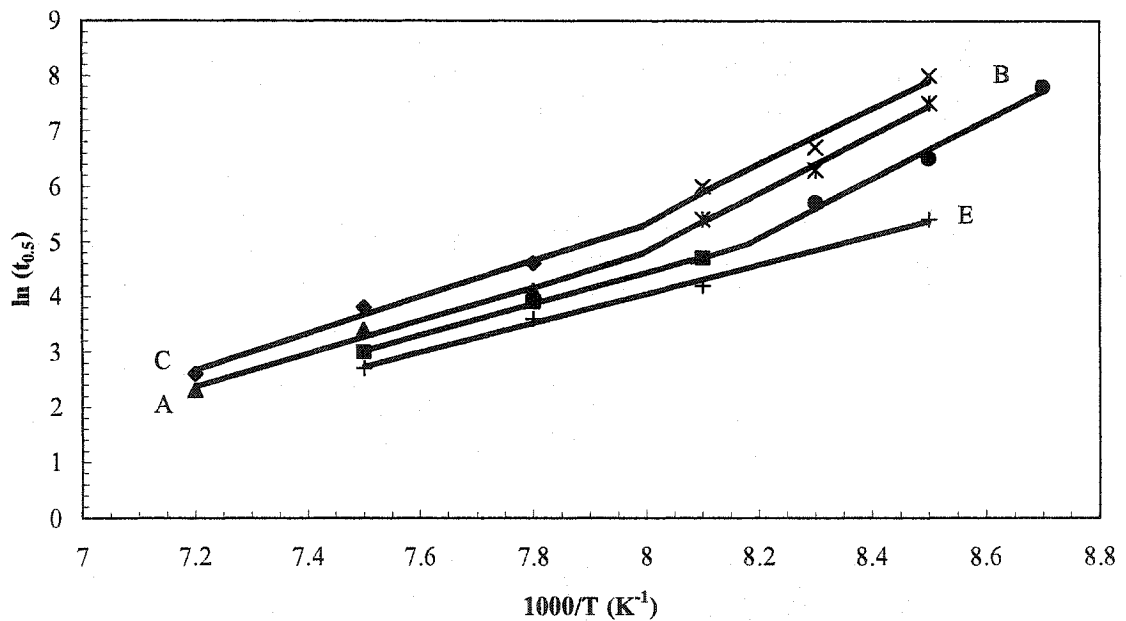


Figure (5-11) Plot of $t_{0.5}$ against the reciprocal of the temperature for the V and Si steels.

The dependence of A_{srx} of Eq. 5-9 on the silicon and vanadium concentrations can now be determined, as shown in Figure (5-12), leading to the following linear relation:

$$A_{srx} = (0.4 ([Si]+[V]) + 1.1) \times 10^{-17} \dots\dots\dots 5-11$$

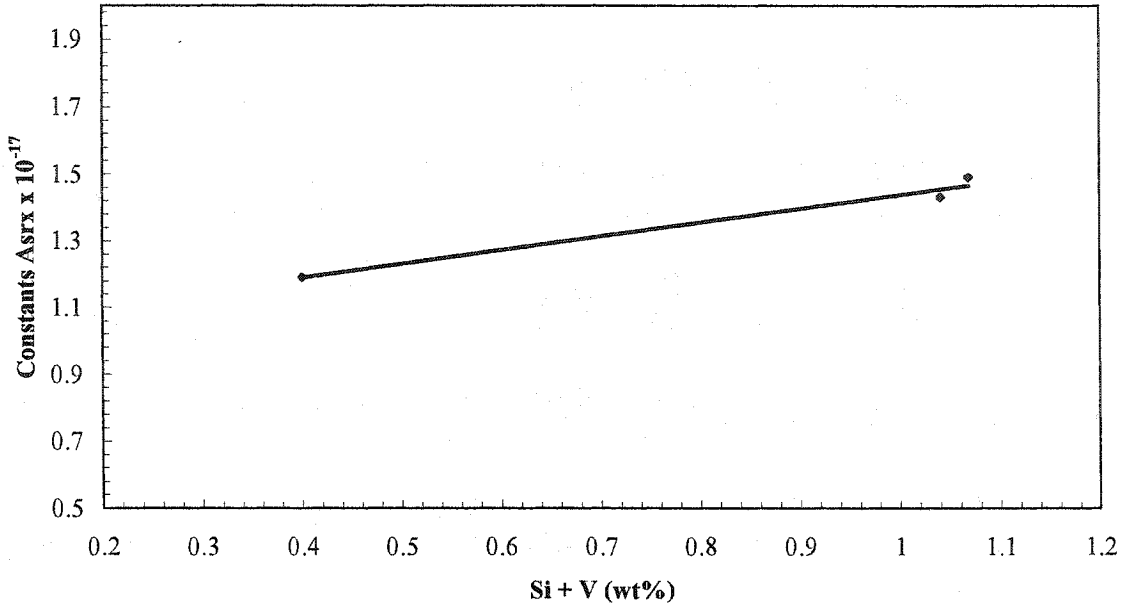


Figure (5-12) Effect of V and Si on the constant A_{srx} .

The $t_{0.5}$ expression derived in this work takes the following final form

$$t_{0.5} = (0.4 ([V + Si]) + 5.4) \times 10^{-17} \epsilon^{-2} d_0^2 \epsilon^{-0.4} \exp \left[\frac{300 \times 10^3}{RT} \right] \dots\dots\dots 5-12$$

A comparison between the predicted and measured values of $t_{0.5}$ is made in Figure (5-13). This can be compared with Figure (5-14), in which A_{srx} has not been adjusted for V and Si. As can be seen, the effect of Si and V is significant.

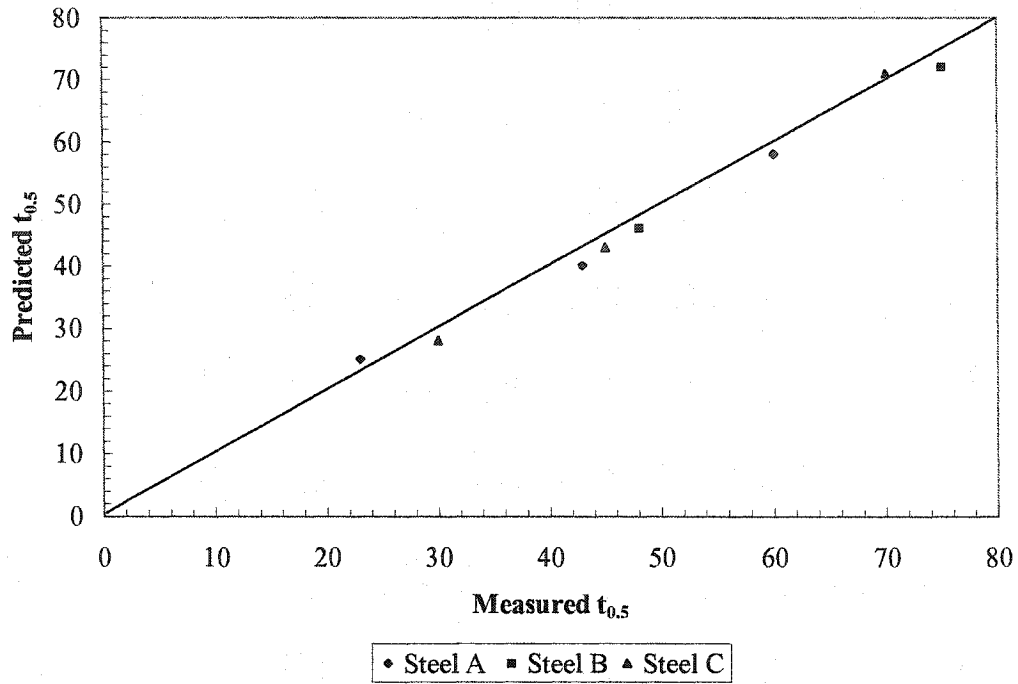


Figure (5-13) Comparison between measured $t_{0.5}$ and those predicted with the effect of $[Si + V]$ included. (The line indicates a perfect correlation.)

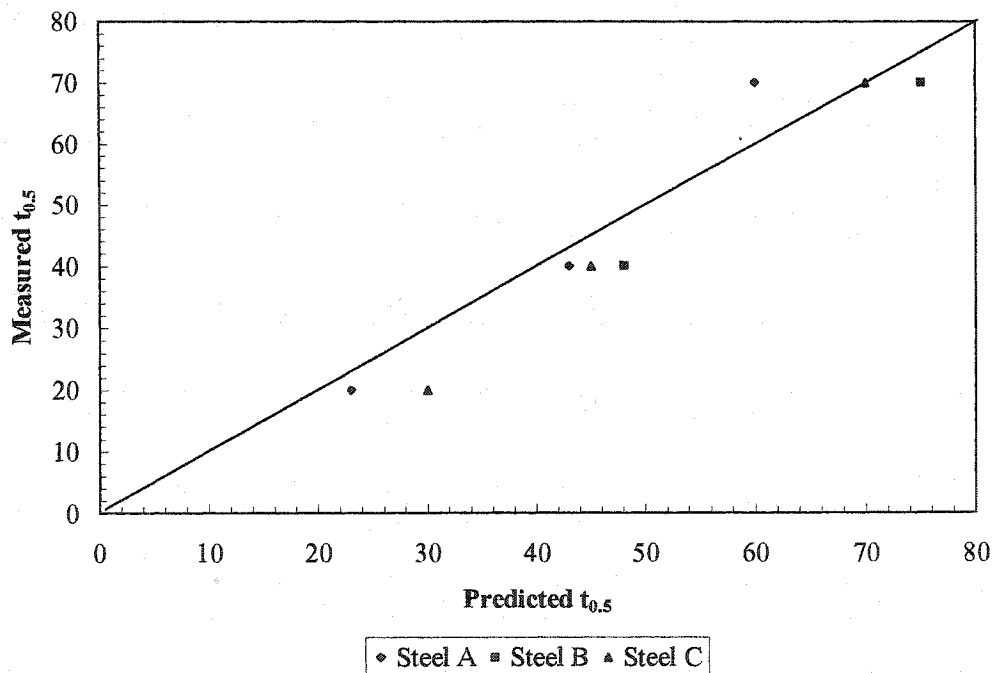


Figure (5-14) Comparison between measured $t_{0.5}$ and those predicted without the effect of $[Si + V]$ showing poor agreement. (The line indicates a perfect correlation.)

5.2.3. Recrystallization Precipitation Temperature Time Diagram

Recrystallization-precipitation-temperature-time (RPTT) diagrams can be used to better understand the recrystallization precipitation interaction and to design rolling schedules. Referring to Figure (4-27), for steel A, the temperatures and times that correspond to different recrystallized fractions, such as 0.1 and 0.5, as well as the strain induced precipitation start, P_s , and finish, P_f , times, have been obtained from the softening curves presented in the results section. Recall that the P_s and P_f curves were drawn on the basis of the plateaus seen in the recrystallized fraction versus time curves. In this way the RPTT diagram shown in Figure (5-15). Note that precipitation is detected at times greater than about 100 second, corresponding to recrystallized fractions greater than 0.1 and as high as 0.5. On the other hand, the nose of the P_s curve would intercept the line corresponding to a recrystallized fraction close to 0.5. Furthermore, the lines corresponding to a recrystallized fraction equal to or less than 0.1 did not intercept the curve P_s . In other words, precipitation only seemed to occur if the recrystallized fraction was greater than 0.1. After the P_f curve, the recrystallized kinetics behaved in a manner similar to that which was observed prior to precipitation. This means that as the temperature dropped, more time was necessary to obtain the recrystallized fraction after straining.

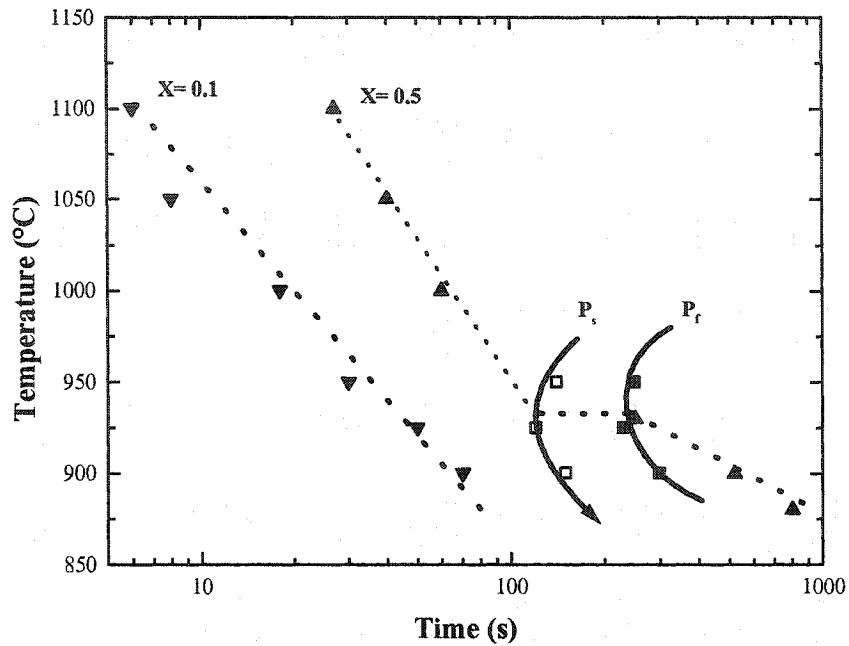


Figure (5-15) Recrystallization-precipitation-temperature-time diagram.

As can be seen from the kinetic results, above 950 °C no plateaus were seen presumably because full recrystallization occurred before any precipitation occurred. Precipitation start times for the steels tested are summarized in **Table 5-3**. As can be seen from the table there was little difference between these times, but the results consistently indicate that the precipitation kinetics are ranked as follows: steel C > steel A > steel B.

Table 5-3 Precipitation start time for the three tested steels as detected by the fractional softening method

Temperature °C	Precipitation start time, seconds		
	A	B	C
950	145		110
925	130	150	115
900	150	160	140
875		210	

5.2.4. Modeling of Precipitation Kinetics

According to the classical theory of diffusion controlled nucleation [173-178], which has been summarized by Russell [179], the steady state nucleation rate J_s is given by

$$J_s = N \frac{D_o X}{a^2} \exp\left(\frac{Q}{RT}\right) \exp\left(-\frac{\Delta G^*}{kT}\right) \dots\dots\dots 5-13$$

where, N is the number of nucleation sites per unit volume, X is the effective concentration of the rate controlling element, D_o is the diffusivity of the rate controlling element, a is the lattice parameter of the austenite, and ΔG^* is the critical free energy for nucleation.

Following Aaronson and Lee [180] the critical free energy is given as:

$$\Delta G^* = \frac{16\pi\gamma^3 f}{3(\Delta G_{chem})^2} \dots\dots\dots 5-14$$

where f is a modifying factor that arises for nucleation at dislocations or grain boundaries, γ is the interface free energy, and ΔG_{chem} is the chemical free energy

According to Dutta and Sellars [181], the chemical free energy is related to the supersaturation, k_s ,

$$\Delta G_{chem} = - \left(\frac{RT}{V_m} \right) \ln k_s \dots\dots\dots 5-15$$

where V_m is the mole fraction of carbonitride. This gives:

$$J_s = \alpha [Nb] \exp \left(- \frac{Q}{RT} \right) \exp \left(\frac{16\pi\gamma^3 V_m N_o f}{3RT (-RT \ln k_s)^2} \right) \dots\dots\dots 5-16$$

Considering that a number N^* of nuclei per unit volume must be formed in time $t = P_s$ for nucleation to be detected

$$P_s = \frac{N^*}{J_s} \dots\dots\dots 5-17$$

The combination of equations 5-16 and 5-17 leads to

$$P_s = C [Nb]^{-1} \exp \left(\frac{Q}{RT} \right) \exp \left(\frac{B}{T^3 (\ln k_s)^2} \right) \dots\dots\dots 5-18$$

where

$$C = A \varepsilon^{-1} Z^{-1} \dots\dots\dots 5-19$$

$$B = \frac{16\pi V_m^2 N_o}{3R^3} \dots\dots\dots 5-20$$

Dutta and Sellars [181] developed a model for strain-induced Nb(C,N) precipitation, based on classical nucleation theory Eq. 5-18. The model was then fitted to experimental data published by various authors, who used a wide range of chemical compositions. For this work, this equation has been modified for the precipitation start time of vanadium precipitates as follows:

$$P_s = A[V]^{-1} \varepsilon^{-1} Z^{-0.5} \exp \left\{ \frac{Q_d}{RT} \right\} \exp \left\{ \frac{B}{T^3 (\ln k_s)^2} \right\} \dots\dots\dots 5-21$$

where

$$A = 3 \times 10^{-6} \quad B = 2.5 \times 10^{10}$$

[V] = Concentration of V in solution, wt %

Q_d = activation energy for diffusion of V in austenite 293000 Jmol^{-1} [182]

Here, the solubility of VN and VC are considered separately through k_s , the solubility parameter

$$k_s \text{ for VN} \quad [V][N]/10^{3.84 - 8990/T} \quad [183]$$

$$k_s \text{ for VC} \quad [V]^{4/3} [C]/10^{7.06 - 10800/T} \quad [184]$$

Initial calculations indicated that the assumption of VC precipitation gave a closer fit to the measured data, hence only the VC predictions are shown. The P_s times in steels A, B and C obtained by this equation are compared graphically with the experimental data in Figure (5-16) for a strain of 0.08 and strain rate of 0.01s^{-1} , and are also listed in **Table 5-4**.

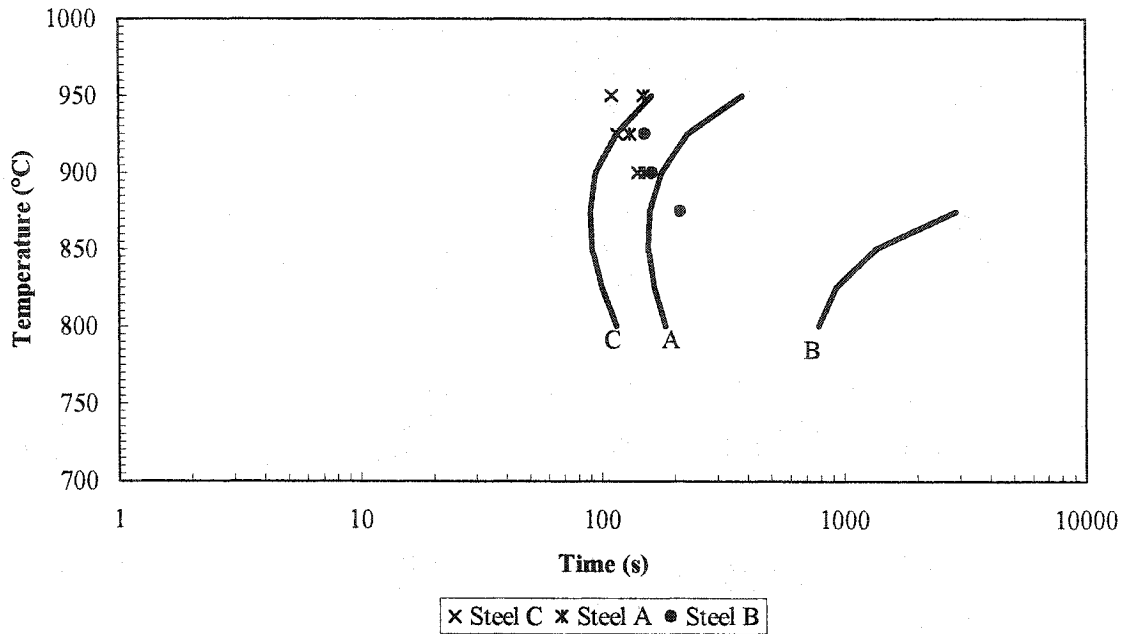


Figure (5-16) Comparison between experimental PTT data and the VC precipitation equation 5-21 for steels A, B and C.

Table 5-4 Precipitate start times for steels A, B and C; predicted and measured

Temperature °C	Predicted (sec)			Measured (sec)		
	A	B	C	A	B	C
950	381	-	161	145		110
925	227	115*	115	130	150	115
900	175	3.75*	94	150	160	140
875	157	2880	89		210	
850	155	1350	91			
825	164	926	99			
800	183	789	113			

* Hours

There are a number of differences between the model predictions and the measured data. It is apparent from Figure (5-16) that the kinetics of the steels used in this work were generally faster than those predicted, which is also mirrored by the observation that the C-curve noses were higher than predicted by approximately 100 °C. In addition, the convergence of the curves as the temperature decreased was much more extreme in the case of the actual results, and took place at a higher temperature. Even at higher temperatures, there was no real difference between the measured P_s values of the steels, except at 950 °C. The discrepancy between the predictions and the results was the highest for B. Steel B had an unconventionally high level of Si, which may have increased the VC precipitation rate [185-187]. On the other hand, the closest match with the model occurred in the case of steel C, where the V content was considered normal but the silicon content was high.

It is interesting to note that all these steels seemed to have similar kinetics. This suggests that the results could be significantly influenced by the very high C contents of these steels, suggesting that the Dutta-Sellars approach needs to be modified in some way for hypereutectoid microalloyed steels. However, experimental values generated by Medina et al. [186] for a low carbon V microalloyed steel (0.12 % C and 0.06 %wt V) were also compared to the modified Dutta-Sellars analysis Eq. 5-21. In this work [186], the recrystallized fraction was determined for temperatures between 1100 to 850 °C at a strain of 0.35 and a strain rate of 3.63 s⁻¹. Figure (5-17) again shows poor agreement between the calculated and measured data. This shows that there are significant differences between Nb and V precipitation characteristics, and more work is required to generate a viable V precipitation model. From the current results, it is therefore very difficult to ascertain whether or not there is an influence of Si on the precipitation rate of VC.

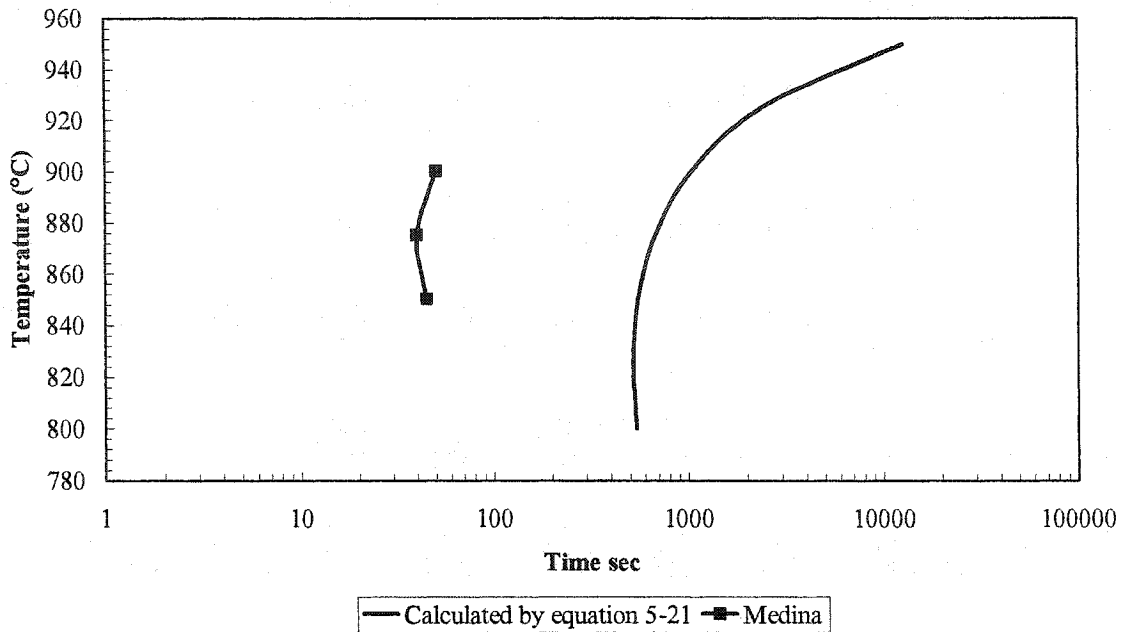


Figure (5-17) Comparison between the Dutta-Sellars model modified for VN precipitation in a low C steel, and the data of Medina et al. [186].

5.3. Metadynamic Recrystallization

The kinetics of metadynamic recrystallization are usually described by an Avrami equation Eq. 5-8, which incorporates an empirical time constant for 50% recrystallization, $t_{0.5}$.

As the data generated in this work were for a constant prior austenite grain size, a simplified expression of the following form was derived to describe the data:

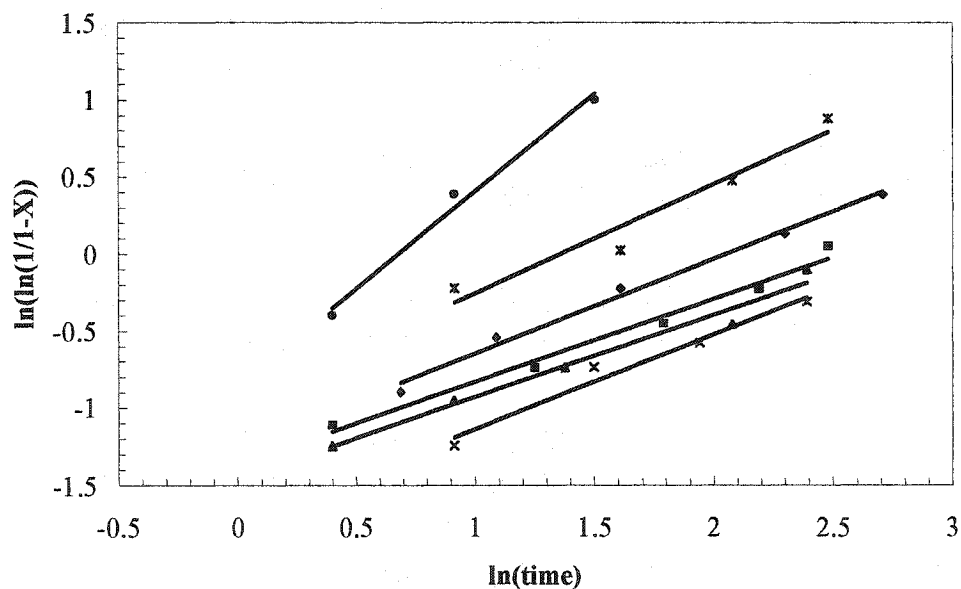
$$t_{0.5} = A_{MDRX} \dot{\epsilon}^p \exp \left[\frac{Q_{app}}{RT} \right] \dots\dots\dots 5-22$$

5.3.1. Determination of n

From equation 5-8, in order to determine n , the softening results were plotted as $\ln(\ln(1/X))$ vs. $\ln(\text{time})$ plots. The results are presented for different conditions of temperature and strain rate, as shown in Figure (5-18) for the three steels studied. In all cases, deformation was interrupted at the peak of dynamic recrystallization. The exponent n was determined for metadynamic recrystallization. The average value of n was found to be 1.2, which is within the range of values of 1-1.6 observed by other workers (Table 5-5) [9,162,188,189].

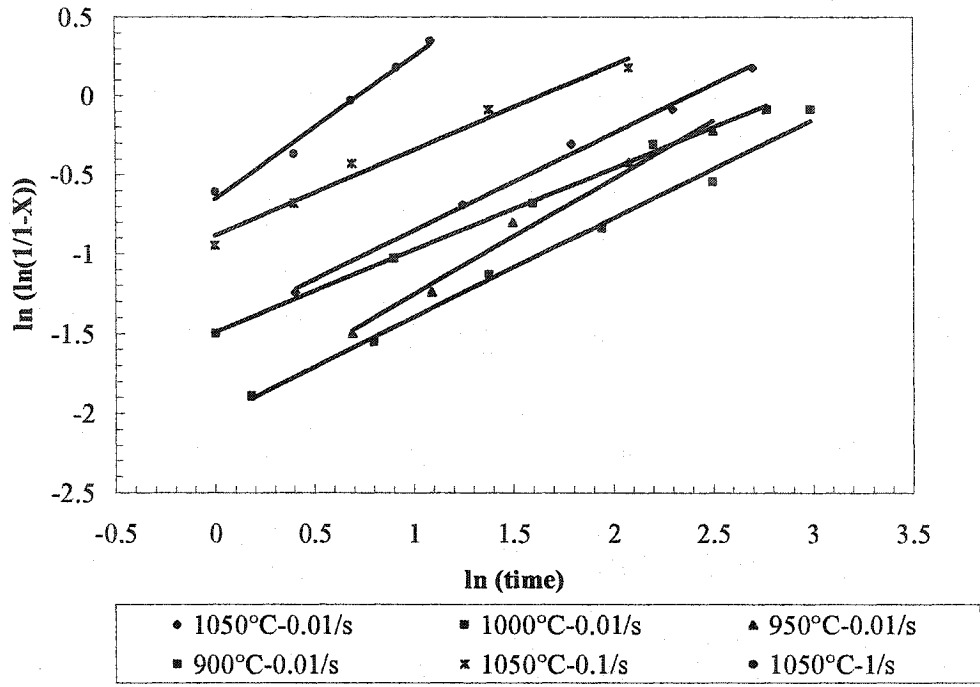
Table 5-5 Listing of exponent 'n' values for SRX and MDRX

	<i>Sellars</i> [9]	<i>Hodgson</i> [188,189]	<i>Petkovic</i> [190]	<i>Laasraoui</i> [169]	<i>Roucoules</i> [42]	<i>Present</i> work
MDRX	1	1.5	1.6	-	1	1.2
SRX	1-2	1	1.2-1.3	1	-	1

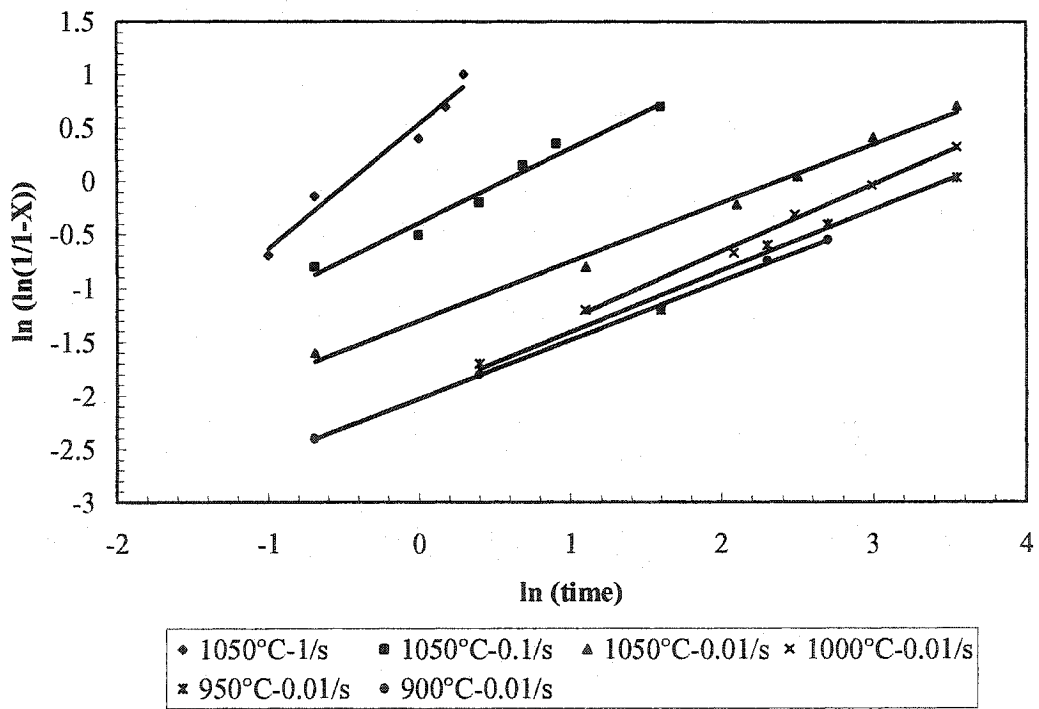


◆ 1050°C-0.01/s	■ 1000°C-0.01/s	▲ 950°C-0.01/s
× 900°C-0.01/s	× 1050°C-0.1	● 1050°C-1/s

(a)



(b)



(c)

Figure (5-18) Dependence of $\ln(\ln(1/(1-X)))$ on $\ln(\text{time})$ for steels A, B and C.

5.3.2. Determination of the Dependence of $t_{0.5}$ on the Deformation Parameters

5.3.2.1. Effect of Strain Rate

The strain rate exponent can be obtained from $\ln(t_{0.5}) - \ln(\text{strain rate})$ plots (Figure (5-19)). The average value of p is -0.6 , which is close to that of Roucoules et al. [49] for metadynamic recrystallization, and is somewhat lower than that observed by Hodgson et al. [192]. The strain rate dependence of metadynamic recrystallization is about twice as strong as for conventional static recrystallization, which is in good agreement with previous work [112,115,119,193].

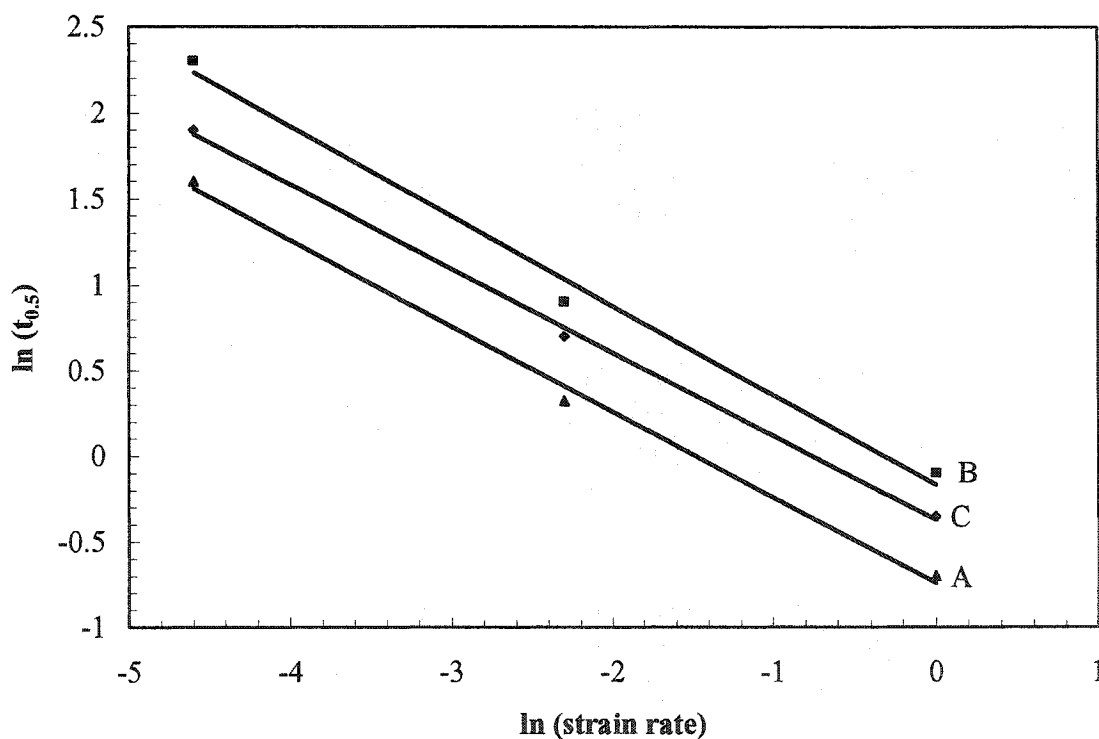


Figure (5-19) Effect of strain rate on the metadynamic $t_{0.5}$.

5.3.2.2. Activation Energy of Metadynamic Recrystallization

The activation energies were determined by using the following Arrhenius relationship:

$$\ln \left(\frac{t_{0.5}}{Z^{-0.6}} \right) = \ln (A) + \left(\frac{Q_{mdrx}}{R} \right) \left(\frac{1}{T} \right) \dots\dots\dots 5-23$$

$$Z = \dot{\epsilon} \exp \left(\frac{Q_{def}}{RT} \right) \dots\dots\dots 5-24$$

where $\dot{\epsilon}$ is the strain rate, T is the absolute temperature and R is the gas constant. Q_{def} is the activation energy derived from the steady state stress; it was found to be 350 kJ/mol for these microalloyed high carbon steels (see section 5.1.2) [194].

The parameter $\ln (t_{0.5}/Z^{-0.6})$ is plotted as a function of the inverse absolute temperature, in Figure (5-20). The activation energy for metadynamic recrystallization can be determined from the slopes and intercepts of these plots. A value of $Q_{mdrx} = 380$ kJ/mol was found for all three steels.

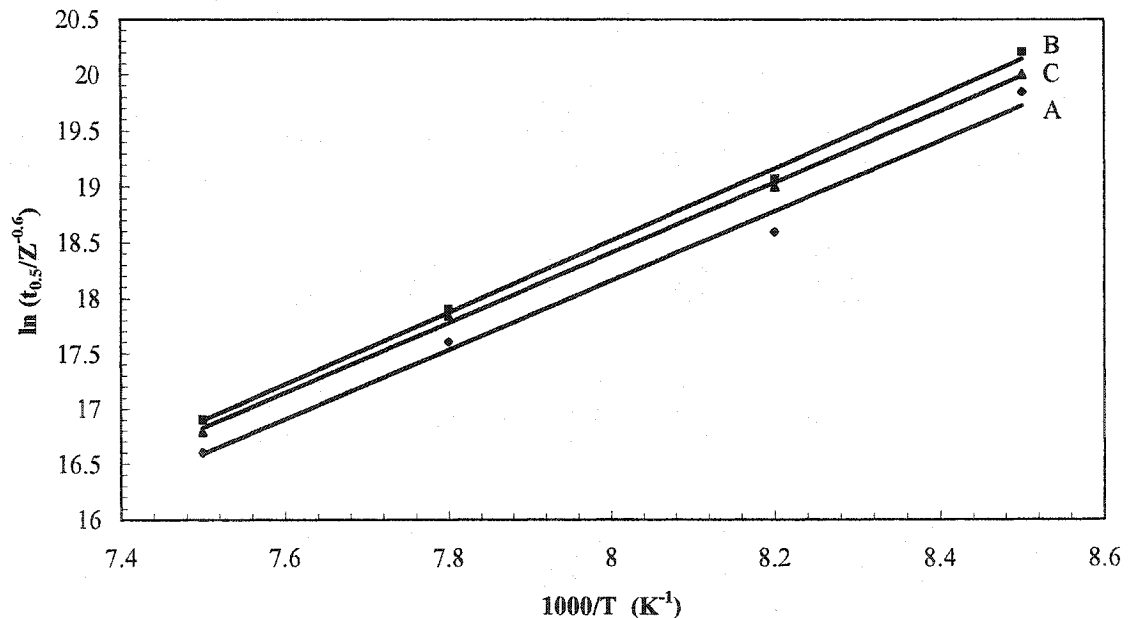


Figure (5-20) $\ln (t_{0.5}/Z^{-0.6})$ plotted as a function of the inverse absolute temperature.

The activation energy in equation 5-25 is an apparent energy, which is a function of the activation energy of metadynamic recrystallization and, through the Zener-Hollomon parameter, also a function of the activation energy of deformation [9].

$$Q_{app} = Q_{mdrx} - 0.6 Q_{def} \dots\dots\dots 5-25$$

A value for Q_{app} of 170 kJ/mole was determined and considerably lower than for conventional static recrystallization (270 or 300 kJ/mol), which is in good agreement with previous work [112,115,119,193].

The effect of Si and V can be included in the Avrami type model through A_{MDRX} , as shown in Figure (5-21), leading to the following linear equation:

$$A_{MDRX} = (1.5 ([Si]+[V]) + 2.8) \times 10^{-8} \dots\dots\dots 5-26$$

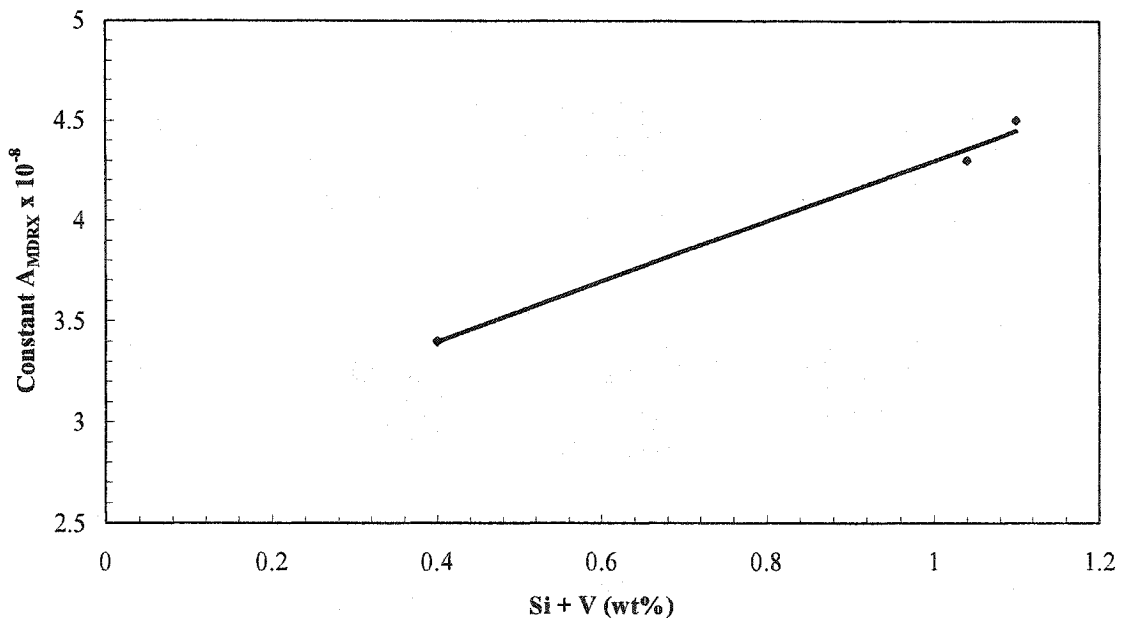


Figure (5-21) Effect of V and Si on the constant A_{MDRX} .

Thus, the $t_{0.5}$ can be expressed as follows:

$$t_{0.5} = (1.5 ([Si] + [V]) + 2.8) \times 10^{-8} Z^{-0.6} \exp \left(\frac{380 (kJ/mol)}{RT} \right) \dots\dots\dots 5-27$$

$$t_{0.5} = (1.5 ([Si] + [V]) + 2.8) \times 10^{-8} \dot{\epsilon}^{-0.6} \exp \left(\frac{170 (kJ/mol)}{RT} \right) \dots\dots\dots 5-28$$

A comparison between the predicted (with the effect of [Si +V] on A_{MDRX}) and measured values of $t_{0.5}$ for both the classical static and metadynamic cases [195,196] are made in Figure (5-22). This can be compared with Figure (5-23), in which A_{MDRX} has not been adjusted for V and Si for either static or dynamic recrystallization. As can be seen, the effect of Si and V is significant.

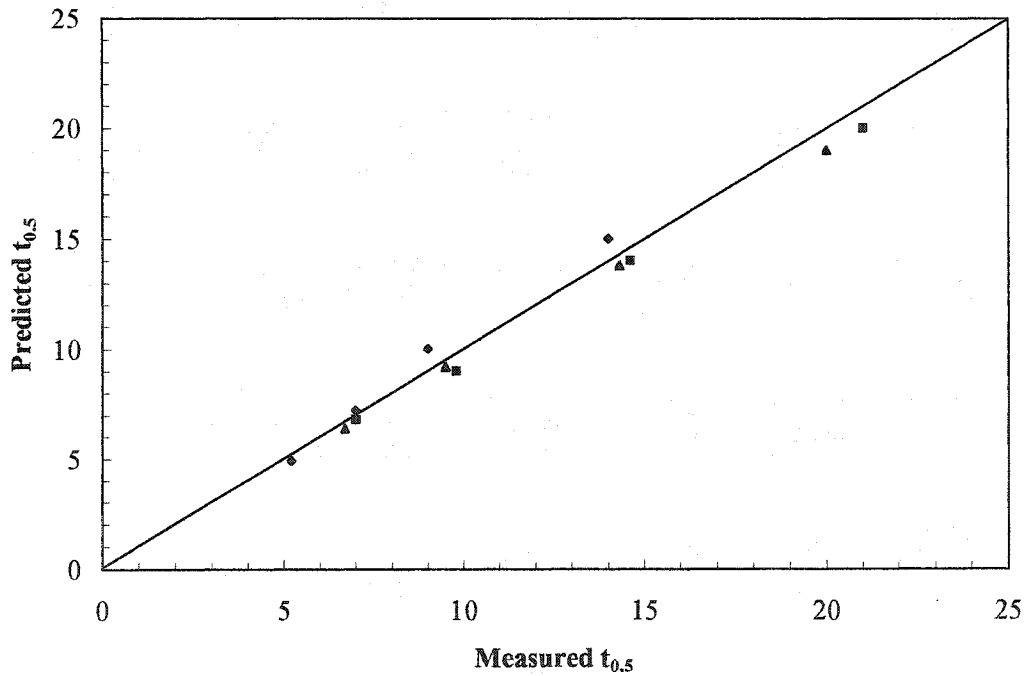


Figure (5-22) Comparison between measured $t_{0.5}$ and those predicted with the effect of [Si + V] included. (The line indicates a perfect correlation.)

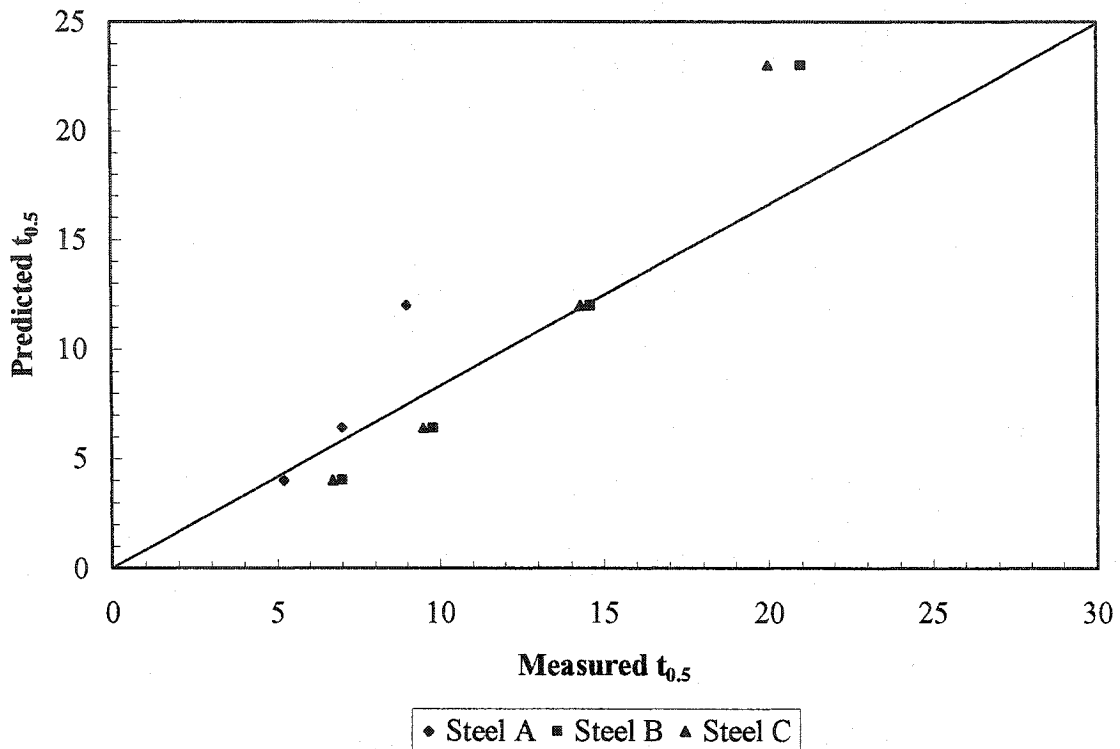


Figure (5-23) Comparison between measured $t_{0.5}$ and those predicted without the effect of [Si + V] showing poor agreement. (The line indicates a perfect correlation.)

It is generally accepted that the effect of the alloying and microalloying elements on retarding the onset of metadynamic recrystallization is related to the atomic size difference between γ -Fe and Mn, Si, V, Mo, Ti and Nb, which increases in the order listed. The effect of Mn could not be determined for these alloys, but it generally plays only a minor role in retarding recrystallization due to its similar atomic size and diffusion rate compared to iron.

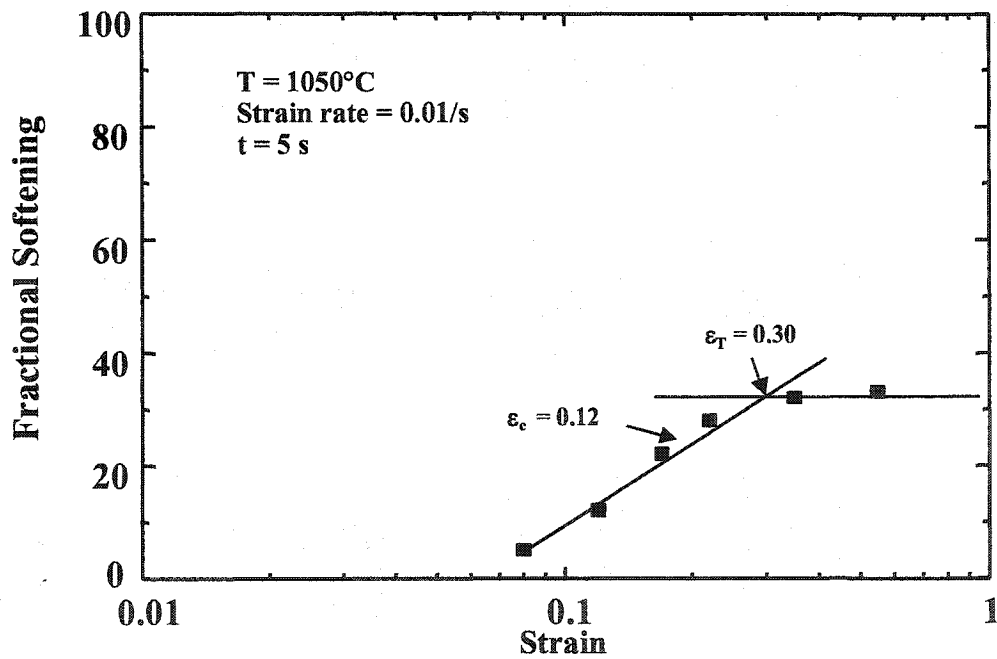
5.3.2.3. Effect of Strain on Softening Behavior

The effect of strain on fractional softening at different strain rates is shown in Figure (5-24) for steel A. As expected, the fractional softening increases up to a certain

strain, ϵ_T , the transition strain. The fractional softening plateau that occurs beyond ϵ_T is due to metadynamic recrystallization, which is independent of the applied strain. The key data from these graphs are summarized in **Table 5-6**. The values for the transition strain are approximately 1.5 higher than the peak strain, which is the same as that obtained by Bai et al. for two different Nb microalloyed steels [197].

Table 5-6 Values of parameters

<i>Strain rate</i> (s^{-1})	<i>Holding time</i> (s)	<i>Critical strain</i>	<i>Transition strain</i>	<i>Fractional softening</i> (%)
0.01	5	0.12	0.30	32
1	0.5	0.32	0.53	44



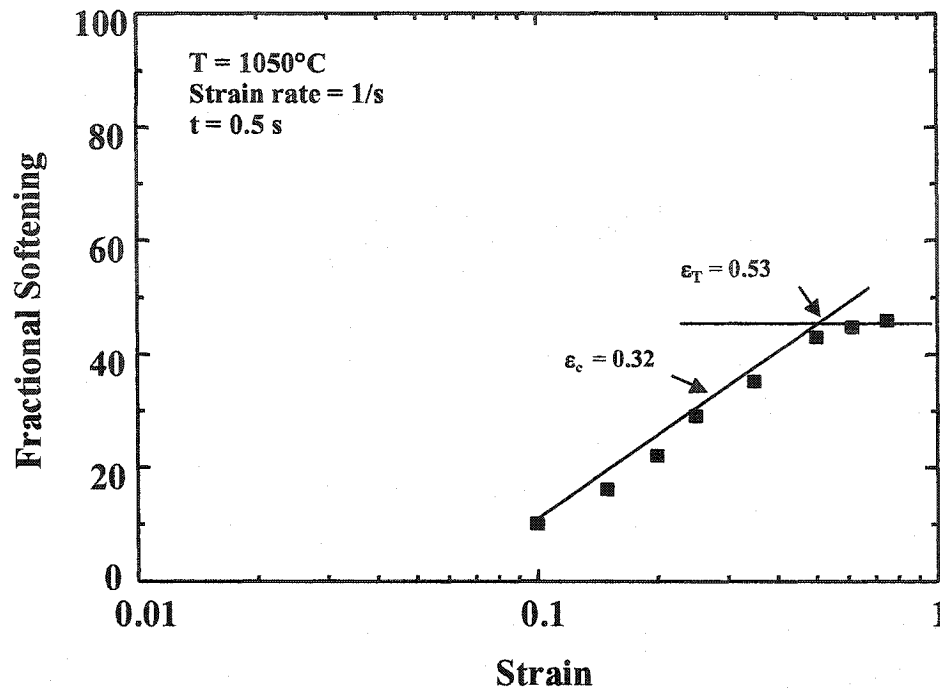


Figure (5-24) Effect of strain on softening for steel A.

5.3.3. Modeling of Static Softening

As indicated by Luton et al. [198], Bai et al. [197] and Uranga et al. [199], the effect of strain on static recrystallization can be modeled by considering the existence of the following three recrystallization regimes, (i) pure classical static, (ii) mixed classical and metadynamic and (iii) pure metadynamic recrystallization,. These three regions are schematically indicated in Figure (5-25), which indicates the static recrystallization mechanisms that correspond with the illustrated levels of applied strain.

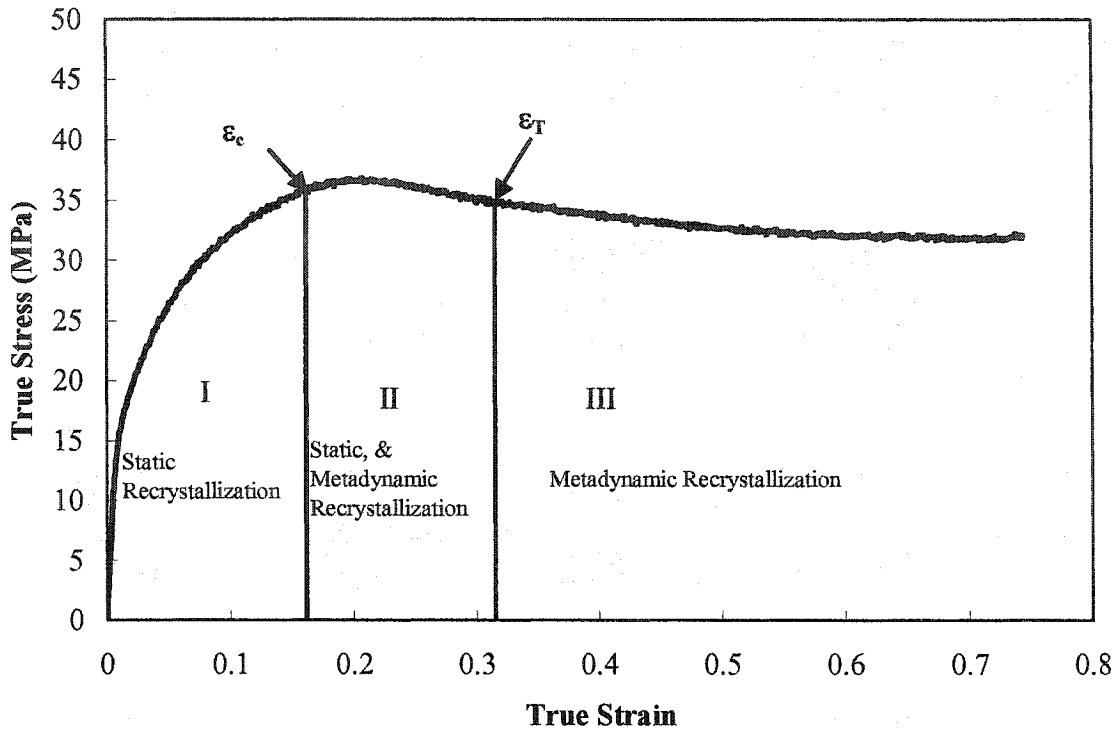


Figure (5-25) Effect of strain on static softening processes

To describe the softening behavior observed in each of these three regions, empirical equations can be fitted to the individual softening processes, and these can be used to model the static kinetics in each region. The empirical equations used to model the softening in the three different regions are indicated in the following:

5.3.3.1. Region I: $\varepsilon < \varepsilon_c$

In this region, recrystallization is due to classical static recrystallization. The equations for specifying $t_{0.5}$ and X in vanadium steels are Eq. 5-8 and Eq. 5-12.

5.3.3.2. Region III: $\varepsilon > \varepsilon_T$

This region is due to metadynamic recrystallization during the interpass intervals. The equations for specifying $t_{0.5}$ and X in vanadium steels are Eq. 5-8 and Eq. 5-28.

5.3.3.3. Region II: $\varepsilon_c < \varepsilon < \varepsilon_T$

In this region both static and metadynamic recrystallization take place. Thus, the total fractional softening due to the two processes can be given by the sum of the individual components [198].

$$X = X^{SRX} + X^{MDRX} \dots\dots\dots 5-29$$

When the static softening has gone to completion

$$X_F = X_F^{SRX} + X_F^{MDRX} = 1 \dots\dots\dots 5-30$$

where the subscript "F" refer to the final contribution of the corresponding mechanism to the completed recrystallization. The kinetics of recrystallization involving both the classical and metadynamic mechanisms can be evaluated using the corresponding Avrami equations:

$$X_{SRX} = X_F^{SRX} \left[1 - \exp \left(-0.693 \left(\frac{t}{t_{0.5 SRX}} \right)^n \right) \right] \dots\dots 5-31$$

$$X_{MDRX} = X_F^{MDRX} \left[1 - \exp \left(-0.693 \left(\frac{t}{t_{0.5 MDRX}} \right)^n \right) \right] 5-32$$

(When the applied strain is between the critical and transition strains, the strain used to calculate the amount of classical static recrystallization is taken to be the critical strain.)

Thus, for t approaching ∞ , the mechanisms approach their corresponding maximum values. A simple approximation for the contribution of metadynamic recrystallization to the transformation after an infinite length of time, X_F^{MDRX} , is:

$$X_{\infty}^{MDRX} = \frac{\varepsilon - \varepsilon_c}{\varepsilon_T - \varepsilon_c} \dots\dots\dots 5-33$$

when $\varepsilon \leq \varepsilon_c$, the contribution of metadynamic recrystallization is zero.

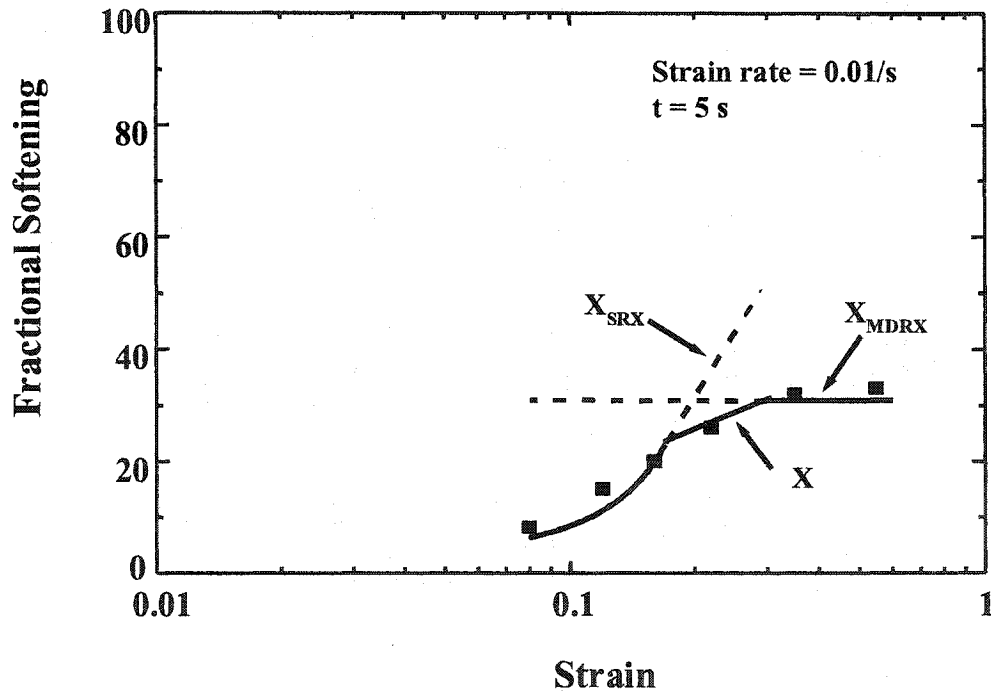
All the equations required to follow microstructural evolution during the hot rolling of high C steel are listed in **Table 5-7**.

Table 5-7. List of equations used to model the fraction recrystallized in the microalloyed hypereutectoid steels

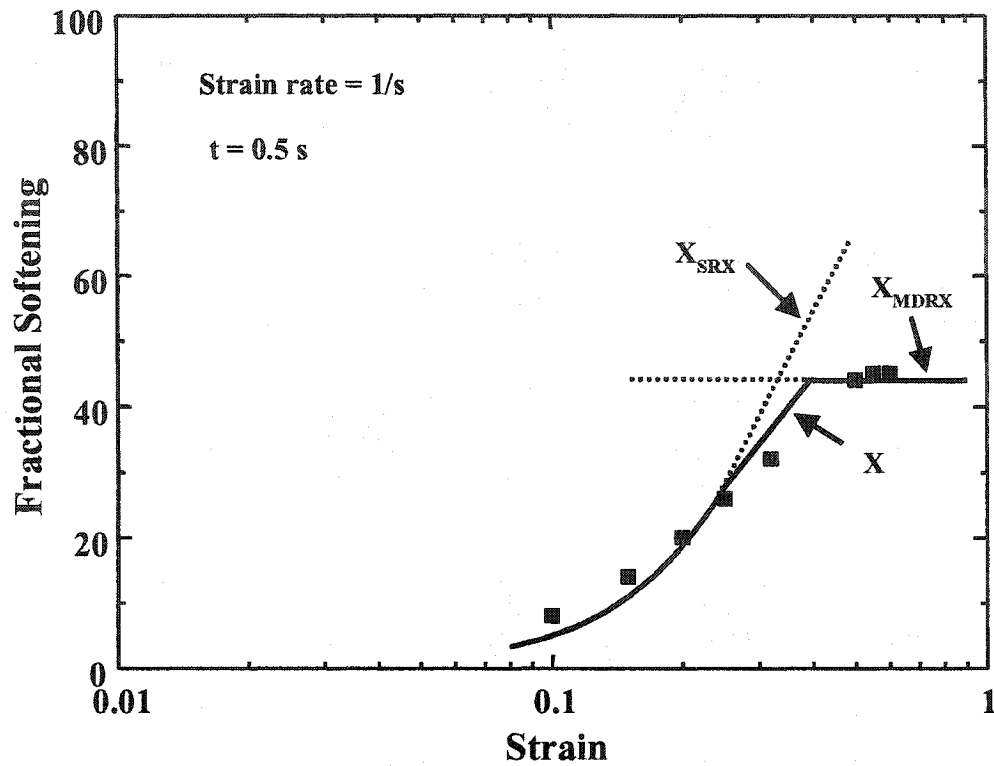
<i>Event</i>	<i>Equation</i>
Fractional softening by SRX and MDRX	$X = 1 - \exp \left[-0.693 \left(\frac{t}{t_{0.5}} \right)^n \right]$
Time for 50% recrystallization	$t_{0.5} = (1.5 ([Si] + [V]) + 2.8) \times 10^{-8} Z^{-0.6} \exp \left(\frac{380 (kJ/mol)}{RT} \right)$
Metadynamic recrystallization	$t_{0.5} = (1.5 ([Si] + [V]) + 2.8) \times 10^{-8} \dot{\epsilon}^{-0.6} \exp \left(\frac{170 (kJ/mol)}{RT} \right)$
Static recrystallization	$t_{0.5} = (0.4 ([V] + [Si]) + 5.4) \times 10^{-17} \epsilon^{-2} d_0^2 \dot{\epsilon}^{-0.4} \exp \left[\frac{300 \times 10^3}{RT} \right]$ $X_{SRX} = X_F^{SRX} \left[1 - \exp \left(-0.693 \left(\frac{t}{t_{0.5SRX}} \right)^n \right) \right]$ $X_{MDRX} = X_F^{MDRX} \left[1 - \exp \left(-0.693 \left(\frac{t}{t_{0.5MDRX}} \right)^n \right) \right]$ $X_F = X_F^{SRX} + X_F^{MDRX} = 1$ $X_{\infty}^{MDRX} = \frac{\epsilon - \epsilon_c}{\epsilon_T - \epsilon_c}$

5.3.3.4. Comparison of the Empirical Restoration Kinetics with Experimental Data for Steel A

The results are presented as plots of fractional softening vs. strain for a constant static recrystallization time period, as shown in Figure (5-26). The solid line is the prediction based on the empirical constants determined above. The individual data points are the softening measurements obtained from mechanical technique. There is very good agreement between the prediction and the experimental data of softening generated for these steels from all of the tests described above.



(a)



(b)

Figure (5-26) Modeling of post-dynamic softening in the three ranges of deformation.

The model was also used to describe the time for 50% softening, $t_{0.5}$, for strain rates of 0.01 and 1 s^{-1} with $D_0 = 94 \text{ }\mu\text{m}$. When the strain rate was increased from 0.01 s^{-1} to 1 s^{-1} , $t_{0.5}$ decreased from 15 s to 0.8 s, and 3 s to 0.3 s for static and metadynamic recrystallization, respectively. The $t_{0.5}$ values for critical strains (i.e. the strain at which dynamic recrystallization begins) for the strain rates of 0.01 s^{-1} and 1 s^{-1} are 0.13 and 0.3. There is a transition region between the critical strain and transition strain where both static and metadynamic recrystallization softening co-exist during the inter-pass time. Figure (5-27) clearly shows the three distinct regions experimentally, which is well fitted by this analysis.

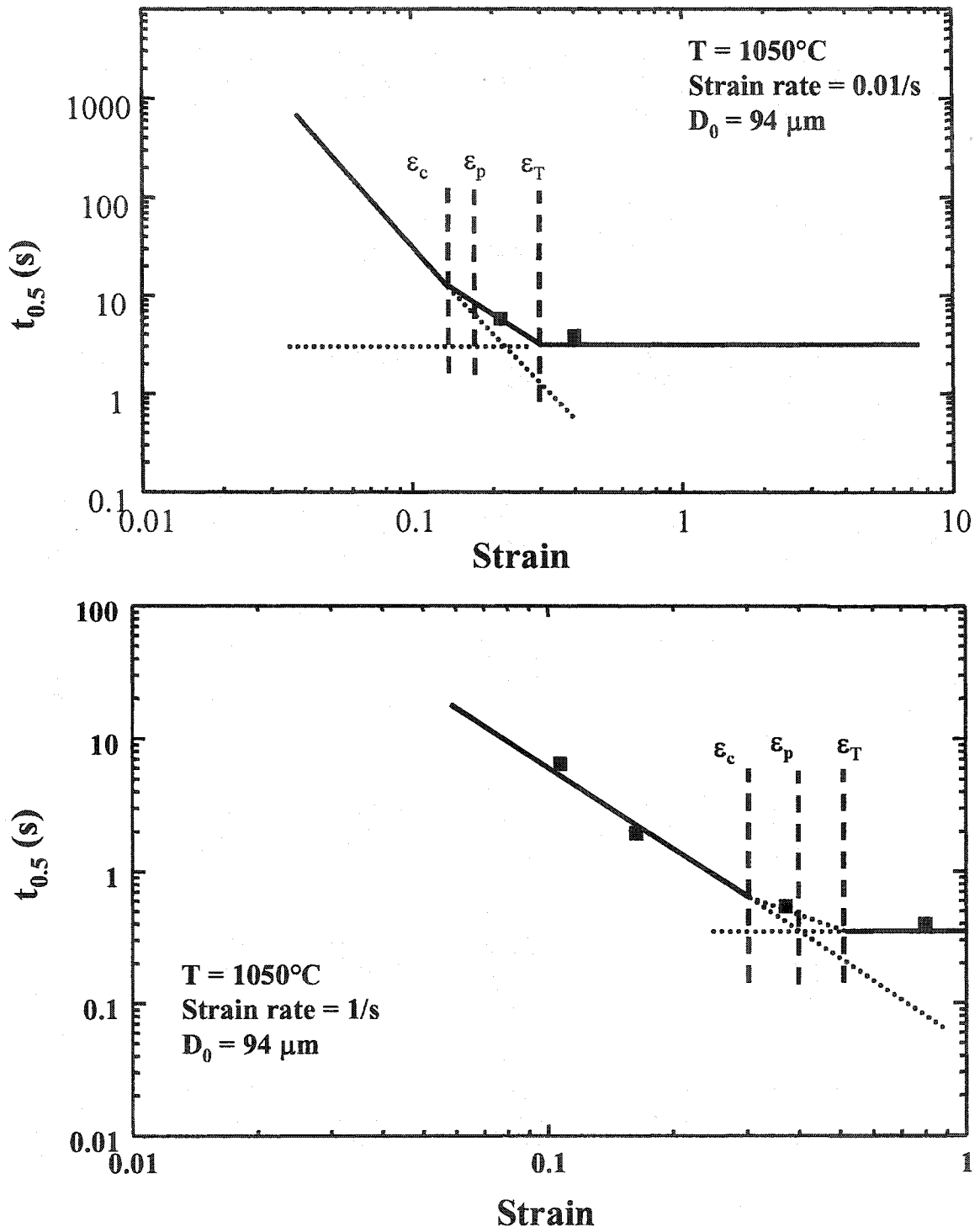


Figure (5-27) Comparison between model and experimental results.

5.4. Hypereutectoid Steel

5.4.1. Modeling the Effect of Deformation Conditions on the Kinetics of Metadynamic and Static Recrystallization

For a given initial grain size, the kinetics of static and metadynamic recrystallization can be described by the following Avrami type equation

Metadynamic:

$$t_{0.5} = A_{MDRX} \dot{\epsilon}^p \exp \left[\frac{Q_{app}}{RT} \right]$$

Static:

$$t_{0.5} = A_{srx} \epsilon^r d_o^q \dot{\epsilon}^s \exp \left[\frac{Q_{rex}}{RT} \right]$$

5.4.1.1 Determination of n

To determine n, the softening results were plotted as $\ln(\ln(1/(1-X)))$ vs. \ln time. The results are presented for different conditions of temperature, strain and strain rate, in Figures ((5-28) and (5-29)). Values of n for static and metadynamic recrystallization were found to be 1.3 and 1.2, respectively. These are similar to the values reported by Sellars [162] and Roucoules et al. [200] for metadynamic recrystallization and Hodgson et al [113], and Laasreaoui and Jonas [163] for static recrystallization. For metadynamic and static recrystallization, n has been reported to increase with decreasing temperature [201, 202]. As well, n has also been found to decrease from 2 to 1 when the grain size was increased from 140 to 530 μm [163, 203]. Furthermore, values of n close to 1 have also been reported for smaller grain sizes [123, 202]. Sellars suggested that such variations in n could be due to differences in the grain size distribution [162].

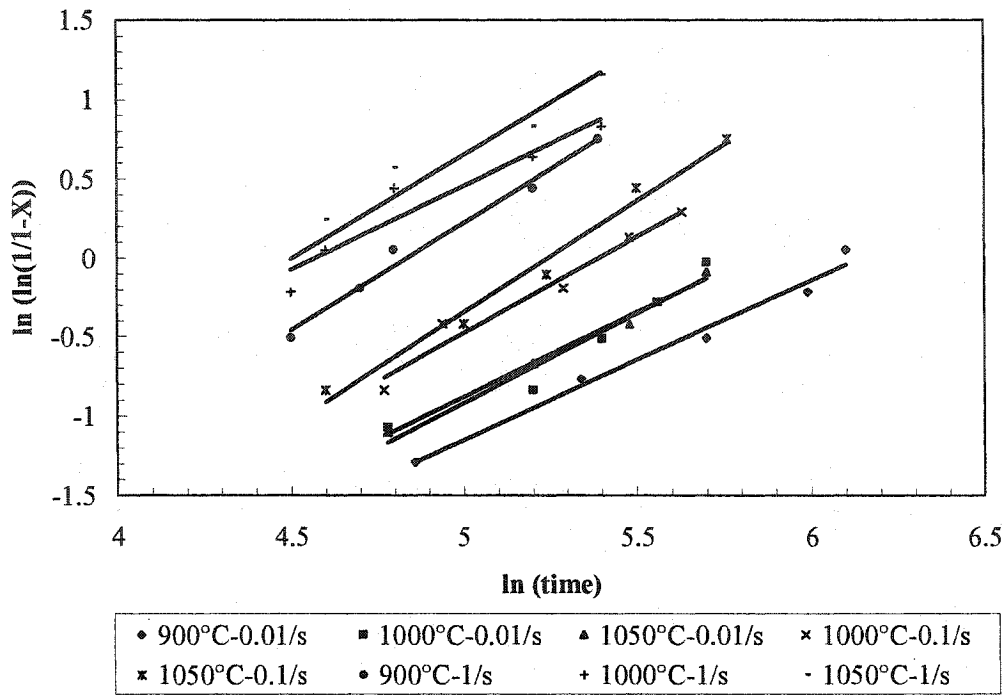


Figure (5-28) Dependence of $\ln(\ln(1/(1-X)))$ on $\ln(\text{time})$ metadynamic recrystallization.

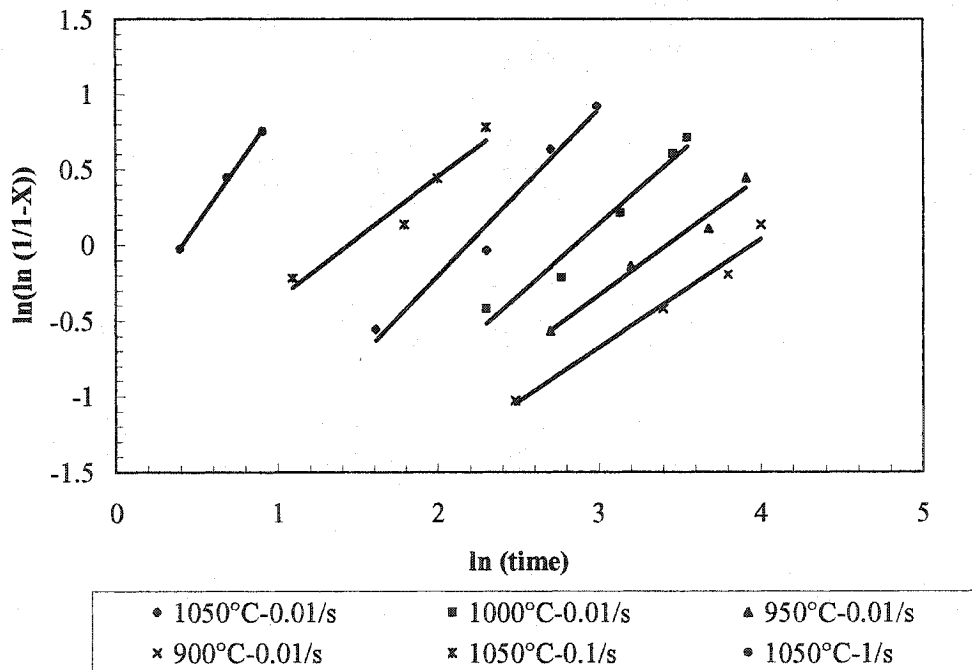


Figure (5-29) Dependence of $\ln(\ln(1/(1-X)))$ on $\ln(\text{time})$ static recrystallization.

5.4.1.2. Effect of Strain Rate

The effect of strain rate on $t_{0.5}$ was determined at constant temperature and strain; under these conditions, $t_{0.5}$ was found to have a power law dependence on strain rate:

$$t_{0.5} \propto \dot{\epsilon}^p$$

Figure (5-30) shows experimental results for the dependence of the time for 50% recrystallization, $t_{0.5}$, on strain rate. Metadynamic recrystallization displays a strain rate dependence about twice as strong as that of static recrystallization. The exponent, p , for static and metadynamic recrystallization was found to be -0.34 and -0.61 , respectively. The present values are similar to those reported by Hodgson and Gibbs [113] and Roucoules et al. [201] for metadynamic recrystallization. The static recrystallization value was in good agreement with values of -0.28 to -0.4 [123,163,202] observed by other workers. The higher values of p for metadynamic recrystallization can be attributed to the finer dynamically recrystallized grains achieved during the higher strain rate deformation, which increases the rate of metadynamic recrystallization. As the peak strain and stored energy are increased with increasing strain rate, the driving force for metadynamic recrystallization is further increased.

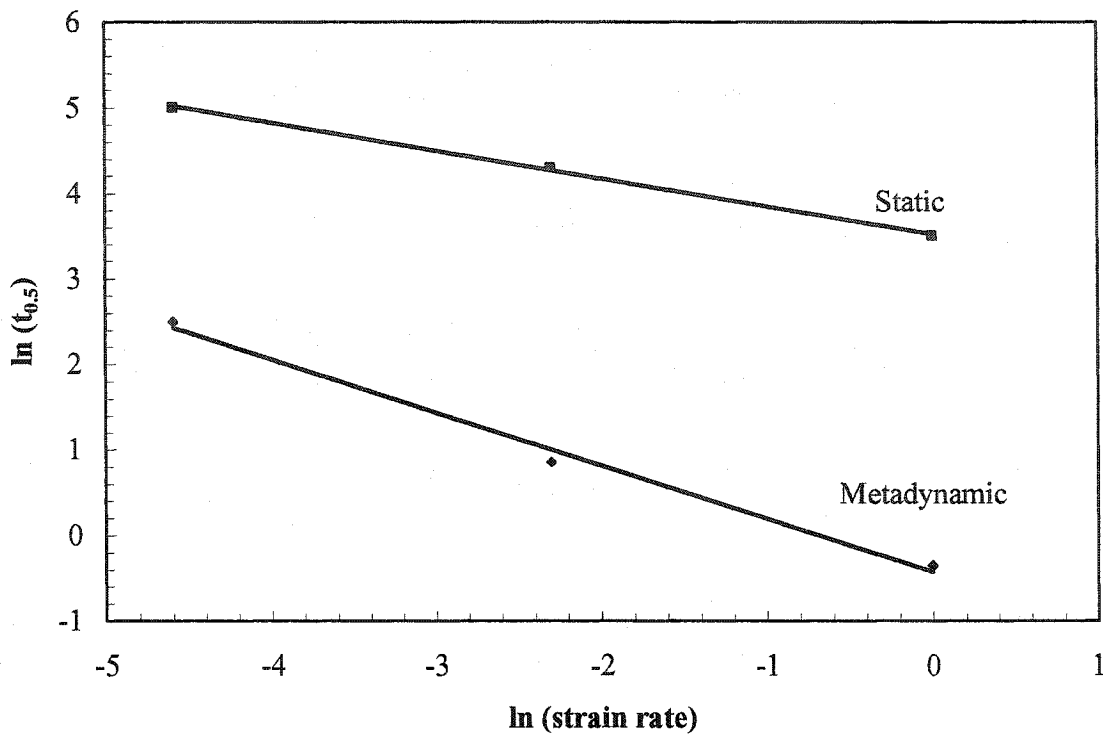


Figure (5-30) Effect of strain rate on the static and metadynamic recrystallization $t_{0.5}$.

5.4.1.3. Effect of Strain

In the case of static recrystallization, the strain stored in the material represents the main driving force for recrystallization and the strain exponent is therefore negative. The effect of strain on $t_{0.5}$ was estimated at constant temperature and strain rate. Under these conditions, $t_{0.5}$ was found to have a power dependence on strain, as shown in Figure (5-31).

$$t_{0.5} \propto \epsilon^r$$

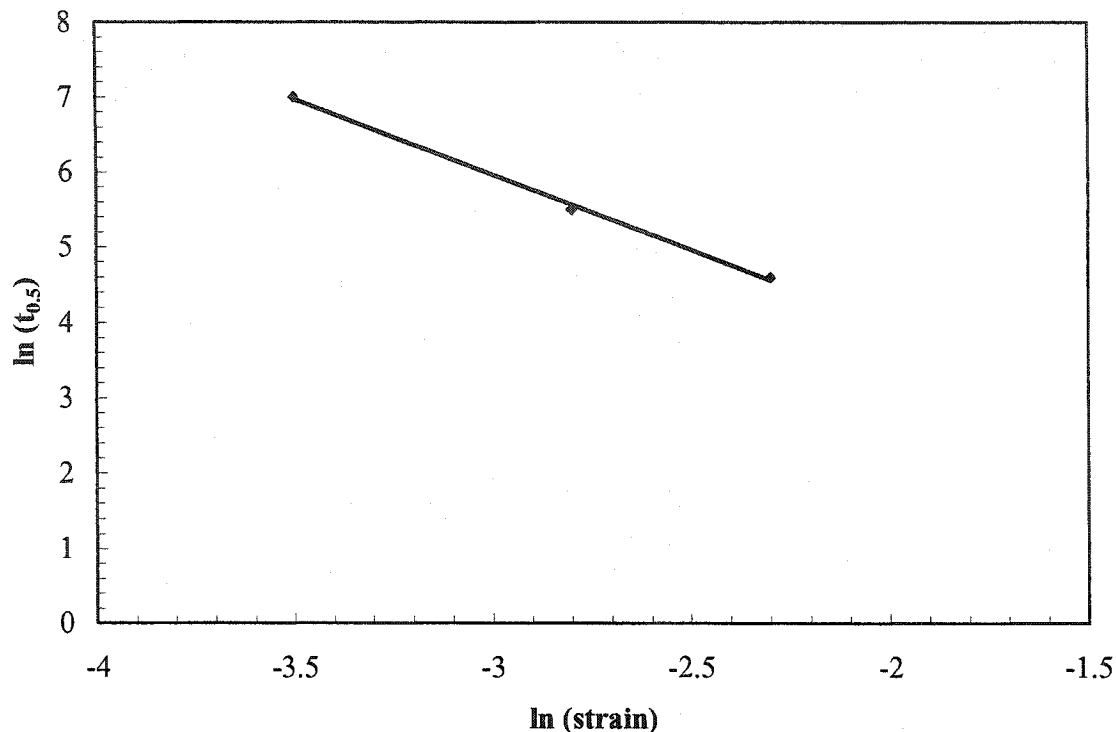


Figure (5-31) Effect of strain on the static recrystallization $t_{0.5}$.

A strain exponent of 2 was found and is in agreement with values 2 to 4 observed by other workers [113,153,161,204-206].

The absence of a strain effect on the kinetics of metadynamic recrystallization is in agreement with previous work as noted earlier.

5.4.1.4. Activation Energy of Deformation

To determine the activation energy for metadynamic recrystallization, the parameter $\ln(t_{0.5}/Z^{-0.61})$ was plotted as a function of the inverse absolute temperature, as shown in Figure (5-32). The activation energy for metadynamic recrystallization can be

determined from the slope and intercept of this plot. A value of $Q_{\text{mdrx}} = 330$ kJ/mol was found for the C-Mn steel used in this work. The activation energy in equation 5-25 is an apparent energy, which is a function of the activation energy of metadynamic recrystallization and, through the Zener-Hollomon parameter, also a function of the activation energy of deformation [9].

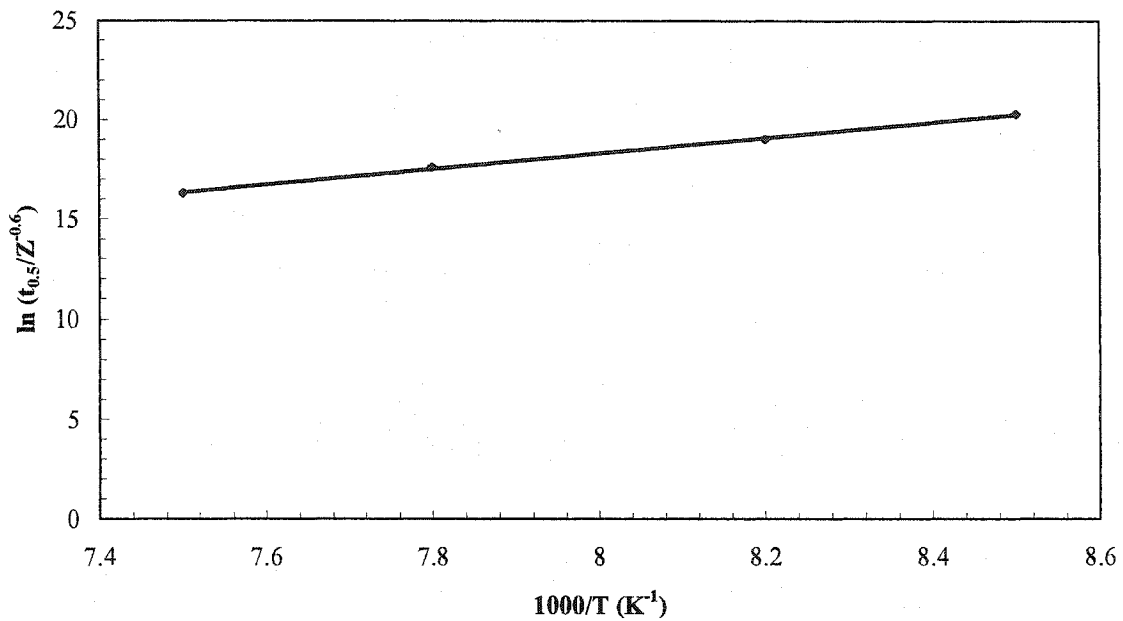


Figure (5-32) $\ln(t_{0.5}/Z^{0.61})$ plotted as a function of the inverse absolute temperature.

The activation energy for deformation and the apparent activation energy, Q_{def} and Q_{app} , were found to be 300 and 146 kJ/mole, respectively. The effect of temperature on metadynamic recrystallization is usually observed to be quite weak. For example, Hodgson et al [112] report values of $Q_{\text{mdrx}} = 230$ kJ/mole, $Q_{\text{def}} = 300$ kJ/mole, and $p = 0.8$ for plain C grades, which result in an apparent activation energy of -10 kJ/mole. In this present work, the activation energy is higher than the activation energy reported by Hodgson et al. [112]. The reason for that is not yet clear.

The activation energy for static recrystallization was determined from the following Arrhenius relationship:

$$\ln t_{0.5} = \ln A + \left(\frac{Q_{\text{rex}}}{R} \right) \left(\frac{1}{T} \right) \dots\dots\dots 5-34$$

The parameter $\ln(t_{0.5})$ was plotted as a function of the inverse absolute temperature, as shown in Figure (5-33). The value of Q_{rex} was determined to be 270 kJ/mole. Usually, the activation energy for static recrystallization is considerably higher than for metadynamic recrystallization [191]. These activation energies indicate that decreasing the temperature retards static recrystallization much more than it affects metadynamic recrystallization.

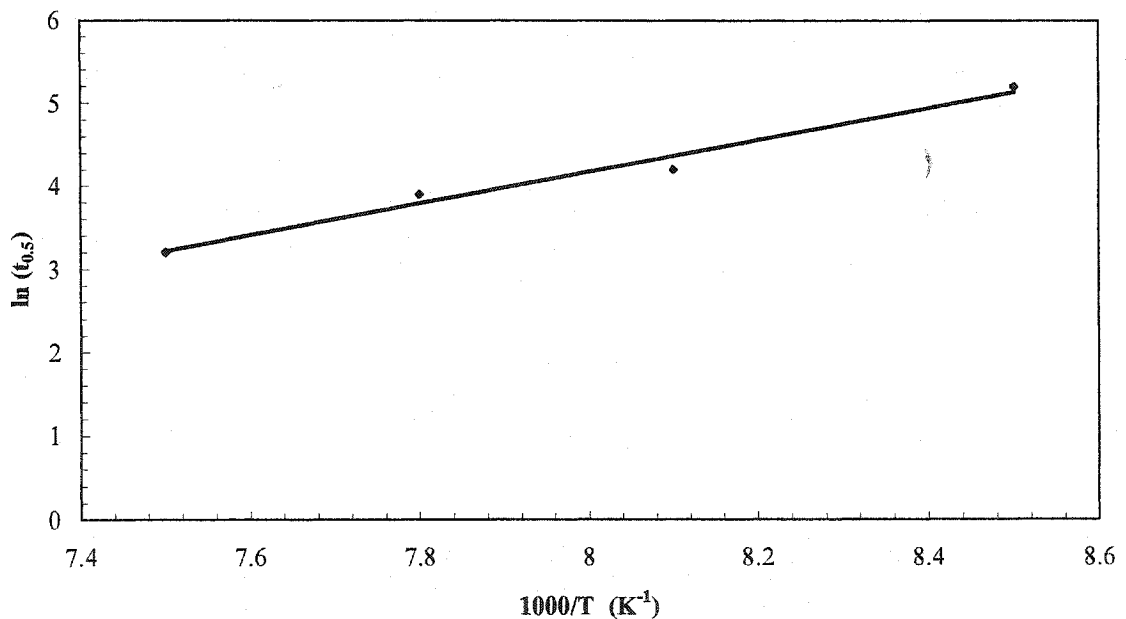


Figure (5-33) $\ln(t_{0.5})$ plotted as function of the inverse absolute temperature.

All the equations required to follow microstructural evolution during the hot rolling of high C steel are listed in **Table 5-8**.

Table 5-8. List of equations used to model the fraction recrystallized in the hypereutectoid steel

<i>Event</i>	<i>Equation</i>
Fractional softening by metadynamic and static recrystallization	$X = 1 - \exp \left[-0.693 \left[\frac{t}{t_{0.5}} \right]^n \right]$
Time for 50% recrystallization	
Metadynamic recrystallization	$t_{0.5} = 1.5 \times 10^{-6} Z^{-0.61} \exp \left(\frac{330000}{RT} \right)$
	$t_{0.5} = 1.5 \times 10^{-6} \dot{\epsilon}^{-0.61} \exp \left(\frac{146000}{RT} \right)$
Static recrystallization	$t_{0.5} = 4.2 \times 10^{-16} \epsilon^{-2} d_o^2 \dot{\epsilon}^{-0.34} \exp \left(\frac{270000}{RT} \right)$

5.4.2. Effect of Carbon Content on Static Restoration

These results can be compared with those of Xu et al. [206], as shown in Figure (5-34), who conducted compression and tension studies on plain carbon steels with carbon contents ranging from 0.054 to 0.84 wt% at a temperature of 860°C, a strain rate of $2 \times 10^{-3} \text{ s}^{-1}$ and initial grain size 16.5 μm . The metadynamic softening curve consists of an almost instantaneous degree of softening due to growth of the dynamically recrystallized nuclei, followed by an incubation period leading to classical static recrystallization. This is then interrupted by grain growth, which presumably reduces the

driving force for recrystallization for some period. Thereafter, static recrystallization resumes, but not to completion.

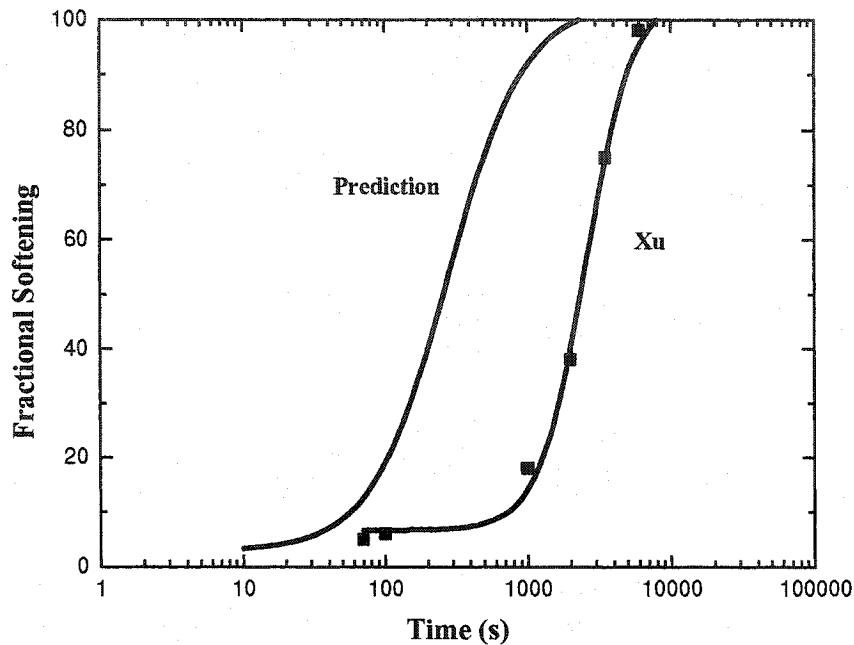


Figure (5-34) Comparison between the model for static recrystallization and the data of Xu et al. for high carbon steel [206].

Xu et al. also show that the static and metadynamic softening rates increase with rising carbon content. This is explained through an increase in the diffusivity of vacancies due to the addition of carbon to austenite, which will promote the static restoration mechanisms. The time for 50% metadynamic recrystallization is in the range of 400-500s for the 0.84% C steel compared to 800 to 1000s for the 0.054 % C steel. Using the equations for metadynamic recrystallization listed in **Table 5-8**, the time for 50% metadynamic recrystallization under the test conditions of Xu et al. is 350s, which compares favourably with their result for the higher C steel.

From Xu et al.'s work, the time for 50% static recrystallization is again faster for the higher C steel, being in the range of 2000-3000s for the 0.84% C material compared

to 4000 to 5000s for the 0.054 C steel. This compares rather unfavourably with the prediction of 260 second using the equation for static recrystallization listed in Table 5-8. In Table 5-9 are listed other equations available in the literature for the time for 50% recrystallization in C-Mn steels, and the predicted times for 50% static recrystallization. There are noticeable differences between the predictions of the models under many conditions. It can be seen that the equations by Choquet et al [202], Senuma and Yada [160, 207] and Ruibal et al. [208] appear to be closest to the current work. None of these predictions is at all close to the kinetics measured by Xu et al. It is not clear why such a large discrepancy exists.

Table 5-9 Prediction equations for static recrystallization of C-Mn steels

Ref.	Equation	$t_{0.5}$ (s)
9	$t_{0.5} = 2.5 \times 10^{-19} d_0^2 \varepsilon^{-4} \exp\left(\frac{300000}{RT}\right)$	46
139	$t_{0.5} = 5.1 \times 10^{-21} d_0^2 \varepsilon^{-4} \exp\left(\frac{330000}{RT}\right)$	22
202	$t_{0.5} = 6.1 \times 10^{-13} d_0^{-0.14} \varepsilon^{-0.95 d_0^{0.22}} \dot{\varepsilon}^{-0.28} \exp\left(\frac{270000}{RT}\right)$	378
160	$t_{0.5} = 2.86 \times 10^{-8} S_v^{-0.5} \varepsilon^{-2} \dot{\varepsilon}^{-0.2} \exp\left(\frac{150000}{RT}\right)$	134
207	$t_{0.5} = 2.2 \times 10^{-12} S_v^{-0.5} \varepsilon^{-2} \dot{\varepsilon}^{-0.2} \exp\left(\frac{250000}{RT}\right)$ $S_v = \frac{24}{\pi d_0} (0.491 \exp(\varepsilon) + 0.155 \exp(-\varepsilon) + 0.1433 (\exp(-3 \varepsilon)))$	421
208	$t_{0.5} = 2.3 \times 10^{-15} d_0^2 \varepsilon^{-4} Z^{-0.18} \exp\left(\frac{274000}{RT}\right)$ $Z = \dot{\varepsilon} \exp\left(\frac{315000}{RT}\right)$	198

5.5. Microstructures

Observation of the pearlitic microstructure of steel E by heat treatment and hot deformation confirmed that a grain boundary cementite network existed at all the isothermal transformation temperatures studied. The grain boundary cementite plates became thinner as the transformation temperature was lowered. Such grain boundary cementite networks in steels A, B and C were not resolvable by optical microscopy. Instead of a continuous cementite network, the carbide layer was obtained by FE-SEM to be discontinuous with the carbide particles along the grain boundaries.

For hypereutectoid steels the occurrence of a continuous grain boundary cementite network introduces considerable difficulty for cold forming operations, such as drawing, since the brittle cementite layer provides an easy crack path for fracture. The ability to restrict the grain boundary cementite network from linking through V microalloying has been attributed to an increase in the driving force for carbide nucleation in the presence of V that leads to additional carbide nuclei at austenite grain boundaries [139,209-212]. Moreover, Han et al. [213] have observed the presence of vanadium carbides, in small quantities, at the prior-austenite grain boundaries, with the majority of the particulates being precipitated in the grain boundary ferrite. This occurrence of VC precipitation has then been suggested by Han et al. [213] to have a twofold effect on grain boundary cementite formation. An effect of the VC formation on the austenite grain boundary is the local depletion of carbon that reduces its diffusion along the boundary to the cementite particles, thereby inhibiting their rapid growth into the boundary [210]. An offset of the carbon being coupled into precipitation is a concomitant promotion of ferrite nucleation and growth, which aids further in inhibiting the continuance of grain boundary cementite.

The findings of our work also suggest a compositional influence of Si on the effectiveness of V microalloy additions to refine the structural characteristics of hypereutectoid steels. Specifically, it was observed that a high content of Si (0.99%)

provided a slight decrease in the prior-austenite grain size even at a low V level (0.078%), as illustrated by the finer grain size of steel B as compared to A in Figure (4-3). In the work of Han [185] and Wada et al. [107], the addition of Si was determined to decrease the solubility of the VC particles in both the austenite and ferrite by raising the carbon activity. This suggests that in the presence of Si, VC formation is promoted in the austenite and ferrite phases [140]. In addition, the lower VC solubility in the presence of Si suggests that precipitation can occur at higher austenitizing temperatures. This would promote austenite grain size refinement as observed in the present work with the V microalloyed steels having different Si contents.

5.5.1. Heat treatment Effect on Nodule Size

To examine the influence of thermal processing on pearlite nodule characteristics, the size of the nodules was plotted as a function of the reheat temperature, as shown in Figure (5-35) for the various hypereutectoid steels (A, B, C and E) at a specific transformation temperature of 620°C. By comparing the behaviors of steels A and E, it can be observed that, under a given transformation condition, the addition of V enables a reduction in the nodule size for a particular reheat temperature. Further reductions in the pearlite nodule size were observed with increasing Si and V contents, as shown in Figure (5-35) for steels B and C, respectively. The progressive decrease observed for the nodule size with decreasing reheat temperature and increasing V and/or Si additions may be inherently related to the effects of these materials and processing parameters on the prior-austenite grain size. In particular, the austenitizing temperature determines the size of the prior-austenite grains, whose boundaries in turn provide nucleation sites for the pearlite nodules. Hull et al. [214,215] have reported that the nucleation rate of pearlite, hence nodule diameter, is very sensitive to the variation in prior-austenite grain size. Therefore, for a specific transformation temperature, which dictates the number of nucleation sites for pearlite formation, the nodule size should be directly related to the prior-austenite grain size, the interdependence of which is plotted in Figure (5-36).

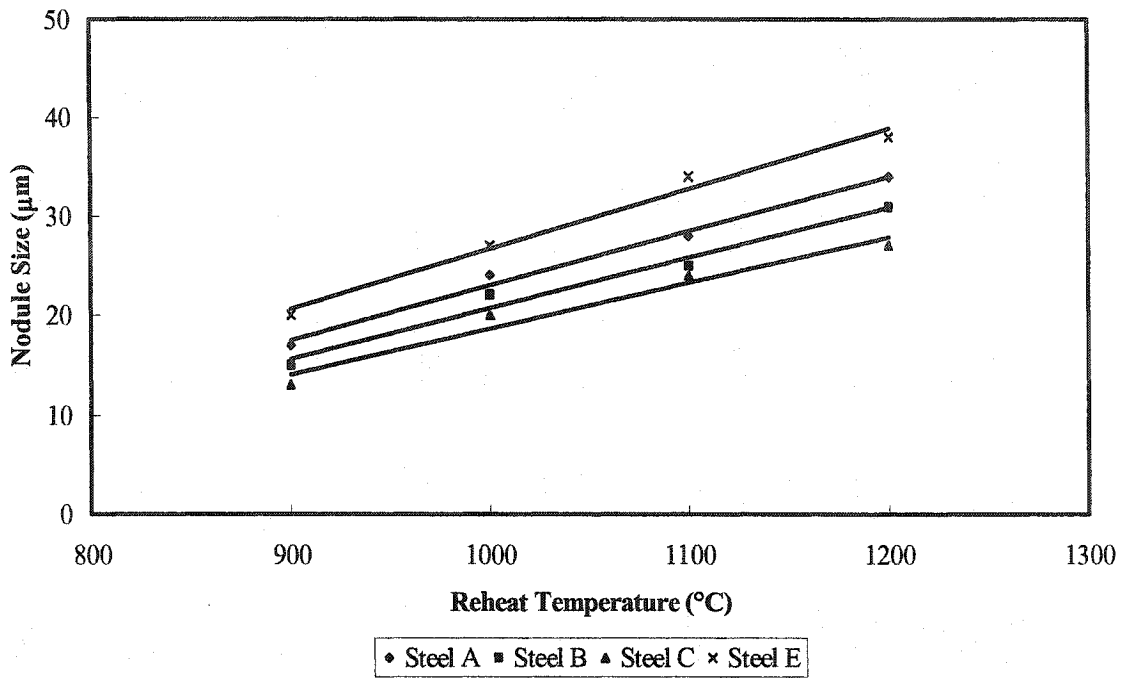


Figure (5-35) Effect of reheat temperature on the nodule size for hypereutectoid steels A, B, C and E processed at a transformation temperature of 620°C.

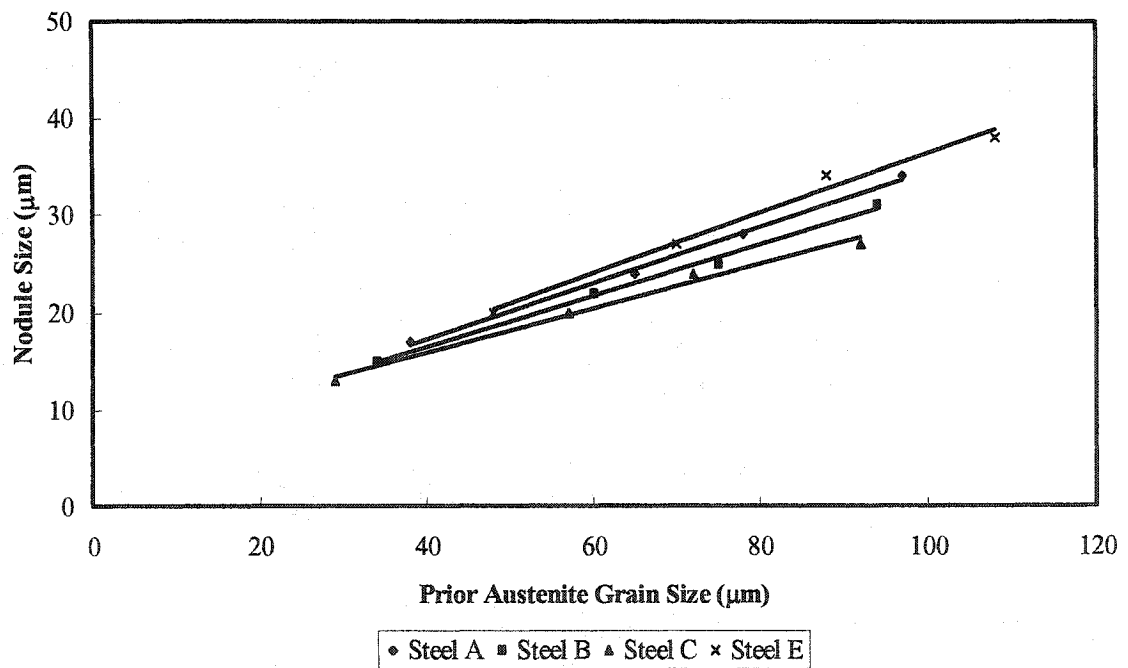


Figure (5-36) Effect of prior-austenite grain size on the nodule size for the hypereutectoid steels A, B, C and E processed at a transformation temperature of 620°C.

It is then not surprising that in the plots of nodule size as a function of the transformation temperature, as illustrated in Figures (5-37 and 5-38) for steels E and A, respectively, four independent curves were assembled according to the prior-austenite grain size. Between 550°C and 620°C, a linear relationship between nodule size and transformation temperature was observed for all the hypereutectoid steels reheated to temperatures between 900 to 1200°C. This dependence of the nodule size on the transformation conditions is mostly likely linked to the increase in the prior-austenite grain size with increasing transformation temperature, as shown in Figures (4-36 and 4-37), as Marder and Bramfitt [62,63] have shown through cinephotomicrography using a hot-stage that nodules nucleate only at austenite grain boundaries.

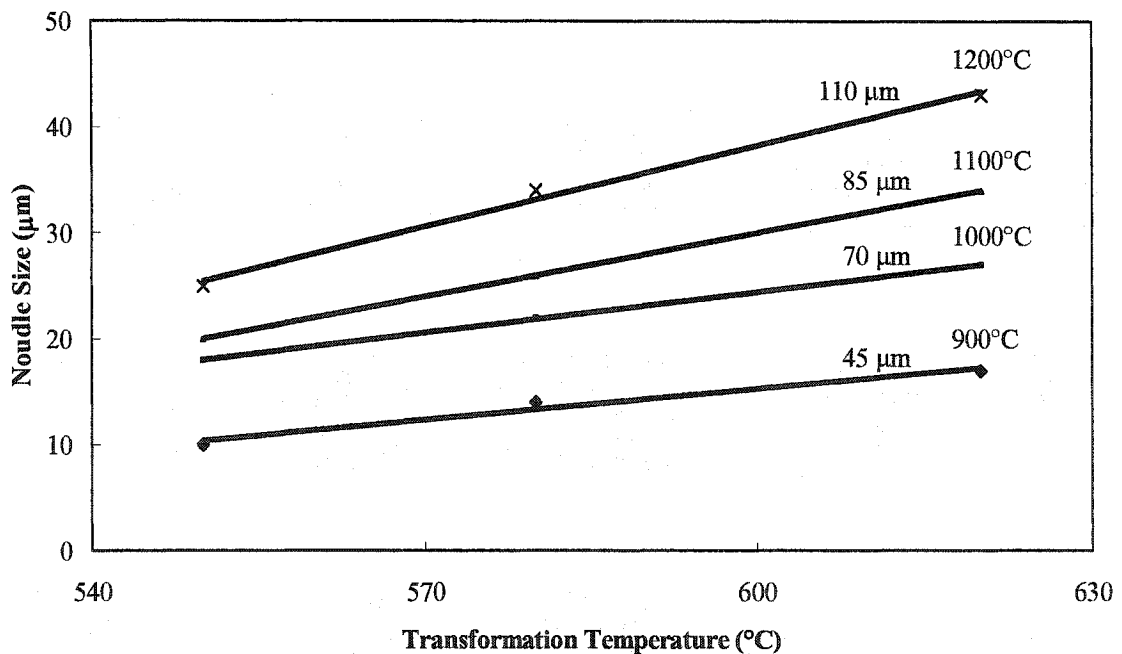


Figure (5-37) Effect of transformation temperature on nodule size for different prior-austenite grain sizes (reheat temperature) for steel E.

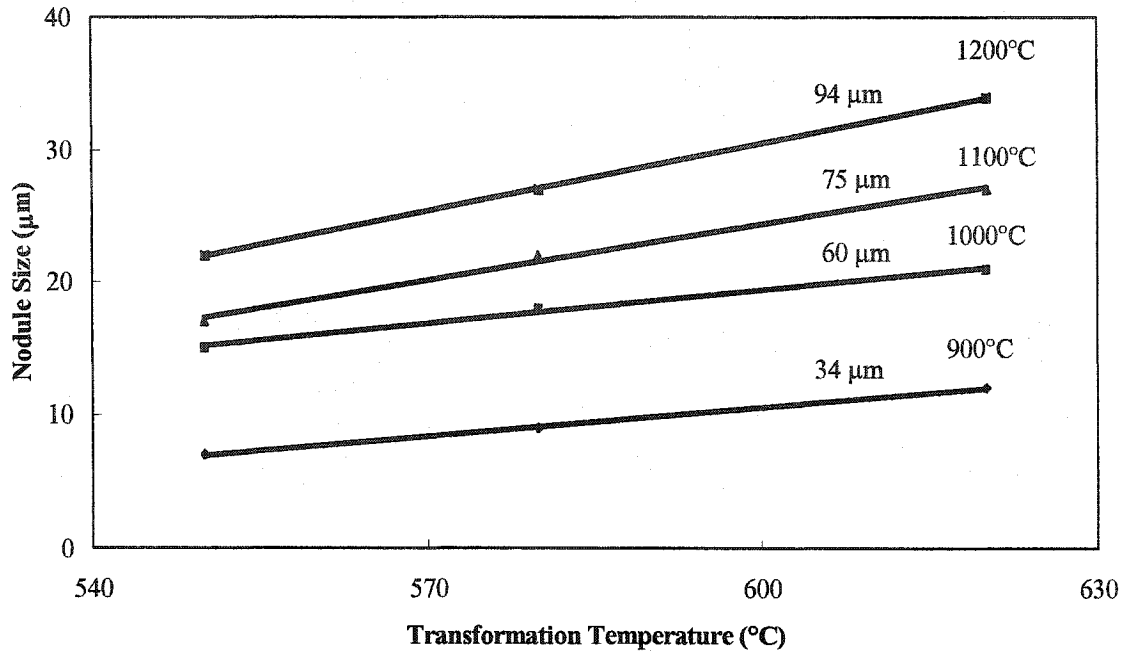


Figure (5-38) Effect of transformation temperature on nodule size for different prior-austenite grain sizes (reheat temperature) for steel A.

5.5.2. Heat treatment Effect on Pearlite Colony Size

The effect of reheat temperature on the pearlitic colony structure was investigated by plotting the pearlite colony size as a function of the prior-austenite grain size for steels A, B, C and E, as shown in Figure (5-39) for the 620°C transformation temperature. The change in pearlite colony size with prior-austenite grain size that was observed was within the 0.6 μm error in size measurement and thus a negligible effect was concluded for all the hypereutectoid steels investigated. This finding is in agreement with previous work by Pickering and Garbarz [72] who have reported that the prior-austenite grain size affects the morphology of pearlite nodules rather than the size of the colonies. Specifically, Garbarz and Pickering [216] have shown that the dependence of the pearlite colony size on the transformation temperature is similar to that of the interlamellar spacing variation with the transformation conditions. In their work, for a coarse prior-

austenite grain structure, the pearlite was shown to have a clear nodular microstructure, while with a finer austenite grain size, the pearlite was comprised of individual "units" limited to a few colonies [216]. Hence, Garbarz and Pickering [216] have reported that the austenite grain size has an effect on the transformation of the pearlitic structure from a nodular appearance at a grain size of 180 μm to one that is colonial for grain sizes less than 25 μm . In the present work, for the isothermal temperature condition of 900°C, it was observed that the nodular structure was slightly more difficult to identify for the microalloyed steels, probably due to the occurrence of this transformation in to a colonial structure on account of the finer austenite grain size (near 30 μm).

In present work, the effect of the transformation temperature on the pearlite colony size was determined for steels A, B, C and E as illustrated in Figure (5-40) for austenitizing conditions of 1200°C. For all the hypereutectoid steels examined, the pearlite colony size was determined to increase with increasing transformation temperature and the relationship appears to be similar to that reported in the work of Garbarz and Pickering [216]. The variation in the pearlite colony size with transformation temperature has been attributed to the dependence of the interlamellar spacing on cooling rate from the reheat temperature and the isothermal transformation temperature, of which only the latter was relevant for the present work. In particular, Marder and Bramfitt [62,63] have indicated that the apparent mechanism for pearlite transformation is volume diffusion, and, thus the interlamellar spacing, along with the pearlite colony size, is dependent on the growth velocity which in turn is related to the transformation temperature.

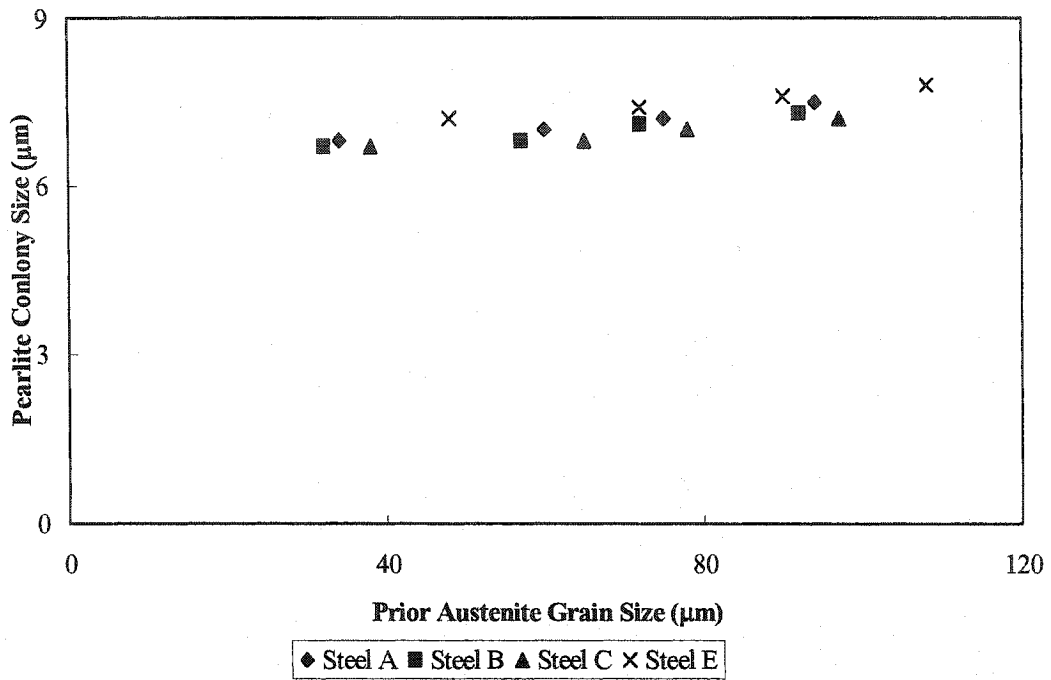


Figure (5-39) The effect of the prior austenite grain size on pearlite colony size in steels A, B, C and E.

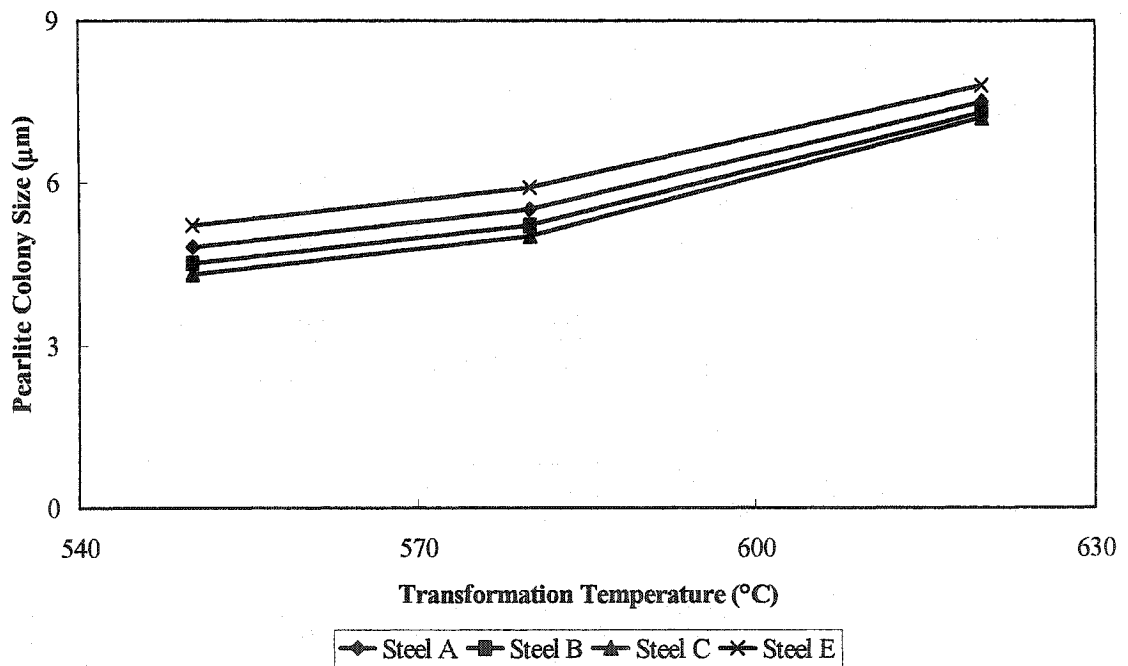


Figure (5-40) The effect of average pearlite transformation temperature on pearlite colony size in steels A, B, C and E.

5.6. Mechanical Properties

5.6.1. Heat treated Specimens

5.6.1.1. Strength

5.6.1.1.1. Hypereutectoid steel

The dependence of the yield strength of high carbon steels on pearlite spacing has been previously reported in the literature to following a Hall-Petch type relationship:

$$\sigma_y = \sigma_o + K_y S^{-m} \dots\dots\dots 5-35$$

The yield stresses calculated for the hypereutectoid steel using equation 5-35, by using the values of Hall-Petch parameters as listed in **Table 5-10**, are compared with the experimental data, in Figure (5-41). It can be seen that the data generated using equation 5-35 and the parameters generated from the 0.80% C steel underpredicted the strengths of this steel. On the other hand, the parameters derived from the 0.85% C steel give a slight overprediction of the strength. This discrepancy between the predictions is probably due to the grain boundary cementite that may give an additional strengthening effect, which is not included in Eq. 5-35.

Table 5-10 Some reported values of the Hall-Petch parameters

<i>C</i>	<i>Mn</i>	<i>Si</i>	<i>m</i>	σ_o	K_y	<i>Ref</i>
0.80	0.87	0.17	0.5	-45.0	7.2	61
0.85	0.67	0.18	0.5	-60	7.6	217

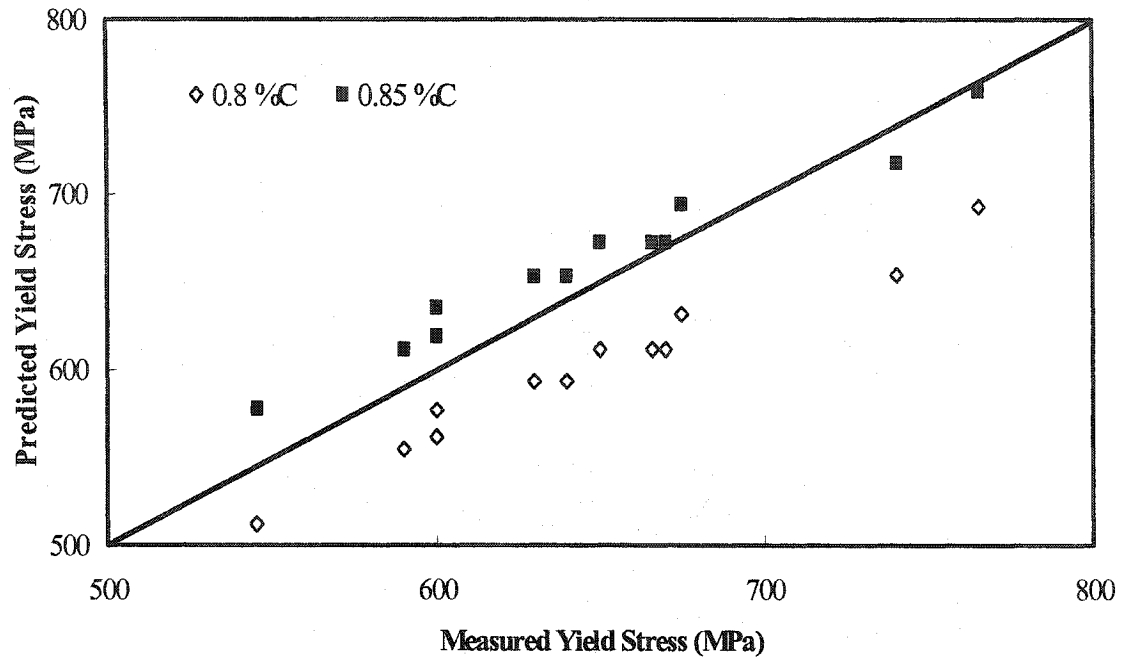


Figure (5-41) Predicted and measured yield stresses for two hypereutectoid steels. The line indicates a perfect correlation between predicted and measured values.

Hyzak and Bernstein [61] have suggested equation 5-36, to describe the relationship between yield stress and, not only the lamellar spacing, but also two other microstructural features in fully pearlitic microstructures, i.e. the pearlite colony size (P) and d , the prior austenite grain size, (in μm):

$$\sigma_{ys} = 2.18 S^{-1/2} - 0.4P^{-1/2} - 2.88 d^{-1/2} + 52.30 \dots\dots\dots 5-36$$

The yield stresses in the hypereutectoid steels of this work obtained by the calculation are compared with the experimental data in Figure (5-42) for different reheated temperature and transformation temperatures; these comparisons are also listed in Table 5-11. From Figure (5-42), it can be seen that the experimental data and the

predictions follow similar trends, although the predicted values are much lower than the experimental values. Again, this may be due to the grain boundary cementite in steel E, which seems to give an additional strengthening effect that has not been included in Eq. 5-36. From Table 5-11, it can be seen that, for the microstructures examined in this work, according to Eq. 5-36, the interlamellar spacing accounts for most of the yield strength, on average, 85 % of the yield stress, with the austenite grain size and pearlite colony size making up 6 and 3% of the yield stress. However, it is interesting to note that the Hyzak and Bernstein equation gives a much worse prediction compared to the simple interlamellar spacing relationships, despite the fact that more microstructural parameters have been considered by Hyzak and Bernstein. In fact, Hyzak and Bernstein did not explain the contributions to yield stress of either the pearlite colony size or the prior austenite grain size.

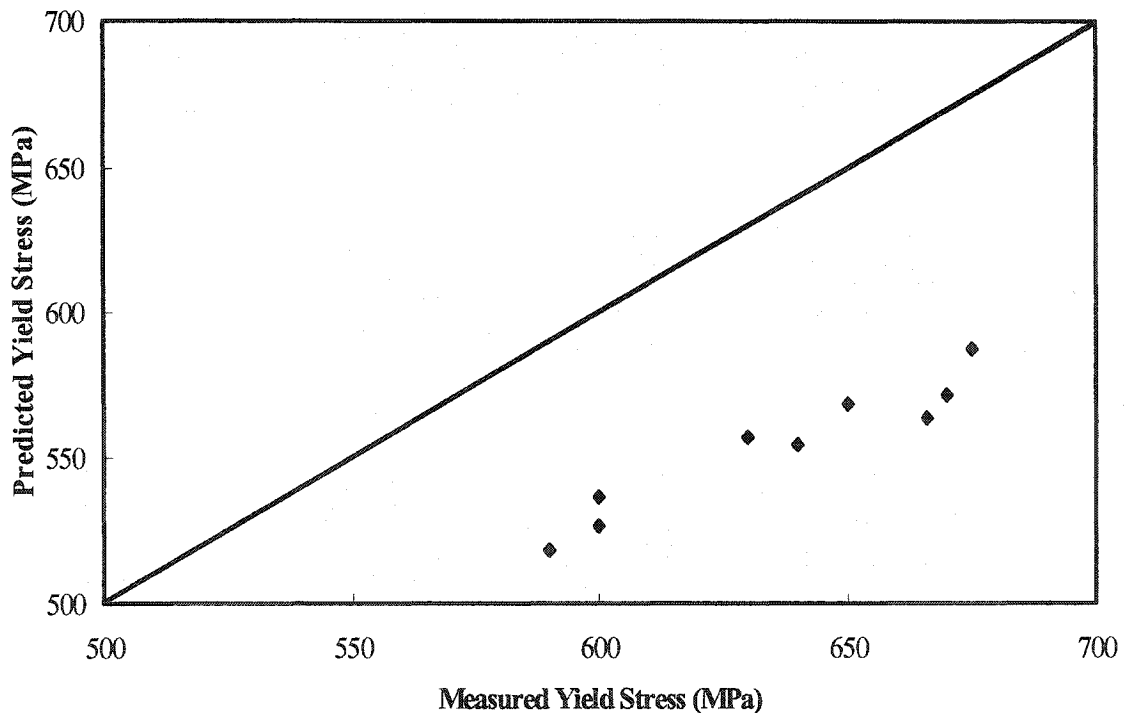


Figure (5-42) Predicted and measured yield stresses for hypereutectoid steel. The line indicates a perfect correlation between predicted and measured values.

Table 5-11 Yield Stress analyses for hypereutectoid steel

$2.18 S^{-1/2}$	$0.4 P^{-1/2}$	$2.88 d^{1/2}$	σ_0	σ_y
480.07	14.32	27.90	52.32	490.15
518.54	16.46	27.90	52.32	526.47
550.00	17.54	27.90	52.32	556.85
511.48	14.60	30.91	52.32	518.26
550.00	17.05	30.91	52.32	554.32
568.03	18.07	30.91	52.32	571.35
533.57	14.80	34.66	52.32	536.41
568.03	17.37	34.66	52.32	568.30
587.97	18.25	34.66	52.32	587.35
568.03	14.90	41.85	52.32	563.57
610.17	17.88	41.85	52.32	602.72
648.74	18.85	41.85	52.32	640.33

5.6.1.1.2. Vanadium and Silicon Steels

As mentioned in chapter 4, steel A, which had an intermediate V level and a low Si level was stronger than steel E, which had no V additions. Additions of V could strengthen pearlite by the formation of precipitates in the ferrite phase, which were detected by the FE-SEM microscope. Steel B, which had a higher Si and a lower V level, exhibited an increased strength over the plain C steel mainly due to the Si solid solution mechanism. Figures (4-46 and 4-47) showed that in steel C, which had an intermediate Si content and a high V level, the strength was greater than those obtained by equivalent separate additions of these elements, indicating an effect of both carbides and Si in solid solution.

The yield stresses calculated for steels A, B and C again using equation 5-35, by using the values of the Hall-Petch parameters as listed in Table 5-10, are compared with the experimental data, in Figure (5-43). Here, the parameters derived from the 0.80% C steel give a very good prediction of the strengths of these steels below 700MPa. However, above 700 MPa, the model underpredicted the strength. By contrast, the parameters generated from the 0.85% C steel gave overpredictions of the strength at low strength values, but gave a slightly better fit at strength levels above about 750 MPa. These results are consistent with an effect of grain boundary cementite, and precipitation strengthening. Thus, the microalloyed steels have no grain boundary cementite and, at low strength levels, have low levels of precipitation strengthening. Therefore, the equation for 0.8% C predicts the strengths well at the low end. The equation for the 0.85% C overpredicts because it includes the effect of grain boundary cementite. At the higher strength level, the 0.8% C model underpredicts because it does not take into account precipitation, whereas the 0.85% C model has a grain boundary cementite component in it, which partially 'accounts for' the precipitation strengthening. Since the 0.8% C prediction is good at the low strength levels, it thus appears that increased Si does not contribute strongly to the yield strength.

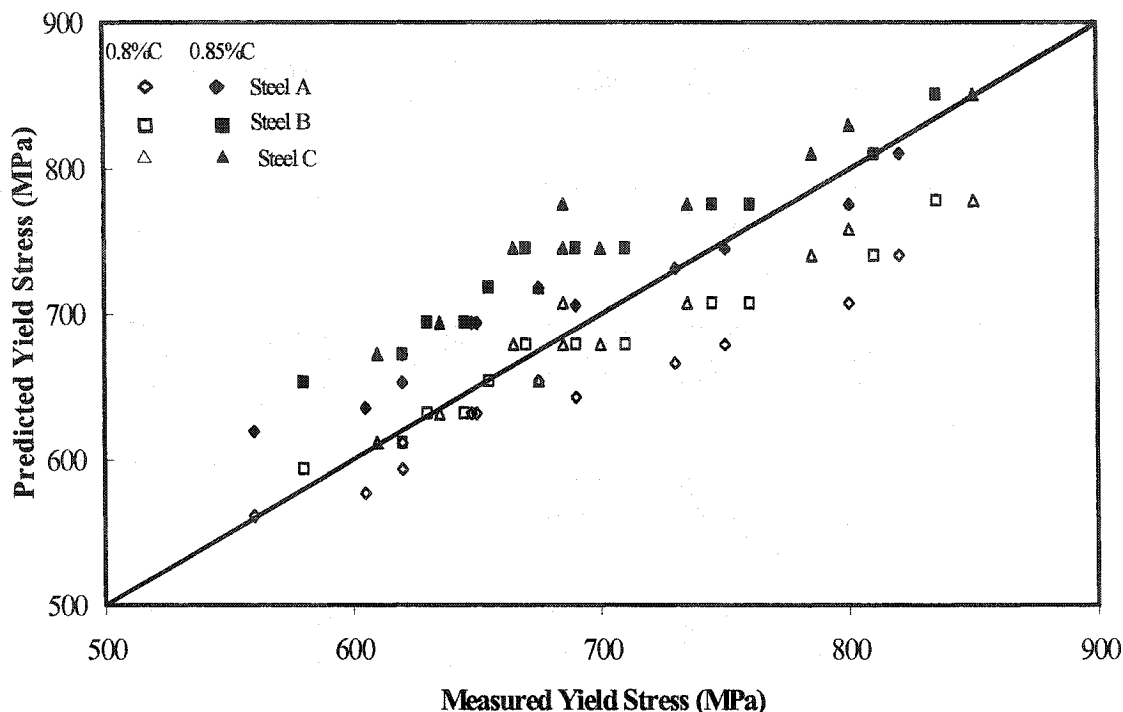


Figure (5-43) Predicted and measured yield stresses for steels A, B and C.

The yield stresses in steels A, B, C and E obtained by using equation 5-36 are compared with the experimental data in Figure (5-44) and reveal a number of differences between the predictions and the measured data. It is apparent from Figure (5-44) that the measured yield stress values of the steels used in this work were again generally higher than predicted. At yield stresses below 700 MPa, for all steels, the predictions are closer to the actual results. It is interesting to note that the Hyzak and Bernstein equation predicts the strengths of the microalloyed steels slightly better than the steel with no V or Si additions. The equation still underpredicts the strengths of these steels, probably because the effects of V precipitation are not included in the prediction. Also there is increasing deviation with increasing strength, which may be due to an increasing influence of V precipitates.

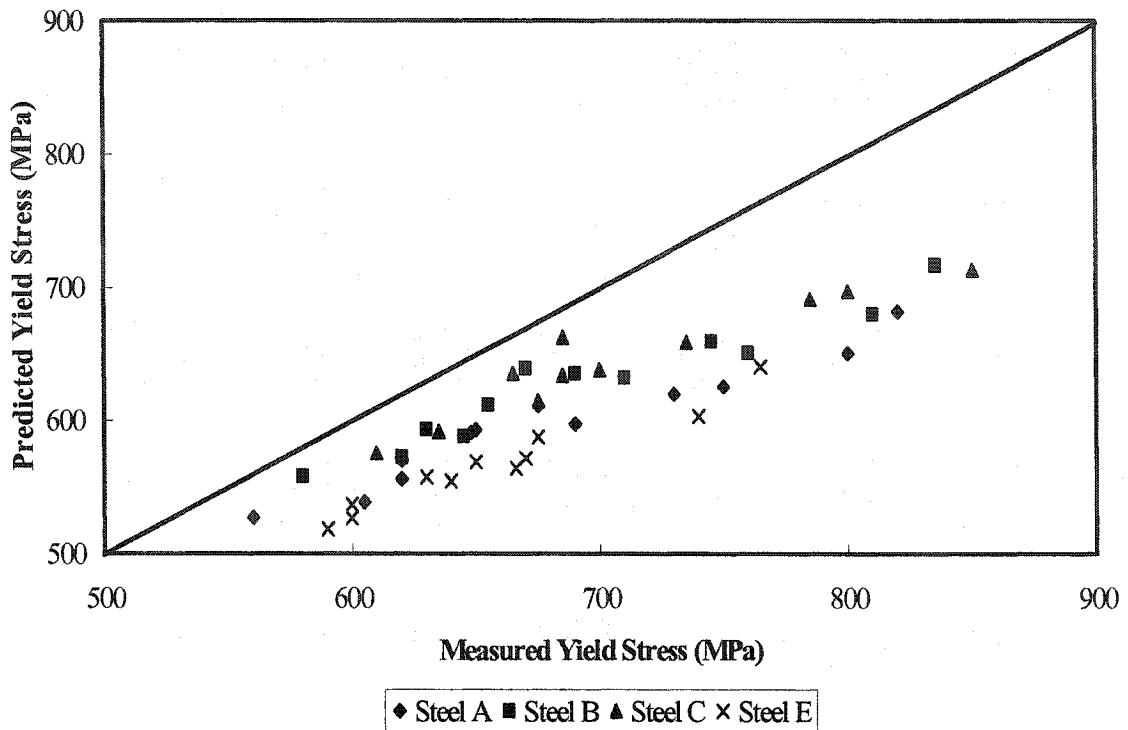


Figure (5-44) Predicted and measured yield stresses for steels A, B, C and E.

5.6.1.2. Ductility

Gladman et al. [147] indicated that the refinement of the pearlite colony size has a significant effect on toughness in high carbon steels, since the pearlite colony boundaries can act as obstacles to brittle crack propagation in much the same way as ferrite grain boundaries do. Similarly, the ductility can be improved by refining the austenite grain size. Both of these affect the interlamellar spacing. Therefore, both the strength and the ductility increase with decreasing interlamellar spacing as shown in Figure (5-45).

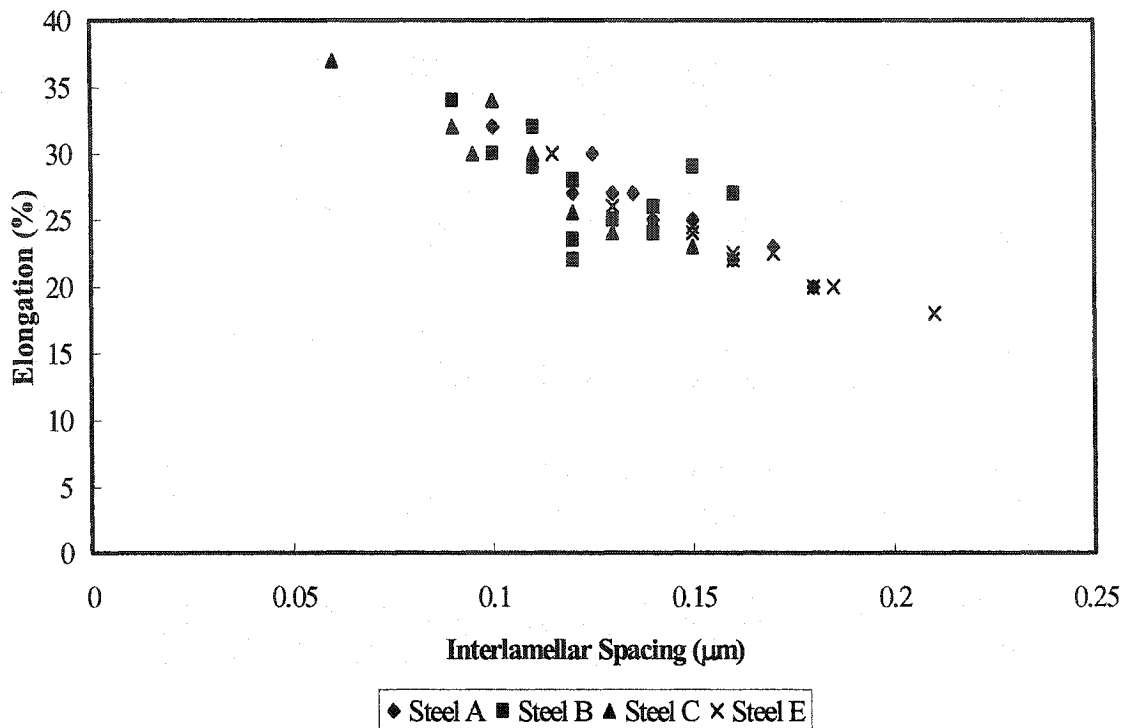


Figure (5-45) Elongation versus interlamellar spacing of pearlite for steels A, B, C, and E.

Hyzak and Bernstein [61] also generated an equation (Eq. 5-37) to describe the relationship between ductility (reduction of area) and microstructure in fully pearlitic steels:

$$R_a = 1.24 \times 10^{-1} S^{-1/2} + 2.66 \times 10^{-1} P^{-1/2} + 1.85 d^{-1/2} - 4.7 \times 10^1 \dots\dots\dots 5-37$$

The ductilities in steels A, B C and E obtained by the calculation are compared with the experimental data in Figure (5-46) for different reheat temperatures and transformation temperatures, and these are also listed in Table 5-12. There is again no exact match between the measured and predicted ductilities, but the trends are similar. At higher ductilities, there is a tendency for the model to predict higher ductilities than are actually measured. This may indicate that some of the mechanisms leading to

microstructural refinement are detrimental to ductility, for example, precipitation. Note that the steel that had been predicted as having the highest ductility is steel C, which has the highest V level. Interestingly, there seems to be no noticeable difference in the ductility of steel E, compared to the other steels, which suggests that there is no strongly negative effect of the grain boundary cementite on the ductility as measured by shear punch testing.

Examination of the regression coefficients indicates that the prior austenite grain size and pearlite spacing have similar influences on the ductility, with the pearlite colony size having a more modest effect.

Compared to Figure (5-45), the Hyzak and Bernstein equation does not appear to give a significantly improved fit to the data over the lamellar spacing alone.

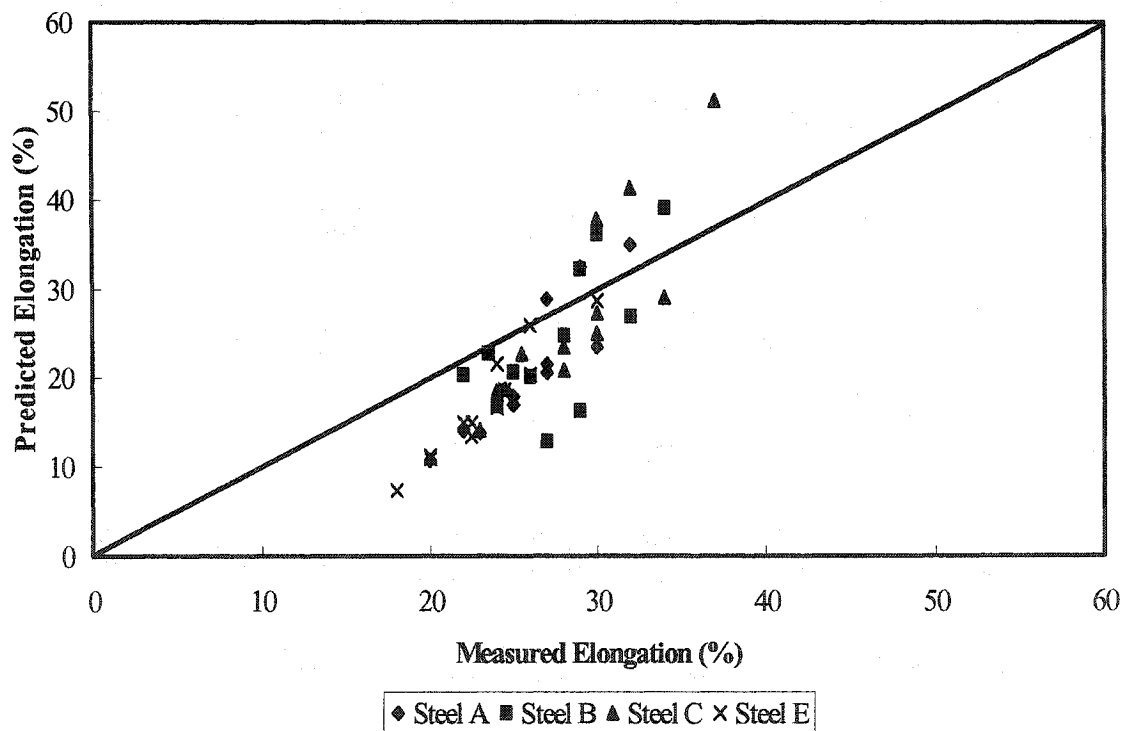


Figure (5-46) Predicted and measured elongations for steels A, B, C and E.

Table 5-12 Ductility analyses for hypereutectoid steel

$0.124 S^{1/2}$	$0.266 P^{1/2}$	$1.85 d^{1/2}$		%
27.05	9.52	17.80	47.1	7.28
29.22	10.95	17.80	47.1	10.87
31	11.66	17.80	47.1	13.36
28.82	9.71	19.72	47.1	11.16
31	11.34	19.72	47.1	14.96
32.01	12.01	19.72	47.1	16.65
30.07	9.84	22.11	47.1	14.93
32.01	11.55	22.11	47.1	18.58
33.14	12.14	22.11	47.1	20.29
32.01	9.913	26.70	47.1	21.53
34.39	11.89	26.70	47.1	25.88
36.56	12.53	26.70	47.1	28.70

5.6.2. Hot Deformed Specimens

5.6.2.1. Strength

5.6.2.1.1. Hypereutectoid steel

Again the equation from Hyzak and Bernstein does not match exactly with the experimental results, as shown in Figure (5-47), but certain trends are revealed. There is no effect of hot deformation, apart from generally refining the pearlite, and therefore creating higher strength microstructures.

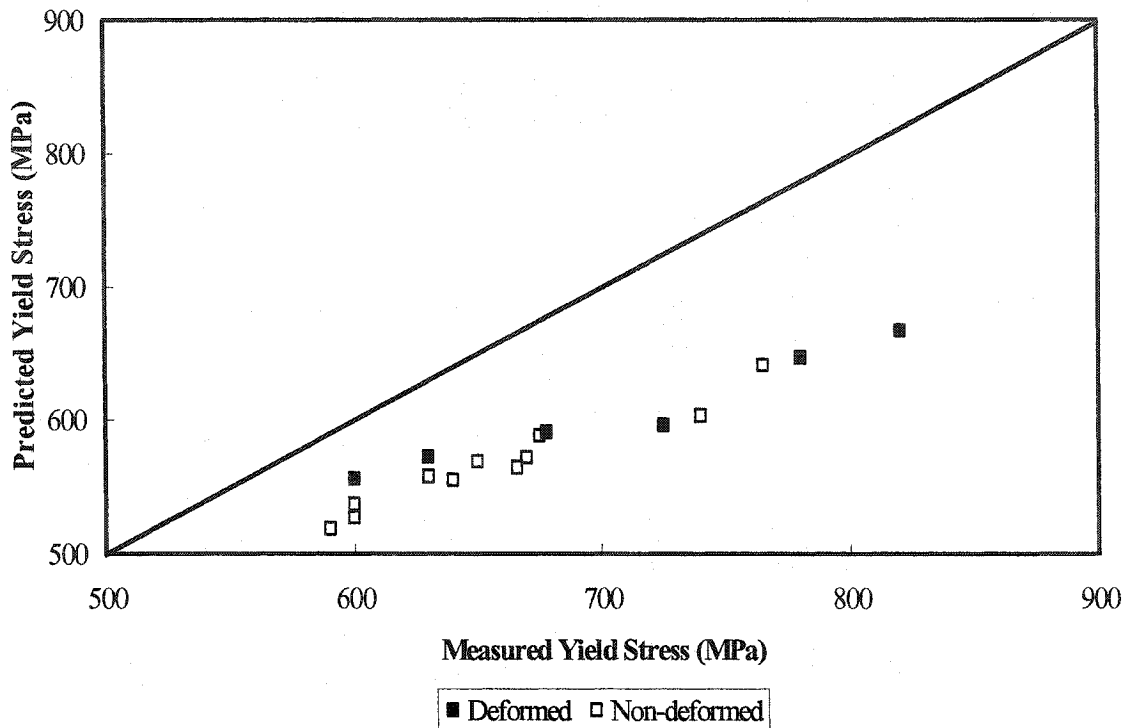


Figure (5-47) Predicted and measured yield stresses for hypereutectoid steel

5.6.2.1.2. Vanadium and Silicon Steels

Mechanical property evaluation of steels A, B, C and E indicates that increased strength values, when compared to the properties of the heat treated steels; these can be attributed to the refined interlamellar spacing, pearlite colony size, nodule size and austenite grain size.

Figure (5-48) is a plot of the predicted yield stress (from equation 5-36) versus the measured yield stress. Here, it can also be seen that the measured yield stress values of the steels used in this work were generally higher than the predicted yield stress values. It is interesting to note that the yield stresses of the hot deformed steels were slightly better predicted by the Hyzak and Bernstein equation, especially at the higher strength levels.

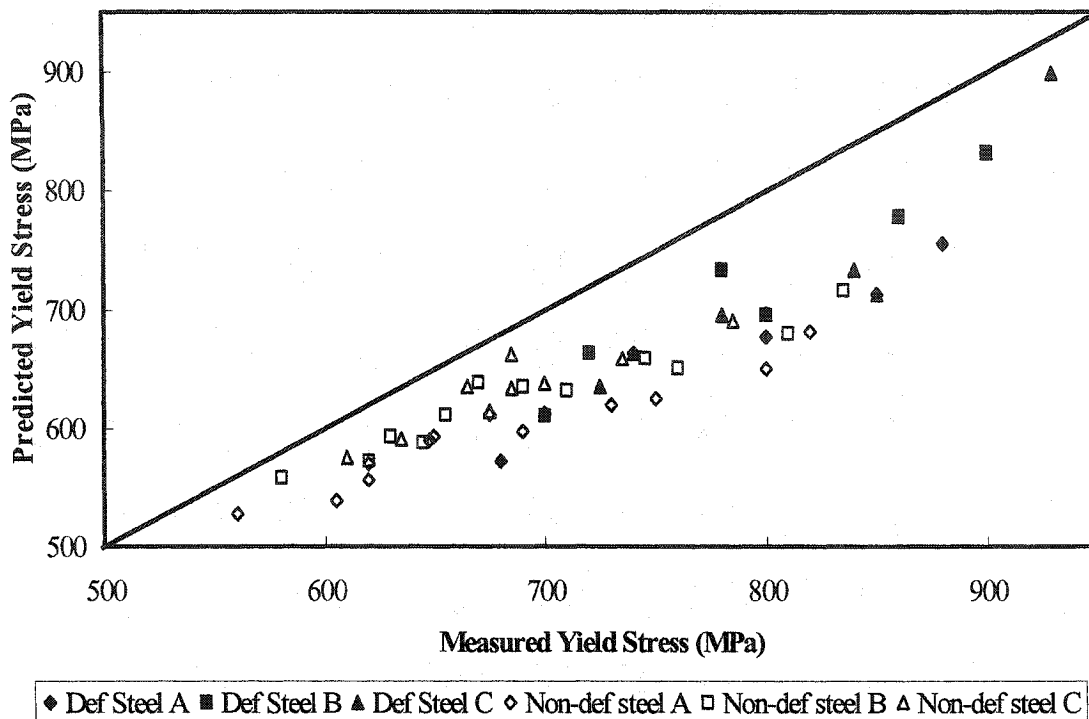


Figure (5-48) Predicted and measured yield stresses for steels A, B, C and E

5.6.2.2. Ductility

In general, the effect of hot deformation was to increase the ductility, mainly due to the generally refined pearlite structure. The elongation was plotted as a function of the interlamellar spacing for the various hypereutectoid steels (A, B, C and E), as shown in Figure (5-49) for different deformation processes. It can be seen that the ductility increases with decreasing interlamellar spacing.

Comparisons with the Hyzak and Bernstein ductility predictions for all the hot deformed steels are shown in Figure (5-50). Based on this analysis, it can be seen that there are two groups of data generated using equation 5-37. There was also some indication of similar behavior in the ductility of the heat treated specimens (Fig 5-46), but it was not as pronounced. This is probably due to the prior austenite grain size parameter

in equation 5-37, since, for each group, the austenite grain size is the same. When the austenite prior grain size parameter is removed from equation 5-37, the two groups of data converge, as shown in Figure (5-51). This indicates that the effect of prior austenite grain size is not adequately accounted for in equation 5-37. Indeed, Hyzak and Bernstein do not explain why the prior austenite grain size would affect the ductility.

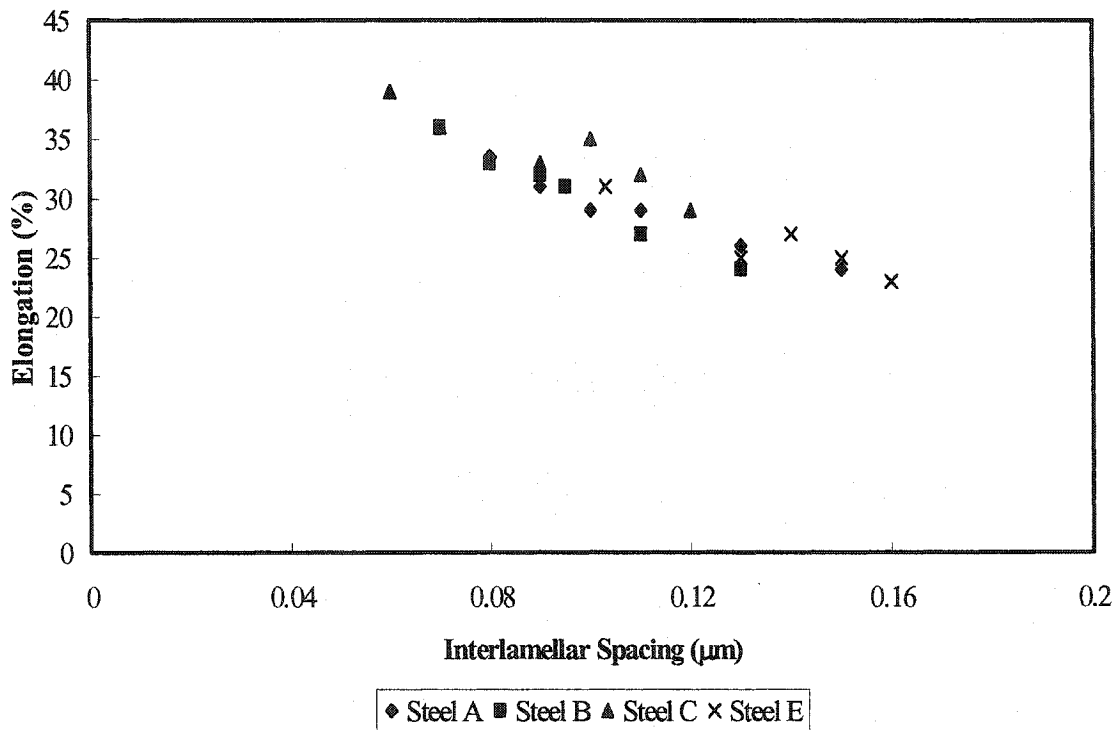


Figure (5-49) Elongation versus interlamellar spacing of pearlite for steels A, B, C and E

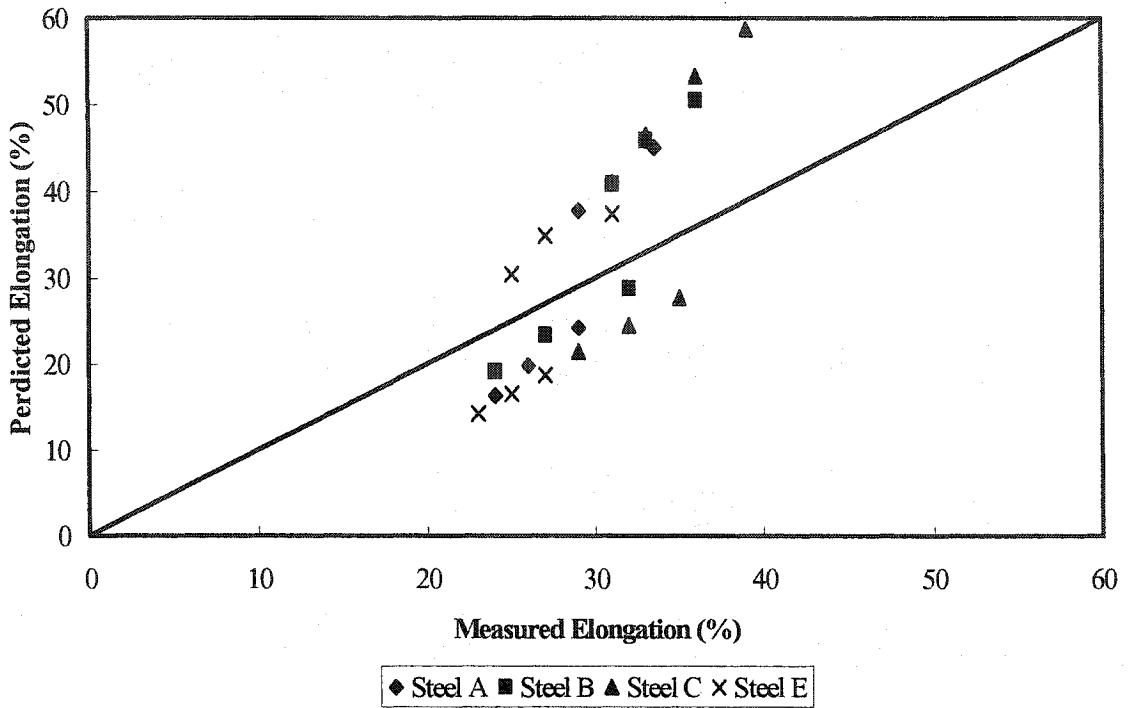


Figure (5-50) Predicted and measured elongations for steels A, B, C and E.

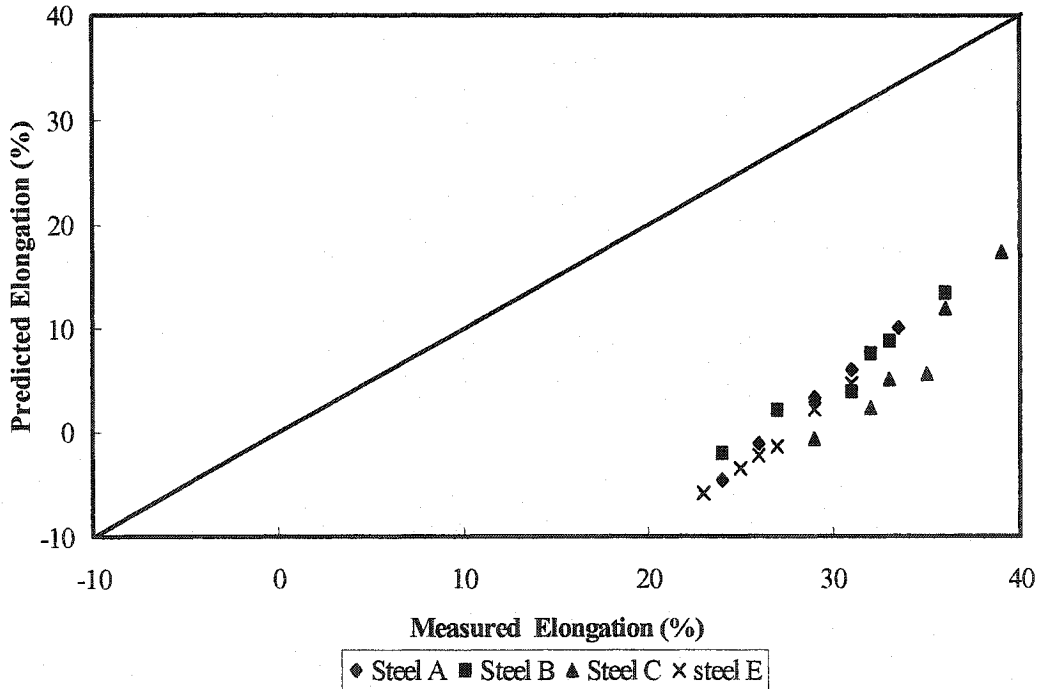


Figure (5-51) Predicted and measured elongations for steels A, B, C and E without the prior austenite grain size parameter.

CHAPTER 6

In this present research, dynamic recrystallization, static recrystallization and metadynamic recrystallization, were studied in plain carbon and microalloyed hypereutectoid steels. Microstructures and mechanical properties were also characterized. Based on the experimental results and the discussion, the following conclusions can be drawn regarding each of these topic areas:

Dynamic Recrystallization for Hypereutectoid Steels and Microalloyed Hypereutectoid Steels

1. Vanadium addition decreases the reheated austenite grain size.
2. The activation energy for deformation " Q_{def} " derived from the peak strain is lower than that from the steady state stress.
3. The activation energy for deformation " Q_{def} " in microalloyed hypereutectoid steels is higher than in plain carbon hypereutectoid steels.
4. There is a change in the temperature dependence of the peak strain at low temperatures this can be attributed to V (C, N) precipitation.
5. Higher concentrations of vanadium in solution increase the peak strain.

6. Equations to predict the peak strain and the dynamic recrystallization grain size for plain carbon and microalloyed hypereutectoid steels have been generated.

Static and Metadynamic Recrystallization for Hypereutectoid Steels and Microalloyed Hypereutectoid Steels

1. Equations to predict the metadynamic and static recrystallization kinetics and the recrystallization grain size for plain carbon and microalloyed hypereutectoid steels have been generated. These incorporate the effect of V and Si.
2. Comparison of the kinetics of metadynamic and static recrystallization shows that metadynamic recrystallization is the more rapid of the two.
3. The activation energies of metadynamic and static recrystallization are 136 and 270 kJ/mole, respectively.
4. Austenite recrystallization rates are decreased by the addition of V and Si.
5. Plateaus in the recrystallization kinetics appear to be due to the initiation and progress of strain-induced VC precipitation.
6. From the current results, it is very difficult to ascertain whether or not there is an influence of Si on the precipitation rate of VC.
7. The activation energy of the V steels was constant at temperatures higher than 940°C and 970°C for steels A, C and B respectively, and increased markedly as the temperature decreased below 940°C. This can be related to the precipitation of VC.
8. The precipitations start curves for VC precipitation derived from the Dutta-Sellars model does not match well with the experimental data.
9. A three-component kinetics model has been used to analyze the restoration. According to this model, when strained into the partial dynamic recrystallization region, the subsequent static softening arises from a linear combination of static and metadynamic recrystallization.

Microstructural and Mechanical Properties for Hypereutectoid Steels and Microalloyed Hypereutectoid Steels

1. The addition of vanadium significantly increases the flow stress of these steels, particularly at temperature below 800°C.
2. A grain boundary cementite network exists in hypereutectoid steels without vanadium and silicon additions.
3. The thickness of the cementite network increases with increasing reheat temperature. This is likely due to the larger austenite grain size reducing the grain boundary area available for proeutectoid cementite nucleation.
4. The nodule size is controlled by the transformation temperature and prior austenite grain size. The higher the transformation temperature and the coarser the prior austenite grain size, the larger is the nodule size.
5. Characterizing the nature of precipitates using the FE-SEM technique provides results similar to those obtained by transmission electron microscopy, but with a greater ease of sample preparation and statistical confidence.
6. By using low voltage imaging on a FE-SEM, spheroidal shape precipitates, between 20-30 nm, in microalloyed steels can be resolved.
7. The precipitates form in the ferritic lamellae with an aligned distribution of regular arrays that are separated by 10-20 nm.
8. The precipitates are characterized as being vanadium carbide.
9. Vanadium and silicon additions increase the strength and ductility of hypereutectoid steels through refinement of the microstructure.
10. Vanadium and silicon additions eliminate the cementite films along the prior austenite grain boundaries. This slightly decreases the strength for a given pearlite structure, but does not influence the ductility, as measured by shear punch testing.
11. Hot deformation improves the mechanical properties by microstructure; refinement, the strength is significantly higher than that of the heat-treated specimens, and the ductility is increased.

STATEMENT OF ORIGINALITY AND CONTRIBUTION TO KNOWLEDGE

1. The dynamic, static, and metadynamic recrystallization kinetics were determined for hypereutectoid steels with and without vanadium and silicon additions, for the first time.
2. A three-component model has been used exclusively in this work as the basis for analysis of the restoration curves obtained during the hot working of these steels. According to this model, when strained into the partial dynamic recrystallization region, the subsequent static softening arises from a linear combination of classical static and metadynamic recrystallization.
3. It was noted that current models do not effectively predict the precipitation behavior for VC formation, suggesting that, for these alloying additions new phenomena need to be considered.
4. The nature of the precipitates in the microalloyed steels was characterized using FE-SEM techniques, which was ascertained in this work to be as effective as TEM methods in resolving the dimensional and composition features of the particulates with the added benefits of simplicity and statistical confidence.
5. For the first time, the effect of reheat temperature on the cementite network thickness was determined. It was shown that the cementite network thickness increases with increasing reheat temperature; this is most likely due to the larger austenite grain size reducing the available grain boundary area that exists for proeutectoid cementite nucleation. This finding has considerable practical implications due to the role of the cementite thickness in strengthening.
6. A significant effect of the grain boundary cementite on the yield strength was found.

1. K. Han, G.D.W. Smith and D.V. Edmonds, *Metall., Trans.*, **26A** (1995), 1617.
2. A.D. Batte, D. V. Edmonds and R. W. K. Honeycombe, in "Strength of Metals and Alloys", Metals Park, OH, American Society for Metals, **2**, (1970), 585.
3. T. Gladman, D. Dulieu and I.D. McIvor, *Microalloying 75*, New York, Union Carbide, (1977), 56.
4. J.J. Jonas, C.M. Sellars and W.J. McG. Tegart, *Met. Rev.* **14**, (1969), 1
5. J.J. Jonas and M.J. Luton, *Advances in deformation processing*, eds. by J.J. Burke and V. Weiss, Plenum Publishing Corp. (1978), 215
6. Tamura, C. Ouchi, T. Tanaka and H. Sekine, *Thermomechanical Processing of High Strength Low Alloy Steels*, London, Butterworths, (1988), 32.
7. J.H. Beynon and C.M. Sellars, *ISIJ Int.*, **32**, (1992), 359.
8. W.L. Roberts, *Deformation Processing and Structure*, 1982 ASM Material Science Seminar, ed. By G. Krauss, (1982), 109.
9. C.M. Sellars, *Hot Working and Forming Processes*, ed. by C.M. Sellars and G. J. Davies, *Met. Soc.*, London, (1980), 3.
10. P.D. Hodgson, Ph.D. Thesis, University of Queensland, Australia, (1993).
11. T. Sakai and J.J. Jonas, *Acta Metall.*, **32**, (1984), 189
12. M.J. Luton and C.M. Sellars, *Acta Metall.*, **17**, (1969), 1033
13. T. Sakai, M.G. Akben and J.J. Jonas *Acta Metall.*, **31**, (1983), 63
14. J.P. Sah, G.J. Richardson and C.M. Sellars, *Metal Science*, **8**, (1974), 325
15. L. Blaz, T. Sakai, and J.J. Jonas, *Metal Science*, **8**, (1983), 609.
16. W. Roberts and B. Ahlblom, *Acta Metall.*, **26**, (1978), 801
17. J. Jaipal, C.H.J. Davies B.P. Wynne, D.C. Collinson, A. Brownigg, P. D. Hodgson *Proc. of Inter. Conf. Thermomechanical processing of steels, and other materials*, Wollongong, (1997), 539
18. S.-H. Cho, K.-B. Kang and J.J. Jonas, *Mater., Sci. & Techno.*, **18**, (2002), 389.
19. S. Serajzadeh and A. Karimi Taiher, *Materials and Design*, **23**, (2002), 271
20. J.J. Jonas and T. Sakai, *Les Traitements Thermomecaniques*, 24eme colloque de Metallurgie INSTN, Saclay, (1981), 35
21. R.W. Cahn, *Physical Metallurgy*, North Holland Publishing Co., Amsterdam, (1965), 925
22. R.W.K. Honeycombe, *The Plastic Deformation of Metals*, ASM, Metals Park, Ohio, (1984), 290.
23. C.M. Sellars and J.A. Whiteman, *Met. Sci.*, **13**, (1979), 187.
24. P.R. Barraclough and C. M. Sellars, *Met. Sci.*, **13**, (1979), 257.
25. M. Suehiro, K. Sato, H. Yada, T. Senuma, H. Shigefuji and Y. Yamshita, *THERMEC 88*, ed. by I. Tamura, (1988), 807.
26. S. Yada, *Proc. Int. Conf. on Phys. Metallurgy of Thermomechanical Processing of steels and other Metals*, Thermec 88, ed. I. Tamura, Tokyo, Japan ISIJ, (1988), 791
27. S.F. Medina and P. Fabregue, *J. of Mat. Sci.* **26**, (1991), 5427
28. E. Anelli, *ISIJ Int.*, **32**, (1992), 440
29. D.C. Collinson, P.D. Hodgson and C. H. J. Davies *THERMEC 97*, eds., by T. Chandra and T. Sakai, Wollongong Australia, (1997), 483.
30. H.J. Whittaker et. al *cstis suppl. Tans. Iron steel inst. Japan*, (1971), 11

31. K.J. Irvine, F.B. Pickering and T. Gladman *J. Iron Steel Inst.* **208**, (1970), 717
32. A. Grange, *Fundamental of deformation processing Syracuse university*, (1964), 299
33. T. Tanaka, T. Enami, M. Kimura, Y. Saito, and T. Hatomura, *Iron and Steel Institute of Japan* (1982), 14.
34. M G Akben and J.J. Jonas *HSLA steels Technology and application, Conf. Proc. ASM* (1984), 149
35. K.H. Chestnut, D.L. Baragar, J.D. Boyd, *Microalloyed Bar and Forging Steels*, Ed. by M. Finn, Hamilton, ON, (1990), 14.
36. T. V. Floros, A.A. Macchione and M.G. Akben, *HSLA steels*, eds D.P. Dunne and T. Chandra, South Coast Printers, (1985), 92
37. S. Yamamoto, C. Ouchi and T. Osuka, *Thermomechanical Processing of Austenite*, eds. A.J. DeArdo, G.A. Ratz. and P.J. Wary. TMS-AIME (1982), 613
38. J.N. Corde and R. E. Hook *Metall. Trans.* **1**, (1970), 111
39. M. Korchynsky and H. Stuart, *Symposium low alloy high strength steel Dusseld of metallurgy* (1970), 17
40. P. Choquet, P. Fabregue, J. Giusti, B. Chamont, J.N. Penzant and F. Blanchet, *Proc. Int. Sym. Mathematical Modelling Hot Rolling of Steel*, Hamilton ed. by S. Yue, CIM, (1990), 34
41. W. Roberts, A. Sandberg and T. Siwecki, *HSLA Steels Technology and Applications, Conf. Proc., ASM*, (1984), 67.
42. C. Roucoules, Ph.D. Thesis, McGill University, Montreal, (1992).
43. I.P. Kemp, P.D. Hodgson, and R.E. Gloss, *Proc. Conf. Modelling of Metal Rolling Processes*, London, (1993), 149.
44. C. Roucoules, S. Yue and J.J. Jonas *Proc. Conf. Modelling of Metal Rolling Processes*, London, (1993), 165
45. H.W. Mead and C.E. Birchenall, *Trans. AIME*, **206**, (1956), 1336
46. D.C. Collinson, P.D. Hodgson and B.A. Parker, *Modeling of Metal Rolling Processes*, IOM, London, (1993), 283
47. D.C. Collinson, P.D. Hodgson and C.H.J. Davies *Thermec 97, Wollongong Australia* (1997), 56
48. D.C. Collinson, P.D. Hodgson and B.A. Parker, *Advance in hot deformation textures and microstructures* ed by J.J. Jonas, T.R. Bieler and K.J. Bowman, TMS, Mass. (1993), 41
49. P.J. Wary, *Metal. Trans.* **13**, (1982), 125
50. K. Lx, P.D. Hodgson and D.C. Collinson, *ISIJ Int.*, **38**, (1998), 1121
51. P.D. Hodgson, L.O. Hazelden, D.L. Matthews and R.E. Gloss, *Microalloying 95, Conf. Proc. Pittsburgh, PA*, (1995), 341
52. Le Bon, J. Rofes-Vernis and C. Rossard, *Met. Sci.*, **9**, (1975), 36
53. T.V. Floros, *Master's Thesis McGill University*, 1984
54. P.R. Swann, *Electron Microscopy and Strength of Crystal*, ed. by G. Thomas and J. Washburn, NY, (1963), 131
55. T. Chandar, I. Weiss and J.J. Jonas, *Can. Metall. Quart.* **20**, (1981), 42

56. R.K. Amin and F.B. Pickering, Thermomechanical. Processing of Microalloyed Austenite, eds by A.J De Ardo et al. AIME Warrendal, Pa, (1982), 1.
57. S. Yamamoto, C. Ouchi and T. Osuka, Thermomechanical. Processing of Microalloyed Austenite, eds by A.J De Ardo et al. AIME Warrendal, Pa, (1982), 613.
58. M.J. White and W.S Owen Met. Trans. **11**, (1980), 597
59. A. Greday, Microalloying 75 Ed M. Korchynsky Union Carbide Corporation NY, (1977), 172
60. R.F. Mehl and W.C. Hagel, Prog. Met. Phys. **6**, (1956), 74
61. J.M. Hyzak, and I.M Bernstein, Metall. Trans., **7**, (1976), 1217
62. A.R. Marder and B. L. Bramfitt, Metall. Trans., **6**, (1975), 2009
63. A.R. Marder and B. L. Bramfitt, Metall. Trans., **7**, (1976), 365
64. N. Ridley, Metall. Trans., **15**, (1984), 1019
65. C. Zener, Trans. AIME **167**, (1946) 550
66. F.B. Pickering et al. Metall. Trans., **21**, (1987), 249
67. F.B. Pickering, in Toward improved ductility and toughness, (1971), 9
68. T. Gladman, I.D. McIvor and F.B. Pickering, J. iron steel inst., **210**, (1976), 916
69. N. Yamakoshi, Y. Nakamura and T. Kaneda wire journal, **10**, (1972), 36
70. K. Nakase and I. M. Bernstein, Metall. Trans. **9**, (1988), 2819
71. L.E. Miller and G.C. Smith, Journal of Iron and Steels Inst. (1970), 998
72. F.B. Pickering and B. Garbarz, Mater. Sci. and Techno, **5**, (1989), 227
73. F.B. Pickering the institute of Metals, London (1989), 10
74. J. Jaiswal and I.D. McIvor Ironmaking and steelmaking, **1**, (1989), 49.
75. R.K. Amin, M. Korchynsky, F.B. Pickering. Met. Techno., **8**, (1981), 250.
76. V.K. Heikkinen, J.D. Boyd, Can. Metall. Q, **15**, (1976), 219.
77. R.W. Pountain, J. Chipman, Trans. AIME, **212**, (1958), 737.
78. M. Korchynsky, Microalloying '95, ISS, Pittsburgh, (1995), 3
79. N.K. Balliger, R.W.K. Honeycombe, Metall. Trans. **11**, (1980), 421.
80. B. Garbarz and R. Kuziak, Microalloying '95, ISS, Pittsburgh, (1995), 409
81. N. Ridley, M. Dougan, G.W. Lorimer, Proc. of Intl. Symp. Phase Transformations During Thermal/Mechanical Processing of Steel, CIM, Vancouver, Aug. 20-24, (1995), 97
82. T. Malis, D. Parsons, and J.D. Boyd, HSLA Steels Technology and Applications, ASM, Metals Park, Ohio, (1983), 1129
83. A.M. Sage, in "Fundamentals of Microalloying Forging Steels, [Eds. by G. Krauss and S.K. Banerji] Warrendale, PA, (1986), 239.
84. F.A. Khallid and D.V. Edmonds, Proc. of Int. Symp. Microalloyed Bar & Forging Steels, CIM, (1990), 1
85. T. Kato et.al Fundamentals of Dual phase steels. Eds R.A. Kot and B.L. Bramfitt, TMS, Warrendale. PA, (1981), 199
86. G. Thomas and J. Y. Koo, structure and properties of Dual Phases Steels, eds R. A. Kot and J. W. Morris, TMS, Warrendale. PA, (1979), 183
87. A.P Coldren and G. T. Eldis, J. Met. **32**, (1980), 41
88. R.G. Davies Metall. Trans. **10**, (1979), 113

89. A.P Coldren, G. Tither, A. Cornford and J. R. Hiam, Formable HSLA and Dual Phase Steels, ed A. T. Davenport, TMS, Warrendale. PA, (1979), 205
90. A. Cornford, J.R. Hiam and R.M. Hobbs, SAE Trans. 88, (1979), 23
91. T. Tanaka, M. Nishida, K. Hashiguchi and T. Kato Structure and properties of Dual Phases steels, eds R. A. Kot and J. W. Morris, TMS, Warrendale. PA, (1979), 221
92. T. Furukawa, H. Morikawa, H. Takechi and K. Koyama, Structure and properties of Dual Phases steels, eds R. A. Kot and J. W. Morris, TMS, Warrendale. PA, (1979), 281
93. T. Tarui, T. Takahashi, S. Ohashi and R. Uemori. I&SM, (1994), 25
94. R. Lagneborg, O. Sandberg and W. Roberts, HSLA Steels-Metallurgy and Applications, Ed J. M. Gray, ASM International, (1986), 863
95. M.G. Akben, Ph.D Thesis, McGill University, Montreal, (1980)
96. H. Ohatani and F. Nakasato, American Society for Metals, Metals Park, Ohio, (1985), 169
97. G.E. Lucas Metall. Trans. 21, (1990), 1105
98. G.E. Lucas, J. W. Sheckherd, G. R. Odette and S. Panchanadeeswaran, Journal of Nuclear Materials, 122-123, (1984), 429
99. G.E. Lucas, G. R. Odette and J. W. Sheckherd, the Use of Small-Scale Specimens for Testing Irradiated, ASTM STP 888, Eds W.R. Corwin and G. E. Lucas, Philadelphia, USA, (1986), 112
100. P. Wanjara, Ph.D Thesis, McGill University, Montreal, (1999)
101. ASTM standard E112-96, Standard Test Methods for Determining Average Grain Size, Annual Book of ASTM Standards, Vol. 03.01, ASTM, Philadelphia, USA, 251.
102. E.E. Underwood Quantitative Stereology Addition-Wesley, Reading, MA (1970)
103. S.A. Saltykov, Stereometric Metallography, 2nd Edition, Metallurgizdat, Moscow, (1958)
104. R.W.K. Honeycombe, Steels Microstructure and Properties, Edward Arnold, London, (1981)
105. S. Serajzadeh and A.K. Taheri, Mat. Letters, 56, (2002), 984
106. S. Zajac, T. Siwecki, W.B. Hutchinson and R. Lagneborg, Mater. Sci. Forum, 284-286, (1998), 295
107. T. Wada, H. Wada, J.F. Elliot and J. Chipman, Metall. Trans. 3, (1972), 1657
108. S. Zajac, R. Lagnebry and T. Siwecki, Microalloying 95, ISS, (1995), 321
109. S. Nanba, M. Kitamura, M. Shimada, M. Katsumata, T. Inoue, H. Imamura, Y. Maeda and S. Hattori, ISIJ Int., 37, (1992), 377.
110. G. Anan, S. Nakajima, M. Miyahara, S. Nanba, M Umemoto, A Hiramatsu, A. Moriya and T. Watanabe: ISIJ Int., 37, (1992), 261.
111. C.M. Sellars: Proc. 7th Int. Symp. on Metallurgy and Materials Science. Eds. by N. Hansen et al, RisØ National Laboratory, Roskilde, Denmark, (1986), 167.
112. P. D. Hodgson and R.K. Gibbs: ISIJ Int., 32, (1992), 1329.

113. P.D. Hodgson and R.K. Gibbs: *Mathematical Modelling of Hot Rolling of Steel*, ed. by S. Yue, Hamilton, Ont., Canada, CIM, (1990), 76.
114. T. Senuma and H. Yada: *Proc. 7th Int. Symp. on Metallurgy and Materials Science*. eds. N. Hansen et al, RisØ National Laboratory, Roskilde, Denmark, (1986), 547.
115. A. Kirihata, F. Siciliano, Jr., T.M. Maccagno and J.J. Jonas: *ISIJ Int.*, **38**, (1998), 187.
116. M. Suehiro, K. Sato, T. Senuma, H. Yada, H. Shigefuji and Y. Yamashita *Proc. Int. Conf. on phys Metallurgy of Thermomechanical Processing of Steels and other Metals, Thermec 88*, ed. I. Tamura, Tokyo, Japan, ISIJ, (1988), 791
117. P.D. Hodgson Ph.D. Thesis, University of Queensland, Australia, (1993)
118. C. Roucoules, P.D. Hodgson, S. Yue and J.J. Jonas, *Metall. Trans.* **25**, (1994), 389
119. D.Q. Bai Ph.D. Thesis, McGill University, Montreal, Canada, (1993)
120. W.P. Sun and E. B. Hawbolt, *ISIJ Int.*, **36**, (1995), 908.
121. C. Roucoules, S. Yue and J.J. Jonas: *Metall. Trans.* **26**, (1995), 181.
122. B. Dutta and C.M. Sellars: *Met. Sci. Technol.*, **3**, (1987), 197.
123. S.F. Medina and J.E. Mancilla, *ISIJ Int.*, **36**, (1996), 1070
124. S.F. Medina, *J. Matr. Sci.* **31**, (1997), 1487
125. S. Kurokawa, J.E. Ruzzante, A.M. Hey and F. Dymont, *Metal. Sci.*, **17**, (1983), 433.
126. W.P. Sun E. B. Hawbolt and T. R. Meadowcroft: *36th MWSP*, (1994), 325.
127. S.F. Medina, A. Quispe, P. Valles and J.L. Banos, *ISIJ Int.*, **39**, (1999), 913.
128. W.J. Liu and J.J. Jonas, *HSLA steels 85*, *Inter. Conf. Beijing China*, ASM, 1985, 1
129. N. Ridley *Phase transformation in ferrous alloyed*, eds. A. R. Marder and J.I. Goldstein, New York, AIME, (1984), 201
130. R.W.K. Honeycombe, *Met. Trans.* **7A**, (1976), 915
131. S.A. Parson and D.V. Edmonds, *Mat., Sci. and Tech.* **3**, (1987), 894
132. B. E. O'Donnely, R. L. Reuben and T. N. Baker, *Metals Technol.* **11**, (1984), 45
133. S.A Hackney and G.J. Shiflet *Acta metal.* **35**, (1987), 1007
134. G. Fournalis *Mater. Sci. Forum*, **284-286**, (1998), 427
135. G. Fournalis and A.J. Baker *Electron Microscopy* **4**, (1990), 204
136. F. A. Khalid and D.V. Edmonds, *J. of Mater. Proc. Tech.* **72**, (1997), 436
137. N. Ridley, M.T. Lewis and W.B. Morrison, *Advances in the physical metallurgy and application of steels*, London, The Metal Society, (1982), 199
138. K. Han, Ph.D. Thesis, Oxford University, England, (1992).
139. K. Han, G.D. W. Smith and D.V. Edmonds in *Proc., Properties and application of Metallic and Ceramic Materials*, VI, ed M.H. Loretto and C.J. Becers, (1992), 855
140. K. Han, T.D. Mottishaw, G.D.W. Smith and D.V. Edmonds *Mater. Sci. and Tech.* **10**, (1994), 955

141. T.D. Mottishaw, G.D.W. Smith, in HSLA Steels Technology and Application, ed M. Korchynsky Metals Park, OH, (1984), 163
142. K. Velandar, B. Lehtinen and O. Sandbrg, Vanadium microalloyed steels for wire rod, Swedish Institute for Metals Research, Stockholm, (1986)
143. F.A. Khalid, D.V. Edmonds, *Mat., Sci. and Tech.* **9**, (1993), 384
144. K. Han, G.D. W. Smith and D.V. Edmonds, *Mat. Sci. and Tech.* **9**, (1993), 56
145. R. W.K. Honeycombe, *Metall. Trans.* **7**, (1976), 915
146. K. Han, T.D. Mottishaw, G.D.W. Smith and D.V. Edmonds, *Mater. Des.* **14**, (1993), 79
147. T. Gladman, I.D. McIvor and F.B. Pickering, *J. Iron steel Inst.* **193**, (1972) 916
148. C.M. Bae, C.S. Lee and W.J. Nam *Mater. Sci. Tech.* **18**, (2002), 1317
149. M. Suehiro, K. Sato, T. Senuma, H. Yada, H. Shigefuji and Y. Yamashita *Proc. Int. Conf. on Phys Metallurgy of Thermomechanical Processing of Steels and other Metals, Thermec 88*, ed. I. Tamura, Tokyo, Japan, ISIJ, (1988), 791
150. N.D. Ryan and H.J. McQueen, *Can. Met. Quart.*, **29**, (1990), 147
151. A. Laasraoui and J.J. Jonas, *Metall. Trans.* **22**, (1991), 1545
152. C.M. Sellars, *Mat. Sci. Tech.* **6**, (1990), 1072
153. M.G. Akben, T. Chandra, P. Plassiard, and J.J. Jonas, *Acta Metall.*, **32**, (1984), 591
154. O. Kwon and A.J. DeArdo, HSLA Steels, Metallurgy and Application, eds by J.M. Gray et al., ASM, Metals Parks, Ohio, (1985), 287.
155. G. Anan, S. Nakajima, M. Miyahara, S. Nanba, M Umemoto, A Hiramatsu, A. Moriya and T. Watanabe: *ISIJ Int.*, **37**, (1992), 261.
156. H.J. McQueen and J.J. Jonas, *Plastic Deformation of Materials* ed by R.J. Arsenault, Academic Press, N.Y. (1975), 393
157. C.M. Sellars, *Metals Forum*, **4**, (1981), 261
158. J.J. Jonas and C.M. Sellars *Proc. of ISS 10th Process Technology Conf.*, Toronto (1992), 67.
159. I. Weiss, T. Sakai and J.J. Jonas *Met. Sci.* **18**. (1984), 77.
160. T. Senuma and H. Yada, *Proc. 7th Int. Symp. on Metallurgy and Materials Science*. Eds. by N. Hansen et al, Denmark, (1986), 547.
161. O. Kwon, *ISIJ*, **32**, (1992), 350.
162. D.R. Barraclough and C.M. Sellars, *Metals Science*, **13**, (1979), 257.
163. A. Laasroui and J.J. Jonas, *Metall. Trans.*, **22**, (1991), 151.
164. C. Garcia-Mateo, B. Lopez, J.M. Rodriguez-Ibabe, *Mater. Sci. and Eng.* **A303**, (2001), 216.
165. I.P. Kemp, P.D. Hodgson, and R.E. Gloss, *Proc. Conf. Modelling of Metal Rolling Processes*, London, (1993), 149.
166. S.F. Medina and J.E. Mancilla, *ISIJ*, **36**, (1996), 1077.
167. M.G. Akben, B. Bacroix and J.J. Jonas, *Acta Metall.*, **31**, (1983), 161
168. S. Koyama, T. Ishii and K. Narita, *Japan Inst. Met. J.*, **35**, (1971), 1089.
169. A. Lassraoui, Ph.D. Thesis, McGill University, Montreal, (1990)
170. S.F. Medina and J.E. Mancilla, *Scripta Metallurgica et materialia* **3**, (1994), 315
171. C. Perdrix IRSID, *Recherche CECA* No. 7210-EA-311, (1987).

172. P. Choquet, B. De Lamberterie, C. Perdrix, and H. Biauxser, 4th int. Steel Rolling Conf. eds. Bfazan et. al IRSID/ATS, Deauville, France, **1**, (1987), B.5.1
173. J.W. Gibbs, the scientific papers of J.W. Gibbs, Longmans, Green and Co., New York, **1**, (1906), 252
174. L. Farker, Z. Physik. Chem., **125**, (1927), 236
175. R. Baker and W. Doering, Ann. der Physik, **24**, (1935), 719
176. R. Baker, Ann. der Physik, **32**, (1938), 128
177. J. Feder, K.C. Russell, J. Lothe and G.M. Pound Advan Phys, **15**, (1966), 111
178. M. Volmer and H. Flood, Z. Physik. Chem, **170**, (1934), 273
179. K.C. Russell Adv. Colloid interfaces Sci. **13**, (1980), 205
180. H.I. Aaronson and J.K. Lee Theory of Phases Transformation, ed H. I. Aaronson, TMS, Warrendale, PA, (1986), 83
181. B. Dutta and C.M. Sellars Mater. Sci. Tech., **3**, (1987), 197
182. J.H. Woodhead, Vanadium in high strength steel, London, Vanitec **3-10**, (1979).
183. M.G. Frohberg and H. Graf Stahl und Eisen, **80**, (1960), 539
184. W. Robert and A. Sandberg, Report I.M. 1489, Swedish Inst. for Metals Research, (1985).
185. K. Han Scripta Metallurgica et Materialia, **28** (1993) 699
186. S.F. Medina, J.E. Mancilla and C. A. Hernandez, ISIJ, **34**, (1994), 689
187. K.J. Irvine, F. B. Pickering and T. Gladman J. Iron and Steel Inst. **205**, (1967), 161
188. P.D. Hodgson, J.J. Jonas, and S.Yue, Proc. Conf. Processing Microstructure and Properties of Microalloyed and other Modern High Strength Low Alloy Steel, Pittsburgh, AIME, Warrendale, PA, (1991), 41
189. P.D. Hodgson, A. Brownrigg and S.H. Algie, Proc. Conf. "Recrystallization 90", ed. T. Chandra, TMS, Warrendale, PA, (1990), 41
190. R.A. Petkovic Ph.D. Thesis, McGill University, Montreal, Canada, (1975)
191. C. Roucoules, P.D. Hodgson, S.Yue and J.J. Jonas, Metall. Trans. **25**, (1994), 38
192. P.D. Hodgson, R.E. Gloss and D. Dunlop, 32nd MWSP Warrendale, PA, (1990), 527
193. S.F. Medina and J.E. Mancilla, ISIJ, **33**, (1993), 1257.
194. A.M. Elwazri, P. Wanjara and S. Yue, MWSP, 42nd, (2000), 3.
195. A.M. Elwazri, P. Wanjara and S. Yue, ISIJ, **43**, (2003), 1087
196. A.M. Elwazri, E. Essadiqi and S. Yue, ISIJ, **44**, (2004), 162
197. D.Q. Bai, S. Yue and J.J. Jonas Thermomechanical Processing of steel, COM 2000. Ottawa, ON, (2000), 669
198. M.J. Luton, R.A. Petkovic and J.J. Jonas Acta Metall. **28**, (1980), 729
199. P. Uranga, A.I. Fernandez, B. Lopez, J.M. Rodriguez-Ibabe, Mater. Sci. Eng. **A345**, (2003), 319
200. C. Roucoules, P.D. Hodgson, S. Yue and J.J. Jonas: Metall. Trans., **25A**, (1994), 389.

201. P. Choquet, P. Fabregue, J. Giusti, B. Chamont, J.N. Penzant and F. Blanchet Proc. Int. Symp. Mathematical Modelling of Hot Rolling of Steel, ed. S. Yue, Hamilton, Ont., (1990), 34.
202. R.A.P. Djaic and J.J. Jonas, *J. Iron Steel*, **210**, (1972), 156
203. S.F. Medina: *Scripta Metallurgica et Materials*, **32**, (1995), 43.
204. W. Roberts, A. Sandberg, T. Siwecki and T. Werlefors: *HSLA Steels Technology and Applications*, Proc. Conf. Philadelphia, ASM, (1983), 67.
205. Z. Xu and T. Sakai: *J. Japan Inst. Metals*, **55**, (1991), 1182.
206. Z. Xu, G. Rong and T. Sakai, *ISIJ*, **35**, 1995, 210.
207. M. Suehiro, K. Sato, T. Senuma, H. Yada, H. Shigefuji and Y. Yamashita Proc. Int. Conf. on Phys Metallurgy of Thermomechanical Processing of Steels and other Metals, Thermec 88, ed. I. Tamura, Tokyo, Japan, *ISIJ*, (1988), 791
208. E. Ruibal, J.J. Urcola and M. Fuentes, *Z. Metallkunde*, **16**, (1985), 568
209. F.A. Khalid and D.V. Edmonds *Scripta Metall. et Mater.* **30**, (1994), 1251
210. J.G. Zimmerman, R. H. Aboron and E.C. Bain, *Trans. ASM*, **25**, (1937), 755
211. M. Dollar, I.M. Berstein and A.W. Thompson, *Acta Metall.*, **36**, (1988), 311
212. T.D. Mottishaw and G.D.W. Smith *HSLA Steels Technology and Applications*, Inst. Conf. Proc. Philadelphia, ASM International, (1983), 163
213. K. Han, G.D.W. Smith and D.V. Edmonds *Metall. And Mat. Trans.* **26A**, (1995) 1617
214. F.C. Hull and R.F. Mehl *Trans. ASM*, **30**, (1942), 381
215. F.C. Hull, R.A. Colten and R.F. Mehl *Trans. AIME*, **150**, (1942), 185
216. B. Garbarz, F.B. Pickering, *Scr. Metall.*, **21**, (1987), 2493
217. K.K. Ray and D. Mondal, *Acta Metall.*, **39**, (1991), 2201